Universidade do Minho
Escola de Engenharia

Ricardo Falcão de Oliveira

Study and development of a holding
chamber for inhalation

April, 2016

Universidade do Minho
Escola de Engenharia

Ricardo Falcão de Oliveira

Study and development of a holding
chamber for inhalation

April, 2016

STATEMENT OF INTEGRITY

I hereby declare having conducted my thesis with integrity. I confirm that I have not used plagiarism or any form of falsification of results in the process of the thesis elaboration.

I further declare that I have fully acknowledged the Code of Ethical Conduct of the University of Minho.

University of Minho, _____

Full name: Ricardo Falcão de Oliveira

Signature: _____

This page was intentionally left in blank

"The first law of thermodynamics says that work is indestructable.

We who use computers know better."

— author unknown

This page was intentionally left in blank

Acknowledgements

Acknowledgements

Abstract

Asthma is a respiratory disease that causes chronic airway inflammation. Affecting more than 300 million individuals worldwide, it is a growing public health hazard. Inhalation therapy is the preferred strategy for medication delivery. This therapy is executed through specific delivery devices, whereas the pressurized Metered-Dose Inhaler (pMDI) is one of the most preferred. However, the pMDI efficiency is highly dependent on a correctly executed inhalation procedure. For children under 5 years old (or elderly individuals), it is advisable to use the pMDI coupled with an add-on device (i.e. spacer). Within the spacers, the Valved Holding Chamber (VHC) is the mostly used, due to its good capacity to reduce the pMDI spray coarse fraction and the oral-pharyngeal deposition ($\approx$80%). Additionally, the VHC's one-way valve allows the patient to maintain his tidal breathing during treatment. The VHC typically delivers a Fine Particle Mass (FPM) that is $\approx$20% of the labelled dose. Several design characteristics dictate the VHC performance, such as, the dimensions and the materials. The study herein focus on the assessment of eight commercial VHCs, through experimental and numerical methods. An experimental setup was developed, allowing the evaluation of the devices at constant flow rate (30 L/min and 60 L/min) and at variable flow (sine breath pattern). The waveform was obtained through a breathing simulator specially developed for this purpose, based in a cam-follower mechanism. The salbutamol sulphate (i.e. Ventolin) was collected using a cascade impactor (i.e. MSLI), and assessed by UV-Vis spectrophotometry analysis. Several metrics, regarding VHC performance, were calculated. Results have shown that the VHC capacity reduce the oral-pharyngeal deposition (64% - 94%), which is deeply related with the VHC valve design. It was observed that the VHC reduces the plume coarse fraction ($\approx$70%), keeping the FPM bioequivalent to the pMDI solo. A correlation between the fine particle fraction and the volume of air passing through the VHC was proposed. Patient relevant metrics were suggested to classify the

Abstract

VHC devices upon quantitative and qualitative characteristics. A Computational Fluid Dynamics (CFD) model was developed where the air flow (i.e. 60 L/min)) was calculated along with the pMDI spray modelling as a discrete phase. The spray particle-wall interaction was modelled using different approaches and compared against literature and experimental data. This study, shed some light upon the spray evaporation process inside the VHC, showing that the efficiency of evaporation process is related with the VHC volume. A new VHC design, based in CFD dimensional optimisation of the VHC body is proposed, which shows an improvement of the FPM delivered.

Palavras chave: Asthma Treatment; Valved Holding Chamber (VHC); pressurized Metered-Dose Inhaler (pMDI); Performance; Computational Fluid Dynamics (CFD); Design.

Resumo

A asma é uma doença respiratória que causa a inflamação crónica das vias aéreas. Mundialmente, afeta mais de 300 milhões de indivíduos e é um problema crescente de saúde publica. A terapia de inalação é a estratégia preferida para administrar a medicação de controlo ou de alívio. Esta terapia é executada através de dispositivos específicos, entre os quais o Inalador Pressurizado com Válvula Doseadora (IPVD) é o mais usual. Contudo, a eficiência do IPVD é dependente de uma técnica de inalação correta. Para crianças com menos de 5 anos (ou idosos), é recomendável o uso do IPVD acoplado a um espaçador. Entre os espaçadores, a Câmara Expansora (CE) é a mais utilizada, devido à sua boa capacidade de redução das partículas grandes do aerossol do IPVD, e da redução da deposição orofaríngeal ($\approx$80%). Adicionalmente, a válvula de sentido único da CE, permite que o paciente mantenha a sua respiração normal durante o tratamento. A CE emite, tipicamente, uma massa de partículas finas (MPF) que é $\approx$20% da dose calibrada do IPVD. Este estudo foca-se na avaliação de oito CEs, através de uma metodologia experimental e numérica. Uma instalação experimental foi projetada para a avaliação dos dispositivos a fluxo constante (30 L/min e 60 L/min) e variável (um padrão respiratório sinusoidal). A onda foi obtida através de um simulador respiratório especialmente desenvolvido para este propósito, o qual foi baseado num mecanismo cam-seguidor. O sulfato de salbutamol (Ventilan HFA) foi recolhido utilizando um impactor em cascata em vários estágios (Aparelho C da Farmacopeia Portuguesa), e quantificado por espetrofotometria UV-Visivel. Foram calculadas várias métricas sobre o desempenho das CEs. Os resultados demonstram a capacidade da CE para reduzir a deposição orofaríngeal (64% - 94%), a qual está intrinsecamente relacionada com o design da válvula do dispositivo. Foi observado que a CE reduz a fração de partículas grandes na pluma ($\approx$70%), mantendo a MPF bioequivalente à emitida pelo IPVD. Foi proposta uma correlação entre a fração de partículas finas e o volume de

Resumo

ar que atravessa a CE. Foram também sugeridas métricas com relevância para o paciente, que classificam as CEs de forma quantitativa e qualitativa. Foi desenvolvido um modelo de Dinâmica Computacional de Fluidos (DCF), onde o fluxo de ar (a 60 L/min) foi calculado juntamente com o aerossol do IPVD, tendo sido este modelado como uma fase discreta. A interação entre partícula e parede foi modelada utilizando diferentes aproximações matemáticas, sendo posteriormente comparadas com a literatura e dados experimentais. Este estudo contribui com um melhor conhecimento do processo de evaporação das gotas do aerossol dentro da CE, onde se verificou que este processo está relacionado com o volume da CE. Foi proposto em novo design para CE, baseado numa otimização das dimensões do corpo da CE, que demonstra melhoria da MPF emitida.

Palavras chave: Tratamento da Asma; Câmara Expansora (CE); Inalador Pressurizado com Válvula Doseadora (IPVD); Desempenho; Dinâmica Computacional de Fluidos (DCF); Design.

Contents

Contents

Contents

List of Figures

List of Tables

List of Symbols

Latin Symbols

a - resultant acceleration [m/s^2]

A_c - area of contact [m^2]

A_p - particle surface area [m^2]

c_1, c_2, c_3 - coefficient for slip correction adjustment factor [-]

c_p - specific heat [J/kg·K]

$c_{p,\infty}$ - heat capacity of the bulk phase [J/kg·K]

C_c - Cunningham slip correction factor [-]

C_D - drag coefficient [-]

$C_{i,s}$ - vapour concentration at the droplet surface [mol/m^3]

$C_{i,\infty}$ - vapour concentration in the bulk phase [mol/m^3]

C_{lim} - coefficient of limitation for turbulence production [-]

C_L - length constant [m]

$C_{r,1}$, $C_{r,2}$, $C_{r,3}$ - coefficient of of curvature correction [-]

C_R - restitution coefficient [-]

d_p - particle diameter [m]

$D_{i,m}$ - mass diffusion coefficient for species i [m^2/s]

D_{inlet} - inlet diameter [m]

D_{min} - minimum diameter in the geometry [m]

$D_{T,i}$ - thermal diffusion coefficient for species i [m^2/s]

e_a - approximate relative error [-]

e_{ext} - extrapolated relative error [-]

List of Symbols

E - energy [J]

E_p - particle material Young Modulus [Pa]

E_w - wall material Young Modulus [Pa]

$\vec{F}$ - external body force [N]

F_A - attraction force [N]

F_D - drag force [N]

$F_{D,wall}$ - drag force for a particle resting in the wall [N]

F_g - gravitational force [N]

F_L - lift force [N]

F_x - axial component of the force [N]

$\vec{g}$ - gravity acceleration vector [m/s^2]

G_k - generation of k [kg/m·s^3]

G_ω - generation of ω [kg/m^3·s^2]

h - convective heat transfer coefficient [W/m^2·K]

h_{fg} - latent heat [J/kg]

h_j - sensible enthalpy for species j [J/kg]

I - unit tensor [-]

$\vec{J_i}$ - mass diffusion of species i [kg/m^2·s]

$\vec{J_j}$ - diffusion flux of the species j [kg/m^2·s]

k - turbulent kinetic energy [m^2/s^2]

k_c - mass transfer coefficient [m/s]

k_{eff} - effective conductivity [W/K·m]

k_p - particle material coefficient [-]

k_t - turbulent thermal conductivity [W/K·m]

k_w - wall material coefficient [-]

k_∞ - thermal conductivity of the bulk phase [W/K·m]

K - elastic constant [-]

Kn - Knudsen number [-]

L_e - eddy length [m]

m_p - particle mass [kg]

$M_{w,i}$ - molecular weight of species i [kg/mol]

N_i - molar flux of vapour [mol/m^2·s]

p - static pressure [Pa]

p_m - apparent order of the method [-]

p_{sat} - saturation pressure [Pa]

Q - volume flow rate [m^3/s]

r - radial coordinate [m]

r_{mesh} - grid refinement factor [-]

R - universal gas constant [J/mol·K]

Rc - coarse mass ratio [-]

Re - Reynolds number [-]

Re$_t$ - turbulent Reynolds number [-]

Re - extra-fine mass ratio [-]

Re$_p$ - particle Reynolds number [-]

Rf - fine mass ratio [-]

R_t - tangential lift-off ratio [-]

S - modulus of the mean rate-of-strain tensor [1/s]

S_h - other heat sources [W/m^3]

S_i - rate of creation of species i [kg/s·m^3]

S_m - mass source [kg/s·m^3]

Sc - Schmidt number [-]

Sc$_t$ - turbulent Schmidt number [-]

Sh$_{AB}$ - Sherwood number [-]

Stk - Stokes number [-]

t - time [s]

t_{cross} - time a particle takes to cross the eddy [s]

t_L - eddy lifetime [s]

T - temperature [K]

List of Symbols

T_{bp} - boiling point temperature [K]

T_p - particle temperature [K]

T_{ref} - reference temperature (298.15 K)

T_{vap} - vaporisation temperature [K]

T_∞ - ambient temperature [K]

U_{inlet} - mean velocity at the inlet [m/s]

$\vec{v}$ - velocity vector [m/s]

v_* - velocity made dimensionless by the k [-]

v_f - fluid velocity [m/s]

v_x - axial component of the velocity [m/s]

v_r - radial component of the velocity [m/s]

$\vec{v}_i$ - velocity vector component i [m/s]

v'_i - velocity fluctuation component i [m/s]

v_p - particle velocity [m/s]

V_C - critical velocity [m/s]

V_f - final velocity [m/s]

V_i - initial velocity [m/s]

V_T - tidal volume [m^3]

x - axial coordinate [m]

X_i - mole fraction of species i in the bulk phase [-]

y - distance to the wall [m]

y^+ - distance to the wall made dimensionless by the friction velocity [-]

y^* - distance to the wall made dimensionless by the k [-]

Y_k - dissipation of k [kg/m·s^3]

Y_ω - dissipation of ω [kg/m^3·s^2]

Y_j - mass fraction of species j [-]

Greek

α - slip correction adjustment factor [-]

Δt - time interval [s]

ε - turbulent dissipation rate [m^2/s^3]

ϕ_k - solution value in the k grid [variable dependent]

ϕ_{ext} - extrapolated solution value [variable dependent]

Γ_k - effective diffusivity of k [kg/m·s]

Γ_ω - effective diffusivity of ω [kg/m·s]

γ - shear rate [1/s]

κ - viscosity ratio [-]

λ - mean free path of a gas molecule [m]

μ, μ_f - fluid viscosity [kg/m·s]

μ_p - particle viscosity [kg/m·s]

μ_t - turbulent viscosity [kg/m·s]

ν_f - fluid kinematic viscosity [m^2/s]

ν_p - particle material Poisson's ratio [-]

ν_w - wall material Poisson's ratio [-]

θ - angle [rad]

ρ - density [kg/m^3]

ρ_f - fluid density [kg/m^3]

ρ_p - particle density [kg/m^3]

$\bar{\bar{\tau}}$ - stress tensor [Pa]

τ_p - particle relaxation time [s]

τ_w - wall shear stress [Pa]

ω - specific dissipation rate [1/s]

Ω - vorticity rate [1/s]

This page was intentionally left in blank

Acronyms

A2A A2A Spacer

ABS Acrylonitrile Butadiene Styrene

AC AeroChamber

AIT "Alberta" idealized adult anatomic throat

ANOVA Analysis Of Variance

API Active Pharmaceutical Ingredient

APSD Aerodynamic Particle Size Distribution

ASME American Society of Mechanical Engineers

BPM Breaths Per Minute

BSA Burst Spectrum Analyser

CAD Computer Aided Design

CDF Cumulative Distribution Function

CFC ChloroFluoroCarbon

CFD Computational Fluid Dynamics

CI Cascade Impactor

CNC Computerized Numerical Control

COPD Chronic Obstructive Pulmonary Disease

CPF Coarse Particle Fraction

CPM Coarse Particle Mass

CSC Compact Space Chamber

DEM Discrete Element Method

DNS Direct Numerical Simulation

DOE Design Of Experiments

DOF Degrees Of Freedom

DPI Dry Powder Inhaler

DPM Discrete Phase Model

DRW Discrete Random Walk

EFPF Extra-Fine Particle Fraction

EFPM Extra-Fine Particle Mass

EIM Eddy Interaction Model

ERV Expiratory Reserve Volume

EWT Enhanced Wall Treatment

FD Full Dose

FPD Fine Particle Dose

FPF Fine Particle Fraction

FPM Fine Particle Mass

FRC Functional Residual Capacity

GCI Grid Convergence Method

HFA HydroFluoroAlkane

IC Inspiratory Capacity

ICS Inhaled Corticosteroids

IP Induction Port

IRV Inspiratory Reserve Volume

LABA Long-Acting β_2 Agonists

LDA Laser Doppler Anemometry

LRN Low-Reynolds Number

LVDT Linear Variable Differential Transformer

MMAD Mass Median Aerodynamic Mass

MSLI Multi-Stage Liquid Impinger

NC NebuChamber

NGI Next Generation Impactor

OCD OptiChamber Diamond

OS Operating System

PC Polycarbonate

PDA Phase Doppler Anemometry

PDF Probability Distribution Function

PIF Peak of Inspiratory Flow

PIV Particle Image Velocimetry

pMDI pressurized Metered-Dose Inhaler

RANS Reynolds-Averaged Navier-Stokes

RE Richardson Extrapolation

RPM Rotations Per Minute

RSM Reynold Stress Model

RV Residual Volume

SABA Short-Acting β_2 Agonists

SAM Soft Anatomical Model

SC Space Chamber

SDOM Standard Deviation Of the Mean

SIMPLE Semi-Implicit Method for Pressure-Linked Equations

SM Sizable Mass

SST Shear Stress Transport

TEM Total Emitted Mass

TLC Total Lung Capacity

UDF User-Defined Function

USB Universal Serial Bus

USP United States Pharmacopeia

V Vortex

VC Vital Capacity

VHC Valved Holding Chamber

VOL Volumatic

1 Introduction

1.1 Motivation

Regarding the strong prevalence of the asthma and other obstructive diseases in the world, the techniques and the devices used in the treatment of these pathologies have been under constant development. Being the inhalation therapy one of the most effective and widespread procedures of treatment in the world, inhalation devices are the object of a great deal of development.

The pressurized Metered-Dose Inhalers (pMDI/MDI) together with the Nebulizers and the Dry Powder Inhalers (DPI) are the three main categories of devices used in the treatment of asthma by inhalation. In the specific case of children, for whom the asthma incidence is stronger and the respiratory coordination to use the pMDI is required, the incorporation of an add-on spacer to the pMDI represents an effective solution. Spacer devices, mainly the Valved Holding Chamber (VHC), coupled to the pMDI correspond to the cheapest and most efficient way to treat the asthma in children (3 to 8 years old) [Can08]. Thus, it is of utmost importance to study the main characteristics of these add-on devices in order to improve its efficiency, suggest further optimisation criteria in terms of geometry features and, at last, propose a new and enhanced design for a VHC device.

1.1.1 Relevance of Research Developments in Inhalation Therapy

The inhalation therapy is cornerstone to the asthma treatment [VCD$^+$08]. Asthma is an inflammatory chronic disease characterised by airway obstruction disorders, in which pMDIs are favoured devices for treatment delivery [Glo14]. This disease already affects over 300 million people worldwide and causes the death of 220 thousand per year. In Portugal, the prevalence of the disease is estimated between 3 to 5% (see Figure 1.1), showing a clear tendency to increase all over the world [MFHB04]. One of the most critical issues in this field of knowledge concerns the effectiveness
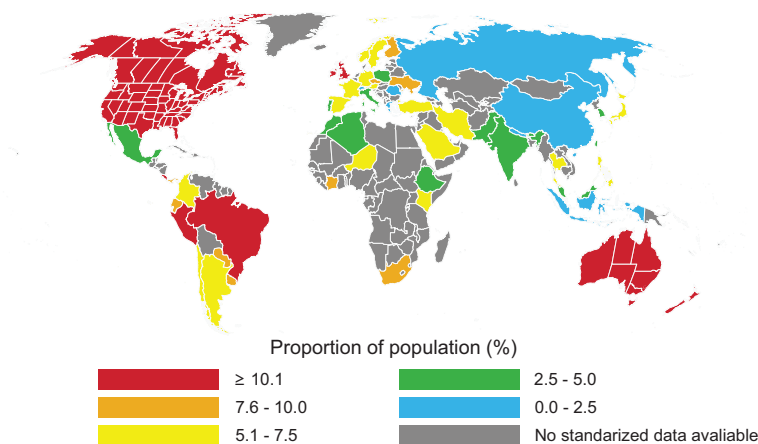
Figure 1.1: Graphical representation of the asthma prevalence in the world

of drug delivery in the patients' lungs during the treatments [Mar07, Abr07]. The drugs used in the asthma treatment have anti-inflammatory and bronchodilator properties, with the objective of reducing the inflammation of the pulmonary tissue (i.e. diameter reduction of the bronchus), thus increasing the pulmonary capacity [Mar07, Dol04].

The nebulizer benefits from a simpler usage procedure but it needs to be attached to a power source, which affects patient mobility. Nebulizers also present a greater waste of drug and require longer treatments sessions. Thus, this inhalation device is reported with a lower efficiency than the other devices [CRR04]. The DPI is one of the most efficient devices but it also has a few important disadvantages. Aside from their high cost, DPIs require a minimum inspiratory flow rate by the patient in order to work with optimum efficiency. Concerning the pMDI, they are the most commonly used for aerosol delivery of bronchodilators in ambulatory patients [DF01, Smy03], and they have been the backbone of inhalation therapy for asthma for, approximately, 60 years

[VCD$^+$08, New06]. Drug dose effectiveness in inhaled delivery is difficult to measure due to the fact that only a small fraction of the pMDI nominal dose reaches the lower respiratory tract. The pMDI is a small, cost-effective and very portable device, containing between 100 and 400 doses. This device comprises a disposable canister with a pressurized mixture of propellants, surfactants, preservatives, flavouring agents and active drugs. This mixture is released from the canister through a metering valve. The best feature of a pMDI device is that is always ready to be used, making it a magnificent example of an engineering solution [Dun97]. Its major drawbacks are the high spray velocities which creates the so called "cold-freon" sensation on the back of the throat and the necessity of inspiratory coordination with the actuation. This causes the younger and/or older patients to not being able to use the pMDI device properly [New06, DF01, Tas98]. With the objective to solve some of the pMDI limitations, spacers were created, back in 1956 [PM61]. These devices can be characterised in three categories: simple tube, Valved Holding Chamber and reverse flow. The most common type is the VHC, in which the drug is fired into the device, reducing the spray high velocity impact in the throat and the need for inspiratory coordination. One of the main advantages of these add-on devices lies on the fact that the patient can keep quiet breathing during treatment. The one-way valve makes the normal respiratory cycle possible by foreclosing the expiration flux back inside the device. VHCs produce a fine, slower-moving, more breathable aerosol with less impaction of drug in the oropharyngeal zone than simple tubular spacers, or even the pMDI alone [DF01]. Although mechanically robust and clinically effective, when properly designed and pre-conditioned, the VHCs can show great performance. However, it is of utmost importance to study numerically and experimentally several causes of inconsistent medication delivery. These include: electrostatic charge; incorrect operation of inhalation and exhalation valves; geometry configuration, total volume, weight, etc. In addition, behavioural factors, such as: the patient not following the instructions for use and maintenance, and imperfect breathing technique. Those factors amplify overall variability. Features, such as, the valve movement indicators that provide patient feedback are helpful in order to minimise these factors [MN07]. Table 1.1 lists the potential factors that may result in inconsistent medication delivery from VHCs.

There are several VHC models in the market but there is a great opportunity to improve its effi-

ciency or propose a new design. Some authors present different materials and geometries but the waste of drug versus price is not settled [New04]. A comprehensive market analysis of the commercial models available is presented in chapter 2. Due to the variety of materials used in their construction, the range of sizes and type of inhalation valves, a deep and meticulous study can provide significant insights into the relationship between those features and efficiency of the VHC devices. Minimising the loss of fine particles by deposition in the VHC is essential to an effective drug delivery to the lungs [ASAT08]. This fraction of particles has a major importance in effectiveness of the treatment because in the smaller airways of the respiratory tract, only particles below 5 μm in diameter can reach the alveolus and enter the blood stream (except those that are exhaled, diameter below 1 μm) [BOS01].

Table 1.1: Potential factors that may result in inconsistent medication delivery from VHCs

Device related	Patient related
Electrostatic charge – associated with both aerosol from the inhaler and inner surfaces of the VHC device	Choice of appropriate VHC and patient interface (mouthpiece or facemask) – infant, child, adult
Inhalation valve function – most important with devices intended for use by infants whose inspiratory flow may not open a valve that has stuck closed	Disease modality and severity – may affect ability to use a particular patient interface
VHC volume in relation to patient breathing pattern – more important for infants and small children	Handling and correct maintenance of the devices - may conduce to inappropriate storage procedures
Universal adapter seal integrity – essential, especially for infants and small children	Improper respiratory maneuver, such as, the patient not hold breath after inhalation

1.1.2 Where is the Research Opportunity?

The research opportunity is related with the possibility of optimising the geometric features of the VHC devices, improving their efficiency without increasing their purchase cost. Therefore, this research opportunity arising from the following research question: Is it possible to develop a VHC with better efficiency? Underlying this main research question, others may be formulated in the quest of VHC optimisation (Figure 1.2).
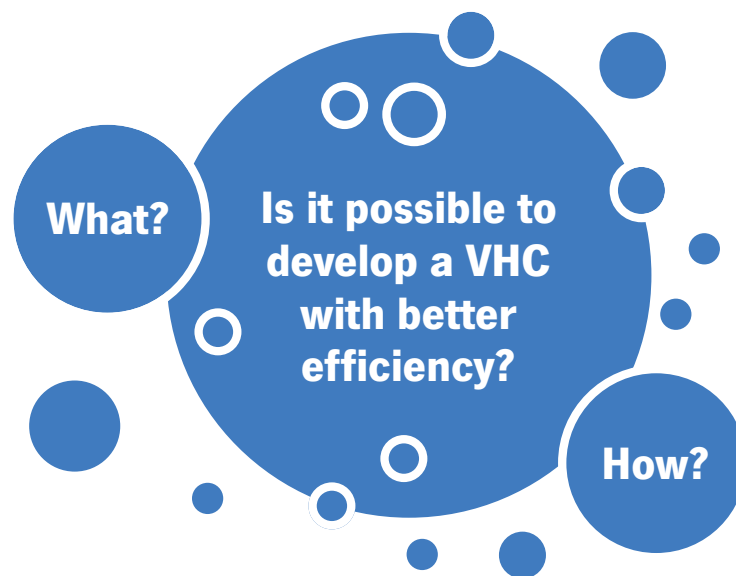
Figure 1.2: Schematic of the most important research points resulting from the research question

The first sub-question requires the understanding of what VHC's characteristics should be improved in order to achieve a better efficiency. To answer this question, the first step of the procedure is to study the devices available in the market. This requires a selection of different devices with distinct geometrical profiles, materials and types of valves to be studied under different conditions.

The second sub-question is to understand how those VHC features can be studied and assessed. Although VHC devices have been proven to enhance the amount of medication that will reach patient lungs, some medication is lost through deposition occurring on the VHC walls. Since one of the aims of this thesis is to investigate the main aspects that influence the drug deposition within several VHC models, the methodology and proper procedures has to be defined to quantify the most important metrics in their evaluation. The drug deposition and relevant metrics can be

quantified experimentally and modelled numerically.

Thus, this work provides the opportunity to use Computational Fluid Dynamics (CFD) tools, as well as, the construction of an experimental apparatus to provide significant validation of the numerical model. CFD methodology provides a cost-effective mean of simulating real flows by using modelling equations (mathematical physical problem formulation) and numerical methods (discretisation methods, solvers, numerical parameters, and grid generation). These approaches allow the engineers to predict the behaviour of systems and understand the relationship between the most important variables and propose optimised solutions without complex experimental setups or construction of prototypes. Yet, experimental methods have played an important role in validating and exploring the limits of the various numerical predictions, since reliable information about physical phenomena is usually given by measurements. In some circumstances, an experimental investigation involving full-scale equipment can be used to predict how the equipment would perform under given conditions.

This thesis also aims to study the effects of different inhalation flow rates (including a breath profile) on the amount of medication that reaches a patient's lungs, using both pMDI solo and coupled with VHC devices. These considerations are very important in order to determine if deposition occurs due to inertial impaction. For a patient suffering from acute asthma, it is important that a sufficient amount of medication reaches the lungs and, therefore, this research intends to optimize the devices and, consequently, improve the life quality of those patients.

1.2   Objectives

The project is focused in the study of the transient airflow, due to the human respiratory cycle, in VHC devices. The study of the drug behaviour inside the device is fundamental to the evaluation of the VHC efficiency. To achieve this main objective, specific objectives can be defined in the project:

- Study the human respiratory cycle in the target population: asthmatic children under 6 years old and persons with reduced inspiratory flow capacity for use DPI devices. This cycle

needs to be mechanically reproduced in the experimental apparatus as an input.

- Develop a computational model using CFD tools where a model for the particle motion inside the VHC, is added. The input parameters to this model are based in the spray characteristics, which will need to be well studied, based in the literature and experimental measurements. The computational model will be developed in FLUENT software (from ANSYS®).

- Construct and validate an experimental apparatus that replicates the human breathing cycle, which will allow the comparison of particle collection for different VHC between the experimental tests and the CFD results. This objective comprises the construction of a fully functional breath simulator. The breath simulator will be based in the principle of volume displacement. It will be composed by an in-house made cylinder connected to a displacement mechanism.

- Assembly of the experimental setup for testing of VHC. To do so, the breath simulator will be coupled to the setup, to create changes in the constant flow in a way that reproduces the human waveform at the United States Pharmacopeia (USP) Induction Port (IP) and therefore in the VHC device to be tested. A cascade impactor, the 5-stages Multi-Stage Liquid Impinger (MSLI) (US Pharmacopeia "Apparatus 4", Portuguese and Eur. Pharmacopeia "Apparatus C") will be used, since it is the equipment available in the laboratory.

- Test and quantify, experimentally, the aerosol Fine Particle Mass (FPM) of the dose emitted by different VHC devices under constant flow (30 L/min and 60L/min), as well as, under an human breathing pattern.

- Perform the numerical simulations using the CFD model to obtain the prediction of the VHC devices performance.

- Validate of the computational model by means of experimental measurements. As the model accuracy increases, the CFD tools will be validated and compared with experimental results and results from similar studies in the literature.

- Develop an improved design of a VHC device by using full factorial Design Of Experiments (DOE) applied to the VHC body expansion corner. The assessment will be numerically performed using FLUENT software (from ANSYS®).

1.3   Research Methodology

The scientific knowledge is not fully predictable and there are no guidelines or an infallible procedure to achieve it. The technical procedures and philosophies to be followed by the researcher are selected according to specific criteria and conditions of the research study. After a detailed description of the project idea, the research methodology can be described as an overall "path" [SLT09]. A simplified way to summarize is shown in Figure 1.3.
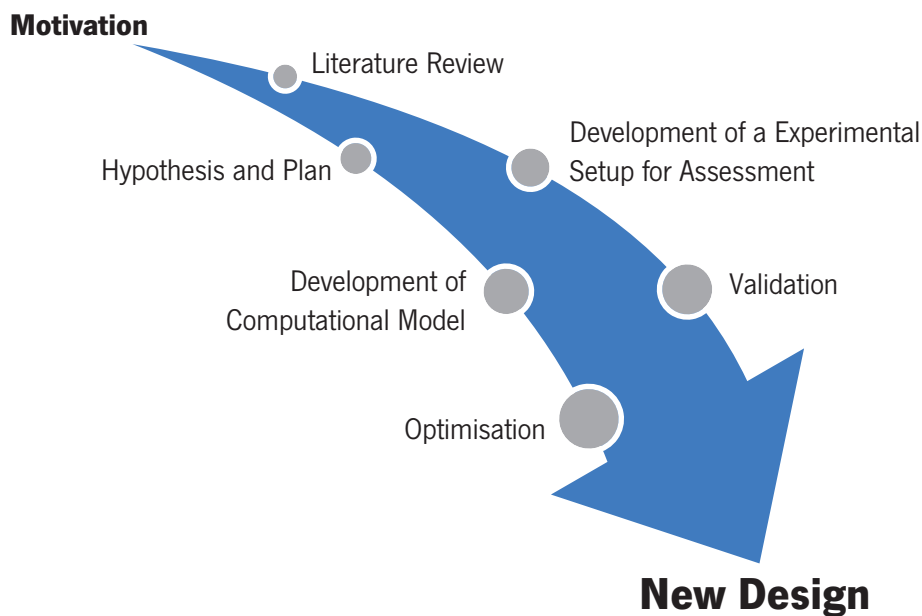
Figure 1.3: Representation of the research process to be used in this project

The methodology that should be followed in order to build up this project starts with a comprehensive literature review, in order to understand all the issues related with the inhalation therapy devices, as well as the state-of-the-art concerning to the numerical modelling techniques and experimental apparatus for testing the device.

The experimentation stage will start with the design and construction of the experimental apparatus. Experimental flow tests will be conducted in order to ensure the reproducibility of the experiments and later the validation of the drug collection through an adequate technique. This will allow calibrating the computational model parameters and later a sensitivity analysis. The validation should be focused in understanding the model sensitivity to key variables used and the best

outcome of the device, for instance, the VHC drug delivery efficiency.

The computational modelling comprises the generation of a numerical model based on CFD tools. The model generation includes the data for the definition of all parameters involved in the physical phenomena simulation. To do so, it is required a comprehensive survey to create the database. This step should include all the variables for the geometry, the dimensional boundary conditions of the simulation. In order to obtain the necessary inputs for the pMDI spray, expert reports and case studies should be assessed.

In the final stage, the optimisation of the geometry will be the main focus. The best geometric design will be obtained through the usage of optimisation methods, searching for the best combination of drug delivery with volume and size constraints. This step of the project will be an iterative process where the results of the computational simulations and the experimental tests will be used to validate the best predicted model and proceed with the new VHC design.

1.4   Structure of the Thesis

The present thesis is organized in nice chapters: (1) Introduction; (2) Background and Literature review; (3) Development of the CFD Model; (4) Project of the Experimental Setup; (5) Experimental Methodology; (6) Experimental Results; (7) Numerical Results; (8) Optimisation of the VHC Geometry by using CFD Models; and finally, (9) Conclusions and future work. In the first chapter, the general motivation for this research work is presented and the framework is provided. The objectives, the research methodology and the main contributions of the present study are also described.

The second chapter concerns the background knowledge in the field of the human respiratory system mechanics, the inhalation therapy and the most used approaches in the treatment of the asthma and other chronic inflammatory diseases with special focus on the add-on devices, the VHC. A concise literature review on the most important experimental and numerical research studies is also presented. The state-of-the-art is divided in $in\ vitro$ studies, $in\ vivo$ studies (both experimental) and numerical studies.

In chapter three, the complete mathematical formulation to develop the computational model is

presented. All the governing equations for fluid and particles flow solving, the definition of Euler-Lagrangian discrete phase tracking model and heat and mass transfer are presented. The fourth chapter reports the project of the experimental setups, describing all the components with special focus on the breathing simulator. In the fifth chapter, the experimental methodology, including the protocol and the procedures, as well as, the equipment used to perform the experimental tests are explained.

The research results are divided in two chapters. Chapter six discloses the main experimental results from the study. The results were divided in four main groups: results from the Full Dose (FD) tests; the results from the Cascade Impactor (CI); the results from a multi-variable comparison; and finally the results for the most relevant metrics for the patient. The numerical results are presented in the seventh chapter. These results are presented considering the analysis of flow distribution along the VHC devices, the drug deposition and the analysis of the particles evaporation during the simulations. It is also presented, an important discussion regarding the validation of both numerical and experimental results, which are then compared with literature data.

Based on the main conclusions from the numerical and experimental work, an optimized design of a VHC device is proposed in chapter eight. The new design was obtained from a DOE study performed using FLUENT. Finally, the main conclusions of the research and some suggestions for further developments are pointed out in chapter nine.

1.5   Contributions of this Work

This thesis provides some contributions for the scientific research community, as well as, for the medical community. The most relevant are given here:

- Report several medically relevant metrics through experimental assessment of the drug (Ventolin) delivered when a pMDI is coupled to commercial VHCs. These metrics provide a source of data on the clinically performance of the VHCs at constant flow rate (30 L/min and 60 L/min) and under a breath pattern (tidal volume of 150 mL).

- Perform an exhaustive experimental analysis to compare different commercial VHC models

tested under controlled conditions. The comparison of the experimental results will allow observing that not all the VHCs in the market have the same performance at the distinct flow rates. This study will also increase the understanding of the importance of the valve design in the distinct VHC performance.

- Develop a numerical model to provide insights into the pMDI spray evaporation phenomena that occurs inside the VHC devices. The realistic parameters used in the simulation will bring the state-of-art, on CFD modelling of spacers, one step forward.

- Use the computational tool to evaluate and optimize the design of the devices for inhalation therapy without expensive production costs of physical prototypes.

- Propose a new design for a VHC device. The new design will represent the most important achievement of the project and its development represents the outcome from the experimental and numerical conclusions. This new design must take into account the most device- and patient-related factors that promote consistent medication delivery.

The fundamental problems in the design and assessment of VHC devices are related with the time consumption of the processes and the cost of manufacturing prototypes. In most of the cases, finding the geometrical parameters of the devices is based on insufficient and costly experimental information. This means that improvements to the design are being achieved through high-cost and time-consuming trial and error procedures. Regarding this, numerical modelling techniques represent a great opportunity to identify the key parameters and, together with a well-founded experimental basis, optimize the devices using a cost effective process.

This page was intentionally left in blank

2 Background and Literature Review

2.1 Human Respiratory Mechanics

The respiratory system's main function is gas exchange, providing oxygen (O_2) to the body tissues and eliminating carbon dioxide (CO_2). The exchange of gases takes place at the alveoli, where O_2 diffuses into the lung capillaries in exchange for carbon dioxide. Exhalation begins after the gas exchange and the air containing CO_2 begins the return journey through the bronchial airways and back out to the external environment, through the nose and/or mouth. Secondary functions of the respiratory system include filtering, warming, and humidifying the inhaled air. This includes the vocal cords in the larynx for sound generation, the lungs for homeostasis, and the olfactory bulbs (in the nose) for smell, as presented in Figure 2.1 [TIA13].

The respiratory system can be separated into regions based on function or anatomy. Anatomically, the respiratory system can be divided into the upper and lower respiratory tracts. The upper tract includes the organs located outside of the chest cavity area (e.g. nose, pharynx, larynx), whereas the lower respiratory tract includes the organs located almost entirely within it (i.e. trachea, bronchi, bronchiole, alveolar duct, alveoli and diaphragm).

Functionally, there is the conducting zone (nose to bronchioles), which consists of the respiratory organs that form a path to conduct the inhaled air into the deep lung region.

The majority of the large inhaled particles are entrapped by this filtration mechanism, or impact on the walls of the nasopharynx due to the turbulent flow. When breathing through the mouth, air

filtration and heating does not occur, and the resistance to air flow is lower. These reasons, make mouth breathing a more effective route for the administration of aerosol medication. The right lung has 10% higher volume than the left one (due to the need to accommodate the heart), which makes it more susceptible to infections. The different lengths and angles of the bronchi also have an impact on the aerosol particles lung deposition. There are around 23 generations from the trachea to the alveoli sacks, where the upper 16 generations are considered to be the conducting zone and the lower seven correspond to the respiratory zone [TIA13].
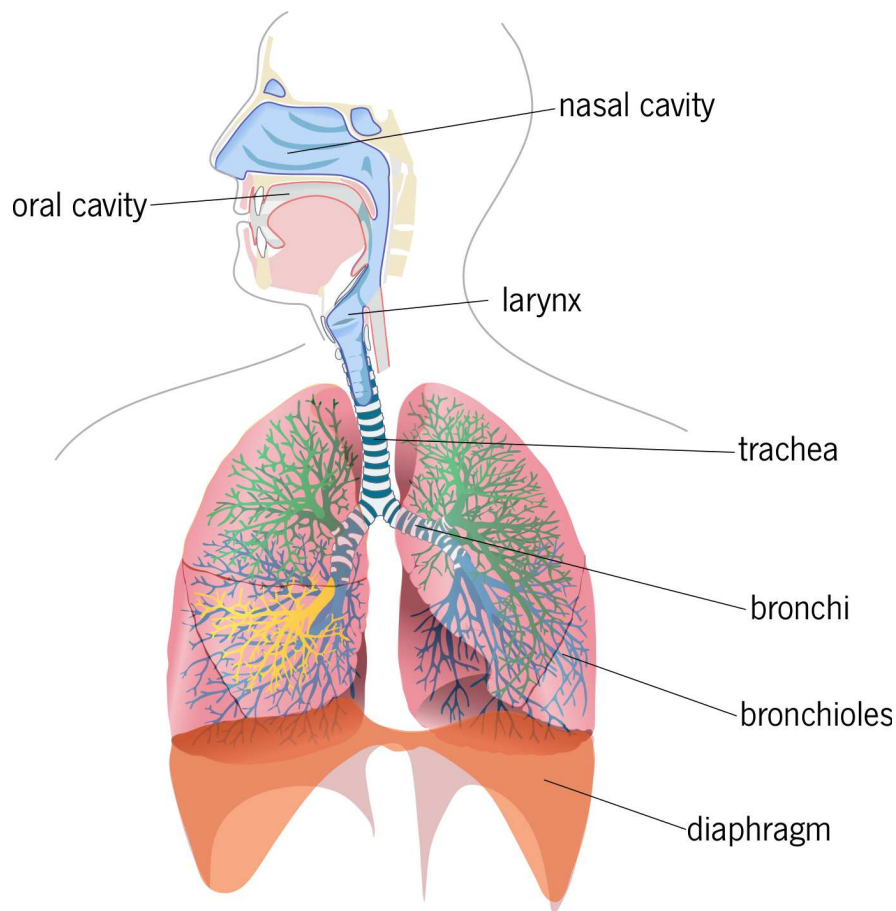
Figure 2.1: Respiratory system divided by the upper and lower respiratory tract regions

The respiratory zone (from the alveolar duct to the alveoli) consists of tiny passageways, where gas transport occurs by diffusion. The alveolar ducts are small polyhedral sacks (with a large surface area), where the air can diffuse due to the fact that the walls are only one cell thick. It is of vital importance that the alveoli contain residual air volume (even during exhalation) because,

when collapsed, the alveoli require a large amount of pressure to re-inflate. To prevent this from occurring, the alveolar walls are covered with a lipid substance (a surfactant), which will maintain their stability to remain continuously open.

The thoracic cavity is constituted by the ribs, the diaphragm, the sternum and the intercostal muscles. The diaphragm provides approximately 75% of the power required for perform a quiet breathing, where the remaining 25% is provided by the ribcage movement.

2.1.1 Breath Profile

The breathing is a respiratory process composed by two phases: the inhalation – the movement of the air into the lungs; the exhalation – the movement of the air to the outside. In this process, the pleural fluid between the lungs and ribcage act simultaneously as a lubricant, allowing unrestricted movement. During quite breathing (i.e. tidal breathing), the inhalation movement starts with the contraction of the diaphragm. This creates negative pressure inside the thoracic cavity forcing the lungs to expand, consequently, the air flows into them. Exhalation is a passive process whereby the diaphragm and the intercostal muscles do not contract, so that the diaphragm rises and the ribs move downwards. Thus, the volume of the lungs decreases, forcing air out [TIA13].

Other muscles, such as the sternocleidomastoid muscles, are more involved in inhalation and, with increased force, the ratio of time for inhalation to time for exhalation decreases. The exercise practice or hyperventilation may induce this increased force. As well as the major muscle groups, muscles in the linings of the airway walls are also used in respiration. The expansion and the contraction of the airways, due to these muscles, assist in increasing and decreasing lung volumes. This affects the diffusive process of gas exchange. The inhalation flow rates fluctuate, due to several of reasons: lungs volume/capacity, patient age, weight, physical activity and respiratory health.

Inspiratory flow rates are important when administering therapeutics drugs as an aerosol, or for inhalation therapy. The devices such as pMDIs, DPIs and nebulisers are affected by inspiratory flow rates as they influence the locations of the lungs that the aerosol will reach, the amount that will be taken in during one breath, and the turbulence that will be present in the flow.

Spirometry is the most used methodology to evaluate the respiratory capacity. This technique allows the diagnosis of respiratory diseases through the evaluation of certain indexes. Those are compared with predicted values, based in age, gender, weight, and ethnicity [DS03].

Figure 2.2 depicts a healthy adult typical flow-volume curve, against one from a adult with asthma and one with Chronic Obstructive Pulmonary Disease (COPD) [Mil05]. It can be seen that the presence of asthma affects the adult capacity to exhale, reducing its flow rate. The COPD not only reduces the exhalation flow rate but also reduces the volume of air exchanged.

| Normal healthy adult | Adult with asthma | Adult with COPD |
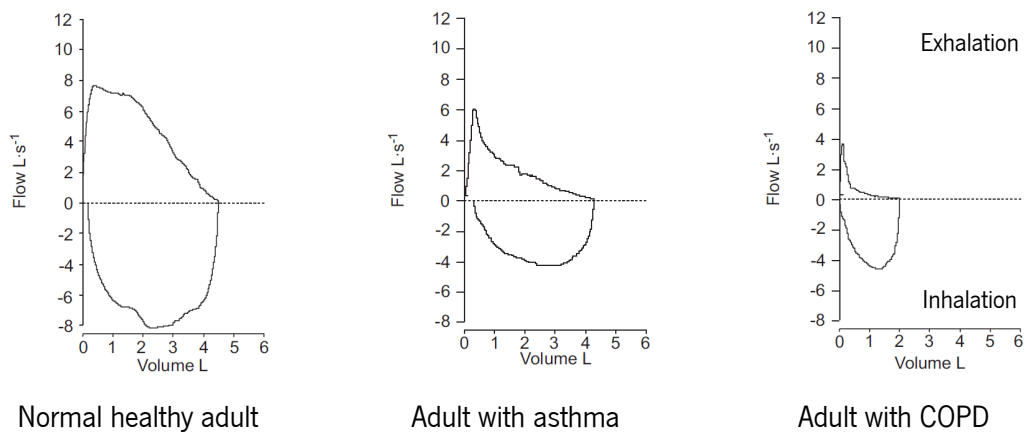
Figure 2.2: Flow-volume typical curves for adults: healthy, asthma and COPD [Mil05]

Human breathing waveform is usually characterised by two parameters: the number of Breaths Per Minute (BPM) and the duty cycle (i.e. the ratio of the inhalation time to the tidal breath duration). These two characteristics, together with the current volume of air during quiet breathing, can define a typical waveform. The breath patterns are usually approximated to a sine or square waveform, and those three parameters give it shape [DM04]. Nikander et al. (2001) performed an experimental assessment of the nebulizer rate of delivery using a human breathing pattern, a sine waveform and a square waveform. They concluded that the shape of the waveform had no influence in the rate of delivery from the nebulizer [NDSW01].

2.1.2 Pulmonary Capacity

The volume and the compliance capacity of lungs and chest wall, influence the behaviour of the respiratory system. Normally, the lung volumes are measured with a spirometer, and its lung capacity is then inferred from the measurements. The lung capacity and the air volumes displaced, are of vital importance in determining health of this organ (see Figure 2.3).
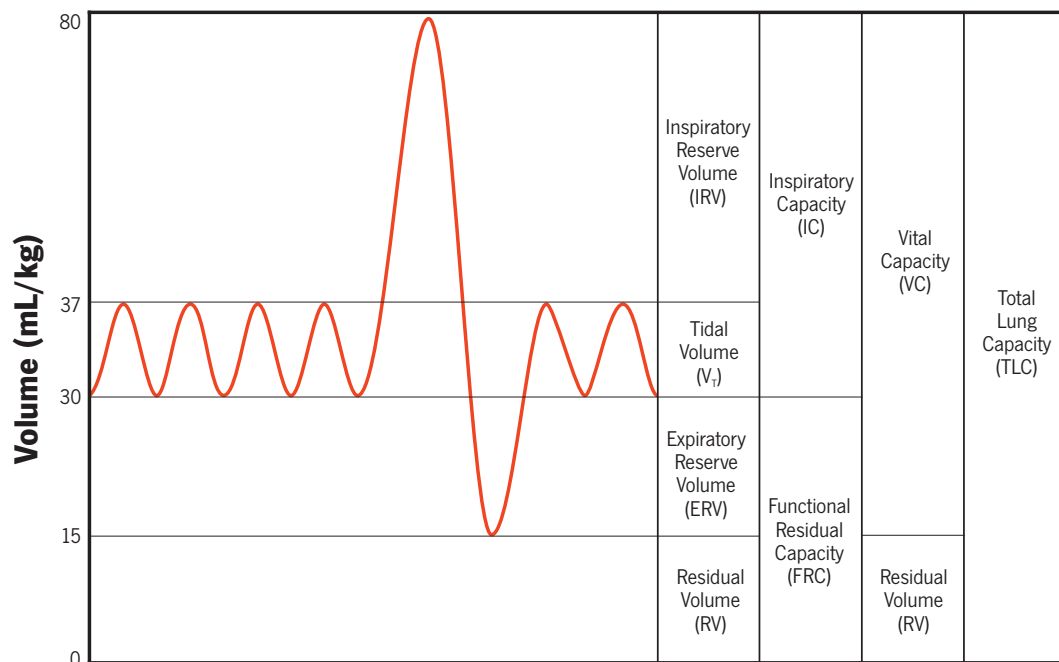
Figure 2.3: Representation of the vital lung capacities and volumes

There are five volumes and four capacities used to characterize the lung operation [TIA13]:

- Total Lung Capacity (TLC) is the total air volume supported by the lungs.
- Tidal Volume (V_T) is the amount of air that is inhaled and exhaled during normal quiet breathing. 7–9 mL/kg of ideal body weight $\approx$8–10% of TLC.
- Inspiratory Reserve Volume (IRV) is the maximum air volume that can be inhaled above the tidal volume.
- Expiratory Reserve Volume (ERV) is the maximum volume that can be exhaled below the tidal volume.
- Residual Volume (RV) is the volume left in the lungs after maximum exhalation.

- Functional Residual Capacity (FRC) is the volume of air left in the lungs after a tidal exhalation.

- Inspiratory Capacity (IC) is the maximum volume of air that can be inhaled.

- Vital Capacity (VC) is the air volume difference between a forced inhalation and a forced exhalation.

Gas exchange through the respiratory system occurs either by convection or diffusion. The factor that determines the type of exchange occurring between two gases, is given by the ratio of the diffusive time to the convective time for transport. In the upper airways, the gas transport is mostly done by convective transport, whereas at the lower generations of the respiratory system, diffusion is the main process of gas transport. The gas exchange across the alveoli membrane is controlled by diffusion mechanism, that occurs due to the large surface area.

2.1.3   Respiratory Diseases

Asthma, COPD and bronchitis are diseases that affect the conductive and gas exchange zones of the human respiratory system. These diseases seriously affect the capacity for normal respiratory function, due to the airway inflammation.

COPD is a disease that frequently occurs later in patients' life and, predominantly, corresponds to an effect from smoking habits. COPD increases the airway resistance due to various factors: clogging of the airways due to the excess of mucous, loss of airways elasticity, or inflammation of the airways. Treatment of COPD includes the delivery of bronchodilators to reduce airway inflammation. As the disease is obstructive and restrictive, the total lung capacity is reduced and, consequently additional treatment is required. Those treatments can include: pulmonary rehabilitation, in order to learn how to use the reduced amount of available air; or supplemental oxygen [TIA13].

Bronchitis is an infection disease, which results in inflamed bronchi, generally caused by a viral source. Its treatment is similar to the ones associated with COPD. Bronchitis can be treated with medication, such as, inhaled salbutamol sulphate in order to reduce the inflammation at the bronchi [Spr14].

Asthma is also a chronic disease involving the airways in the respiratory tract. Asthma symptoms are coughing, chest tightness and dyspnoea (shortness of breath). These symptoms are due to increased resistance to air flow. The asthma attacks are caused by airway hyper-reactivity, in which the bronchi and bronchioles suffer a great constriction, causing increased resistance to air flow. This hyper-reactivity is due to, for example, inhaling allergens or exercise (particularly in the cold environments). The bronchial hyper-reactivity is usually associated to the increase in mucous production. The treatment is usually done by inhalation therapy, where pMDIs are a preferred device. A third of asthma patients show symptoms before the age of ten and, in most cases, it is diagnosed before the age of 40 [MN07].

2.2 Inhalation Therapy

According to Crompton, inhalation therapy can be traced as far back as 4000 years ago in India, and many "hundreds of ingenious devices and hopeful medications" (according to Sanders) have been discovered so far. Inhalation therapy is so important nowadays that is hard to imagine the treatment of asthma without a proper inhalation therapy procedure, an inhalation device, and a the necessary drug [Cro06, San07].

Briefly reviewing the antecedents of contemporary inhalation therapy and medicines used for the management of asthma over the last 50 years, Crompton presents the 19th century hand-held glass bulb nebuliser up to the introduction of the first pMDI, which came into common clinical practice in 1956 [Cro06]. Sanders, detailing the inhalation therapies since ancient times, refers several inhaler devices, such as: the C. Bennet's inhaler (dated from 1654); the J. Mudge's inhaler (from 1778, and adapted from a pewter tankard); the first pressurised inhaler (presented in 1858, in Paris, France, by Sales-Girons); the Improved Nelson inhaler (proposed in 1865 by S. Maw & Sons, London) which is still being manufactured up to this day; and the Siegle's steam spray inhaler (a German invention from early 1860's that marked the beginning of the nebuliser therapy) [San07].

2.2.1 Medication

Anti-inflammatory and bronchodilator drugs are used with the objective of reducing the inflammation of the pulmonary tissue, which causes the diameter reduction of the bronchus [Dol04, Glo14]. In the inhalation therapy, the drugs used are divided in several groups, being the two major ones the Inhaled Corticosteroids and the bronchodilators agonists of long and short action [Dol04]. Within them, there are different active molecules, although each has its own major delivery system associated, some of them are:

- Short-Acting β_2 Agonists (SABA)
    - Salbutamol (Ventolin)
    - Levalbuterol (Xopenex)
- Long-Acting β_2 Agonists (LABA)
    - Salmeterol (Serevent Diskus)
    - Formoterol (Foradil)
- Inhaled Corticosteroids (ICS)
    - Budesonide (Plumicort)
    - Beclomethasone dipropionate (QVAR)
    - Fluticasone propionate (Flovent)

A study about medication prescribed for asthma treatment, to children, up to 15 years old, in six countries (Belgium, Ireland, Italy, Portugal, Spain, England, North Ireland and Scotland), has shown that the most prescribed drugs are the SABA and LABA, mainly in emergency situations [JBGJ00].

Another study, made in Holland, shows that the major prescribed medication (82%) to treatment of asthma in 165 children during the first 4 years of living, was the β_2-agonists by inhalation [ZSB$^+$08].

In Trindad and Tobago, a study was carried out with asthmatic patients of all ages. The study concluded that the majority of them use salbutamol drug (Ventolin) as the prescription of choice [PCS01]. Most recently, the Inhaled Corticosteroids are used, in small doses, for daily control

medication of asthma symptoms [Glo14, Tan15].

2.2.2 Inhalation Delivery Devices

In the inhalation therapy, the mostly used delivery devices are: the nebulizers; the DPI; and the pMDI, which can be coupled with an add-on device [DD11, DF01, DM04, New04].

Nebulizer

Introduced in the 1800s, nebulisers were one of the first devices used for aerosol drug delivery. These devices convert a liquid into aerosol droplets suitable for patient inhalation through a mouthpiece or face mask. The use of nebulisers for the treatment of asthma is declining, but they are still used if the prescribing physician suggests it, or if a patient requests it. Nebulisers are also still used for drug administration for other illnesses.

Nebulizers use oxygen, compressed air or ultrasonic power to break up medical solutions and suspensions into small aerosol droplets that can be directly inhaled from the mouthpiece of the device. The use of ultrasonic waves is the most expensive, the smallest and the most portable method available, requiring an ultrasonically vibrating crystal. Jet nebulisers use either electrical or gas compressors to pass a stream of air or oxygen through the liquid medication. These devices require a mouthpiece or face mask attached. Because of their shape and size, jet nebulisers are less portable, which represents an inconvenience. Whether ultrasonic or jet, the nebulisers operate continuously while medication is being administered, which takes approximately 10 to 15 minutes. During the procedure, the patient breathes normally through the face mask or mouthpiece. As inhalation only makes up one third of a breathing cycle, the majority of medication released is not actually inhaled. This problem is only solved with a specially designed mouthpiece to control the medication release. Yet, this also affects the nebulisers efficiency because part of the delivered medication is entrapped in the plastic walls or in the facemasks. On the other hand, the aerosol large particles that will impact in the device walls do not reach the patient mouth, whereas the small repairable ones do.

The use of Nebuliser is decreasing mainly because the alternative therapies are more convenient,

less expensive and more efficient in treating asthma. However, for illnesses such as arthritis, the nebulisers can still be the preferred method because the patient's conditions (e.g. weakness). At hospitals, because of their design and the lack of requirement for a certain inspiratory flow rate, nebulisers are regularly used when patients can only breathe passively [DD11, Hic03].

Nebulisers are also beneficial for situations where large doses are required, but it has been found that using a large volume spacer with a puffer is also a plausible alternative.

Recently, new nebulizer models have been developed. These models improve the portability by reducing the power consumption an allowing the use of small rechargeable batteries. Some models have the ability to operate upon breath solicitation, reducing the waste of drug. Nevertheless, they are very expensive devices [DD11].

Dry Powder Inhaler (DPI)

A DPI is a handheld device used for administering medication in the form of a dry powder. There are several types of DPIs which use medication stored in different ways: in blister packs, in reservoir devices or, in some cases, the medication can be stored within the device itself (which requires a pre-metering part of the DPI design).

Medication is in powder form and inhalation is the propelling force used to actuate the device. DPIs can be used to deliver medication such as, salbutamol sulphate, but they are more common for use with preventative medication [FBGD00].

When using a DPI, the patient inhales deeply at a rate between 30 L/min and 90 L/min. Because the device is self-actuated (i.e. actuated by the breath) there is no requirement for the patient to synchronise their breathing with actuation, which can be problematic for some patients. This device is also beneficial for patients with arthritic hands as it does not have an external trigger that needs to be pressed. The devices are also portable and small which makes them a good choice in treating of asthma.

Nevertheless, DPI devices are not suitable for all type of asthmatics. The high inspiratory flow rate requirement can be problematic for younger patients and those suffering from COPD, or who have another condition which causes difficulty in taking deep breaths. Without the deep breath, the DPI

will not actuate. In order to have a correct actuation, a substantial pressure drop is required which can only be achieved with a significantly deep breath. DPIs are not usually prescribed to patients under six years old or in the case of elderly sick people. Typically, a DPI deliver between 10-40% of the dose to the bronchi.

The limitations from using a DPI arise when patients exhale into the actuator, as the added humidity can cause obstruction of the powdered medication, meaning that the efficiency decreases in the medication delivery [New06].

pressurized Metered-Dose Inhaler (pMDI)

Regarding the pMDI, it has a low cost and it is widely trusted by the patients and physicians alike. It delivers a dose of medication in the form of an high velocity spray, powered by a propellant kept at high pressure inside the canister. It is very portable and simple to operate and it does not dependent on the patient's Peak of Inspiratory Flow (PIF).

However, its major drawbacks are: the high spray velocity, which creates the so called "cold-Freon" sensation on the back of the throat; and the necessity of inhalation-actuation coordination, which makes impractical for younger and/or older patients to use the device properly. This problem is mitigated the implementation of classes to teach the correct usage procedure, resulting in increased efficiency [New06, DF01, Tas98].

2.3 pressurized Metered-Dose Inhaler (pMDI)

The pMDI, shown in Figure 2.4, is the mostly used aerosol delivery device in the world for the treatment of asthma. In 2000, an estimated production of 800 million units have been reported [Smy03, DF01]. It has been the backbone of inhalation therapy for asthma for approximately 50 years [New06]. The pMDI contains 100 - 400 doses packaged into a small and (very) portable device, that can be easily concealed in a pocket. The best feature of a pMDI device is that, it is always ready to be used, making it a magnificent example of an engineering solution.

Figure 2.4: A pMDI, Ventolin HFA, and its dust cap

2.3.1   Characterisation

The pMDI device essentially incorporates a disposable canister, where the drug formulation is stored, which can be replaced for a new one at any time, mounted in an actuator with a mouthpiece zone and usually a dust cap is included [New06, New05]. The four basic components that can be found in all pMDIs are: the formulation canister; the metering valve; the actuator; and the container [Dun97]. On the following list are described the components of a pMDI device (see Figure 2.5) [DF01, RG99]:

- Canister with O-Ring
- Formulation
    - Active Pharmaceutical Ingredient (API)
    - Propellant(s)
    - Surfactant(s)
    - Lubricant(s)
    - Co-Solvent(s)
- Ferrule Gasket
- Complete Valve
    - Mounting cup
    - Valve core assembly

- Diaphragm

- Stem

- Spring

- Seal

    - Metering tank

    - Retaining cup

- Adaptor with dust cap
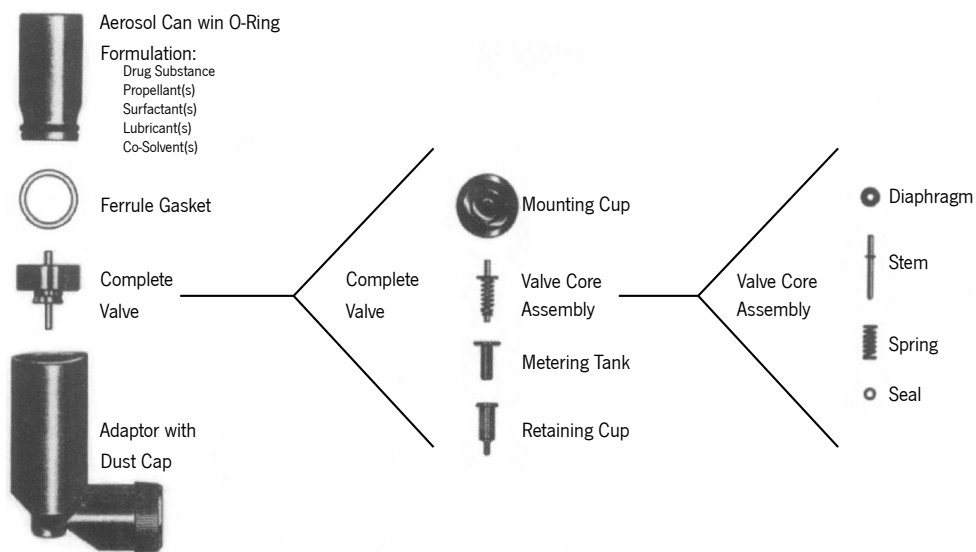
Figure 2.5: The pMDI main components, adapted from [RG99]

The spray pattern and Mass Median Aerodynamic Mass (MMAD) are influenced by: the ambient temperature; the design of the actuator nozzle and valve stem; and by the vapour pressure of the propellant in the formulation [DF01].

The formulation is composed by the drug, the propellants gases and it often contains surfactant and other excipients. In the formulation, the propellant is the component which creates vapour pressure inside the canister, allowing the drug to exit the pMDI and to form a spray plume every time the device is actuated. When the drug particles exit the pMDI, they are encapsulated in a droplet made of propellant, which evaporates as it travels through air. Some of the formulation's characteristics, in one of the most common used medicine in asthma treatment (Ventolin), are

25

listed in Table 2.1.

Table 2.1: Ventolin's formulation showing two propellant types, HFA and CFC [New05]

	Ventolin HFA	Ventolin CFC
Active ingredient	Salbutamol sulphate	Salbutamol sulphate
Excipient	None	Oleic acid
Propellants	HFA-134a	CFC-11/12
Formulation type	Suspension	Suspension

The canisters for a pMDI are typically made of aluminium and they are designed to be light, compact and strong to hold the high internal vapour pressure of 3 to 5 bar made by the propellant in the formulation [New06, New05]. Its typical capacity ranges between 15 mL and 30 mL [Dun97]. The metering valve of a pMDI is crimped into the container. There are several designs of valves but they all work under the same principle: while the canister is in the inverted position, by gravity action, the valve fills a cavity with the formulation through a channel, gathering the desired measured dose; at the priming moment, this channel closes and another one opens in the opposite side of the metering valve, allowing the formulation to rapidly expand into the expansion chamber. The actuator pit and the valve stem constitute the expansion chamber where the propellant begins to boil [Dun97, New05]. This process is often referred as the primary atomisation, where a flash evaporation of the propellant takes place [Dun97, Fin01]. Afterwards, it exits the expansion chamber through the actuator nozzle and it rapidly expands in the shape of a solid-cone plume [Dun97, New05]. In this way, the metering valve of a pMDI is a critical component in the effectiveness of the delivery system. Thus, its main functions are [Tas98, DF01, New06, Smy03, New05, Dun97]:

- Deliver (accurately and reproducibly) a measured volume (20-100 μL), containing between 20-5000 μg of the dispersed drug;
- Form a tight seal for the high pressure propellant in the canister.

The actuator is normally a single plastic piece produced by injection moulding that consists of a

mouthpiece, body and nozzle [New06, Smy03, New05, Dun97, SHB$^+$06]:

- The mouthpiece is the interface part to the patient mouth;

- The body provides support for the canister;

- The nozzle has a very important role in controlling the atomisation process, to guarantee a spray plume formation. The nozzle diameter interferes directly with the particles size distribution [Cla91, CYF$^+$14b, SBB$^+$06].

When the pMDI reached the market in 1956, it was composed of an elongated mouthpiece (around 8 cm); nowadays, it was reduced to a more compact size (from 2 to 3 cm) to improve the portability [New05].

2.3.2 Add-on Devices (spacers)

Despite having a number of advantages, the pMDI is usually coupled to add-on devices in order to improve the fraction of medication that deposits in the lungs. The first known pMDI, produced in the 1950s, had an elongated mouth-piece to the actuator. This was, in fact, the first pMDI spacer device, once the purpose of this design was to provide sufficient distance and time for the propellant to evaporate. Years after, the development of a much larger device to be used by children was reported. Subsequently, a range of add-on products has been described as devices that help patients to get the adequate amount of medicine when a pMDI is used [New04].

These add-on devices are classified in three main categories: simple/tubular spacers; reverse flow devices; and Valved Holding Chamber (VHC). Briefly, it can be summarized the three main roles of the add-on devices: they allow an easier use of pMDIs by reducing the need to coordinate actuation with inhalation; they increase the pulmonary targeting, by lowering the velocity of inhaled drug particles; and they act as an alternative to nebulisers, for delivering large doses of bronchodilators in patients with severe asthma [MN07].

Tubular Spacer

Tubular spacers are the simplest add-on devices to couple with a pMDI. Its operating principle is based in the addition of distance between the patient's throat and the actuator nozzle. This allows the propellant, in the spray's plume, to increase its evaporation rate. It allows reducing the droplets size and decreasing the plume velocity, resulting in lower oral-pharyngeal deposition and improved lung delivery. Nevertheless, the patient needs to be able to breathe in as the pMDI is actuated, because the device does not hold any of the medication. From a practical point of view, this category of add-on devices is an extension to the inhaler mouthpiece, requiring the same inhalation-actuation coordination.

The idea for the spacer was firstly developed by Maison and Porush (1956) [PM61], two decades after the invention of pMDI. By that time the problems regarding the complexity of the pMDI technique were well documented. Their design was simple, consisting of a tubular extension (7.6 cm) of the pMDI actuator mouthpiece. One year passed and a tubular spacer was developed as an accessory for the pMDI [vS59].

A great research effort was made to better understand the spacer dimensions and reach an optimum value. Kirk (1972) studied the elongation of the pMDI actuator mouthpiece from 3.7 cm to 8.0 cm, concluding that this increased the ability to deliver the dose [Kir72]. Móren (1978) shown (through an $in\ vivo$ study) that the optimum spacer length should be 10 cm, beyond this value no further reduction of the impaction was noticed. Increasing the diameter of the tube was proved beneficial for reducing the particle loss and improving the drug delivery [Mor78]. He also suggested that pear-shaped devices could actually be the next best bet for spacer design [MW79]. Barry and O'Callaghan (1995) experimentally correlated the emitted FPM with the length (5 – 50 cm) and diameter (3 – 10 cm) of tubular spacer (and their volume), concluding that both the length and diameter increase the output. A correlation was found between the volume and the FPM, for which volumes above 1 L do not provide greater improvement [BO95].

Reverse Flow Spacers

In the case of the reverse flow add-on devices, the medication plume is initially directed away from the patient into a chamber (equipped with air vents). The air is inhaled through the device's mouthpiece, bringing drug particles along, which rested in the chamber. This type of spacer allows the spray plume to evaporate in the stagnant air of the chamber, prior to being inhaled. This add-on category has no one-way valve, allowing the patient to exhale into the device. The coordination between the actuation and inhalation is nullified, but the tidal breathing is not advisable [New04].

Valved Holding Chamber (VHC)

The valved devices usually contain a inhalation one-way valve, close to the mouthpiece, which represent their most differentiable characteristic. Holding chambers commonly provide the largest distance between the actuator and the patient which is important for a rapid decrease of particles' velocity. Studies demonstrate that there is a correlation between the spray plume velocity and the particle's impaction on the oral-pharyngeal area. The volume of the holding chamber allows the delivery of high quantities of medication, mostly in severe cases of chronic respiratory diseases [New05].

The VHC devices vary in volume, design, materials and features. Concerning the design there are: pear-shaped spacers; straight spacers; and cone-shaped spacers. However, the device volume should not exceed the breathing capacity of the patient, so the medication would not be wasted.

2.3.3 Delivery Procedure

The actuation, also called priming, discharges the spray plume (also known as puff), into the air. The actuation of the pMDI needs to follow some procedure steps to result in an efficient delivery to the patient's lungs, or else almost all drug will be trapped in the throat [PCS01, Fol02]. The procedure can be resumed to a few steps, which are advised for all patients using pMDI solo:

1. Remove the dust cap and hold the inhaler upright
2. Shake the inhaler

3. Exhale fully

4. Place the pMDI actuator in the mouth

5. Breathe in deeply and slowly

6. Press on inhaler (coordinating actuation with inhalation)

7. Keep inhaling for 3 to 5 seconds

8. Hold breath for 10 seconds

9. Exhale slowly

10. One actuation per inhalation

11. Wait 1 minute before second actuation

By studying the technique of the pMDI used by the patients, it was found that the majority of the patients have difficulty to execute all the steps correctly. The study included children (n= 26), adolescent (n= 23), adult (n= 209) and elderly (n= 66) patients. Among them, the children are those with more difficulty in coordinating the inhalation-actuation. The elderly have more difficulties in just doing one actuation per procedure and waiting before going for the second round. Adolescents and adults are the patients with better abilities to use the pMDI device correctly [PCS01].

Without a proper technique, the use of pMDI can not be effective. In the case of corticosteroids, it can even be harmful. This is the reason why several asthma treatment guidelines recommend the use of add-on devices for children under 5 years old. The USA national asthma treatment guidelines state the use of holding chambers for "...children less than 4 years of age will have less difficulty with a pMDI plus VHC with a face mask...". During a child dose (for children under 12 years old) of SABA drugs, it is again stated "4–8 puffs every 20 minutes for 3 doses, then every 1–4 hours inhalation manoeuvre as needed. Use VHC; add mask in children < 4 years" [Nat07]. According to the British guidelines for asthma treatment "children and adults with mild and moderate exacerbations of asthma should be treated by pMDI + spacer with doses titrated according to clinical response". It also states that "In children aged 0-5 years, pMDI and spacer are the preferred method of delivery of β_2-agonists or inhaled steroids. A face mask is required until the child can breathe reproducibly using the spacer mouthpiece". And that "Children receiving β_2-agonists via pMDI + spacer are less likely to have tachycardia and hypoxia than when the same

drug is given via a nebulizer", "There is good evidence that pMDI + spacer is as effective as, if not better than, nebulizers for treating mild to moderate asthma in children aged $\leq$ 2 years" [SB11]. The Global Initiative for Asthma (GINA) report provides global guidelines for asthma treatment with the VHC: "In general, a metered-dose inhaler (MDI) with spacer is preferable to nebulized therapy due to its greater convenience, more effective lung deposition, lower risk of side effects, and lower cost... Use of a spacer also reduces oropharyngeal side effects... In severe acute asthma exacerbations a nebulizer is often used, although an MDI with a spacer is equally effective" [Glo14]. It is also stated that the preferred device for asthma treatment in children ($\leq$ 6 years old) is the pMDI + spacer.

A major literature review on the asthma inhalation treatment, from surveys on medication to delivery devices, was assembled by a group of renowned researchers in the field in 2001 [BRW$^+$01]. In this document, an extensive compilation of studies previously made about asthma is available, and it is possible to find a summary of the previously recommendations on the guidelines related to spacers.

2.4 Valved Holding Chamber (VHC)

The VHCs are coupling devices that attach to pMDI. As previously mentioned, its basic function is to add distance between the spray and the patient's throat, giving it time for the propellant to evaporate. The VHCs remove the plume's ballistic component (i.e. coarse particles); reduce the potential for systemic absorption of drug deposited in oral-pharyngeal ($\approx$80% reduction); and retain the aerosol plume in the chamber allowing the patient to inhale it at his own time [New04]. More importantly, VHC nullify the actuation-inhalation coordination, which gives the patient possibility to inhale the dosage using tidal breathing. The one-way valve at the mouthpiece avoids the patient to exhale inside the chamber.

2.4.1   Characterisation

As shown in Figure 2.6, a VHC consists of four parts: adapter, body, valve and mouthpiece. These may be made from different materials, as well as, the existence of flow indicators (i.e. whistle), dust cap, or even exhalation valve.
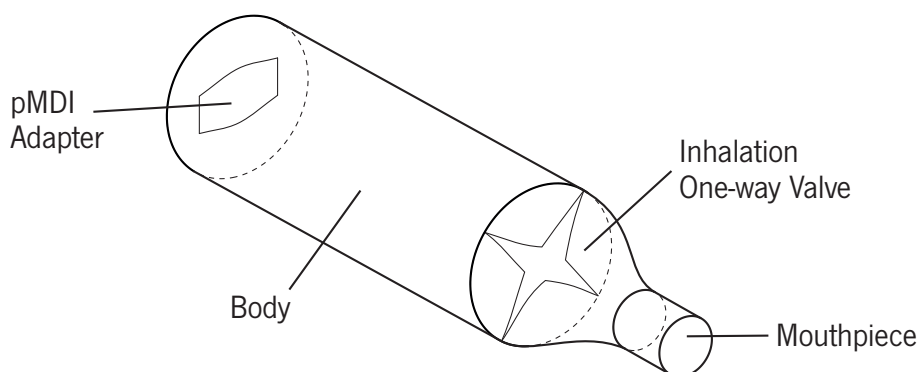
Figure 2.6: Schematic of the VHC components

Its most important characteristic is the one-way valve for inhalation, because this allows the tidal breathing to happen without losing drug particles. Some devices have exhalation one-way valves, which improve VHC's performance. This device is usually accompanied by a facemask, that plays an important role in improving the drug delivery to very young children [MvHvK+14, EFAvV+04]. Many VHCs are lined on the inside with an anti-static coating and their volume varies between 100 and 750 mL. The VHCs volume is related to the patient pulmonary physiology (age-related), the tidal volume.

The materials used have a greater role in the efficiency and cost of VHC devices. Several studies indicate that the electrostatic effect of the material walls affects the emitted dose from the device, reducing the amount of drug that reaches the lungs [Bis95, KCC06, DGB03, WDH+96]. A metal VHC device, Nebuchamber, was developed to avoid this problem, as well as other devices with antistatic properties [Bis95, JWE+02, BO99b]. Other studies suggest that pre-treatment of VHCs with a washing bath in a surfactant solution, before its use, resulted in a reduction of electrostatic charge and increases drug delivery [WDH+96].

Electrostatic charge is a commonly-reported cause of unreliable drug delivery from VHCs. The

electrostatic force can be much higher than the gravity for highly charged particles. Most aerosol particles carry electric charge, which affects aerosol retaining within the VHC device, as well as, the drug deposition at lungs. The electrostatic charge removal is required from the standpoint of achieving consistent deposition of drug particles in the lower respiratory tract [RR13]. Also, electrostatic charges increase as the result of: (1) the friction created by the contact and separation of dissimilar materials; (2) the interaction between pMDI components and particles. VHCs made from non-conducting polymers acquire surface electrostatic charge during manufacture, packaging and even storage process. As a result, if precautions are not taken to mitigate this phenomenon, the efficiency of the drug delivery can be affected. Pre-washing VHCs with solution containing a small quantity of ionic detergent is an acceptable approach to reduce the negative effects of the electrostatic charges since detergents are essentially surfactants with the capability to spread onto a surface as a monolayer.

The VHC valves (inhalation and exhalation) must operate effectively over the entire pressure range during the use of the VHC device. This requirement is a problem for children/infants because they have some difficulties in reaching a pressure of 100 to 300 Pa, below which the valves are stuck closed. The correct valve operation requires at least a 50 mL of tidal volume, an inhalation/exhalation ratio of 40/60 and 30 breaths/min [MN07]. The ability to observe valve movement in response to patient breathing is a significant benefit in confirming their correctly operation.

There is a great diversity regarding the VHC devices volume which can also affect efficiency of drug delivery. Smaller devices are advantageous for infants because of its compact size, portability, easier handling and because they minimise the number of inhalations necessary to empty the chamber.

2.4.2 Requirements

Although efficiency is the major reason why the study is justified, there are some requirements to be taken into account in the study of VHC devices. They can be classified of user or physician nature.

User Requirements

Patient do require some aspects of the VHC device that are related to its usability and transportation. Those should be kept in mind while developing a new VHC [Dol04].

- Portability
    - Lightweight
    - Reduced size
- Cost
    - Simple production process (e.g. injection moulding)
    - Cheap materials (e.g. polymers)
- Easy usage
    - No complex mechanisms
    - Ergonomic
- Easy cleaning
    - If modular, needs to be of easy assembling
    - Cleaning using normal domestic products
- Resistant
    - Avoid losses of efficiency due to the continuous cleaning
    - Endure drops from children usability

These desired characteristics are not always compatible with each other, and seldom are all present in the various types of VHC available in the market.

Physician Requirements

The physician requirements are mostly focused in the efficiency of the device, where the maximisation of the FPM (keeping the bioequivalence with the pMDI solo) is the main concern. Other topics must be taken into account:

- Efficiency

- – Low electrostatic materials

- – Reduction of the spray velocity

- – Functional one-way valve for low inhalation flow rate

- – Features that can perform inhalation flow control

- – Reduced drug entrapment

- Materials

  - – Non harmful (health)

- Volume

  - – Must be adequate to the patient age

2.4.3 Market Analysis

There are several VHC models commercially available in the market. In Table 2.2, the main characteristics of eight commercial VHC devices used in this work, are described. There are other commercial devices, however their availability depends on the country. Many more VHC projects are patented but they never reached the market. The VHC devices described in Table 2.2 are all available in the United Kingdom, and the majority of them were obtained next to the producers (excepting Vortex, Nebuchamber and Volumatic). The most sold VHC devices are the Volumatic, Aerochamber Plus and Vortex. In Table 2.2 is also provided information regarding the devices weight, volume, body length and price, among other characteristics.

In the majority of the VHCs, the adapter is made of a flexible material (e.g. silicon rubber), allowing a good air sealing with most of the commercial pMDI actuators. On the other hand the Volumatic, was developed to be used with the Ventolin pMDI and Nebuchamber was specifically developed to be used with Plumicort pMDI.

Other observable characteristics of these devices were the existence of flow control whistle (present only in Aerochamber and Optichamber), which would activate at a certain inhalation air flow rate. This feature was further studied by Sanders and Bruin (2013), where they observed that the whistle activation is highly dependent on the pMDI product used. This fact is related to the pressure drop associated to each pMDI product. If the pressure in the pMDI actuator is high, than the air will

preferable pass through the whistle, activating it for lower flow rates [SB13]. The development of the whistle is based in the vibration (and sound waves) produced by air turbulence around a blunt body, this geometry is dimensioned for a given flow rate. Its development is made by trial and error, which is a very time consuming process.

Among the eight VHC devices selected, some common design characteristics were observed, such as the valve. Thus, the devices were grouped by their valve design (see Table A.5).

- **Leaflets** - an open-centre design that is composed by several (e.g. four) leaflets, bending from the centre to the sides, similar to the heart valves.

  - Compact Space Chamber (CSC)
  - Space Chamber (SC)
  - A2A Spacer (A2A)

- **Duck** - an open-centre design that is similar to a duck beak, opening the centre by bending of two surfaces.

  - NebuChamber (NC)
  - OptiChamber Diamond (OCD)
  - Vortex (V)

- **Annulus Flap** - an non open-centre design that is composed by a annulus ring, where the innermost edge zone bends.

  - AeroChamber (AC)

- **Coin** - an non open-centre design that is a rigid body with a coin shape, that moves upon flow solicitation to allow or restrict air passage.

  - Volumatic (VOL)

Table 2.2: Main features of eight commercial VHC devices available in the market

Commercial Name	A2A Spacer	AeroChamber Plus	Nebuchamber	OptiChamber Diamond	Vortex	Compact Space Chamber Plus	Space Chamber Plus	Volumatic
Acronym	A2A	AC	NC	OCD	V	CSC	SC	VOL
Photo								
Category	dissipative	dissipative	dissipative	dissipative	dissipative	non-dissipative	non-dissipative	non-dissipative
Company	Clement Clarke International	Trudell Medical International	AstraZeneca	Philips Respironics	PARI	Medical Developments	Medical Developments	Glaxo Smith Kline
Adapter Material	silicone rubber	silicone rubber	stainless steel	silicone rubber	silicone rubber	silicone rubber	silicone rubber	Polycarbonate
Body Material	antimicrobial and antistatic polymer	StatBan - antistatic polymer	stainless steel	ABS antistatic	Polycarbonate + aluminium coating	Polycarbonate	Polycarbonate	Polycarbonate
Valve Material	silicone rubber	silicone rubber	silicone rubber	silicone rubber	silicone rubber	silicone rubber	silicone rubber	Polycarbonate
Weight [g]	41.5	56.1	120.9	57.0	70.5	50.7	60.9	150.9
Volume [mL]	210	149	250	140	194	160	230	750
Body Length [mm]	129	102	144	97	126	112	150	193
Availability in Portugal	no	yes	*	yes	yes	no	no	yes
Price NHS-UK [£]	4.15	4.79	*	4.49	6.28	4.26	4.26	3.81
Patents	-	US5042467, US5848588, US6293279, US7360537, USRE43174, USRE45068	US5881718, US6435176	US20130186393	US7562656, US8074641	-	-	USD295321
Visible Inhalation Valve	yes	yes	no	no	yes	yes	yes	yes
Whistle	no	yes	no	yes	no	no	no	no
Exhalation Valve	no	yes	yes	yes	yes	yes	yes	no
Universal Adapter	yes	yes	no	yes	yes	yes	yes	no

* The device was discontinued.

Some of the eight VHCs are equipped with an exhalation one-way valve (i.e. CSC, SC, AC, OCD and NC). This is a great feature, that seals potential co-flows during inhalation and reduces excessive pressure against the inhalation valve during exhalation phase (see section A.5). Volumatic and A2A Spacer simply possess two air vents, for the exhalation flow to escape. However, the larger the vent dimension, the higher is the co-flow entering during inhalation. This reduces the volume of air inhaled from the VHC body (containing drug particles), and lowering the effectiveness of the treatment.

Despite the Nebuchamber has been discontinued, the study will include this device due to the fact that its body is entirely made of stainless steel. Given the fact that the material highly affects the efficiency of the VHC device, the Nebuchamber will allow to infer if this device high weight is counterbalanced by its efficiency, in comparison to more recent devices in the market.

2.5 Literature Review

This section presents a few literature studies involving VHC devices. Those studies are divided in four sub sections: reviews, $in\ vivo$, $in\ vitro$ and numerical.

2.5.1 Reviews

Wong et al. (2012) reports the increasing use of CFD-DEM approach in numerical studies for predicting the drug deposition and delivery in inhalation devices. The increase in the use of this approach can be seen for the number of recent studies concerning DPI devices. They point that the use of numerical tools is not a replacement of experimental evaluation and should be used with careful considerations on the numerical models used. CFD predictions should always be accompanied with some experimental validation data [WFT+12].

Ruzycki and his team (2013) compile the use of CFD tools in the prediction of drug deposition for inhaler design. He overviews the numerical software's used in the simulation of nebulizers, DPIs, pMDIs with and without spacers. The authors concluded that the use of CFD is becoming more common in pharmaceutical applications, for improving medical devices or study drug deposition in

the airways, stating that the most beneficial results are those provided with experimental validation [RJF13].

Nikander et al. (2014) review the historic evolution of spacers and VHCs starting 1970s up to today, focused in the spacer design, patented inventions, adherence and technique [NNDP14].

2.5.2 In Vivo Studies

Newman and his collaborators (1984) evaluated the aerosol delivery using a VHC device (750 mL) in nine patients, using an $in\ vivo$ radiotracer technique. Results shown that the throat deposition was greatly reduced and the lung deposition is similar to the pMDI solo when properly used [NMLJ$^+$84]. A delivery efficiency study was made by Olof Selroos and Maija Halme in a Finnish hospital, with nine asthmatic adults medicated with a corticosteroid drug. The results shown that patients that do not use a pMDI with the Volumatic VHC, tend to ingest excess of drug, which bring adverse health effects to the human system, therefore the patients are advised to rinse their mouth after treatment [SH91].

Other study explores how the usage of a metal versus a plastic VHC, can produce different results in young asthmatic children. Bisgaard focused the study in a group of 164 children aged from 6 months to 7 years old. The results show that a plastic VHC might cause age dependence in the delivery of drug in opposite to the metal one [Bis95].

Castro-Rodriguez and his team (2004) compared the efficacy of drug delivery using a pMDI+VHC against the use of nebulizer, for asthmatic children under 5 years old, in an emergency department. The pMDI+VHC has proven to be more effective than the nebulizer, by decreasing the hospitalisation time [CRR04].

Khan and his team (2006) analysed the efficacy of fluticasone delivered by two VHC devices (AeroChamber Plus - conventional and AeroChamber Max - antistatic) in twelve children (1 - 6 years old). The drug delivery was assessed through blood samples taken from the subjects 1 hour after the treatment. Results have shown that the antistatic VHC increased the drug delivered [KTH$^+$06].

Rodriguez-Martinez et al. (2012) assessed the pMDI, with or without a spacer (a tubular and a

VHC). A two-sequence crossover clinical trial for the treatment in 31 stable asthmatic children (6-18 years old) was used, by assessing their spirometry. Results showed that the use of both spacers produced similar treatment results [RMSBCR12].

Ditcham et al. (2014) conducted a survey in asthmatic children (3-5 years old), using radiolabeled albuterol, on the effect of using a VHC with or without a facemask. Lung delivery was higher 4.4% when the facemask was used [DMZ$^+$14].

Minh et al. (2014) studied the patient (children 1 – 4 years old) compliance, air flow and facemask force. The research was conducted using a custom made OptiChamber Diamond, that was embed with a Facemask Datalogger, for recording the air flow passing through the VHC and the force made by the patient for keeping the facemask sealed against the face. Results show that older children emptied the VHC faster with fewer breaths and showing better cooperation. The mean force applied by the patients was ≈4 N [MvHvK$^+$14].

2.5.3   In Vitro Studies

Wildhaber and his collaborators (1996) studied the effect of the plastic spacer (i.e. Volumatic) wall electrostatic charge, on the salbutamol sulphate drug delivery. The assessment was executed at constant flow rate of 60 L/min using a MSLI CI, and using different washing techniques for the spacer (i.e. new, used, plastic rubbed, water rinsed, foil covered, cationic detergent coated and anionic detergent coated). Results show an increased drug delivery for cationic detergent coating technique, followed by foil covering and anionic detergent coating. The new spacer out of the box delivered the least dose. The coating using ionic detergent removed the charge for at least 24h [WDH$^+$96].

Finlay et al. (1997) reported the evaluation of two VHC devices (i.e. Aerochamber and Space-Chamber) salbutamol and beclomethasone delivery at 28.3 L/min, collected in a Andersen CI. The Space-Chamber increased (i.e. 32%) the FPM of beclomethasone when compared to the pMDI solo, no differences were found for the salbutamol delivery. Aerochamber delivered similar FPM to the pMDI solo both for beclomethasone and salbutamol. Throat deposition was highly reduced by the use of spacers (i.e. ≈ 98%) [FZM97].

Mitchell and Nagel (1997) evaluated three VHCs (i.e. AeroChamber, Space Chamber and Vent-170), on the delivery of salbutamol and beclomethasone dipropionate. A breath profile passed through the VHC, and the emitted mass was collected in a filter. Results indicate that AeroChamber emitted the highest dose for both formulations, at tidal volumes from 50 mL to 200 mL. The other devices were not able to deliver any drug at 50 mL. The authors concluded that tests mimicking the patient breath pattern are essential to identify differences (i.e. valve operation) that are not observable at constant flow tests [MN97].

Finlay and Zuberbuhler (1998) determined the amount of salbutamol and beclomethasone delivered from pMDI attached to four spacers (i.e. AeroChamber, OptiChamber, Space Chamber and E-Z Spacer), using a variable flow setup for simulating the inhalation profile of an infant, toddler and older child. The results indicate that the emitted FPM dependent on the drug used, spacer model and waveform [FZ98].

Barry and O'Callaghan (1999) evaluated three spacers (i.e. Aerochamber, Nebuhaler and Nebuchamber) on the delivery of budesonide using a breathing simulator (generating sine waves with different tidal volumes). The drug collect increased with the tidal volume (i.e. from 50 mL to 300 mL). This increase was higher (i.e. ≈ 56 μg) for the high volume (i.e. Nebuhaler – 750 mL) and the metal spacers (i.e. Nebuchamber – 250 mL), while it was lowest (i.e. 26.7 μg) for the smallest one (i.e. Aerochamber) [BO99b]

Foss and Keppel (1999) developed a variable flow setup for collecting the salbutamol sulphate (i.e. Ventolin) emitted by four spacers (i.e. MediSpacer, Aerosol Cloud Enhancer, OptiHaler and AeroChamber) when actuated at the start of the inhalation and at the start of the exhalation. This study focused in the evaluation of the spacer devices performance when misused, concluding that the four devices had less FPM delivered when badly actuated. Not only the timing affects the drug delivery, but also the device design has great influence when the inhalation is delayed [FK99].

Barry and O'Callaghan (1999) assessed the drug emitted from three pMDI (i.e. Becotide, Sarevent and Flixotide) through three spacers (i.e. Babyhaler, Volumatic and Aerochamber). The drug assessment was executed using a 4-stage MSLI CI at 60 L/min with an actuation-inhalation delay of 2 s. The results pointed that the each pMDI had a different output for each spacer, leading to the conclusion that each spacer needs to be fully evaluated for each drug prescribed [BO99a].

Chew and Chan (2000) studied the effect of four spacers (i.e. Fisonair, Breath-A-Techm Volumatic and Nebuhaler) in the delivery of two pMDI formulations (i.e. Tilade and Intal), using a Marple-Miller CI at 30 L/min. The results pointed that the high volume spacers (i.e. Fisonair > Nebuhaler > Volumatic) increased the FPM output, while the smaller spacer (i.e. Breath-A-Tech) did the opposite. They concluded that the proper choice of the spacer is important for the optimal delivery of the pMDI dose [CC00].

Rahmatalla and his collaborators (2002) assessed the pMDI QVAR mouth-throat (i.e. idealized Alberta model) deposition under three constant inhalation air flow rates (i.e. 28.3, 60 and 90 L/min) [RZLF02].

The study was conducted using a single filter or an 8-stage Andersen CI for the pMDI with and without a VHC (i.e. Aerochamber). They observed that the VHC contributed to a reduction of the throat deposition between 45% and 66% (higher for lower flow rate). The dose delivered increased with the flow rate from 42% to 69%, whereas the VHC did not added much variation. Results showed that the plume MMAD did not suffered significant changes with the use of a VHC.

Janssen et al. (2002) compared a metal (i.e. Nebuchamber) against a polymer VHC (i.e. Volumatic), in terms of salbutamol (i.e. Ventolin) drug delivery using an Andersen CI at 28 L/min. It was observed that the small volume (i.e. 250 mL) metal spacer was able to deliver a similar dose to the high volume (i.e 750 mL) polymer VHC [JWE$^+$02].

Nagel et al. (2002) evaluated the performance of AeroChamber Plus and Volumatic in the delivery of fluticasone propionate and salmeterol xinafoate using an Andersen CI at 28.3 L/min. The use of either VHC devices increased the FPF in ≈40% for both formulation in comparison to the pMDI solo. Whereas the FPM emitted from the both VHC devices was slightly greater to the pMDI solo [NWBM02].

Asmus and his team (2004) studied the fluticasone delivered through seven VHC (i.e. BreatheRite, E-Z Spacer, EasiVent, AeroChamber, InspirEase, OptiChamber and Space Chamber) and six spacer devices (OptiHaler, ACE, Gentle-Haler, MediSpacer, Elipse and a 6-inch tube). Their FPM was determined using a CI. Results shown the Ellipse (104 μg) to be spacer with higest FPM. Between the VHC devices the Space Chamber (58.3 μg) emitted the highest respirable fraction [ALCH04].

Using a constant flow extraction setup with a laser photometric measurement, Verbanck and

colaborators (2004), assessed the Ventolin (i.e. salbutamol sulphate) emitted over time from a high (i.e. Volumatic) and low (i.e. Aerochamber) volume VHC. Observing that the low volume VHC would take less time to achieved total drug delivery than a high volume VHC. The emitted drug filter collection showed an increased amount for the high volume device [VVSV04].

Rau et al. (2006) assessed the emitted albuterol from Vortex, AeroChamber Max, OptiChamber Advantage, ProChamber, Breathrite, PocketChamber and ACE, with and without pre-treatment, for 2 and 5 s delays between actuation-inhalation. The FPM assessment was conducted in an Andersen CI at 28.3 L/min. The results shown that the AeroChamber Max emitted the highest FPM (i.e. 23.8 μg). Also, it was concluded that the VHC devices made of electrically conductive materials emit higher FPM (for both 2 s or 5 s delays), then those made of non-conducting materials (even when pre-treated) [RCN$^+$06].

Goncalves et al. (2013) compared the performance of three VHC (i.e. Able Spacer, AeroChamber Plus and Vortex) in the delivery of beclomethasone dipropionate and formoterol, using a NGI at 30 L/min. All VHCs reduced the throat deposition in comparison with the pMDI solo. Vortex and AeroChamber Plus presented advantages over the Able Spacer in terms of emitted FPM [GAN$^+$13].

Sheth et al. (2014) evaluated the QVAR FPM delivered from a pMDI when combined with non-conventional spacers (i.e. nebulized reservoir, rolled paper, toilet paper roll, paper towel roll, bottle-holding chamber and bottle spacer) and a commercial one (i.e. AeroChamber). Performance was assessed for two throat models (i.e. USP IP and AIT) using a Respirable Impactor and Aerodynamic Particle Sizer. Any add-on device will reduce the throat deposition and increase the respirable fraction, whereas the paper towel roll had the greatest effect. The actuation-inhalation delay affects the performance, which is mainly mitigated by the use of the paper towel roll or the bottle-holding chamber [SBKM14].

Xu and his collaborators (2014) studied the delivery efficiency of the VHC (i.e. OptiChamber Diamond, AeroChamber Plus, Pocket Chamber and Volumatic) in combination with facemasks, using three age-specific Soft Anatomical Model (SAM) faces. The setup allowed the testing of simulated breathing patterns and assessment of the mask leakage and delivered dose. The lowest leakage was found for the OptiChamber Diamond + LiteTouch facemask [XHvH$^+$14].

Hatley and collaborators (2014) assessed the drug delivery of two pMDI (i.e. albuterol and be-

clomethasone) with or without a VHC (i.e. OptiChamber Diamond - antistatic, AeroChamber Plus - conventional and AC Z-Stat - antistatic) at 15 and 30 L/min, using an NGI. The two antistatic VHCs were equivalent for both formulation, and their emitted FPM has higher (at 15 L/min) than the conventional VHC [HvHSS14].

2.5.4 Numerical Studies

Kleinstreuer and his team (2007) numerically studied the delivery of pMDI (HFA and CFC) spray droplets to the patient lungs using a human upper airway model with or without the use of a spacer. Results showed that HFAspray is more efficiency than CFC, delivering a higher dose to the lungs. The addition of the spacer to the pMDI provided an increase in the delivered dose by removing the coarse fraction of the plume [KSZ07].

Oliveira and his collaborators (2012) modelled the airflow inside various VHC body and valve designs, using an inhalation profile. Their aim was to study the air flow patterns and the formation of recirculation zones as well as their size. Results showed that some designs were more proficient than others, having fewer recirculation zones. They concluded by proposing a new design for VHC [OTS+12].

Oliveira et al. (2014) simulated the drug delivered by four VHC devices (i.e. A2A Spacer, Aerochamber Plus, Nebuchamber and Volumatic) at 30 L/min. The particles were considered inert, three particle size distributions were injected and tracked in FLUENT using Euler-Lagrangean approach. The results showed that coarser plumes tend to get more deposited inside the VHC device, Volumatic has higher deposition than the other devices and that Nebuchamber has the greatest throat deposition. Also it was observed that Aerochamber delivers the highest amount of FPM [OTMT14a].

Oliveira and his team (2014) focused in the numerical modelling of the pMDI spray in still air, using a realistic approach that accounted for the evaporation of the propellant. Results shown a rapid air temperature drop of 3.3 degrees Celsius near the actuator nozzle and air velocity increase of 3.27 m/s [OFT+14].

Yazdani and his team (2014) numerically studied the air flow inside three spacers (i.e. type I, type

II and type III) and their drug delivery, by modelling the injection of a pMDI (i.e. Proventil HFA) spray in an air co-flow at 30 L/min. Using FLUENT they manage to track the a batch of solid inert particles, using an Euler-Lagrangean approach, and predict the deposition fraction on those spacer devices. They notice that certain types of spacer designs are more prone to particle deposition by impaction than others. Not all spacer designs perform equally for all formulations [YNY+14].

Yousefi et al. (2015) modelled the drug deposition in idealized oral airway geometry, at 15, 30 and 60 L/min air flow rates, to optimize a VHC one-way valve design. Particles were modelled as an inert discrete phase using Euler-Lagrangean approach. It was noticed that particle deposition occurred mostly at the larynx, and this effect increases with the flow rate growth. The results pointed some guidelines for developing an impaction plate, located downstream the one-way valve. This would direct the particle + air jet towards specific zones where the oral deposition is lower [YIT15].

This page was intentionally left in blank

3 Development of the CFD Model

3.1 Mathematical Modelling

The Navier-Stokes equations are a specific application of the fluid conservation principle, which are not possible to solve by conventional numerical means, as each of them implies several considerations according to the specifics of the problem. The equations for the mass and momentum conservation are given bellow, and are only applicable to a non-accelerating reference frame and for viscous flows (i.e. presence of turbulence).

3.1.1 Mass Conservation

Mass conservation implies that the mass entering a control volume equals the mass flowing out, creating a balance between input and the output flows for a certain volume. This concept is mathematically expressed by Equation 3.1, which is valid for compressible and incompressible flows [ANS13, VM95, FP03, Whi98].

$$\frac{\partial \rho}{\partial t} + \nabla \cdot (\rho \vec{v}) = S_m \tag{3.1}$$

where S_m is the source of mass added to the continuous phase (air in this case) by the dispersed phase (particles/droplets) caused by vaporisation, for example. ρ stands for density, t for time and $\vec{v}$ represents the velocity vector.

Equation 3.2 presents the special case for 2-D axisymmetric geometries.

$$\frac{\partial \rho}{\partial t} + \frac{\partial}{\partial x}\left(\rho v_x\right) + \frac{\partial}{\partial r}\left(\rho v_r\right) + \frac{\rho v_r}{r} = S_m \tag{3.2}$$

where x and r are, respectively, the axial and radial coordinates and v_x and v_r their, respectively, velocity components.

3.1.2 Momentum Conservation

Momentum conservation is given by Equation 3.3, where p represents the static pressure, $\rho\vec{g}$ and $\vec{F}$ correspond respectively to the gravitational body force and the external body force (interaction with the dispersed phase, for example). The $\overline{\overline{\tau}}$ identifies the stress tensor and is given by the Equation 3.4.

$$\frac{\partial}{\partial t}\left(\rho\vec{v}\right) + \nabla \cdot \left(\rho\vec{v}\vec{v}\right) = -\nabla p + \nabla \cdot \left(\overline{\overline{\tau}}\right) + \rho\vec{g} + \vec{F} \tag{3.3}$$

$$\overline{\overline{\tau}} = \mu\left[\left(\nabla\vec{v} + \nabla\vec{v}^T\right) - \frac{2}{3}\nabla \cdot \vec{v}I\right] \tag{3.4}$$

where the μ represents the molecular viscosity, I is the unit tensor, and the second term on the right hand side of the equation $\left(-\left(2/3\right)\nabla \cdot \vec{v}I\right)$ accounts for the effect of volume dilation. For 2-D axisymmetric flows, equations get a bit more complex due to the need to separate axial from radial momentum, and they are described by Equations 3.5 and 3.6.

$$\frac{\partial}{\partial t}\left(\rho v_x\right) + \frac{1}{r}\frac{\partial}{\partial x}\left(r\rho v_x v_x\right) + \frac{1}{r}\frac{\partial}{\partial r}\left(r\rho v_r v_x\right) = -\frac{\partial p}{\partial x} \tag{3.5}$$
$$+ \frac{1}{r}\frac{\partial}{\partial x}\left[r\mu\left(2\frac{\partial v_x}{\partial x} - \frac{2}{3}\left(\nabla \cdot \vec{v}\right)\right)\right]$$
$$+ \frac{1}{r}\frac{\partial}{\partial r}\left[r\mu\left(\frac{\partial v_x}{\partial r} + \frac{\partial v_r}{\partial x}\right)\right] + F_x$$

$$\frac{\partial}{\partial t}\left(\rho v_r\right) + \frac{1}{r}\frac{\partial}{\partial x}\left(r\rho v_x v_r\right) + \frac{1}{r}\frac{\partial}{\partial r}\left(r\rho v_r v_r\right) = -\frac{\partial p}{\partial r}$$
$$+ \frac{1}{r}\frac{\partial}{\partial x}\left[r\mu\left(\frac{\partial v_r}{\partial x} + \frac{\partial v_x}{\partial r}\right)\right]$$
$$+ \frac{1}{r}\frac{\partial}{\partial r}\left[r\mu\left(2\frac{\partial v_r}{\partial r} - \frac{2}{3}\left(\nabla \cdot \vec{v}\right)\right)\right]$$
$$- 2\mu\frac{v_r}{r^2} + \frac{2}{3}\frac{\mu}{r}\left(\nabla \cdot \vec{v}\right) + F_x \tag{3.6}$$

where

$$\nabla \cdot \vec{v} = \frac{\partial v_x}{\partial x} + \frac{\partial v_r}{\partial r} + \frac{v_r}{r} \tag{3.7}$$

3.1.3 Turbulence

RANS Formulation

In this work, the turbulence was modelled using a Reynolds-Averaged Navier-Stokes (RANS) approach, using linear eddy viscosity models of three equations, more specifically the $k - \omega$ Shear Stress Transport (SST) model. In Reynolds averaging the instant velocities are composed by mean velocity (or time averaged) and fluctuating components (see Equation 3.8).

$$v_i = \bar{v}_i + v_i' \tag{3.8}$$

where the $\bar{v}_i$ is the mean and the v_i' is the fluctuating velocity components (i=1,2,3 – for three dimensions). Likewise this formulation, accounting for mean and fluctuating parts, is applicable for pressure and other scalar quantities (e.g. energy or species concentration).

By substituting expressions using this form for the flow variables into the instantaneous continuity and momentum equations (3.1 and 3.3) and taking a time average yields the ensemble-averaged mass and momentum equations. When written in a Cartesian tensor form, the variables are presented as in Equations 3.9 and 3.10.

$$\frac{\partial \rho}{\partial t} + \frac{\partial}{\partial x_i}\left(\rho v_i\right) = 0 \tag{3.9}$$

$$\frac{\partial}{\partial t}\left(\rho v_i\right) + \frac{\partial}{\partial x_j}\left(\rho v_i v_j\right) = -\frac{\partial p}{\partial x_i} + \frac{\partial}{\partial x_j}\left[\mu\left(\frac{\partial v_i}{\partial x_j} + \frac{\partial v_j}{\partial x_i} - \frac{2}{3}\delta_{ij}\frac{\partial v_l}{\partial x_l}\right)\right] \tag{3.10}$$
$$+ \frac{\partial}{\partial x_j}\left(-\rho\overline{v_i' v_j'}\right)$$

Equations 3.9 and 3.10 are known as the RANS equations. These are similar to Equations 3.1 and 3.3 but with additional terms that represent the effects of turbulence. These turbulent Reynold stresses $(-\rho\overline{v_i' v_j'})$ need to be modelled using linear or non-linear eddy viscosity models.

Boussinesq Approach

Modelling the turbulence stresses in Equation 3.10 requires the application of an approach known as the Boussinesq hypothesis, described in Equation 3.11. This hypothesis is used to relate the Reynolds stresses to the mean velocity gradients, in an isotropic way by means of the turbulent viscosity (μ_t).

$$-\rho\overline{v_i' v_j'} = \mu_t\left(\frac{\partial v_i}{\partial x_j} + \frac{\partial v_j}{\partial x_i}\right) - \frac{2}{3}\left(\rho k + \mu_t\frac{\partial v_k}{\partial x_k}\right)\delta_{ij} \tag{3.11}$$

This approach has a relative low computational cost since the turbulent viscosity is computed as a function of two equations, k and ω. Since the turbulence is considered isotropic, this approach is highly related to the linear eddy viscosity models. The isotropic limitation is only questionable in the case of highly swirling flows and stress-driven secondary flows. In such cases, a Reynold Stress Model (RSM) should be used.

Turbulence Model

The Wilcox $k - \omega$ model developed in 1988, is a model with great applicability on Low-Reynolds Number (LRN) flows near wall regions. This model has two transport equations that represent the turbulent properties of the flow. The first variable is the turbulent kinetic energy, k. The second variable is the specific dissipation, ω. The first determines the energy of the turbulence, while the second defines the scale of the turbulence. However, its main limitation is the lack of sensitivity in the freestream zone of the flow (i.e. outside the shear layer).

Menter, in 1993, developed a model that successfully blends the Wilcox $k - \omega$ model (for treatment

of wall regions) and the $k - \epsilon$ model (for treatment of the freestream zone) [Men93]. It includes a blending function that handles the transition between the two models, which was given the name of SST $k - \omega$ model. Due to the nature of this study, this was the model of choice.

The Equations 3.12 and 3.13 allow the calculation of the turbulence transport parameters, k and ω, respectively.

$$\frac{\partial}{\partial t}\left(\rho k\right) + \frac{\partial}{\partial x_i}\left(\rho k v_i\right) = \frac{\partial}{\partial x_j}\left(\Gamma_k \frac{\partial k}{\partial x_j}\right) + G_k - Y_k \tag{3.12}$$

$$\frac{\partial}{\partial t}\left(\rho \omega\right) + \frac{\partial}{\partial x_j}\left(\rho \omega v_j\right) = \frac{\partial}{\partial x_j}\left(\Gamma_\omega \frac{\partial \omega}{\partial x_j}\right) + G_\omega - Y_\omega + D_\omega \tag{3.13}$$

In the Equations 3.14 and 3.15, G_k and G_ω represent the generation of k and ω, respectively. S represents the modulus of the mean rate-of-strain tensor and is defined by Equations 3.16 and 3.17. The turbulent viscosity, μ_t, is given by Equation 3.18.

$$G_k = \mu_t S^2 \tag{3.14}$$

$$G_\omega = \frac{\alpha}{v_t} G_k \tag{3.15}$$

$$S \equiv \sqrt{2 S_{ij} S_{ij}} \tag{3.16}$$

$$S_{ij} = \frac{1}{2}\left(\frac{\partial v_i}{\partial x_j} + \frac{\partial v_j}{\partial x_i}\right) \tag{3.17}$$

$$\mu_t = \frac{\rho k}{\omega} \frac{1}{\max\left[\frac{1}{\alpha^*}, \frac{SF_2}{\alpha_1 \omega}\right]} \tag{3.18}$$

A correction for LRN is introduced by means of α^* that damps the turbulent viscosity (defined in Equation 3.19). This is calculated using a turbulent Reynolds (Re$_t$ - defined in Equation 3.20), that

will make α^* become equal to 1 in high Reynolds number.

$$\alpha^* = \alpha_\infty^* \left(\frac{0.024 + \text{Re}_t/6}{1 + \text{Re}_t/6} \right) \tag{3.19}$$

where

$$\text{Re}_t = \frac{\rho k}{\mu \omega} \tag{3.20}$$

In Equation 3.15, the value of α is given by Equation 3.21. Where α^*, α_∞ and Re_t are given be Equations 3.19, 3.22 and 3.20, respectively.

$$\alpha = \frac{\alpha_\infty}{\alpha^*} \left(\frac{\alpha_0 + \text{Re}_t/2.95}{1 + \text{Re}_t/2.95} \right) \tag{3.21}$$

$$\alpha_\infty = F_1 \alpha_{\infty,1} + (1 - F_1) \alpha_{\infty,2} \tag{3.22}$$

where

$$\alpha_{\infty,1} = \frac{\beta_{i,1}}{\beta_\infty^*} - \frac{0.41^2}{\sigma_{\omega,1} \sqrt{\beta_\infty^*}} \tag{3.23}$$

$$\alpha_{\infty,2} = \frac{\beta_{i,2}}{\beta_\infty^*} - \frac{0.41^2}{\sigma_{\omega,2} \sqrt{\beta_\infty^*}} \tag{3.24}$$

In Equations 3.12 and 3.13, the terms Γ_k and Γ_ω, which account for the effective diffusivity of k and ω, respectively, are calculated by Equations 3.25 and 3.26.

$$\Gamma_k = \mu + \frac{\mu_t}{\sigma_k} \tag{3.25}$$

$$\Gamma_\omega = \mu + \frac{\mu_t}{\sigma_\omega} \tag{3.26}$$

whereas the turbulent Prandtl numbers, σ_k and σ_ω, are calculated by Equations 3.27 and 3.28.

$$\sigma_k = \frac{1}{F_1/\sigma_{k,1} + (1 - F_1)/\sigma_{k,2}} \tag{3.27}$$

$$\sigma_\omega = \frac{1}{F_1/\sigma_{\omega,1} + (1 - F_1)/\sigma_{\omega,2}} \tag{3.28}$$

In Equations 3.27 and 3.28 it can be found the blending functions previously referred, F_1 and F_2, calculated accordingly to Equations 3.29 and 3.30. y is the distance to closest wall and D_ω^+ is the positive portion of the cross-diffusion term given be Equation 3.32.

$$F_1 = \tanh\left(\Phi_1^4\right) \tag{3.29}$$

$$F_2 = \tanh\left(\Phi_2^2\right) \tag{3.30}$$

$$\Phi_1 = \min\left[\max\left(\frac{\sqrt{k}}{0.09\omega y}, \frac{500\mu}{\rho y^2\omega}\right), \frac{4\rho k}{\sigma_{\omega,2}D_\omega^+ y^2}\right] \tag{3.31}$$

$$D_\omega^+ = \max\left[2\rho\frac{1}{\sigma_{\omega,2}}\frac{1}{\omega}\frac{\partial k}{\partial x_j}\frac{\partial \omega}{\partial x_j}, 10^{-10}\right] \tag{3.32}$$

$$\Phi_2 = \max\left[2\frac{\sqrt{k}}{0.09\omega y}, \frac{500\mu}{\rho y^2\omega}\right] \tag{3.33}$$

In Equations 3.12 and 3.13, Y_k and Y_ω account for the turbulence dissipation of k and ω, respectively, calculated by Equations 3.34 and 3.35.

$$Y_k = \rho\beta^* k\omega \tag{3.34}$$

$$Y_\omega = \rho\beta\omega^2 \tag{3.35}$$

where β^* is given by Equation 3.36.

$$\beta^* = 0.09 \left(\frac{4/15 + (\text{Re}_t/8)^4}{1 + (\text{Re}_t/8)^4} \right) \tag{3.36}$$

and β is given by Equation 3.37.

$$\beta = F_1 \beta_{i,1} + (1 - F_1) \beta_{i,2} \tag{3.37}$$

Cross-diffusion term, D_ω, present in Equation 3.13, is defined accordingly to Equation 3.38. This term provides the model with a procedure to blend the $k - \varepsilon$ and the Wilcox $k - \omega$ models.

$$D_\omega = 2 (1 - F_1) \rho \frac{1}{\omega \sigma_{\omega,2}} \frac{\partial k}{\partial x_j} \frac{\partial \omega}{\partial x_j} \tag{3.38}$$

The SST $k - \omega$ model is based in a few constants that are used throughout the model formulation previously presented, and are defined as:

$\sigma_{k,1} = 1.176, \ \sigma_{k,2} = 1.0, \ \sigma_{\omega,1} = 2.0, \ \sigma_{\omega,2} = 1.168, \ \beta_{i,1} = 0.075,$

$\beta_{i,2} = 0.0828, \ \beta_\infty^* = 0.09, \ \alpha_1 = 0.31, \ \alpha_\infty^* = 1.0, \ \alpha_0 = 1/9$

Curvature Correction

The SST $k - \omega$ model does not account for the streamline curvature, which in this particular case is paramount. Smirnov and Menter (2009) developed a correction to provide the model with sensitivity to streamline curvature, as described by Equation 3.39 [SM09].

$$f_{rotation} = (1 + C_{r1}) \frac{2r^*}{1+r} \left[1 - C_{r3} \tan^{-1} (C_{r2} \tilde{r}) \right] - C_{r1} \tag{3.39}$$

Equation 3.39 will be used to calculate a multiplier of the turbulence production term (previously given by Equation 3.14) as described by Equations 3.40 through 3.42. With $C_{r1} = 1.0, C_{r2} = 2.0$ and $C_{r3} = 1.0$.

$$G_k \rightarrow G_k \cdot f_r \tag{3.40}$$

$$f_r = \max\left[0, 1 + \left(\tilde{f}_r - 1\right)\right] \tag{3.41}$$

$$\tilde{f}_r = \max\left[\min\left[f_{rotation}, 1.25\right], 0\right] \tag{3.42}$$

This will limit the turbulence generation between 0 and 1.25, for cases of strong convex geometry (stagnated flow) to cases of strong concave geometry (with high production of turbulence). r^* and $\tilde{r}$ are given by Equations 3.43 and 3.44, respectively.

$$r^* = \frac{S}{\Omega} \tag{3.43}$$

$$\tilde{r} = 2\Omega_{ik}S_{jk}\frac{DS_{ij}}{Dt}\frac{1}{\tilde{D}} \tag{3.44}$$

where the vorticity rate (Ω) is calculated by Equations 3.45 and 3.46, respectively.

$$\Omega = \sqrt{2\Omega_{ij}\Omega_{ij}} \tag{3.45}$$

$$\Omega_{ij} = \frac{1}{2}\left(\frac{\partial v_i}{\partial x_j} - \frac{\partial v_j}{\partial x_i}\right) \tag{3.46}$$

The value for $\tilde{D}$ is determined by Equations 3.47 and 3.48.

$$\tilde{D} = \Omega D^3 \tag{3.47}$$

where

$$D^2 = \max\left[S^2, 0.09\omega^2\right] \tag{3.48}$$

Turbulence Production Limiters

Excess of turbulence energy, G_k, is generated in zones of flow stagnation. Limiting the generation of turbulence energy is a way to avoid this problem for which there are two available methods in the solver. One (see Equation 3.49) is based on the application of a coefficient of limitation, C_{lim}, which takes the value of 10.

$$G_k = \min\left[G_k, C_{lim}\rho\varepsilon\right] \tag{3.49}$$

The second method (see Equation 3.50) is to recalculate the production of turbulence energy considering the vorticity rate of the flow, that in stagnation zones will be very small.

$$G_k = \mu_t S\Omega \tag{3.50}$$

When in the presence of a simple shear flow, S and Ω are equal and Equation 3.50 equals Equation 3.14.

Wall Boundary Turbulence Treatment

Walls deeply influence the turbulence in the flow, the no-slip (i.e. zero velocity) condition at the walls has to be satisfied and it will influence the mean velocity field of the flow. Additionally, the turbulence is changed by the distance to the wall. When very close to it, viscous damping occurs reducing the tangential velocity fluctuations and the normal velocity fluctuations are reduced by kinematic blocking. As the distance from the wall increases, so the turbulence rapidly increases by the production of kinetic energy (due to large mean velocity gradients).

Figure 3.1 illustrates the near-wall region divided into three layers: viscous sublayer (innermost - with laminar behaviour), fully-turbulent layer (outermost - with the turbulence playing major role) and the buffer sublayer (intermediate - where the viscosity and turbulence contribute equally).

The near-wall region (i.e. inner layer) is influenced by the viscosity in different degrees, accordingly to the wall distance ($y^+ \equiv \rho\left[\sqrt{\tau_w/\rho}\right]y\Big/\mu$).

To correctly model the wall influence in the flow, semi-empirical functions (i.e. wall functions) are
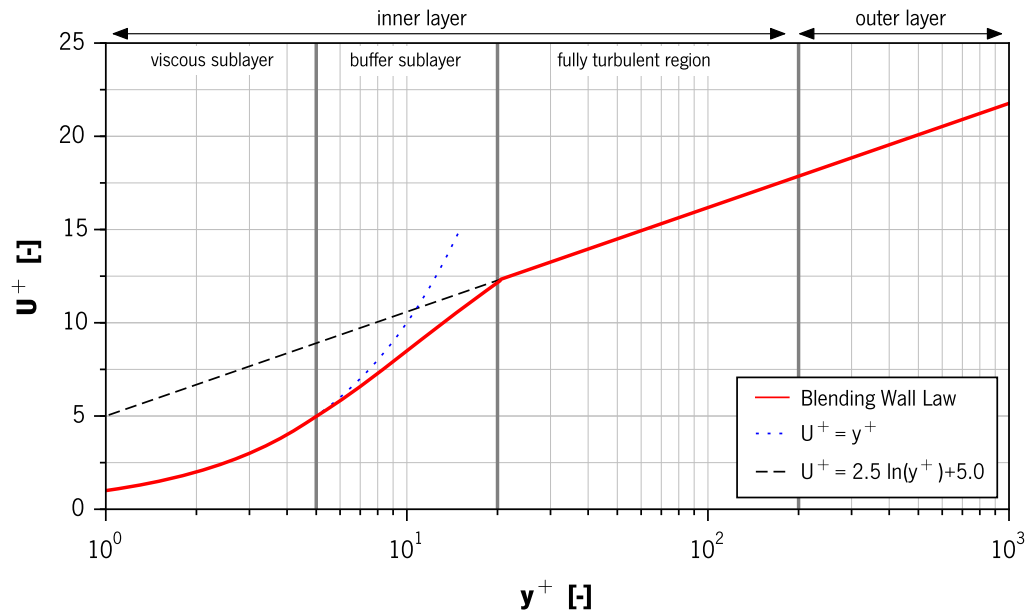
Figure 3.1: Wall law used in the flow regions of the inner layer

used to connect the near-wall region to the fully-turbulent region. Turbulence models will receive modified terms that account for the wall presence and its influence in the turbulence generation. This approach is adequate for coarse meshes with few refinement in the wall region (y^+>15). Another approach is to apply an adequate mesh refinement in the wall region (> 10 nodes) that envelops the viscous and buffer sublayers. This method will resolve this near-wall region and the turbulence models gain validity close to the wall. Obviously this is better for cases where the near-wall phenomena are very important.

The solver (FLUENT) has an integrated approach when the $k - \omega$ turbulence model is used, and will use by default a near-wall model known as Enhanced Wall Treatment (EWT) ω-Equation (EWT-ω). This model integrates the ω-equation through the viscous sublayer without the need for applying the two-layer approach. As it is insensitive to the value of y^*, it will blend the viscous sublayer formulation with the logarithmic layer formulation based in the value of y^*.

The value of ω in the wall, ω_w, is given by Equation 3.51, that depends on the value of ω^+ which can be assessed by Equation 3.52.

$$\omega_w = \frac{\rho \left(v^*\right)^2}{\mu} \omega^+ \tag{3.51}$$

$$\omega^+ = \begin{cases} \dfrac{6}{\beta\left(y^+\right)^2} & \text{, for laminar layer} \\[2em] \dfrac{1}{\sqrt{\beta^*_\infty}} \dfrac{\mathrm{d}v^+_{turb}}{\mathrm{d}y^+} & \text{, for turbulent layer} \end{cases} \tag{3.52}$$

Gharbi and his team (2011) showed an interesting comparison of DNS data with three distinct wall treatment models [EABB11]. Further discussion on this matter is given by Monticelli (2011) [Mon11].

3.1.4 Heat Transfer

The energy balance in a fluid is described by Equation 3.53.

$$\frac{\partial}{\partial t}\left(\rho E\right) + \nabla \cdot \left(\vec{v}\left(\rho E + p\right)\right) = \nabla \cdot \left(k_{eff}\nabla T - \sum_j h_j \vec{J_j}\right) + S_h \tag{3.53}$$

being the effective conductivity, $k_{eff} = k + k_t$. The turbulent thermal conductivity (k_t) is defined accordingly to the turbulence model used. The $\vec{J_j}$ represents the diffusion flux of the species j. Fluid energy transfer by conduction is given by the term $\nabla \cdot (k_{eff}\nabla T)$. Species diffusion energy is calculated by the term $\nabla \cdot \left(\sum_j h_j \vec{J_j}\right)$. S_h represents the contribution of other heat sources, such as, energy transfer from discrete phase. E is calculated by Equation 3.54.

$$E = h - \frac{p}{\rho} + \frac{v^2}{2} \tag{3.54}$$

Here, the sensible enthalpy h is defined, for incompressible flow, in Equation 3.55. Y_j represents the mass fraction of species j, and h_j given by Equation 3.56. T_{ref} was assumed to be 298.15 K.

$$h = \sum_j Y_j h_j + \frac{p}{\rho} \tag{3.55}$$

$$h_j = \int_{T_{ref}}^{T} c_{p,j}\,dT \tag{3.56}$$

3.1.5 Species Transport

When this model is used the fluid is considered to be composed by various species. It is then possible to define different gases with specific mass fractions and properties. The "air" was then composed by N_2, O_2, H_2O and HFA-134a. The solver calculates the conservation of the species accordingly to Equation 3.57.

$$\frac{\partial}{\partial t}\left(\rho Y_i\right) + \nabla \cdot \left(\rho \vec{v} Y_i\right) = -\nabla \cdot \vec{J_i} + S_i \tag{3.57}$$

where, S_i is the rate of creation of species i by addition from the dispersed phase (i.e. vaporisation) and any user-defined sources. This equation will be solved for $N-1$ species where N is the total number of species present in the fluid phase. Given the fact that the mass fraction of the species must add to one, the mass fraction of the Nth specie is calculated as one minus the sum of the $N-1$ solved mass. N_2 was chosen as the Nth since it possesses the largest mass fraction, reducing the impact of numerical errors.

The mass diffusion, $\vec{J}$, in turbulent flows is calculated by Equation 3.58, that arises from the gradients of concentration and temperature. The $\vec{J_i}$ is the diffusion of each specie i, Sc_t is the turbulent Schmidt number (considered as 0.7), the $D_{T,i}$ represents the thermal diffusion coefficient, and $D_{i,m}$ represents the mass diffusion coefficient.

$$\vec{J_i} = -\left(\rho D_{i,m} + \frac{\mu_t}{Sc_t}\right)\nabla Y_i - D_{T,i}\frac{\nabla T}{T} \tag{3.58}$$

3.1.6 Discrete Phase Model (DPM)

The DPM model will treat the fluid as a continuum phase, for which the Navier-Stokes equations were solved, and the discrete phase as a set of particles/droplets that are tracked along the domain using an Euler-Lagrange approach. These discrete entities will exchange energy, mass and momentum with the continuum phase. This approach is well suited for situations where the interactions particle-particle are not dominant. For this to happen, the volume of particles has to be lower than 10% of the domain's volume.

Particles will be subjected to a force balance equation (3.59) that will be integrated over time. The

resulting force, when applied to a particle during a time interval, will cause it to move a certain distance.

$$\frac{\mathrm{d}\vec{v}_p}{\mathrm{d}t} = F_D \left(\vec{v}_f - \vec{v}_p\right) + \frac{\vec{g}\left(\rho_p - \rho_f\right)}{\rho_p} + \vec{F} \qquad (3.59)$$

where F_D is the drag force given by Equation 3.60, $\vec{g}$ is the gravitational acceleration, and $\vec{F}$ is an additional acceleration term that results from different formulation models available on the solver (e.g. "virtual mass" force, rotation of the reference frame, thermophoretic force), which can be used accordingly to the phenomena in study. Additionally, this force can be provided by an external calculation by means of a User-Defined Function (UDF).

$$F_D = \frac{18\mu}{\rho_p d_p^2} \frac{C_D \mathrm{Re}_p}{24} \qquad (3.60)$$

where the Re_p is given by Equation 3.61. The subscripts f and p indicate that a variable corresponds to the fluid or particle/droplet, respectively.

$$\mathrm{Re}_p \equiv \frac{\rho_f d_p \left|\vec{v}_p - \vec{v}_f\right|}{\mu_f} \qquad (3.61)$$

The trajectory equations, as well as mass and energy transfer from/to the continuous phase, are solved over time by integration using discretized time steps. Equation 3.62 predicts the trajectory of the particle when integrated over time. Equation 3.63 is the generalized form of the Equation 3.59.

$$\frac{\mathrm{d}x_p}{\mathrm{d}t} = v_p \qquad (3.62)$$

$$\frac{\mathrm{d}v_p}{\mathrm{d}t} = \frac{1}{\tau_p}\left(v_f - v_p\right) + a \qquad (3.63)$$

where a represents the resultant acceleration given by the combination of all forces (except the drag force) and τ_p indicates the particle relaxation time (i.e. the time a particle takes to aerodynamically respond to a flow directional change) is given by Equation 3.64.

$$\tau_p = \frac{\rho_p d_p^2}{18\mu_f} \qquad (3.64)$$

The analytical integration of the Equations 3.62 and 3.63 is given by Equations 3.65 and 3.66, where the values for τ_p, a and v are constant during a certain time interval, where the superscripts $n+1$ and n indicate the present and previous position, respectively. These equations will be solved numerically using the Euler implicit discretisation scheme, whose detailed information can be found elsewhere [ANS13].

$$x_p^{n+1} = x_p^n + \Delta t \left(v_f^n + a\tau_p \right) + \tau_p \left(1 - e^{-\frac{\Delta t}{\tau_p}} \right) \left(v_p^n - v_f^n - a\tau_p \right) \tag{3.65}$$

$$v_p^{n+1} = v_p^n + e^{-\frac{\Delta t}{\tau_p}} \left(v_p^n - v_f^n \right) - a\tau_p \left(e^{-\frac{\Delta t}{\tau_p}} - 1 \right) \tag{3.66}$$

Another methodology, is to compute Equations 3.62 and 3.63 using a Runge-Kutta scheme, where the ordinary differential equations are solved in an integrated manner that will automatically chose the best sub time step needed for each Runge-Kutta cycle to provide the result within an acceptable error margin.

The solver (FLUENT) is equipped with an automatic routine for selecting the most adequate methodology to integrate the equations for particle displacement and velocity. The decision is based upon the variations in the forces acting on the particle at each time interval. The Runge-Kutta routine is applied when the forces acting on the particle change along the integration step; otherwise the Analytical approach is used.

Heat and Mass Exchange

FLUENT is equipped with specific laws for the handling of mass and heat exchange for droplets. In this case, the droplet received heat, followed by evaporation, possible boiling and cooling . The injected droplet is composed by HFA at -58 °C, liquid at this point, that suffers a rapid heating (see Equation 3.67) when $T_p < T_{vap}$. This process can be called an inert heating since no mass transfer occurs.

$$m_p c_p \frac{dT_p}{dt} = h A_p \left(T_\infty - T_p \right) \tag{3.67}$$

where m_p is the mass of the particle, c_p is the heat capacity of the particle, A_p is the surface area of the particle, T_∞ is the temperature of the continuous phase, h the convective heat transfer coefficient.

As soon as the droplet temperature reaches the temperature of vaporisation, $T_{vap} \leq T_p < T_{bp}$, the process of mass transfer is initialised, and it is finalised when the boiling point is reached or until the volatile fraction is totally consumed. This transfer was calculated using a diffusion controlled model, which assumes that the vaporisation is slow and mainly controlled by the diffusion gradient. Equation 3.68 defines the flux of vapour that is diffused into the continuous phase. The vaporisation process stops if the T_p falls below the dew point. The solver does not take into account condensation effects.

$$N_i = k_c \left(C_{i,s} - C_{i,\infty} \right) \tag{3.68}$$

where the N_i represents the molar flux of vapour and k_c is the mass transfer coefficient.

$C_{i,s}$ is the vapour concentration at the droplet surface and is estimated using Equation 3.69, assuming that the partial pressure of vapour ar the interface is equal to the saturated vapour pressure, p_{sat}, at the droplet temperature, T_p.

$$C_{i,s} = \frac{p_{sat}\left(T_p\right)}{RT_p} \tag{3.69}$$

$C_{i,\infty}$ is the vapour concentration in the bulk gas, given by Equation 3.70, where X_i represents the local (i.e. cell) bulk mole fraction of species i, p is the absolute pressure and R is the universal gas constant.

$$C_{i,\infty} = \frac{X_i p}{RT_\infty} \tag{3.70}$$

Equation 3.71 allows for the calculation of k_c used in Equation 3.68, using a correlation based in the Sherwood number (Sh). Sc represents the Schmidt number (Sc $= \mu/\rho D_{i,m,p}$).

$$\text{Sh}_{AB} = \frac{k_c d_p}{D_{i,m,p}} = 2.0 + 0.6\text{Re}_d^{1/2}\text{Sc}^{1/3} \tag{3.71}$$

The mass of the droplet is reduced over time accordingly to Equation 3.72, where $M_{w,i}$ is

the molecular weight of species i, and $D_{i,m,p}$ is the binary diffusion coefficient of the volatile component in the droplet.

$$m_p\left(t + \Delta t\right) = m_p\left(t\right) - N_i A_p M_{w,i} \Delta t \tag{3.72}$$

The heat transfer to the droplet during vaporisation process if given by Equation 3.73.

$$m_p c_p \frac{\mathrm{d}T_p}{\mathrm{d}t} = h A_p\left(T_\infty - T_p\right) - \frac{\mathrm{d}m_p}{\mathrm{d}t} h_{fg} \tag{3.73}$$

where the h_{fg} stands for latent heat that multiplies by the rate of evaporation, $\mathrm{d}m_p/\mathrm{d}t$. If $T_p \geq T_{bp}$ and the droplet mass exceeds the non-volatile fraction, a boiling process is initialised by the solver, being the calculation governed by Equation 3.74.

$$\frac{\mathrm{d}\left(d_p\right)}{\mathrm{d}t} = \frac{4k_\infty}{\rho_p c_{p,\infty} d_p}\left(1 + 0.23\sqrt{\mathrm{Re}_d}\right)\ln\left[1 + \frac{c_{p,\infty}\left(T_\infty - T_p\right)}{h_{fg}}\right] \tag{3.74}$$

where $c_{p,\infty}$ represents the heat capacity of the continuous phase and the k_∞ is the thermal conductivity of the continuous phase.

Particle Turbulent Dispersion

In a turbulent flow, the particle/droplet trajectory is affected by the turbulent fluctuations in the velocity caused by the eddies. This is modelled by a stochastic tracking theory that takes into account the turbulence influence by tracking several "tries" paths for the same particle, obtaining the averaged trajectory.

The solver (i.e. FLUENT) is equipped with a model to handle the particle dispersion named Discrete Random Walk (DRW), that is actually the Eddy Interaction Model (EIM) developed by Gosman and Ionnides (1983) [GL83]. Equation 3.75 defines the considered Lagrangean integral time (i.e. eddy lifetime), T_L, for the $k - \omega$ model, where C_L was considered to be 0.3.

$$t_L = C_L \frac{1}{\omega} \tag{3.75}$$

The eddy length, L_e, is given by Equation 3.76, where it was considered to be of random length,

provided through a generation of a Gaussian random number (r) between 0 and 1.

$$L_e = -t_L \ln\left(r\right) \tag{3.76}$$

The time that a particle takes to cross an eddy is calculated using Equation 3.77, where τ_p is the particle relaxation time (see Equation 3.64) and $\left|v_f - v_p\right|$ is the relative velocity.

$$t_{cross} = -\tau_p \ln\left[1 - \left(\frac{L_e}{\tau\left|v_f - v_p\right|}\right)\right] \tag{3.77}$$

The interaction between the continuous phase eddy and the particle is assumed to occur in the smallest time between t_L and t_{cross}, as described by Equation 3.78. Subsequently, a new value of instantaneous velocity is calculated.

$$\min\left(t_L, t_{cross}\right) \tag{3.78}$$

The turbulent isotropic behaviour of this model is present in the calculation method for the velocity fluctuations for each velocity component, see Equations 3.79 to 3.82.

$$\sqrt{{v'}_1^{\,2}} = \sqrt{{v'}_2^{\,2}} = \sqrt{{v'}_3^{\,2}} = \sqrt{\frac{2k}{3}} \tag{3.79}$$

$$v'_1 = \zeta\sqrt{{v'}_1^{\,2}} \tag{3.80}$$

$$v'_2 = \zeta\sqrt{{v'}_2^{\,2}} \tag{3.81}$$

$$v'_3 = \zeta\sqrt{{v'}_3^{\,2}} \tag{3.82}$$

where ζ is a normally distributed random number.

The RSM is a possible approach to overcome the isotropic assumption, through a considerable computational cost. The EIM can give incorrect results for flows dominated by diffusion, where the particles are not uniformly distributed. Particles smaller than a few microns, tend to deposit in

zones of low turbulence (i.e. stagnation zones).

3.2 Geometry Definition

3.2.1 Valves Geometries

The eight VHC devices' valves used in the present study were modelled in SolidWorks®, based in dimensions obtained from direct measurement alongside with image measurements of open valves (see chapter A.4). The 3-D models of the valves are represented in Figure 3.2, whereas those designs can be grouped into four categories.
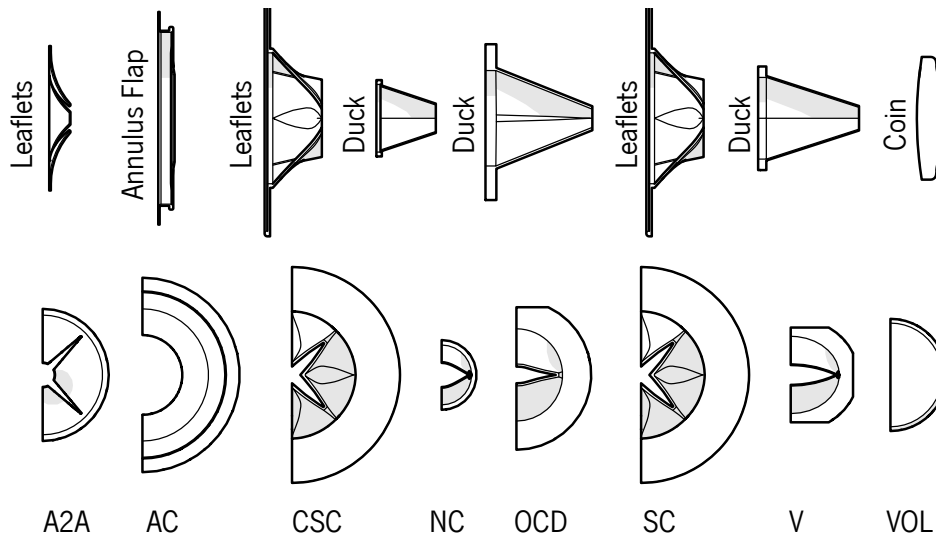
Figure 3.2: Side and top views representation of the VHC's valves used in the study, rendered in an open position at 60 L/min

A Duck type is present in Nebuchamber, Optichamber and Vortex; Leaflets in A2A Spacer, Compact Space Chamber and Space Chamber; Annulus Flap in Aerochamber; and a Coin in Volumatic. Unique to its design, in the Coin valve type, the air flows around the valve, whereas for all the others, the air passes through the valves (i.e. open-centre valve). This Coin concept presents a larger obstacle for air flow like a bluff body, which shall lead to higher particle deposition on the valve.

3.2.2   VHC Geometries

Through direct measurements the VHCs' bodies were rendered as depicted in Figure 3.3. The devices were represented very close to their actual aspect, such as the material type and transparency. All the devices mouthpiece are distinct from each other, except the Compact Space Chamber and Space Chamber whose difference is in its body length.
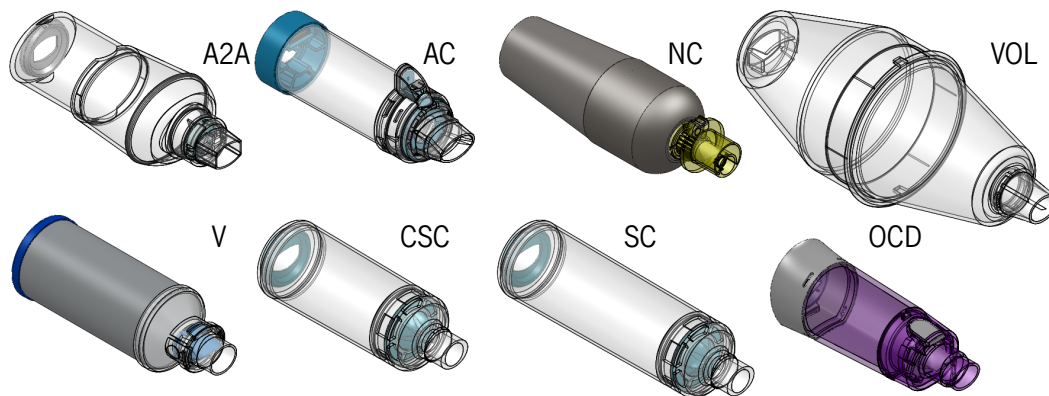
Figure 3.3: Geometrical representation of the eight VHC devices under assessment in this study, in isometric perspective with all devices at the same scale factor

3.2.3   Complete Domain

The necessary computational fluid domain was obtained from the internal space of each geometry combined with the USP IP internal volume and the pMDI mouthpiece. An example of the final geometry is given in Figure 3.4, whereas the Cartesian origin point was placed at the location of the pMDI nozzle for each assembly. To reduce the simulation time, only half of the domain was represented, given that a symmetry plane was present along all the geometry. The symmetry plane is represented by the gray area in Figure 3.4.

This procedure was repeated for all VHC devices geometries, with simplifications added to some details of the geometry, such as the removal of small connection steps in junctions of large diameter. These details would only increase the number of mesh elements without bringing any relevant

influence for the flow field. Since most of those details were located in regions of fluid stagnation. Because of their geometrical complexity, the Optichamber Diamond and the Vortex geometries were not evaluated numerically, given the lack of computational resources.
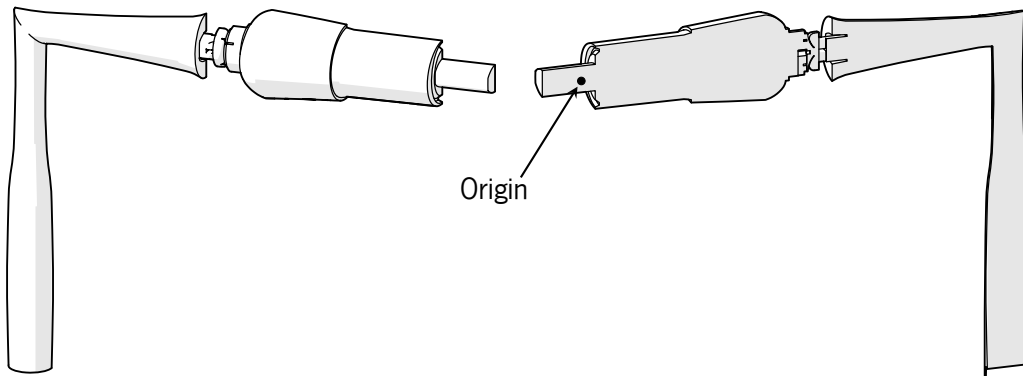
Figure 3.4: Geometrical representation of the simulation domain for the A2A Spacer geometry

3.3   Mesh Generation

The numerical mesh, for all the geometries, was generated using Meshing software from ANSYS®. Due to the complexity of the geometries used, it was not possible to create structured meshes. Therefore, only unstructured meshes were used, being made up mostly by tetrahedral elements in the bulk and prismatic elements near the wall. Specific VHC geometric details and highly varying dimensions made it impossible to use a general element size, therefore automated algorithms for mesh generation were applied. Those account for the proximity between surfaces, applying mesh refinements in zones of reduced cross-section. Wall refinement was applied to all geometries by means of an automated algorithm that required the definition of the number of prismatic layers and the cell growth factor. The algorithm analyses the size of the surrounding elements and builds the wall refinement layers by keeping the elements skewness in check. The height of the first layer was provided in a way that the value of y^+ was close to 1. In Table 3.1 it is provided some mesh characteristics used in the creation of the numerical meshes.

Once the meshes were created some quality metrics can be used. This can give some insight into the stability of the solution before numerical calculations. If a grid is full of highly skewed elements it will lead to numerical problems and rounding errors in the calculations. Figure 3.5 provides

the comparison between the different meshes on three relevant quality metrics. The vertical axis represent the frequency of elements with various quality metric indexes. Results are presented in the form of a normal statistical distribution, calculated upon the average, standard deviation, minimum and maximum values for each mesh.

Table 3.1: General numerical mesh characteristics with averaged values obtained from the various meshes produced

Feature	Value
Mesh elements	89k - 883k
Boundary Layers	10 - 15
First Boundary Layer Height (mm)	0.02 – 0.05
Maximum Element Size (mm)	3.5 - 10.0
Minimum Element Size (mm)	0.126 – 0.220
Volume of Domain (mm^3)	74k – 484k

The aspect ratio metric quantifies the ratio between the lengths of the element edges (a value of 1 refers for a perfect square). It is calculated by dividing the length of the longest edge by the shortest edge. This is a metric that is important to evaluate the quality of prisms. The skewness metric quantifies how close to ideal (an equiangular element) a cell is, being its value between 0 and 1. For tetrahedral elements, the equilateral volume index is applied and, it is obtained by dividing the difference between an optimal cell size and the current cell size, by the optimal cell size. Elements with skewness close to 0 are perfect while those close to 1 are of very poor quality. Element quality provides an overall quality metric that ranges between 0 and 1. This metric is based on the ratio of the element volume to the edge length (also a value of 1 indicates a perfect square). Orthogonal quality of a cell is the minimum value that results from calculating the normalized scalar product of the face's area vector and a vector connecting the cell's centroid to the corresponding face; and the normalized scalar product of the face's area vector and the vector connecting the face and cell centroids. Therefore, the worst cells will have an orthogonal quality closer to 0 while the best will have an orthogonal quality closer to 1.
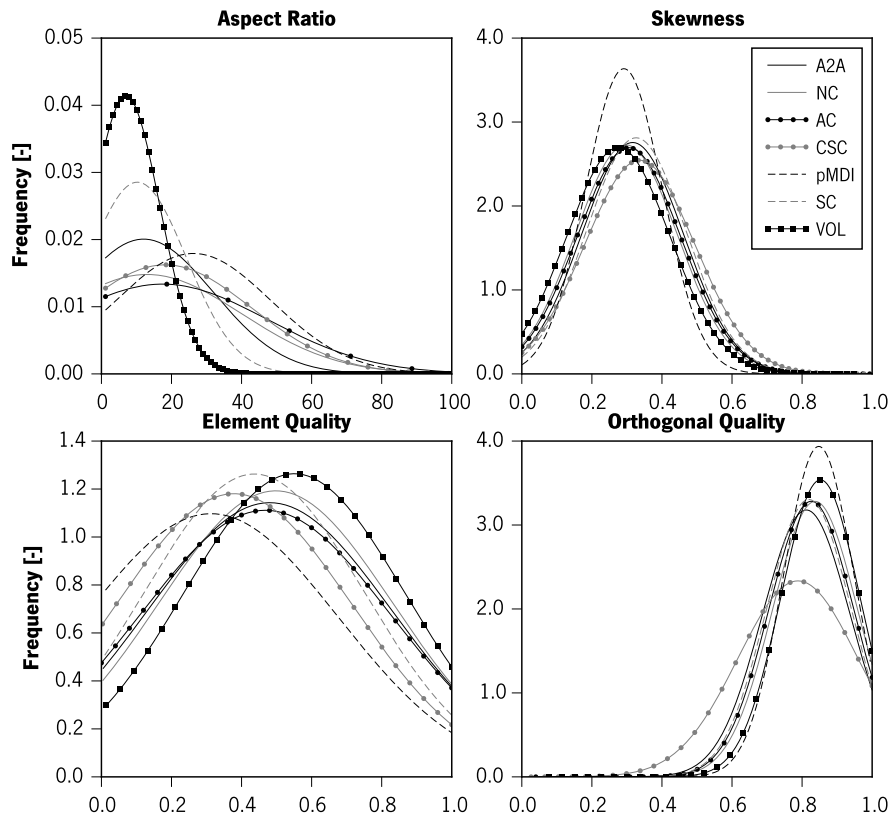
Figure 3.5: Mesh quality distribution for several meshes used in simulations according to four quality metrics: Aspect Ratio, Skewness, Element Quality and Orthogonal Quality

The meshes obtained have an aspect ratio distributions averaging around 15, which is within the acceptable range (high values are found in the elements in the boundary layer refinement). The pMDI solo mesh has the highest average value of aspect ratio. The skewness distributions are similar for all meshes, with an average around 0.35, which indicates a very good mesh quality. All values are bellow 0.8, which means that all elements are above good quality. Element quality metric distributions show that Volumatic has the best mesh (with average closer to 1), and the worst is found for pMDI solo. Orthogonal quality has averages around 0.85, except for the CSC (i.e. 0.8). The lowest value is ≈ 0.35, which is well above the minimum required for the solver (i.e. 0.1). An orthogonal quality above 0.2 indicates that the mesh is of good (or higher) quality.

3.4   Gas Properties

The continuous phase was considered a mixture of four species (i.e. gases), in different mass fractions: O_2, H_2O, HFA-134a and N_2. Each component has its own properties, some of them are dependent on the temperature, as described in Table 3.2. Mixing laws, weighted by the mass fraction of each species, were used to assess the mixture density, specific heat, thermal conductivity and viscosity.

3.5   Boundary Conditions

The boundary conditions present in the numerical domains were the same for all the geometries tested, and they are defined in detail in Table 3.3. The pMDI mouthpiece was considered a wall that would entrap all particles upon collision. The categorisation of each surface in a given group allows for detailed post-processing analysis of the particles characteristics entrapped there.

The mid-plane surface (corresponding to the delimiting surfaces of positive z-axis) was considered to be a symmetry condition. This forces the non-existence of a fluid gradient at that surface and that a flow directed towards this surface is mirrored by a symmetrical stream with the same characteristics. Mathematically, the solver assumes a zero flux for all quantities across a symmetry boundary: there is no shear stress, no convective flux, the normal component of the velocity is zero, and diffusion is not present across the symmetry.

The exit section was defined as an Outflow condition, meaning that the fluid reaching this boundary will exit the domain without any variable being forced to meet a certain condition. This is advisable to be used in cases whereas no knowledge is possessed downstream the domain and only in regions where the flow is developed. For this reason, an extension of the exit section was added to the geometries, before applying the outflow boundary condition.

Table 3.2: Gas components properties

Name	Properties	Value
Oxygen, O$_2$	Density, ρ (kg/m^3)	1.2999
	Specific Heat c_p (J/kg.K)	$834.8265 + 0.292958T - 1.495637\text{E-}4T^2 + 3.413885\text{E-}7T^3 - 2.278358\text{E-}10T^4$
	Thermal Conductivity, k (W/m.K)	0.0246
	Viscosity, μ (kg/m.s)	1.919E-5
	Molecular Weight, M_w (kg/kmol)	31.9988
	Mass Diffusivity Coefficient (m^2/s)	2.0E-5
Nitrogen, N$_2$	Density, ρ (kg/m^3)	1.138
	Specific Heat c_p (J/kg.K)	$979.043 + 0.4179639T - 1.176279\text{E-}3T^2 + 1.674394\text{E-}6T^3 - 7.256297\text{E-}10T^4$
	Thermal Conductivity, k (W/m.K)	0.0242
	Viscosity, μ (kg/m.s)	1.663E-5
	Molecular Weight, M_w (kg/kmol)	28.0134
	Mass Diffusivity Coefficient (m^2/s)	$1.8\text{E} - 5$
Water Vapour, H$_2$O	Density, ρ (kg/m^3)	0.5542
	Specific Heat c_p (J/kg.K)	$1563.077 + 1.603755T - 2.932784\text{E-}3T^2 + 3.216101\text{E-}6T^3 - 1.156827\text{E-}9T^4$
	Thermal Conductivity, k (W/m.K)	0.0261
	Viscosity, μ (kg/m.s)	1.34E-5
	Molecular Weight, M_w (kg/kmol)	18.01534
	Mass Diffusivity Coefficient (m^2/s)	2.4E-5
Hydrofluoroalkane, HFA-134a	Density, ρ (kg/m^3) [LMF16]	$2.844816\text{E}1 - 1.973320\text{E-}1T + 5.593704\text{E-}4T^2 - 5.689913\text{E-}7T^3$
	Specific Heat c_p (J/kg.K) [LMF16]	$6.146563 - 5.810724\text{E-}2T + 2.063815\text{E-}4T^2 - 2.383358\text{E-}7T^3$
	Thermal Conductivity, k (W/m.K) [LMF16]	$-1.274201\text{E-}6 + 4.873137\text{E-}8T - 1.615986\text{E-}11T^2$
	Viscosity, μ (kg/m.s) [LMF16]	$-1.041363\text{E-}2 + 7.983640\text{E-}5T$
	Molecular Weight, M_w (kg/kmol) [Fin01]	102.03
	Mass Diffusivity Coefficient (m^2/s) [Fin01]	$-5.725646\text{E-}6 + 5.265307\text{E-}8T$

T represents the temperature as a variable in the equations (value in Kelvin)

Table 3.3: Boundary conditions and relevant input values for the models used

Name	Type	Value
Entrance (Velocity Inlet)	Volumetric Flowrate (L/min)	60
	Turbulence Intensity (%)	5
	DPM Wall Condition	Reflect
	Temperature (K)	293.15
	Mass Fraction O_2	0.21
	Mass Fraction H_2O	0.0073
	Mass Fraction HFA	0.0
Exit (Outflow)	DPM Wall Condition	Escape
VHC body and valve, USP, pMDI mouthpiece (No-Slip Walls)	Velocity (m/s)	0.0
	DPM Wall Condition	see section 3.7.3
	Temperature	No heat exchange
	Mass Fraction O_2	No diffusive flux
	Mass Fraction H_2O	No diffusive flux
	Mass Fraction HFA	No diffusive flux

3.6 Solver Configuration

The numerical simulations were performed using FLUENT 15.0 from ANSYS$^\circledR$ as the solver. According to the previously stated, the turbulence model used in the calculations was the $k - \omega$ SST from Menter (1993) [Men93]. The solver used is pressure-based. This type of solver ensures the mass conservation of the velocity field by solving the pressure equation. Specifically, the pressure equation is obtained by derivation of the continuity and momentum equations (of the corrected velocity field) by the pressure, while enforcing mass conservation. The governing equations of the model are non-linear and are linked together in a way that the solution can only be obtained through an iterative process. A segregated algorithm is employed to solve these equations in a sequential way, one after the other, using the Semi-Implicit Method for Pressure-

Linked Equations (SIMPLE) algorithm, fully described elsewhere [ANS13, VM95]. The spatial discretisation scheme used in the simulations was the second order upwind scheme, applied to solve the turbulence, species, energy and momentum equations [ANS13]. This procedure is in accordance with the best practice guidelines for CFD simulations [Sul00]. Any iterative numerical process needs a convergence criterion. For the energy it was assumed a value of 1E-6 and for all other variables it was set at 1E-4. The simulations were carried out as unsteady over time where the fluid was considered to be incompressible and Newtonian. The gravitational acceleration was applied, downwards along the y-axis, with a magnitude value of 9.81 m/s^2. An automated method was used to decide the fluid time step accordingly to the convergence rate of the previous step. This method is described elsewhere [ANS13]. Nonetheless, the values were limited between 5E-5 seconds and to 0.1 seconds.

3.7 pMDI Spray

The pMDI formulation of Ventolin is composed by drug particles (crystals) of salbutamol sulphate, suspended in a propellant HFA-134a (liquid at the pressure of 3 atm). The solution is kept within an aluminium canister that includes a metering chamber, which precisely doses a fixed volume of content. The solution will rapidly expand upon contact with the atmospheric pressure (i.e. 1 atm). This is called the first atomisation process and occurs inside the metering chamber and actuator channels. This evaporation process needs a high amount of heat to occur (this is a reason for the need to wait between actuations), lack of energy will lead to formation of ice that blocks the actuator nozzle. Several studies were carried out in close proximity to the nozzle orifice, to measure the spray characteristics and behaviour, so those parameters can be of use to the numerical modelling.

Accordingly to several studies, at the nozzle exit the spray exhibits a distribution of propellant droplets, that can contain or not, one of more drug particles encapsulated in their volume [SSM12]. Some authors even point out the release of propellant gas bubbles in the centre of the nozzle [MSDK$^+$16].

For this study the spray behaviour is characterised by the secondary atomisation downstream the

nozzle. FLUENT is very limited for modelling pharmaceutical sprays. So it was considered that all the droplets had the same amount of propellant by defining a limit for evaporation process (i.e. mass fraction of HFA is 99.05%). Once this value is reached the "droplet" will retain its mass being considered a solid particle (i.e. made solely of API drug) for wall collision purposes. The evaporated mass will add to the gas species present in the continuous phase (i.e. HFA-134a gas). This limitation, forces the injected particles with higher diameter to have higher amount of drug mass, while smaller droplets have smaller drug mass. The following sections will focus on the materials definition and models specific to the spray modelling.

3.7.1   Materials Properties

The droplet is composed by liquid propellant (i.e. HFA-134a) and its properties are given in Table 3.4. Additionally, the properties of salbutamol sulphate and wall materials found in VHC devices are reported as well. When appropriate they will be used in wall-particle interaction models.

3.7.2   Drag Law

The aerodynamic interaction between the discrete phase and the continuous phase is assessed through a drag law, that provides the Equation 3.60 with a drag coefficient which is a function of the Reynolds number (see Equation 3.61) of the particle/droplet. A great deal of research has been carried out over the last decades upon drag coefficient laws for droplets, bubbles and particles; and the best compendium is given by Clift, Grace and Weber [CGW05]. Drag effects for pharmaceutical particles are well documented by Finlay [Fin01]. Accordingly to Clift, droplets with a high viscosity ratio between phases (i.e. $\kappa = \mu_p/\mu_f$, in this case is between 22 and 38) can be considered non-deforming. Additionally, for droplets very small (i.e. under 1 μm) it was observed that there is no formation of the Hill's internal recirculation spherical vortex [CGW05], therefore the spherical drag law for rigid spheres is the most adequate approach for handling the problem.

Table 3.4: Properties of the spray droplets and surface materials

Name	Properties	Value
HFA-134a, liquid	Density, ρ (kg/m^3) [LMF16, KSZ07]	$1.905004\text{E}3 - 1.278338T - 3.479706\text{E-}3T^2$ | 1300 (after evaporation)
	Specific Heat c_p (J/kg.K) [LMF16]	$1.298229 - 2.121241\text{E-}3T + 8.294360\text{E-}6T^2$
	Latent Heat (J/kg) [Fin01]	$3.883988\text{E}5 - 7.025714\text{E}2T$
	Vaporisation Temperature (K) [Fin01, BCLM11]	213.15
	Boiling Temperature (K) [LMF16, Dun97]	247.15
	Volatile Fraction (%)	99.05
	Saturation Vapour Pressure (Pa) [Fin01]	$-9.802710\text{E}6 + 1.31117\text{E}5T - 5.931\text{E}2T^2 + 9.0939\text{E-}1T^3$
	Mass Diffusivity Coefficient (m^2/s) [Fin01]	$-5.725646\text{E-}6 + 5.265307\text{E-}8T$
Salbutamol Sulphate	Young Modulus (GPa)	3.38
	Poisson's Ratio (-)	0.5
Aluminium	Young Modulus (GPa)	69.0
	Poisson's Ratio (-)	0.334
Silicon Rubber	Young Modulus (GPa)	0.05
	Poisson's Ratio (-)	0.48
ABS	Young Modulus (GPa)	2.2
	Poisson's Ratio (-)	0.35
PC	Young Modulus (GPa)	2.2
	Poisson's Ratio (-)	0.37
Stainless Steel	Young Modulus (GPa)	180.0
	Poisson's Ratio (-)	0.305

T represents the temperature as a variable in the equations (value in Kelvin)

The solver is equipped with the spherical drag law from Morsi and Alexander (1972) [MA72]. This law is made by several branches applicable to specific intervals of Reynold number, as described in Equation 3.83. Here are only reported the relevant intervals, by estimation of the maximum Reynolds number, this should be close to 500 (considering the air velocity to be 0.01 m/s).

$$C_D = A + \frac{B}{\text{Re}_p} + \frac{C}{\text{Re}_p^2} \tag{3.83}$$

where

$$\text{Re}_p \leq 0.1$$
$$\begin{cases} A = 0.0 \\ B = 24.0 \\ C = 0.0 \end{cases}$$

$$0.1 < \text{Re}_p \leq 1.0$$
$$\begin{cases} A = 3.69 \\ B = 22.730 \\ C = 0.903 \end{cases}$$

$$1.0 < \text{Re}_p \leq 10.0$$
$$\begin{cases} A = 1.222 \\ B = 29.1667 \\ C = -3.8889 \end{cases}$$

$$10.0 < \text{Re}_p \leq 100.0$$
$$\begin{cases} A = 0.6167 \\ B = 46.5 \\ C = -116.67 \end{cases}$$

$$100.0 < \text{Re}_p \leq 1000.0$$
$$\begin{cases} A = 0.3644 \\ B = 98.33 \\ C = 2778.0 \end{cases}$$

Several authors have used of this drag law in their numerical simulations [LHDX08, YIT15, GA04, KHDL15, LV07]. However, a slip correction factor, C_c, for small diameters should be applied [Hin99]. This factor takes into account that very small particles start being affected by the air molecules that collide against its surface increasing the drag coefficient predicted for LRN. The slip correction factor, (C_c - see Equation 3.84), was initially proposed by Cunningham (1910) [Cun10] and it is based in the Knudsen number (Kn - see Equation 3.85) of the particle. Its value becomes more relevant for submicrometer ($d_p \leq 1.0$ μm) particles [Cun10]. The parameter λ represents the mean free path of a gas molecule and it was considered to be 65 nm for the present temperature range. The value of α is given by Equation 3.86 and its coefficients (c_1, c_2, c_3) are empirical [AR85]. Based in the work of Longest (2007), the values used were $c_1 = 2.34$, $c_2 = 1.05$ and $c_3 = -0.39$ [LX07].

$$C_c = 1 + \alpha \cdot \text{Kn} \tag{3.84}$$

$$\mathrm{Kn} = \frac{2\lambda}{d_p} \tag{3.85}$$

$$\alpha = c_1 + c_2 \exp\left(c_3/\mathrm{Kn}\right) \tag{3.86}$$

Once the propellant is fully evaporated, the resultant solid drug particle is not spherical at all. The non-sphericity effect of the drag coefficient was not taken into account in the modelling due to lack of accurate input parameters. Nevertheless, the work of Chhabra and his collaborators (1999) provide a deep insight into this matter by comparing several drag laws available [CAS99]. Feng and Kleinstreuer (2013) used CFD to model the transport of ellipsoidal particles along a pipe flow. This work lead the way to a deeper understanding of the non-sphericity effect in the particle rotation, drag and turbulence generation [FK13]. In Figure 3.6 it is shown the comparison of the Stokes drag law versus that proposed by Morsi and Alexander, with or without the Cunningham slip correction factor.
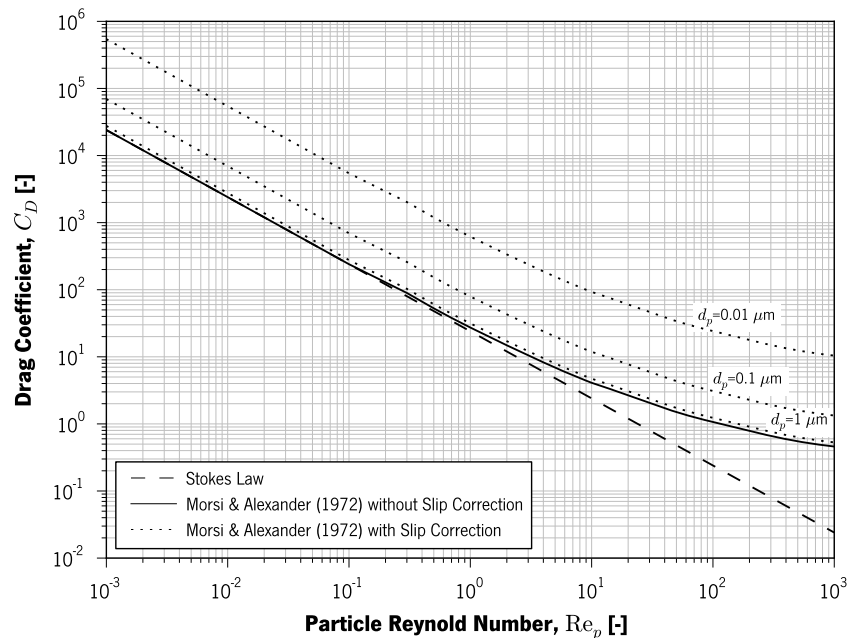
Figure 3.6: Comparison of different drag laws and the effect of slip correction factor as a function of the particle diameter

The Stokes law is adequate for slow, viscous flows, where the Morsi and Alexander law follows it closely. As the particle Reynolds number increases ($Re_p > 0.2$), the two formulations rapidly diverge. The slip correction based on particle diameter is negligible for diameters above 1 μm, increasing rapidly as the particle diameter reduces.

3.7.3   Wall-Particle Interaction Models

The collision of droplets/particles against a solid wall is a complex matter that depends upon an interaction of several forces requiring considerations to be made. Here, the discrete phase was considered to be composed by liquid droplets or solid particles if the total evaporation of the propellant has occurred. Distinct wall collision options were considered:

- Trap;
- Reflect;
- Critical velocity based model;
- Tangential lift-off ratio based model.

Trap

This model is already implemented in the solver and it is designed to entrap a droplet or particle that collides onto the boundary. The discrete element is then removed from all tracking calculations.

Reflect

The reflect option, also included in the solver, will respond to a discrete element collision on the boundary by recalculating the bouncing velocity components. It applies a restitution coefficient (C_R) to the particle velocity, that makes possible to stipulate a dampener factor for modelling the energy lost during the collision. C_R = 1.0 represents a perfectly elastic collision, in which no kinetic energy is dissipated, while values of C_R = 0.0 represents the opposite, a perfectly inelastic collision, where all kinetic energy is dissipated and there is no separation between the bodies upon contact (this is equivalent to the Trap model). In the models used in this work, it was considered

that no energy was dissipated upon contact ($C_R = 1.0$). However, the influence of this factor in the results was not assessed, and additional models can be employed to estimate its value based on the characteristics of the particles and walls [Tom06].

Critical Velocity Based Model

In this case all particles or droplets collisions were modelled accordingly to a model presented by Brach and Dunn (1992) that predicts the particle deposition upon a ratio between the discrete element normal velocity to the wall and its correspondingly critical velocity [BD92]. This model was implemented in a numerical study of a DPI powder emission [MAK13]. The Dunn model, considered in this work, treated the problem as a rigid body impact taking in account the following assumptions [BD95]:

- The particle is considered to be spherical in the contact region and its centre of mass is vertically aligned with the contact point;
- Non deforming bodies;
- The collision period is very short;
- Large contact forces;
- Finite velocity changes.

Figure 3.7 depicts the collision of a rigid particle with a rigid wall surface, in addition to the velocity vector before (V$_i$) and after collision (V$_f$). The referential normal, n, and tangential, t, directions are represented relatively to the wall orientation. Particle rotation is not considered in this work. The determination of the critical velocity, V_C, is given by Equation 3.87. Particles with normal component of the velocity before impact, V_n, less or equal to the V_C value are entrapped. If the initial velocity particle is so high that its normal component can overcome the critical velocity, the particle will reflect accordingly to the Reflect model previously described (considering $C_R = 1.0$).
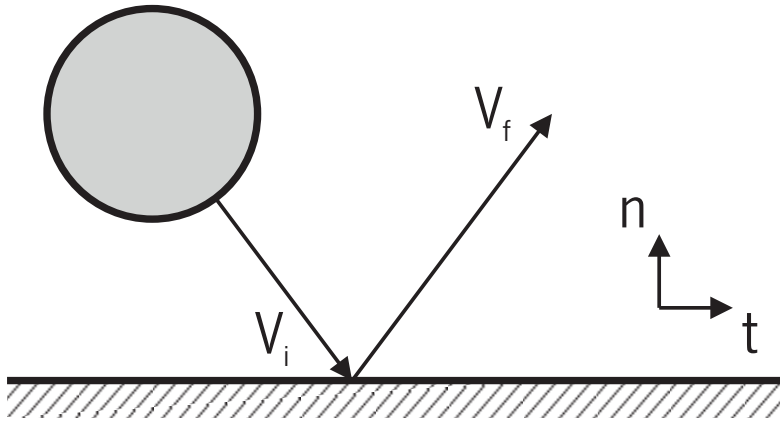
Figure 3.7: Velocity vectors representation of the particle wall collision along with the normal and tangential referential

$$V_C = \left(\frac{2E}{d_p}\right)^{10/7} \tag{3.87}$$

where E is the effective stiffness parameter and is given by Equation 3.88:

$$E = 0.51 \left(\frac{5\pi^2 \left(k_w + k_p\right)}{4\rho_p^{3/2}}\right)^{2/5} \tag{3.88}$$

The values of k_w and k_p are obtained by Equation 3.89:

$$k_w = \frac{1-\nu_w^2}{\pi E_w} \quad k_p = \frac{1-\nu_p^2}{\pi E_p} \tag{3.89}$$

where ν and E represent the Poisson's ratio and Young Modulus, respectively. The subscripts w and p, indicate whether the variable refers to the wall or particle, respectively. The relevant properties are given in Table 3.4.

Tangential Lift-off Ratio Based Model

The model given by Shi and Bayless (2007) uses the forces ratios, acting on a particle when in contact with the wall, as a correction for CFD prediction of powder deposition in a cyclone separator [SB07]. This model was also reported by other studies [IDQ08]. The model was applied to the angled surface of the cyclone funnel. The force calculation was simplified and the ratio equations

were referred to the angle between the wall and the horizontal plane. Figure 3.8 represents the forces acting on a particle resting in a surface angled with the horizontal plane.
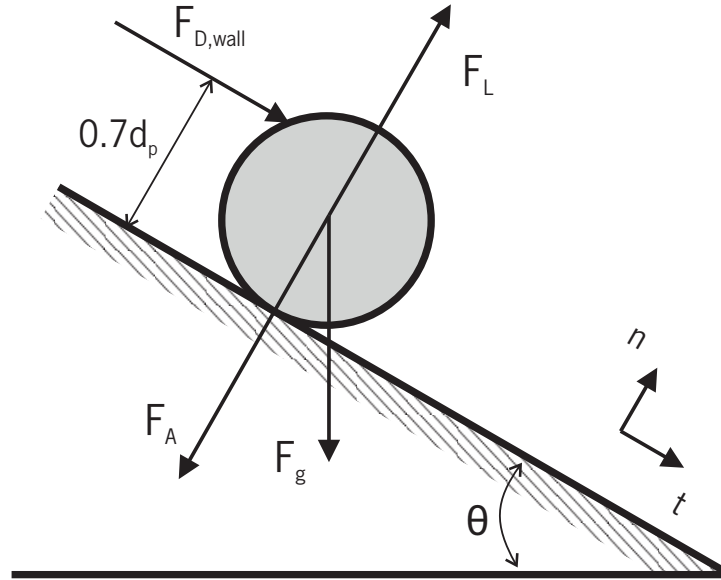
Figure 3.8: Representation of the forces acting on a particle upon contact with an angled (θ) wall surface

In the case of the VHC geometry, the wall takes any possible orientation regarding the horizontal plane. Shi model includes the ratio for vertical lift-off, the ratio for the sliding and the ratio for the tangential lift-off. After an evaluation of the different ratios, the tangential lift-off ratio is the dominant and is the only considered for particle reflection in this work. Equation 3.90 provides the value of the tangential lift-off ratio (R_t).

$$R_t = \frac{(0.7 d_p) \, F_{D,wall} + A_c F_L + 0.5 d_p F_g \sin \theta}{A_c \left(F_A + F_g \cos \theta \right)} \tag{3.90}$$

where a is the area of contact, which depends of the material of the two bodies and is given by Equation 3.91 [JKR71]:

$$A_c = \left(\frac{6 \pi d_p^2 \sigma}{4K} \right)^{1/3} \tag{3.91}$$

where the elastic constant K is given by Equation 3.92:

$$K = \frac{4}{3} \left(k_w - k_p \right)^{-1} \tag{3.92}$$

The forces present in Equation 3.90 are: gravity (F_g), drag ($F_{D,wall}$), lift (F_L) and adhesion (F_A). Equation 3.93 gives the value for F_g:

$$F_g = gm_p \tag{3.93}$$

The adhesion force is obtained through Equation 3.94, accordingly to the JKR model [JKR71], where σ represents the surface energy (assumed to be equal to 0.001 J/m^2).

$$F_A = \frac{3}{4}\pi\sigma d_p \tag{3.94}$$

The value of $F_{D,wall}$ was obtained from Equation 3.95 for particles resting on a plate accordingly to O'Neill work [O'N68], being γ is the shear rate and $f = 1.7009$.

$$F_{D,wall} = 6\pi\mu_f\gamma\frac{d_p^2}{4}f \tag{3.95}$$

The Lift force (F_L) is given by Equation 3.96 from the work of Acrivos (1985) for spheres on a resting plane at small Reynolds shear flow regime [LA85]. In this Equation, ν_f stands for the kinematic viscosity of the fluid.

$$F_L = 9.22\frac{\gamma\mu_f d_p^2}{4}\frac{\gamma d_p^2}{4\nu_f} \tag{3.96}$$

Other forces

Particle-wall interaction is a very complex matter and many theories are available in the literature. In this work some effects were not possible to take into account, such as the electrostatic attraction [Hin99, VLP09], the capillarity force from humidity in air [SMB00] or the contact force with deformation [BD92], load and unloading cycles [Tom06].

3.7.4 Spray Distribution

The spray droplets were injected into the domain at the position corresponding to the pMDI actuator nozzle. Since the primary atomisation was not modelled, it was necessary to program the droplets spatial distribution at the nozzle exit. This was done by means of a Python language script that provided the solver with an input file containing the characteristics of each "stream" to be tracked.

Alongside the distribution, it was also given other characteristics, such as: the temperature, diameter, mass flow, velocity components and spatial position. The droplets were all assumed to enter the domain at 215.15 K (-58 °C). This value is based on experimental studies of the Ventolin spray plume passing through a set of thermocouple sensors [BCLM11, GSV99]. Accordingly to the reported data, the spray temperature at the nozzle orifice can be lower than that considered here. Another important parameter is the maximum spray plume velocity, although it is extremely difficult to measure such quantity at the exact nozzle orifice position. Several data sources were taken into consideration for defining the maximum velocity. Experimentally, the Ventolin spray was recorded using a high-speed camera (the data being reported in section A.3). By image analysis, it is possible to estimate a spray velocity of ≈50 m/s at 33 mm from the nozzle. Liu and his team (2012) measured the Ventolin plume velocity, using PDA, at 54 mm from the nozzle and reported it to be 10.3 m/s [LDG12]. Clark (1996) reports a peak velocity of 35 m/s at 50 mm from orifice [Cla96]. Dunbar and his collaborators (1997) reported that the maximum velocity of a HFA-134a plume is found along its axis with a value of ≈50 m/s at 25 mm from nozzle [DWM97]. Using PIV technique, Crosland and his collaborators (2009), reported the Ventolin plume velocity field over time, and showed a value of ≈63 m/s at 25 mm from the nozzle orifice at the beginning of the actuation [CJM09]. Wigley, Versteeg and Hodson (2002) assessed the spray velocities at the near-nozzle zone using a LDA/PDA system and reported a value of ≈90 m/s at 1 mm from the nozzle [WVH02]. As the velocity decreases rapidly as the distance from the nozzle increases, so it was assumed that the spray injection velocity had a value of 120 m/s.

The spray angle is another important parameter to model the spray plume. Using information of the spray impaction pattern, from a plate located at 70 mm downstream from the nozzle, Smyth and his team (2006) data suggested that the cone angle is ≈16 degrees [SHB+06]. A PIV assessment on the spray cone angle made by Crosland and his collaborators (2009), reported a value of 20.8 degrees [CJM09]. Dunbar (1996) measured the cone angle of a HFA-134a pMDI spray and reported a value of 21.6 degrees [Dun96]. Given the fact that the pMDI plane-orifice spray exits the orifice aperture rapidly, its high velocity jet expands radially. However, upon contact with the slow velocity of the air, the angle reduces by friction with ambient air at periphery of the spray. For modelling purposes, the full cone angle value was assumed to be 40 degrees.

The nozzle diameter depends on the pMDI product actuator, and its dimension will strongly influence the particle size distribution. Smaller nozzle diameters produce finer sprays [New05, SSHM13, SBB+06]. Differences in the emitted mass between a flat, flat curved, cone and curved cone nozzle designs were reported by Chen (2014) [CYF+14a]. Additionally, they reported the effect of the electrostatic charge of the actuator material on the delivered mass [CYF+14b]. Cheng and his team (2001) reported a value of 0.254 mm of nozzle diameter for an HFA-134a formulation [CFYZ01]. Measurements of the pMDI Ventolin HFA-134a actuator used in the experimental tests were conducted using a measuring microscope (Model 175-901 from Mitutoyo, Japan) with an accuracy equal to 2 μm, and it was observed a nozzle diameter averaged 0.50(6)±0.01(0)mm. The time duration of the spray can be assessed by high-speed image, by PIV, by laser measurements over time or by impaction plate. Crosland (2009) reported a Ventolin spray duration of approximately 100 ms [CJM09]. Previously published work reported the value obtained by high-speed imaging to be also 100 ms [OTT+12]. McCabe (2012) reported the Ventolin plume duration to be around 150 ms [MKBZ12]. Gabrio (1999) verified that the Ventolin spray plume duration had an average of 94.5 ms [GSV99]. Based on this evidence, the spray modelled considers the spray duration to be 100 ms.

The Ventolin label claims a dose per actuation of 100 μg. Using this value and the spray duration of 100 ms mass flow rate of the spray was assumed to be 1E-6 kg/s.

The spray size distribution is the most relevant input for this model; it can be defined using different statistical functions, whereas the literature reports that two of them have been widely used in the pharmaceutical aerosol area: the Log-Normal (Equation 3.97) and the Rosin-Rammler (Equation 3.98).

$$\text{PDF}\,(d_p; \mu, \sigma) = \frac{1}{d_p \sigma \sqrt{2\pi}} e^{-(\ln(d_p) - \mu)^2 / 2\sigma^2}$$

$$\text{CDF}\,(d_p; \mu, \sigma) = \frac{1}{2} erfc \left[-\frac{\ln(d_p) - \mu}{\sigma\sqrt{2}} \right] \tag{3.97}$$

where the μ represents the mean diameter, σ is the geometric standard deviation and $erfc$ is the complementary error function.

$$\text{PDF}\,(d_p; \lambda, k) = \frac{k}{\lambda}\left(\frac{d_p}{\lambda}\right)^{k-1} e^{-(d_p/\lambda)^k}$$

$$\text{CDF}\,(d_p; \lambda, k) = 1 - e^{-(d_p/\lambda)^k}$$

(3.98)

λ represents the mean diameter and k is the distribution spread.

Dunbar and Hickey (2000) studied the best distribution and fitting method for empirical data obtained from a pMDI spray using an Andersen eight-stage cascade impactor. They concluded that the best fitting method is through the nonlinear least squares of the PDF and that the Log-Normal produced a better fit to the data than the Rosin-Rammler function [DH00]. However, these distributions will approximate the spray by a unimodal function, when in reality, several peaks have been identified [OTT+12]. Moreover, the spray size distribution is variable over time due to its complex liquid-vapour movements inside the expansion chamber, with the addition of cavitation effects near the nozzle orifice [WVH02, SBB+06].
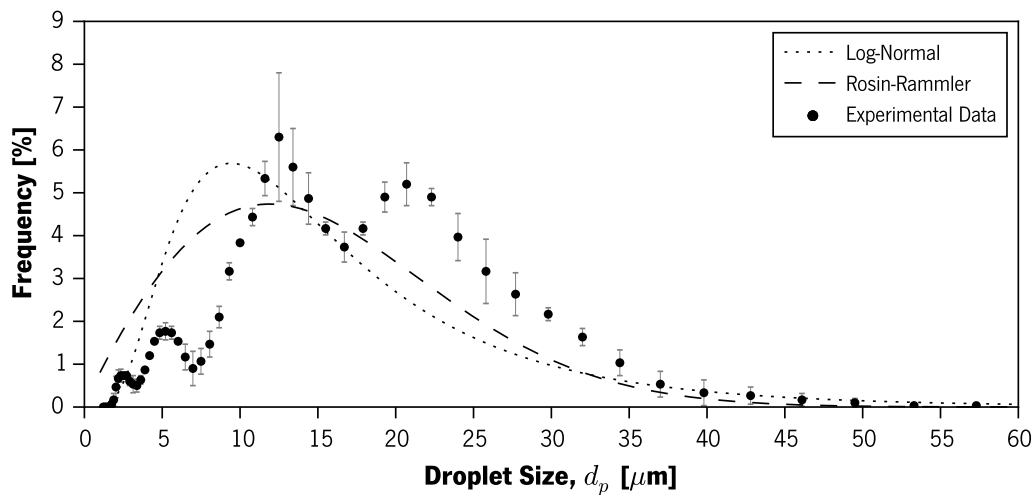
Figure 3.9: Measured spray size distribution and two corresponding statistical distribution

Given the fact that the spray distribution is modelled by means of an input file for the solver, experimental particle size distribution data were obtained to be used as an input, removing the need for mathematical modelling of the distribution. The spray was measured using the laser

diffraction technique (particle sizer model 2600 from Malvern, UK), using a polynomial function for data processing. The droplet diameter ranged from 1 μm to 60 μm. For comparison purposes, the experimental data are plotted against the two distributions (see Figure 3.9) and differences are observed [OTT[+]12]. A data fit was also carried out using the least squares methodology upon the CDF functions.

Figure 3.10 shows the spray pattern at the nozzle orifice and the side view of the velocity vectors for each injected droplets. As represented, the droplet spreading in the nozzle orifice was done using a random generation algorithm that is independent of the droplet diameter. Further studies are required for assessing the influence of the droplet pattern spatial distribution and its influence in the deposition occurring inside the device. Other methods can be considered such as, randomly spread the droplet by diameter along the radial direction.

This code allows the specification of the number of different diameters within the given distribution as well as the number of random spatial positions at the nozzle. Each diameter is present at each spatial position generated, multiplied by a fixed number of times. In the present simulations, the total number of streams injected was 3600 per injection step.
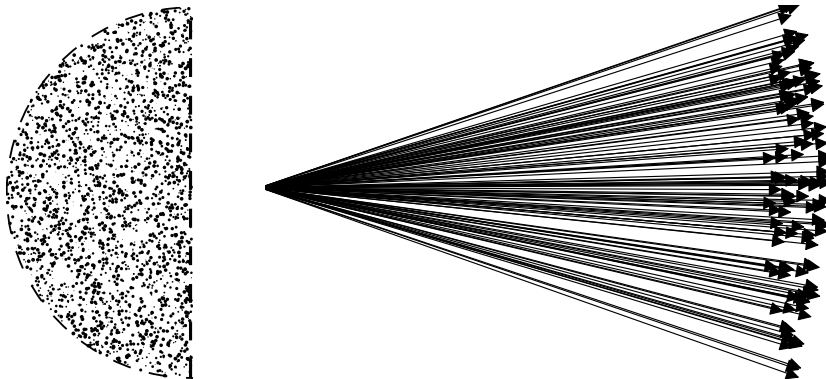
Figure 3.10: Spray spatial distribution at the nozzle orifice

3.7.5   Tracking Model Configuration

The droplets were injected within 0.01 s apart during 0.1 s. Their interaction with the continuous phase considered a two-way turbulence coupling, as well as mass and heat transfer. The tracking

algorithm was performed at the beginning of each continuous phase time step. Apart from the drag force, the Brownian motion and Saffman lift forces were also considered [ANS13].

The particle tracking had an stochastic model for predicting the influence of the turbulence velocity fluctuations in the particles trajectories as described in section 3.1.6. As stated this model has a limitation that it over estimates the normal component of the velocity fluctuations close to a wall. This characteristic induces the simulation results with a small error, leading to over deposition. Some corrections were developed to overcome this problem by modelling this contribution according to the distance to the wall as proposed by Matida (2000) [MNT00]. The equations are based in the work of Wang and James (1999) that was obtained by fitting DNS data [WJ99]. Other authors had also followed this modelling technique [LHDX08, YIT15, LHCB07]. Dehbi (2008) approached the problem with a continuous random walk model, by applying the normalized Langevin equations to determine the fluid fluctuations near wall [Deh08]. An application of this model to a throat deposition CFD study was made in 2011 by Dehbi [Deh11].

3.8 Grid Discretisation Uncertainty Analysis

3.8.1 Methodology

A grid study for estimating the uncertainty due to the discretisation was carried out using the Grid Convergence Method (GCI), which is based in the Richardson Extrapolation (RE) method [CGR$^+$08]. Currently, it is the most reliable method available; however its limitations are that the prediction of local RE values do not exhibit a smooth monotonic dependence on the grid resolution. Firstly, it is necessary to estimate a representing cell size (h). This can be done by using Equation 3.99, that estimates an average mesh size for three-dimensional calculations.

$$h = \left[\frac{1}{N} \sum_{i=1}^{N} (\Delta V_i) \right]^{1/3} \tag{3.99}$$

where ΔV_i is the volume of the ith cell and the N is the total number of cells used.

Three grids should be created with different cell sizes ($h_1 < h_2 < h_3$), whereas the refinement factor ($r_{mesh} = h_{coarse}/h_{fine}$) should be greater than 1.3. The grid refinement was done

automatically by changing the maximum cells size and keeping the boundary refinement unchanged. A numerical solution shall be achieved for each grid, assessing the variables of relevance (ϕ) to the problem.

Subsequently, it is calculated the apparent order (p_m) of the method using the Equations 3.100 and 3.101, which can be solved together using a numerical method such as the fixed-point iteration.

$$p_m = \frac{1}{\ln(r_{21})} \left| \ln |\varepsilon_{32}/\varepsilon_{21}| + q(p_m) \right| \tag{3.100}$$

$$q(p_m) = \ln \left[\frac{r_{21}^{p_m} - (1 \cdot \text{sgn}\left[\varepsilon_{32}/\varepsilon_{21}\right])}{r_{32}^{p_m} - (1 \cdot \text{sgn}\left[\varepsilon_{32}/\varepsilon_{21}\right])} \right] \tag{3.101}$$

$\varepsilon_{32} = \phi_3 - \phi_2$, $\varepsilon_{21} = \phi_2 - \phi_1$, and ϕ_k is the solution on the kth grid and $r_{32} = h_3/h_2$, $r_{21} = h_2/h_1$.

The calculation of the extrapolated values is obtained by Equation 3.102.

$$\phi_{ext}^{21} = \frac{r_{21}^{p_m}\phi_1 - \phi_2}{r_{21}^{p_m} - 1} \tag{3.102}$$

The calculation of the approximate relative error is given by Equation 3.103, and Equation 3.104 that estimate the extrapolated relative error. The fine-grid convergence index is obtained through Equation 3.105.

$$e_a^{21} = \left| \frac{\phi_1 - \phi_2}{\phi_1} \right| \tag{3.103}$$

$$e_{ext}^{21} = \left| \frac{\phi_{ext}^{21} - \phi_1}{\phi_{ext}^{21}} \right| \tag{3.104}$$

$$\text{GCI}_{fine}^{21} = \frac{1.25 e_a^{21}}{r_{21}^{p_m} - 1} \tag{3.105}$$

3.8.2 pMDI Solo Grid

The grid uncertainty was evaluated for the pMDI solo geometry, using three sets of grids: 89.5k, 197.2k and 429.4k cells. The variable assessed was the velocity profile taken along the diameter at four locations apart from the origin (see Figure 3.11).
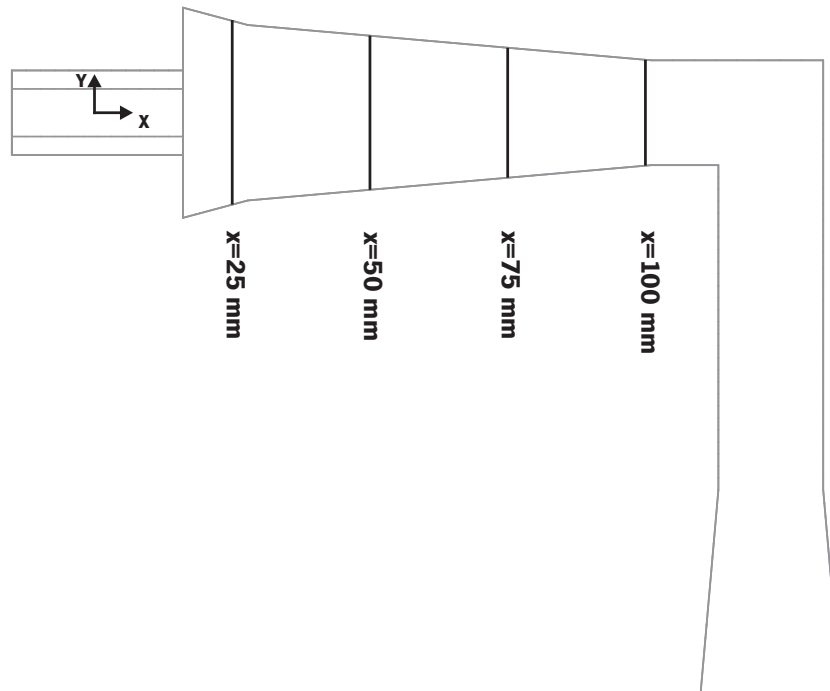
Figure 3.11: Locations of the velocity profiles for the pMDI solo domain

Figure 3.12 depicts the x-component velocity profiles for the three pMDI solo grids. The results show some velocity differences between the grids in zones of high velocity gradient. The differences appear to be higher for zones closer to the entrance.

Using the GCI methodology, the medium and fine grids velocity profiles are given in Figure 3.13, along with the apparent order of the method and the averaged GCI value. The extrapolated absolute error is given in the form of error bars, which identify the zones of highest uncertainty. It was verified that the GCI decreases with the axial displacement, and that the uncertainty is small. This result points out that a coarser mesh might be sufficient for the calculations in this geometry.

The most important variable to evaluate in the study is the amount of fine particles that exit the domain after 2 seconds of simulation. Fine-grid GCI is 1.97% with an uncertainty of 0.81 μg, and

medium-grid GCI is 0.60% with an uncertainty of 0.24 μg.
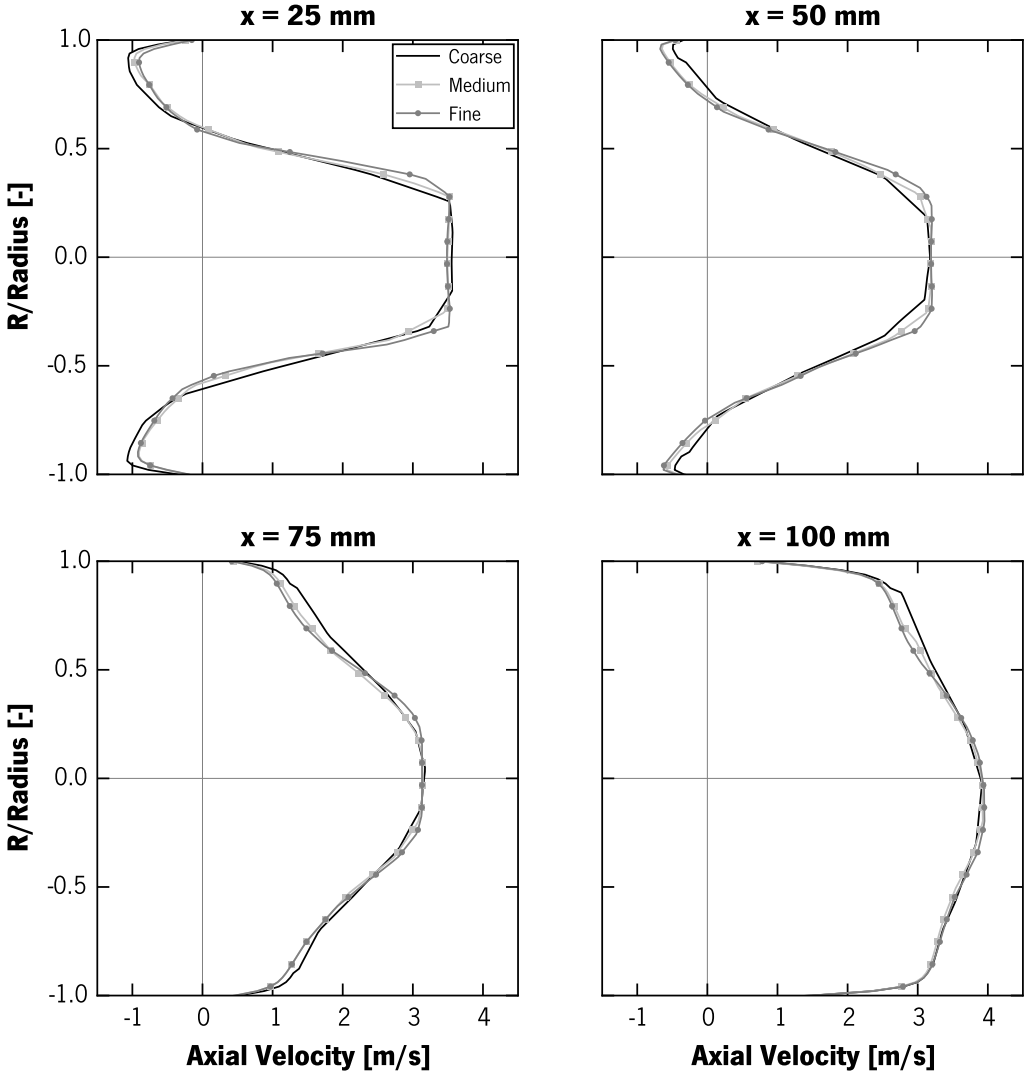
Figure 3.12: Axial velocity profiles for the three pMDI solo grids, took at four locations from the origin (t = 0.6 s)
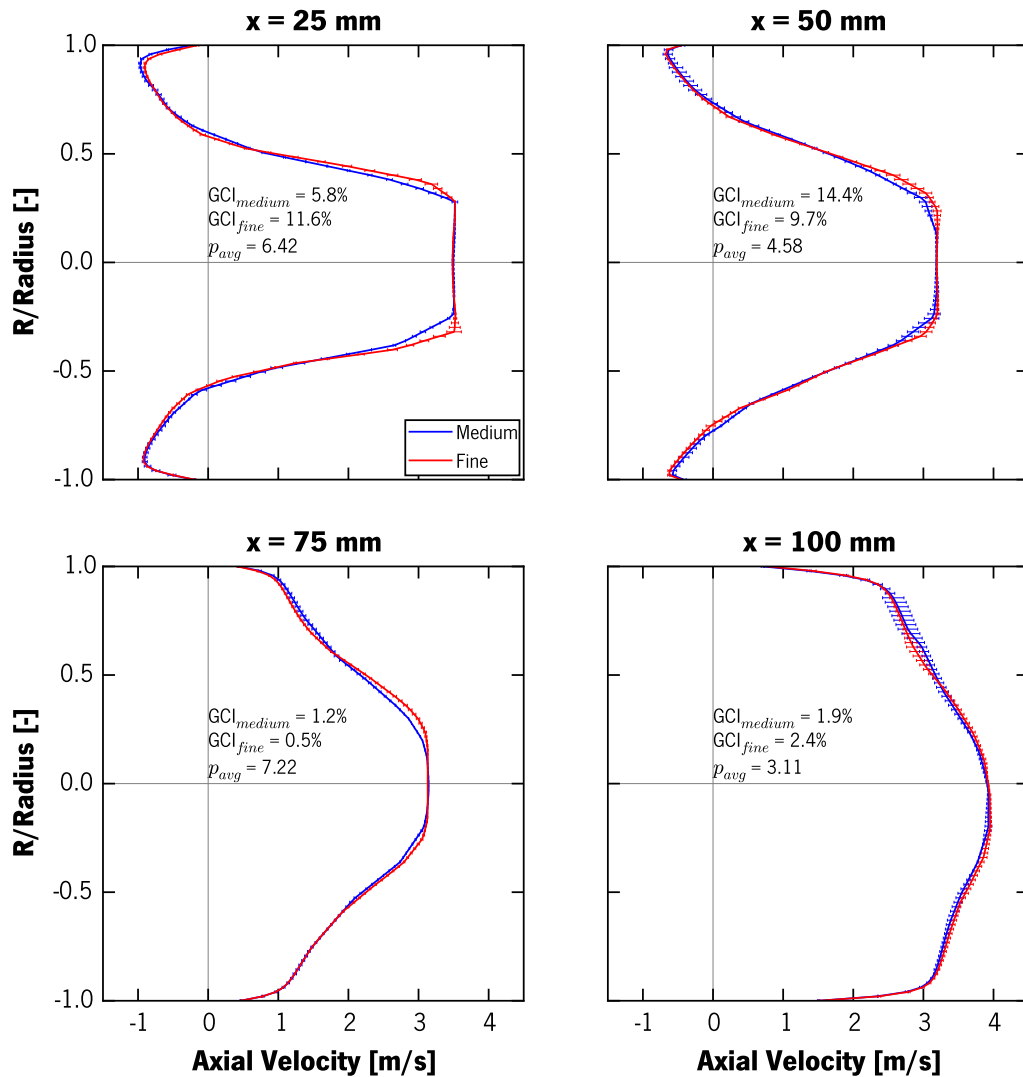
Figure 3.13: Extrapolated axial velocity profiles for the pMDI solo medium and fine grids, taken at four locations from the origin (t = 0.6 s). The absolute extrapolated uncertainty is represented in the form of error bars

3.8.3 CSC Grid

The grid uncertainty was evaluated for the CSC geometry using three sets of grids: 257.7k, 582.3k and 1309.8k cells. The variable under study was the velocity profile taken along the diameter at four locations apart from the origin (see Figure 3.14).
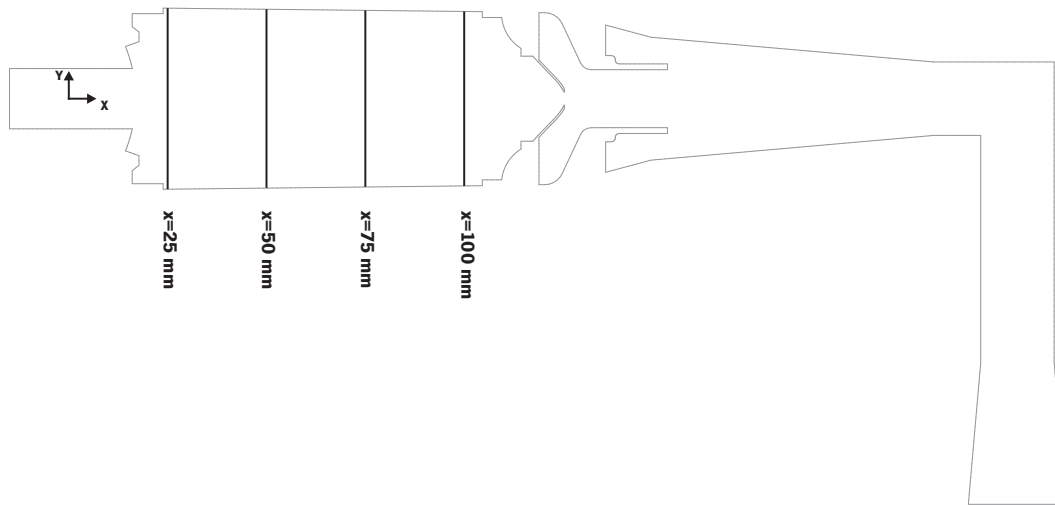
Figure 3.14: Locations of the velocity profiles for the CSC domain

Figure 3.15 depicts the profile for the x-component of the velocity for the three CSC grids. The results show velocity differences between the grids located in the centreline where velocity is maximum. Similarly to the pMDI solo geometry, the highest differences are closer to the geometry inlet section.

Using the GCI methodology, the medium and fine grids velocity profiles are given in Figure 3.16 along with the apparent order of the method and the averaged GCI value. The extrapolated absolute error is given in the form of error bars, which identify the zones of the highest uncertainty. The GCI decrease with the axial displacement up to the 75 mm, however closer to the valve (i.e. 100 mm) the uncertainty increases again. Despite that, the uncertainty is still within reasonable intervals, which might be acceptable for the use of a coarser grid without much influence in the drug deposition results.

The FPM exiting the domain after 4 seconds for the different grids shown a fine-grid GCI is 3.14% with an uncertainty of 0.48 μg, and a medium-grid GCI is 7.94% with an uncertainty of 0.95 μg.
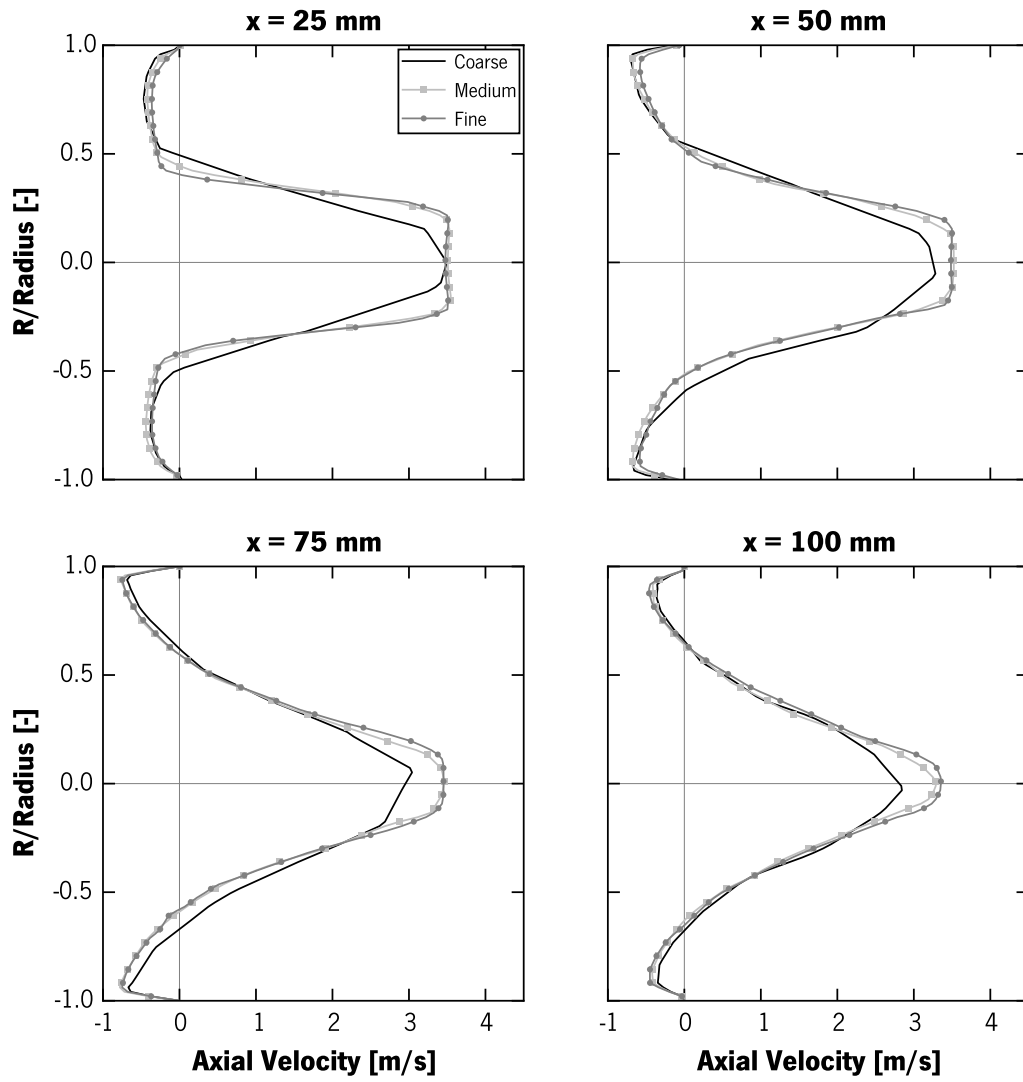
Figure 3.15: Axial velocity profiles for the three CSC grids, taken at four locations from the origin (t = 0.6 s)
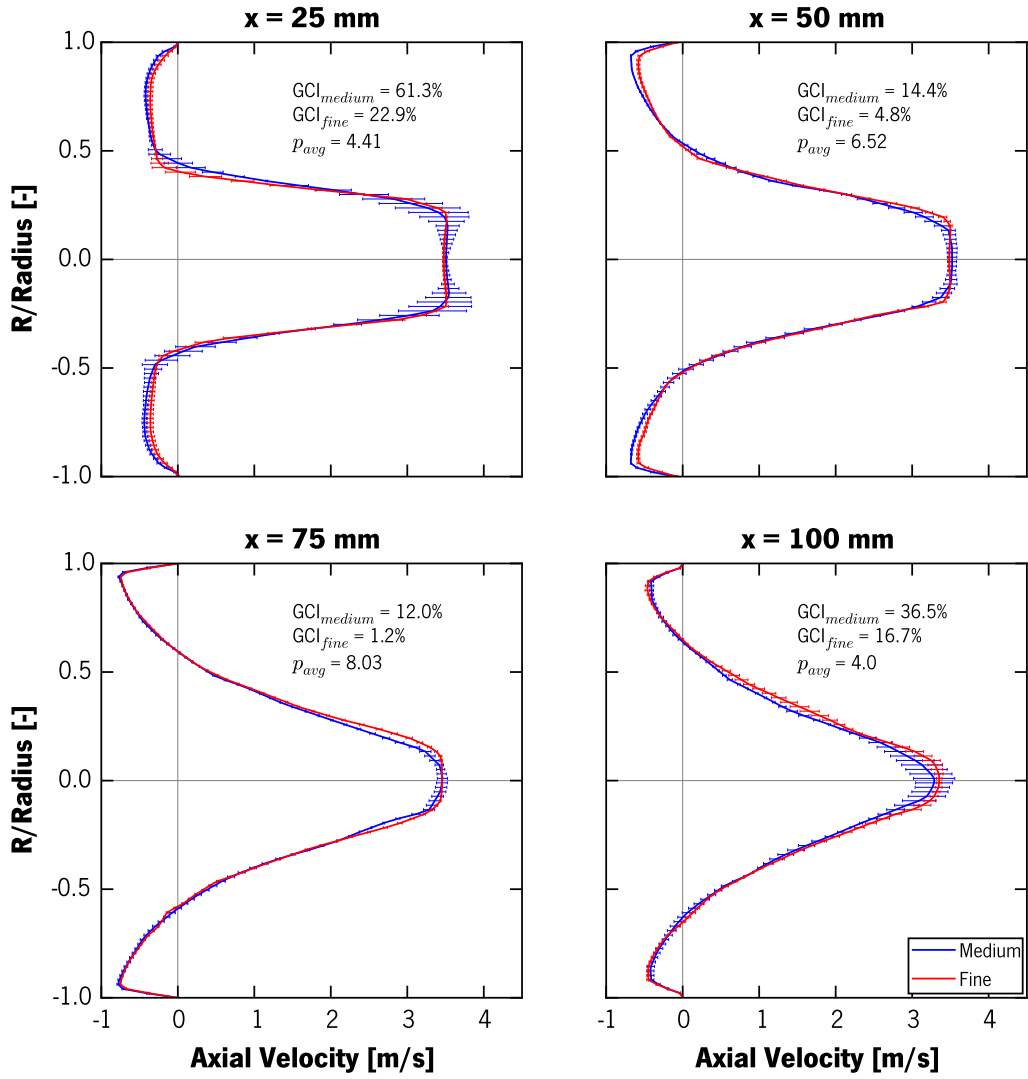
Figure 3.16: Extrapolated axial velocity profiles for the CSC medium and fine grids, taken at four locations from the origin (t = 0.6 s). The absolute extrapolated uncertainty is represented in the form of error bars

4 Project of the Experimental Setup

4.1 Experimental Setups

In order to characterize the pMDI+VHC emitted dose, one can either assess the TEM (using a FD setup) or detail regarding the plume aerodynamic size (using a CI setup).

4.1.1 Full Dose

Constant Flow

Initially some experimental tests were performed with the inhalation devices, at 30 L/min, using a setup for capturing the full emitted dose as illustrated in Figure 4.1.
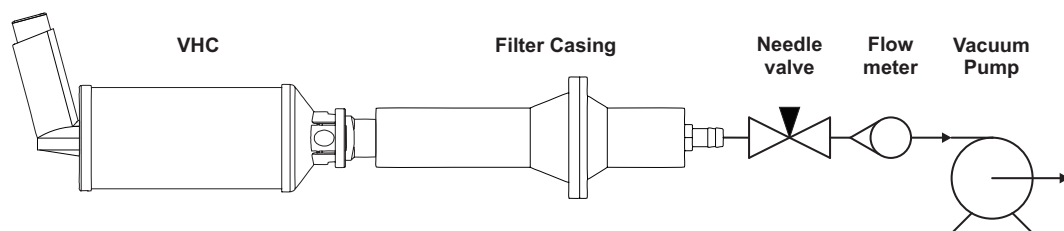
Figure 4.1: Experimental setup schematic for tests at constant flow using a Full Dose collector

This setup includes a vacuum system with a ball valve for flow control, which is connected to a rotameter and allows controlling of the air flow rate. The latter is connected to a house-made

aluminium filter casing that has a geometry with dimensions similar to the upstream portion of the USP IP (see section 4.2.5). The devices were connected to the filter casing, through a house-made silicon universal adapter, for a leakage free fitting. The paper filter used in the experiments was the MN 1674, whose characteristics are fully evaluated in section A.2. Tests were conducted by firing 20 puffs into the setup for the VHC's and 10 for the pMDI solo.

Variable Flow

Figure 4.2 depicts the experimental setup for testing the total emitted dose of the inhalation under a breath pattern (described in section 4.3.1). The setup is composed by the device under test that is connected to the filter casing, and the latter is directly connected to the breath simulator (described in section 4.2.7). A paper filter MN 1674 was used for drug collection and a total of 20 puffs, actuated at the beginning of each inhalation phase, were fired into the VHC.
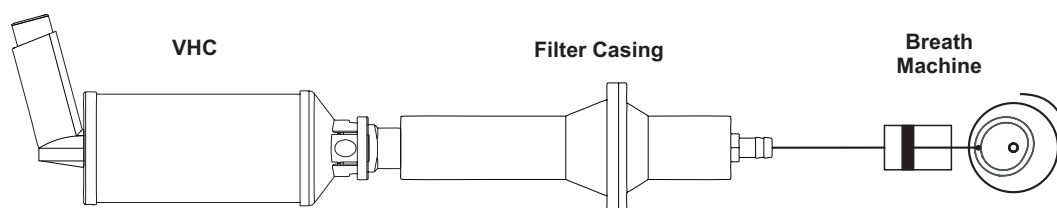
Figure 4.2: Experimental setup schematic for tests at variable flow using a Full Dose collector

4.1.2   Cascade Impactor

Constant Flow

Experimental tests of the drug delivery by the VHC at constant flow rate (i.e. 60 L/min) required an experimental setup that was able to replicate the lung deposition (see Figure 4.3). This is achieved by collecting the drug through an impactor/impinger, specifically in this case, a 5-stage MSLI. The impactor/impinger operation principle allows a mass separation by particle aerodynamic diameter ranges.
The setup is constituted by a MSLI, which is connected to a vacuum system that allows a controlled constant flow rate to be drawn through the impactor. A standardized induction port USP, connected

to the MSLI entrance, allows for a rough replication of the throat deposition effect. The VHC device under assessment is connected to the USP IP entrance, using an universal silicon adapter. Constant flow rate is drawn through the VHC during the test while several pMDI puffs are fired into the device. The collected mass at each part of the setup allows the quantification and the evaluation of the device performance.
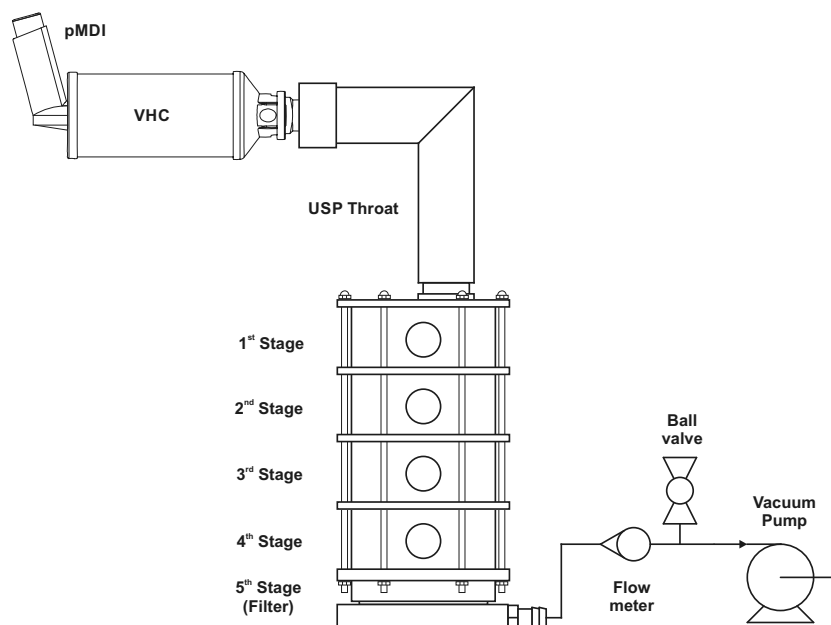
Figure 4.3: Experimental setup schematic for tests at constant flow using a cascade impactor

Variable Flow

The variable flow setup was used for VHC devices experimental evaluation of the emitted dose when the device is under a breath pattern. This approach is a more realistic way of testing VHC, since these devices have in their constitution an one-way valve that only properly works when the flow rate passing through it goes from zero to positive values and down again. This setup allows the movement of the valve, making it able to test the device valve efficiency in the delivery of the drug. In this experimental setup (see Figure 4.4), an MSLI was used for drug collection. The impactor has the need to work at constant and controlled flow rate, to provide accurate results. Therefore it is necessary to combine a variable flow rate pattern with the constant impactor flow rate. This was firstly achieved by Finlay [Fin98] and Foss [FK99], whose research teams approach

the problem by creating two flow circuits:

- a constant flow rate circuit between a compressed air source and the vacuum system that passes through the impactor;
- a variable flow rate circuit that results from adding (exhalation) or subtracting (inhalation) a flow pattern to the constant flow rate created by the compressed air source. At the impactor entrance, a T-junction separates the variable from the constant flow. This allowed the variable flow to be the only one reaching the VHC device that is connected to the IP.

An improvement to the typical T-junction was developed as a Mixer, for which geometric dimensions were optimized to minimize the pressure drop and particle-wall interaction.
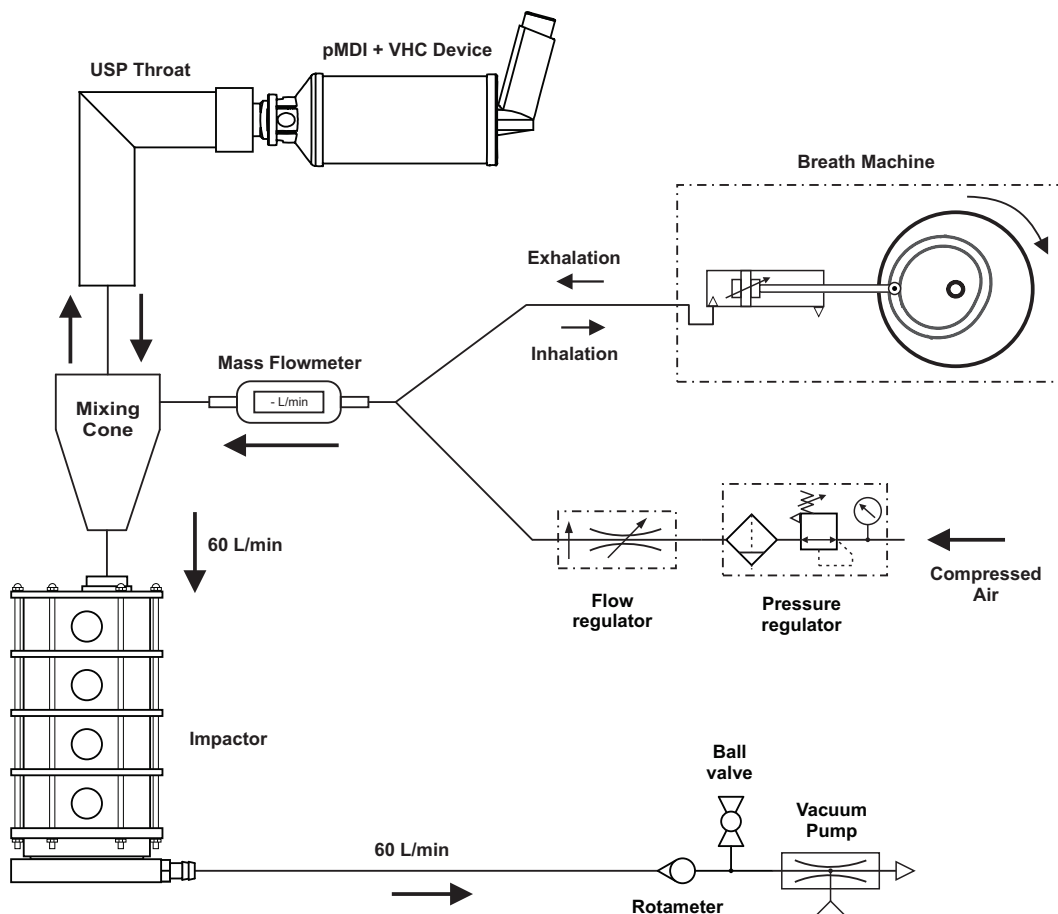
Figure 4.4: Experimental setup schematic for tests at variable flow using a cascade impactor

Figure 4.5 depicts the two extreme situations whereas the variable flow is added or subtracted to

the constant flow rate circuit.

The introduction of a breath simulator machine is an essential part of this setup, which provides the desired breath pattern that is used to evaluate the VHC device. A mechanical system was developed based in a form-closed cam-follower mechanism, where a continuous spin motion is converted to a variable linear motion, which is connect to a pneumatic piston rod that delivers a specific airflow wave.
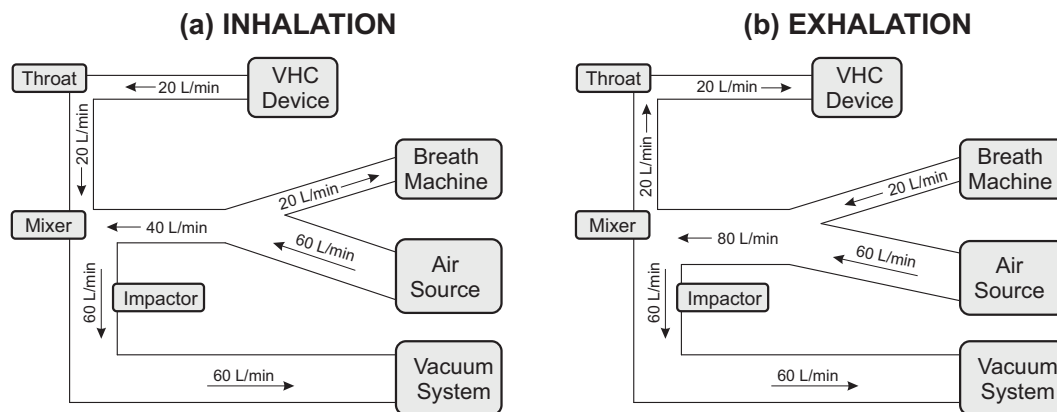
Figure 4.5: Flow rate routes for two scenarios: (a) subtraction (i.e. inhalation) or (b) addition (i.e. exhalation) of flow rate to the constant flow rate circuit

4.2 Main Experimental Setup Components

4.2.1 Vacuum System

The choice of the vacuum pump had to respect two important requirements: it could not be lubricated with oil to ensure the non-contamination of the air during the experimental tests; on the other hand it has to be able to overcome the pressure drop caused by the MSLI. In the MSLI device, the high pressure drop is caused by the paper filter in the last stage; so it was essential to start by evaluating different paper filters and choose the most adequate. This analysis is presented in section A.2, whereas it was chosen the paper filter MN 619 (from Macherey-Nagel, Germany) for usage with the MSLI.

Given a pressure drop of 37.7 kPa at 60 L/min, the vacuum pump needed, at least, to overcome this value. Several pumps with different mechanisms were studied, although the most cost-effective

and adequate choice was the oiless rotary vanes mechanism, more specifically the GS-6 model from General Europe Vacuum, Italy (see Figure 4.6).

This equipment included a three-phase motor of 370 W that powered the vanes. This selected equipment is capable to create a maximum flow of 123 L/min (at inlet atmospheric pressure) with a ultimate vacuum of 150 mbar and it is equipped with a silencer (attached to the outlet) that reduced the noise to 60 dB. Due to the pressure drop caused by the filter and the other setup components, two GS-6 pumps were installed in parallel. An escape ball valve was also added, in a T-junction, for flow rate control.

Figure 4.6: Vacuum system constituted by two GS-6 pumps in parallel

4.2.2 Compressed Air Source

The compressed air was obtained from the University pipe line, which was controlled through a pressure regulator with a filter (Model N204-D00 from Camozzi, UK) where its value was fixed in 2 bar. Additionally, a flow regulator (Model FCA88 from Brooks, USA) was coupled to ensure a flow rate of 60 L/min, measured in a rotameter (D10A11 from ABB, Switzerland). The objective of this procedure is tho account for sudden grid pressure fluctuations. This allowed a constant flow rate to be used in the variable flow experiments. The equipment used is displayed in Figure 4.7.

Figure 4.7: Air compressed source with the assembly of the pressure regulator and flow regulator

4.2.3   Flow Meters

As previously described, a rotameter (see Figure 4.8) was used for constant flow measurements in the setup, allowing for a control of the flow during the experiments. The latter was calibrated using three methodologies fully described in the section A.1. The rotameter was installed in a laboratory clamp universal support and it was placed in a vertical position. Percentage scale marks allow the user to read the float position and thus the flow rate. Additionally, a mass flow meter (Model 4043 from TSI, USA) was used for calibration and digital recording during the variable flow experiments. The flow meter was calibrated by the manufacturer for different types of gas. This device is composed by a hot-wire that estimates the flow rate based on voltage readings and by correlation with several calibration curves incorporated in its microprocessor. Additionally, pressure and temperature sensors allow to account for these variables influence and well as register them. The equipment is shown in Figure 4.9.

Figure 4.8: Rotameter used in the experimental setup

Figure 4.9: Mass flowmeter used in the rotameter calibration and in the variable flow setup

4.2.4   Mixing Cone

This device has the function to replace the classic T-junction, allowing for the smooth interaction between the two intersecting flows. The upstream flow coming from the VHC, which transports the drug particles, has a lower mean velocity than that delivered by the compressor plus breathing

machine (Figure 4.4). This may result in the projection of the drug particles towards the "Tee" walls. To avoid this effect, it is necessary to gently mix both flows, keeping the particles in the core of the jet.

Therefore, the device shall have a conical shape, similar to a cyclone separator, where a concentric tube enters the funnel. The design of such device was based in the work of Miller [Mil02]. The airflow, coming from the compressor plus breath machine, enters the funnel at the top (through inlet ports) and it is forced downwards, pushing the air from the inner tube and keeping the particles in the centre of the flow. This effect strongly reduces the drug deposition in this intersection, and it minimizes the influence of this component in the drug assessment setup.

Through the use of CFD software, the dimensions and number of air inlet ports were assessed. FLUENT® from ANSYS® [ANS13] was the software of choice for the study, where two flow cases were tested: the maximum exhalation flow (60 L/min plus 22 L/min) and the maximum inspiration flow (60 L/min minus 11 L/min). Due to the vacuum system function extracting air through the MSLI at 60 L/min, the same flow condition was applied in the outlet boundary of the mixing cone device. The top inlet of the concentric tube was kept at the atmospheric pressure and the flow passing there was assessed, to verify if the design performs its function properly.

Taking into account that the top concentric tube inlet has a fixed diameter defined by the USP throat (i.e. ⌀25.4 mm) and the bottom outlet has also a fixed diameter (i.e. impactor entry ⌀26.8 mm), only the length of the concentric tube was assessed. Also, the influence of 1, 2 or 4 inlet ports was studied in order to understand their impact in flow introduction at the top of the mixer funnel.

Figure 4.10 shows an axial cross section of the mixing cone with the main dimensions. Amongst them, the distance that was changed in the simulation study is marked with a red **X**. Although it is an axisymmetric geometry, the inlet at the top has a circular section, and it is positioned evenly spaced around the perimeter, accordingly to the number of inlet sections.
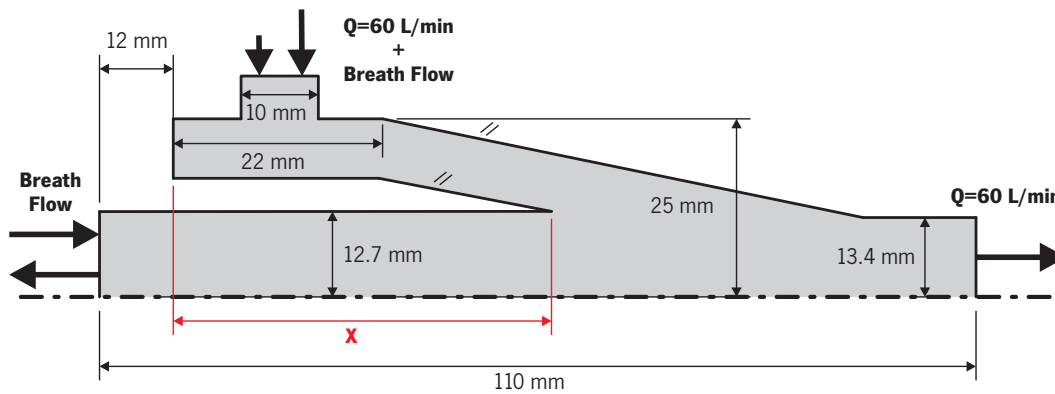
Figure 4.10: Schematic revolution section cut of the mixer design

The two angled lines are identified with a parallel ($//$) symbol. As the **X** dimension increases, the distance between those two parallel lines decreases. A sampling plane (parallel the bottom exit and distancing 105-**X** mm) was created. In this location it occurs, the change in the flow direction and mixing of both flows. The objective is to make this mixing as smoother as possible, therefore, the velocity and direction at this point, are assessed. Also, the pressure drop coefficient is evaluated for all the cases tested.

In order to identify the best dimensional value for **X**, a design analysis study was performed. By varying the **X** distance between an upper and lower bounds (i.e. 25 mm and 70 mm), a correlation function was obtained through 2nd order polynomial regression, for each output parameter previously described. Both inhalation and exhalation cases were evaluated using the ANSYS® software. The results are shown in Figure 4.11, and it can be observed that, the best dimension for **X** is between the values of 35.0 and 50.0 mm, where the values of pressure drop coefficient ($K = (p_{in} - p_{out}) / (0.5 \rho_f V_{in}^2)$) are the lowest.

In Figure 4.12, the results from the simulations for **X**=40 mm, for (a) exhalation and (b) inspiration, are represented. The results are shown in the form of fluid streamlines and velocity magnitude contours, in a quarter of geometry that includes the 4 inlets configuration. Results show a smooth transition of the flow in inspiration and exhalation stages. The exit at the bottom shows an undisturbed flow just upstream of the impactor. After post-processing of the results, the value for pressure drop coefficient is 2.13 for inspiration and 3.67 for exhalation. The velocity field at the sampling plane is similar for both cases in the bottom exit portion of the geometry.

Also, the flow at the top exit has the expected values at both cases, i.e. the flow rate delivered by the breath machine.
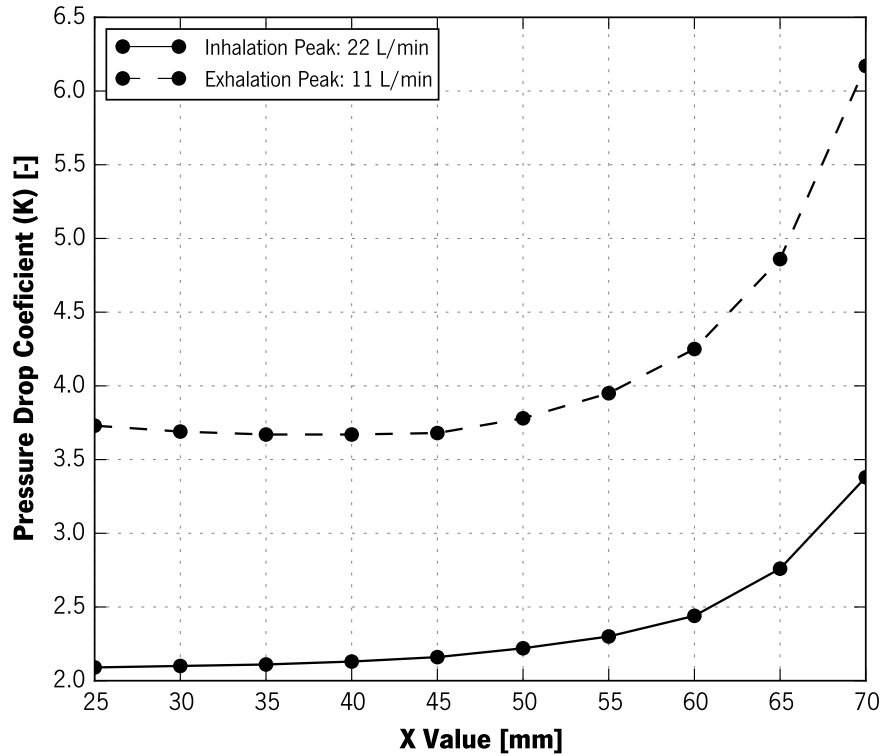
Figure 4.11: Results of pressure drop for the mixer design upon several values for **X** dimension, two curves represent the inspiration and exhalation points

A subsequent numerical assessment of the pressure drop coefficient results for 1, 2 or 4 entries was made, with results respectively, 6.99, 3.52 and 2.11 for the inspiration phase. This suggests that, the use of 4 inlets is the best configuration. Visual inspection of the results also showed a more stable flow region close to the exit of the device, showing an axisymmetric flow.

This device was manufactured in aluminium with four side entries. However, latter on during the testing procedure, it was found that using a triple T-junction connecting the four side entries resulted in complications for the disassembly and washing procedures. Hence, the device was modified to be used with only one side entrance.
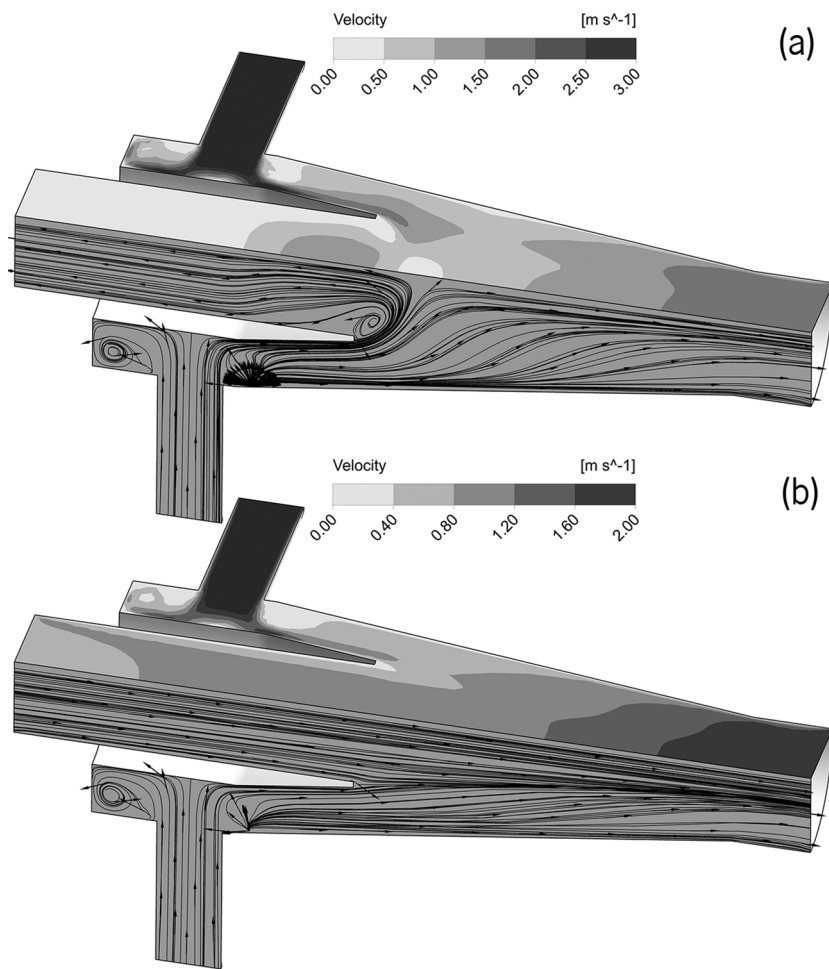
Figure 4.12: CFD results for the mixer chosen design of one quarter geometry: (a) exhalation and (b) inspiration

4.2.5 USP IP

As depicted in Figure 4.3, the pMDI and the VHC were fitted into a home-made silicon universal adapter, which was attached to the USP IP (made of aluminium accordingly to the standardized dimensions present in US Pharmacopeia [US 14]), as depicted in Figure 4.13.

The standardized USP throat model (with a 90 degrees bend) is a fairly known representation of the human throat. Nowadays, the latest standardized throat model is closer to a human physiologic throat and it is known as the "Alberta" idealized adult anatomic throat (AIT). Some studies point that the AIT model shows a more correct drug deposition than the USP model [ZFM04, LHDX08, Che14]. Nevertheless, the AIT latest equipment was not available in the laboratory and due to economical

reasons it was not feasible to acquire or produce it. Since USP model is still acceptable in the Pharmacopoeia and fairly known, is was the device of choice.
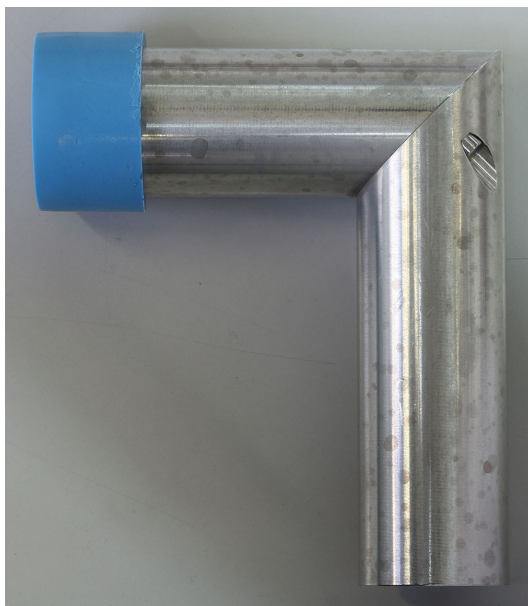
Figure 4.13: USP IP aluminium model with the silicon universal adapter attached

The universal silicon adapter was based in the VHC actuator adapter design, made with a rubber material that allowed for large deformations and that could create a tight seal around the different VHC mouthpieces designs. It was designed using the CAD software SolidWorks®. A simple deformation simulation (using explicit dynamics software LS-DYNA® from ANSYS®) was carried out to study if the dimensions were able to tight seal around the Ventilan® pMDI actuator. Simulation results proved that the design represent a feseable solution. Hence a two part aluminium mould was produced by CNC milling so the liquid silicone (Smooth-Sil 950, Smooth-On from USA) could be poured into it. Afterwards, the silicon sealed in the mould was exposed to a curing process of 24 hours in an oven. The silicon universal adapter was then tested for mechanical resistance to manual handling (by compressing and stretch). Afterwards it was also washed with a 0.01M NaOH solution to a 20 mL flask to investigate the possibility of contamination. Results showed no contamination (0.00 ± 0.00 abs at 244 nm).

4.2.6   Multi-Stage Liquid Impinger (MSLI)

Impacting collectors have been used to measure particle size for a wide range of sprays. In particular for inhaler derived aerosols, it has been the most widely used method [Mar04]. Mitchell and Nagel have extensively reviewed this type of particle size analysers, their strengths and limitations [MN03].

The theoretical principles of an impactor are based on the solution of the two dimensional Navier Stokes equations of a fluid around a target oriented perpendicularly to the impinging flow. This flow field is subsequently coupled with Newton's equation of motion to model the trajectories of particles/droplets through various stages and geometries. In its basic form, the impactor consists of a jet of a known diameter that exits from an nozzle diameter (D) located at a certain distance (S) from the flat target that acts as a collector (see Figure 4.14).
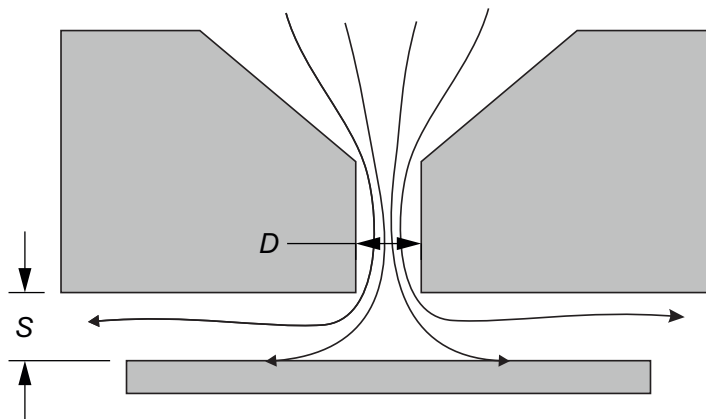
Figure 4.14: Schematic of the impactor working principle

As the flow exits the orifice, its streamlines diverge in the vicinity of the collection surface. The high inertia particles move through the streamlines and impact on the target surface. The Stokes number (Stk) defines the critical particle size (aerodynamic diameter d_p) that will impact the collection surface through Equation 4.1:

$$\text{Stk} = \frac{\rho_p C_c d_p^2 U_f}{2\mu_f D} \tag{4.1}$$

where C_c is the Cunningham slip, ρ_p is the particle density, U_f is the gas velocity at the orifice exit and μ_f is the fluid viscosity.

The particle collection efficiency of an ideal impactor will increase in a step from 0 to 100% at a critical Stk. For each impactor stage, the corresponding cut-off diameter (d_{50}) can be calculated through Equation 4.2.

$$\sqrt{C_{50}}d_{50} = \left[\frac{9\pi\mu_f nD^3}{4\rho_p C_c Q} \right]^{(1/2)} \sqrt{\text{Stk}_{50}} \tag{4.2}$$

where n accounts for the number of circular nozzle orifices, Q refers to the flow rate and subscript 50 identify conditions at 50% efficiency.

A cascade impactor consists of several stages with progressively decreasing cut sizes, assembled in series, so that an aerosol is separated into various fractions according to the number of stages assembled. The design of the CI can be tailored to measure the size down to sub-micron particles. The Glass Twin Impinger is used to separate the large from the small particles. The former are deposited in the upper tract of the respiratory system while the later are most likely to reach the alveoli. For inhaler testing, it is desirable that at least 5 stages are assembled with cut off aerodynamic diameters within the range 0.5 - 5.0 µm. One of the most widely used is the Anderson type impactor with 8 stages. The testing of aerosols usually involves the operation at a constant flow rate (i.e. 28 L/min) although this does not represent the conditions typical of a tidal respiratory cycle.

The CI available in the laboratory was the 5-stage Multi-Stage Liquid Impinger (MSLI) (last calibrated in 2014 by Westech, UK), see Figure 4.15. Although, this equipment has cut-off stage diameters calibrated at 60 L/min, a simple formula (provided in the Pharmacopeia) can used to correct for different flow rates (between 30 L/min and 100 L/min). The studies were conducted at 30 and 60 L/min, whereas the cut-off diameters are presented in Table 4.1.

Table 4.1: Cut-off diameters for all the stages at 30 and 60 L/min constant flow

Flow rate (L/min)	Stage 2	Stage 3	Stage 4	Stage 5
30	18.4	9.6	4.4	2.4
60	13.0	6.8	3.1	1.7

Values come in micrometres (µm), except when indicated otherwise

Figure 4.15: Pharmacopoeia 5-stage MSLI apparatus

4.2.7   Breathing Simulator

The breathing simulator has the purpose of replicating a human breath waveform by means of a mechanical system. The system is composed by the spin motor that provides a continuous rotation motion, two worm gear speed reducers coupled in tandem to reduce the motor Rotations Per Minute (RPM) output, one form-closed cam-follower mechanism and a pneumatic cylinder. The spin motor rotational movement actuates a cam, which transforms its movement to a non-uniform linear translational follower's displacement. The latter is connected to the pneumatic cylinder piston. An overview of the house-made assembled mechanism is shown in Figure 4.16.

The cam-follower mechanism is fully dependent on the breath waveform that is intended to be replicated. It is also limited by the pneumatic cylinder piston cross section area and the angular velocity of the cam. Meaning that, this design can only reproduce a pre-defined waveform; a different one would imply changing the spin velocity, cam plate and possibly the pneumatic piston.
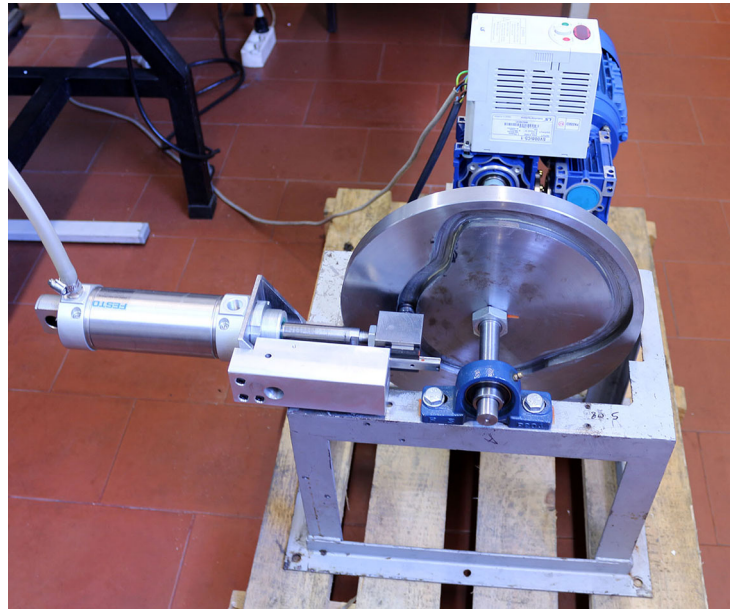
Figure 4.16: Photograph of the house-made breath simulator to deliver the designed breath waveform

4.3   Design of the Breathing Simulator

4.3.1   Breath Profile

The first step in designing the breathing simulator mechanism is to define the respiratory profile, which is the intended output. Thus, a target patient waveform was studied (i.e. an asthmatic children under 6 years old).

An asthmatic child breathing profile shows certain characteristics that are different somehow from a healthy child. The VHC use is intended for children and elder without the capacity for breathing-actuation coordination. According to the Canadian normative for VHC testing (Dolovich and Mitchell, 2008), a good simplified approach for the shape of the respiratory cycle (flow vs. time) corresponds to a sinusoidal function [DM04, CZR08]. Also, other authors presented experimental data that supports this assumption [JAC$^+$05].

For a correct definition of the sinusoidal wave, it is of utmost importance to obtain the suitable experimental data of breathing frequency BPM, duty cycle (ratio of inspiration time per total cycle time) and tidal volume of inspired air. The respiratory frequency ranges from 20 to 30 BPM,

and increases in the presence of asthma [DM04, BOS01, BP09, MGH+99]. It is known that the duty cycle values for these children are approximately 0.44 [MGH+99, CAM+01, KCD+05], but it decreases with the presence of a respiratory disease [BOS01, KCD+05]. Although the tidal volume varies with height, weight, gender and with asthma pathology, data from various sources show that it ranges from 150 to 180 L/min [DM04, BOS01, BP09].

Enlightened by these data, the following values were assumed to be the most adequate: a frequency of 30 BPM, a duty cycle of 0.33 and a tidal volume of 150.0 mL. The breathing cycle used in the simulations is represented in Figure 4.17.
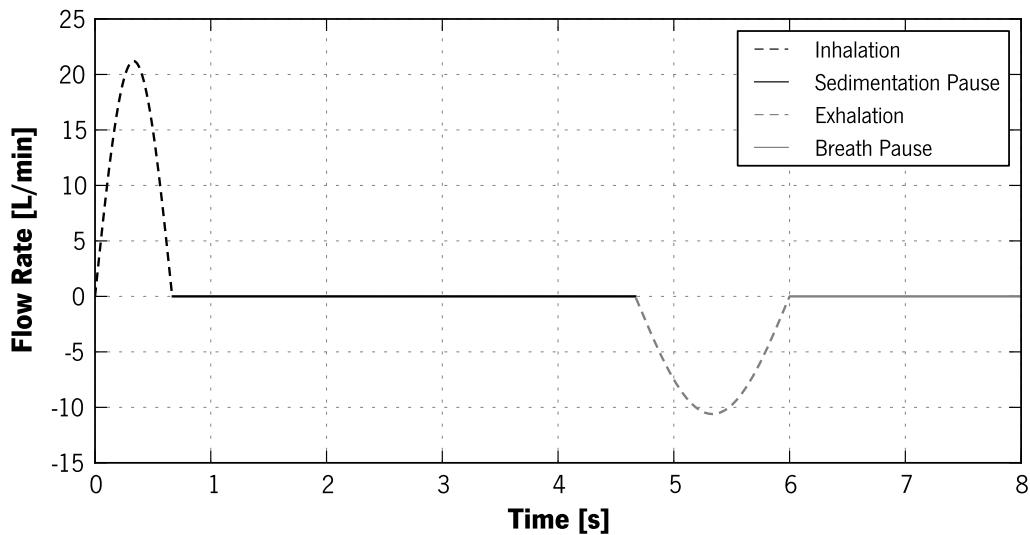
Figure 4.17: Breath profile developed to be used in the variable setup testing

The amplitude of the inspiratory sinus (21 L/min) was obtained by fitting the integral of a sine function to the tidal volume. The same procedure was applied for the exhalation phase. A pause of 4 s after inspiration was added, to guarantee the sedimentation of drug particles inside the lungs. This delay is recommended for improved efficacy in drug delivery. After the exhalation phase, a 2 s pause was added, which is proposed by Mitchell and Dolovich, as well as, the Canadian normative for VHC testing [CZR08, MD12]. This delay is intended to simulate the poor coordination of an asthmatic patient using a VHC.

4.3.2 Calculation of the Cam Tracks

Figure 4.17 depicts the initial condition for the design of the cam-follower profile. The piston shall move accordingly to reproduce the flow rate as described. In the present case, the varying flow rate of the respiratory cycle was obtained by the use of a cam/cylinder combination. This design is robust and it can provide accurate flow profiles at a low construction cost. Alternatively the volume flow rate could be delivered by a step motor driving the piston/cylinder. This option would be more expensive to develop though with added flexibility of operation. However, as the current study is focused on a particular group of patients, this limitation is not extremely severe.

After assuming the internal diameter of the cylinder, D_p, the corresponding circular area is calculated. This area should be corrected by subtracting the cross section area of the internal rod, D_r, if present inside the cylinder. Dividing the sine waves by the value of the piston cross section area, the piston velocity is obtained. Through the integration of the velocity (y') function, the acceleration (y'') is obtained, and from acceleration integration, the jerk (y''') is calculated. In opposition, by derivation of the velocity, the displacement (y) function is obtained. The four functions are shown in Figure 4.18, and they are essential to the definition of the follower path in the cam. Using the profiles for the piston movement and the proper equations for form-closed cam-follower calculation, the profile is obtained by the approximation of a curve tangent to the position of the follower.

Equation 4.3 is used for the calculation of the follower movement, as [Flo09, Nor02]:

$$F(x, y, \theta) = (x - x_c)^2 + (y - y_c)^2 - R_r^2 = 0 \tag{4.3}$$

where R_r is the radius of the contact roller (i.e. 19.0 mm) and (x_c, y_c) are the roller centre coordinates, given by Equations 4.4 and 4.5 [Flo09, Nor02]:

$$x_c = -(R_b + R_r + s) \cdot \sin \theta \tag{4.4}$$

$$y_c = (R_b + R_r + s) \cdot \cos \theta \tag{4.5}$$
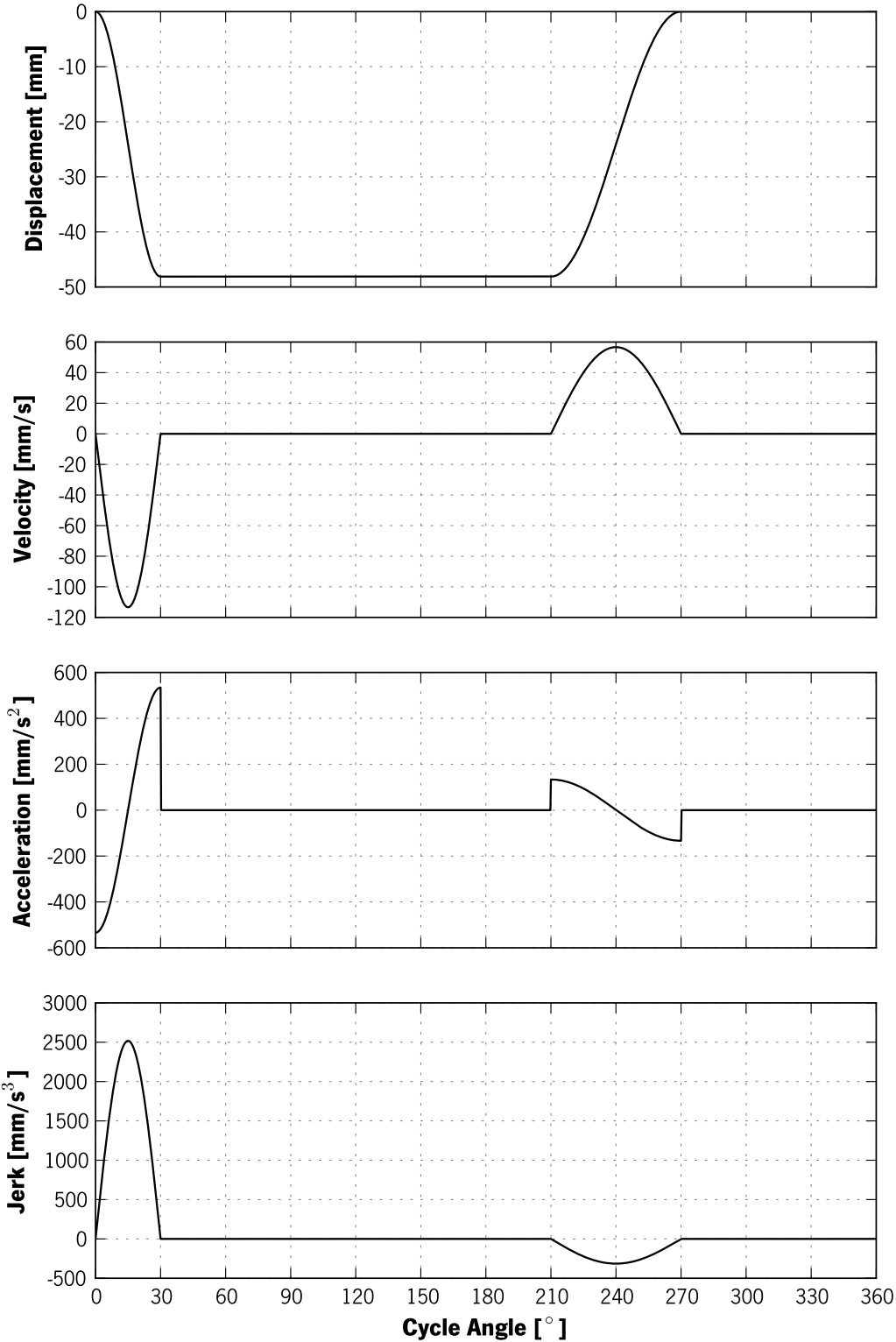
Figure 4.18: Cam profiles (displacement, velocity, acceleration and jerk) calculated for the chosen cam/cylinder dimensions

In these equations R_b is the base radius of the cam, s is the displacement (see Figure 4.18). Differentiating Equation 4.3 with respect to θ, Equation 4.6 is obtained [Flo09, Nor02]:

$$\frac{\partial F}{\partial \theta} = -2(x - x_c)\frac{\mathrm{d}x_c}{\mathrm{d}\theta} - 2(y - y_c)\frac{\mathrm{d}y_c}{\mathrm{d}\theta} = 0 \tag{4.6}$$

The derivatives of Equations 4.4 and 4.5 with respect to θ are given by Equations 4.7 and 4.8 [Flo09, Nor02]:

$$\frac{\mathrm{d}x_c}{\mathrm{d}\theta} = -(R_b + R_r + s)\cos\theta - \frac{\mathrm{d}s}{\mathrm{d}\theta}\sin\theta \tag{4.7}$$

$$\frac{\mathrm{d}y_c}{\mathrm{d}\theta} = -(R_b + R_r + s)\sin\theta - \frac{\mathrm{d}s}{\mathrm{d}\theta}\cos\theta \tag{4.8}$$

where $\mathrm{d}s/\mathrm{d}\theta$ represents the velocity of the follower (see Figure 4.18). Solving, simultaneously, Equations 4.3 and 4.6, Equations 4.9 and 4.10 for cam profiles coordinates, are obtained [Flo09, Nor02]:

$$x = x_c \pm R_r \left(\frac{\mathrm{d}y_c}{\mathrm{d}\theta}\right)\left[\left(\frac{\mathrm{d}x_c}{\mathrm{d}\theta}\right)^2 + \left(\frac{\mathrm{d}y_c}{\mathrm{d}\theta}\right)^2\right]^{-\frac{1}{2}} \tag{4.9}$$

$$y = y_c \mp R_r \left(\frac{\mathrm{d}x_c}{\mathrm{d}\theta}\right)\left[\left(\frac{\mathrm{d}x_c}{\mathrm{d}\theta}\right)^2 + \left(\frac{\mathrm{d}y_c}{\mathrm{d}\theta}\right)^2\right]^{-\frac{1}{2}} \tag{4.10}$$

Equations 4.9 and 4.10 represent the inner and outer profiles for the cam, as shown in Figure 4.19. All these calculations have been programmed using Python language and a script was computed. Several dimensional configurations for the base diameter and piston diameter were assessed. Also, the following constrains were introduced:

- cylinder feasible diameters could not be outside the manufacturer range;
- the maximum feasible displacement could not be outside the cylinder manufacturer range;
- cam outer profile could not be located at less than 6.0 mm to the maximum disk diameter (i.e. 310.0 mm);
- cam inner profile could not be located at less than 5.0 mm to the disk bore diameter (i.e. 27.0 mm).

Within such restrictions and the cylinder D_p manufacturer constrains, several possible combinations were obtained. Amongst all the feasible solutions, those presenting the lower value for pressure angle was selected (i.e. Base diameter: 250.0 mm and Piston diameter: 63.0 mm).
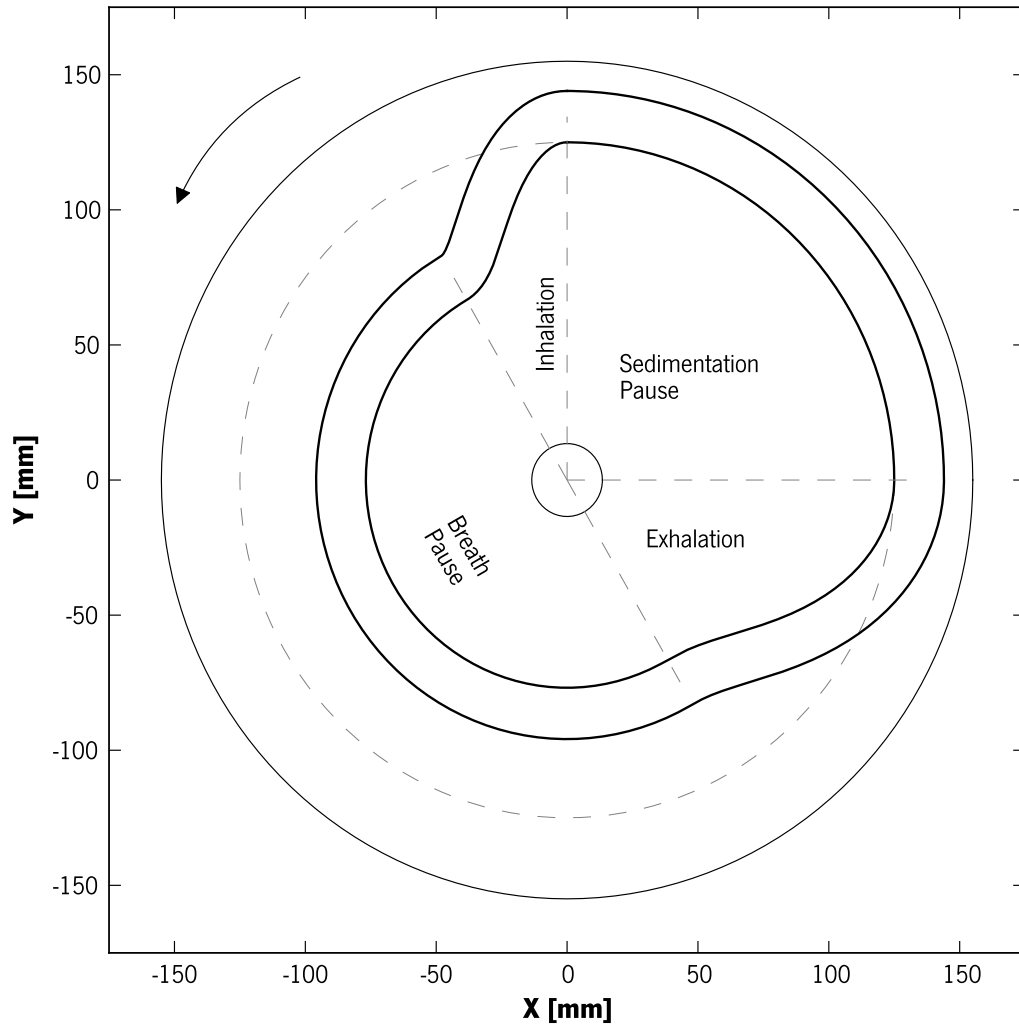
Figure 4.19: Final design of the cam profile, showing the outer and inner profile tracks along with the base diameter, the inner and outer borders

4.3.3   Cam Mechanism Performance Analysis

A cam follower mechanism performance can be numerically evaluated in the design phase, before its experimental validation. This can be done using different metrics, herein were calculated the pressure angle, curvature and backlash impact.

In the contact point formed between the two curves (cam profile and roller), the force is transmitted from cam to follower along the common normal (i.e. axis of transmission). The pressure angle is defined by the angle between the direction of motion and the common normal. If the pressure angle presents a value of zero, there is a perfect alignment between the both and therefore all force goes into the movement. High pressure angle values, represent a part of the load not being transformed into movement and results in tangential slip forces on the follower's axis that can lead to fracture. Equation 4.11 allows the calculation of the pressure angle profile along a cam cycle [Flo09, Nor02]. Advisable values of pressure angle are within 30 degrees.

$$\phi = \tan^{-1} \frac{y'}{R_b + R_r + y} \tag{4.11}$$

Curvature radius allows the evaluation of the cam profile curvature at each point of its cycle. By using the general Equation 4.12 and applying it to Equations 4.4 and 4.5, the simplified Equation 4.13 for radial cam with translating roller follower was used to calculate the curvature radius. Its value is then compared with the roller radius (R_r) and a simple geometric analysis can provide conclusions upon the type of cam profile: convex ($\rho_p > R_r$) or concave ($\rho_p < 0$). Design combinations where the profile do not reproduce a desired solution are found when: $0 \leq \rho_p \leq R_r$. Undercutting problems can be found whereas the minimum positive curvature value is smaller than the roller radius.

$$\rho = \frac{\left[\left(\frac{\mathrm{d}x}{\mathrm{d}\theta}\right)^2 + \left(\frac{\mathrm{d}y}{\mathrm{d}\theta}\right)^2 \right]^{\frac{3}{2}}}{\frac{\mathrm{d}x}{\mathrm{d}\theta}\frac{\mathrm{d}^2 y}{\mathrm{d}\theta^2} - \frac{\mathrm{d}y}{\mathrm{d}\theta}\frac{\mathrm{d}^2 x}{\mathrm{d}\theta^2}} \tag{4.12}$$

$$\rho_p = \frac{\left[\left(R_b + R_r + y\right)^2 + \left(y'\right)^2 \right]^{\frac{3}{2}}}{\left(R_b + R_r + y\right)^2 + 2\left(y'\right)^2 - \left(R_b + R_r + y\right) y''} \tag{4.13}$$

The backlash impact force is resultant from the existence of backlash (i.e. the gap between the moving parts whereas exists loss of contact), in cases where the cam angular velocity is very high it is especially important to reduce the influence of this force. For the calculation of this force (see Equation 4.14) is required to assume:

- a backlash average value (i.e. y_{tol} = 0.05 mm);
- the system equivalent mass (i.e. m = 0.48 kg);
- the system stiffness (i.e. k = 1.3E10 N/m).

$$F_c \cong \left[\frac{1}{2} \left(\frac{d^3 y}{d\theta^3} \right)^{\frac{1}{3}} \cdot (6 \cdot y_{tol})^{\frac{2}{3}} \right] \sqrt{m \cdot k} \qquad (4.14)$$

Whereas the system equivalent mass (i.e. m) is calculated through Equation 4.15 and the system stiffness (i.e. k) is given by Equation 4.16.

$$m = \frac{m_{cam} \cdot m_{follower}}{m_{cam} + m_{follower}} \qquad (4.15)$$

Considering: m_{cam} = 12.0 kg, $m_{follower}$ = 0.5 kg.

$$k = \frac{4 \cdot \sqrt{R_r}}{3 \cdot 2 \cdot \left(1 - \frac{\nu^2}{E} \right)} \qquad (4.16)$$

Considering the Young Modulus (E = 1.9E11 Pa) and Poisson's Ratio (ν = 0.27).

Figure 4.20 shows the performance analysis of the cam-follower mechanism, where it is reported the pressure angle, curvature radius and backlash impact force.

Pressure angle reach a peak (i.e. 46.4°) at 17°, a second smaller peak (i.e. 27.7°) is found at the position 235.7°; these values are within an acceptable range (hatched in red dash the non-advisable limits) for the low angular velocity of this system (i.e. 7.5 RPM).

Regarding the curvature radius, it can be observed the existence of some peaks, coming in from points where sharp corners are present. This could be mitigated by increasing the cylinder piston diameter (or increasing the base diameter). Most important is the non-existence of undercutting zones (hatched in red dash), for which the minimum curvature radius is 3 times higher than the roller radius.

The backlash impact force reaches two peaks corresponding to the inspiration and exhalation peaks. The peak values are 250 N and -120 N, and they play an important role for high angular velocity systems which is not the case for the projected system, this effect can only be mitigated by increasing the piston diameter.
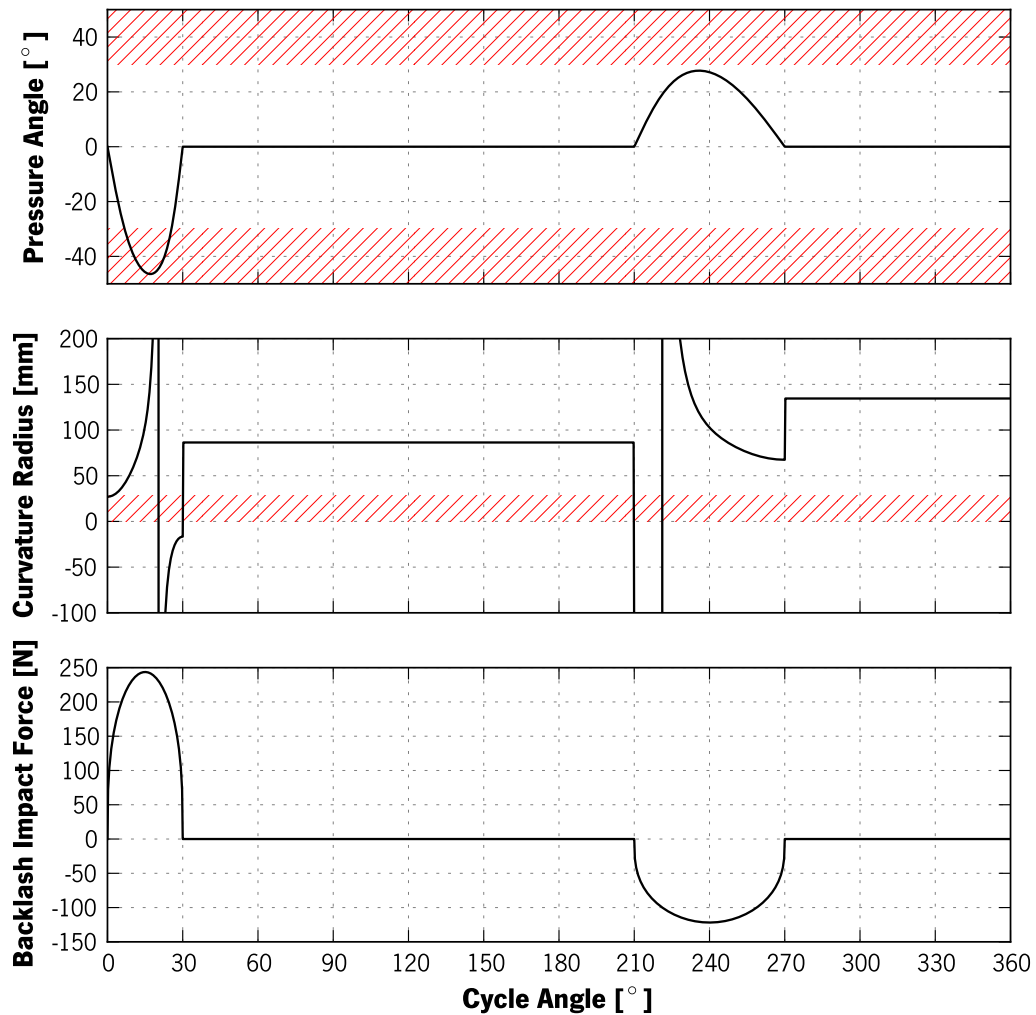
Figure 4.20: Performance profiles (pressure angle, curvature radius and backlash impact) calculated for the chosen cam design

4.3.4   Other Components and Assembly

The cam disk was manufactured by CNC milling of alloyed steel (UNE F-5303) with a surface hardening nitriding process, to provide extra wear resistance. The disk has an outer diameter of 310.0 mm and an inner bore of 27.0 mm, with a thickness of 22.0 mm and a track depth of 10.0 mm.

The rotation movement transmitted to the cam is provided by a three-phase electric motor (model TA713-4 from MEB) spinning at 1,380 RPM for a 50 Hz current. Therefore, two worm gears were

sequentially coupled (model NMT040 from MEB) with a combined ratio of 1:75. To match the RPM of the motor in order to reach the total breathing cycle time (i.e. 8 s per turn=7.5 RPM), it was used a variable frequency drives (model SV008iC5-1 from LS). Such device also allows for the study of other breathing patterns if required. A proper shaft union of the worm gear to the cam axis was made (model flexible coupling union from TRASCO). This device allows a smoother connection mainly in case of vibrations.

An adequate roller to run the form-closed profile of the cam was selected (model S24LW from RBC bearings), which accounted for high levels of friction induced wear.

The roller was attached to a sliding guide, and this one to the cylinder rod. A guide with ball bearings was selected (model REXROTH from BOSCH Group), so it did not added friction to the system while ensured an accurate motion of the linear piston.

A pneumatic cylinder with a 63.0 mm internal diameter and 100.0 mm of stroke length (model DSNU from FESTO) was chosen.

4.3.5   Breath Simulator Validation

The validation of the output generated by the designed breath machine, which is based in a form-closed cam-follower mechanism, was executed by evaluating both the follower's displacement and the airflow output (see Figure 4.21).

The final configuration of the breath machine accounts for a constant flow rate of 60 L/min passing through the pneumatic cylinder outlet port. However, this creates a positive pressure that the mechanism needs to overcome. By placing the mass flow meter downstream of the junction of both flow rates (i.e. constant 60 L/min plus the generated waveform) it allows a better evaluation of the real breath pattern being generated.

The air flow rate was measured by the mass flow meter (Model 4043 from TSI, USA), and from this data it was subsequently subtracted the constant air flow of 60 L/min, resulting the generated waveform by the breath machine. The linear displacement was acquired by connecting a Linear Variable Differential Transformer (LVDT) (DCTH2000 from RDP Electronics, UK) to the piston rod. The LVDT sensor was connected to a data acquisition system (NI USB-6009 from National

Instruments, USA) which was connected to the computer by USB interface, while the mass flow

meter was directly connected to the computer by Serial Port.
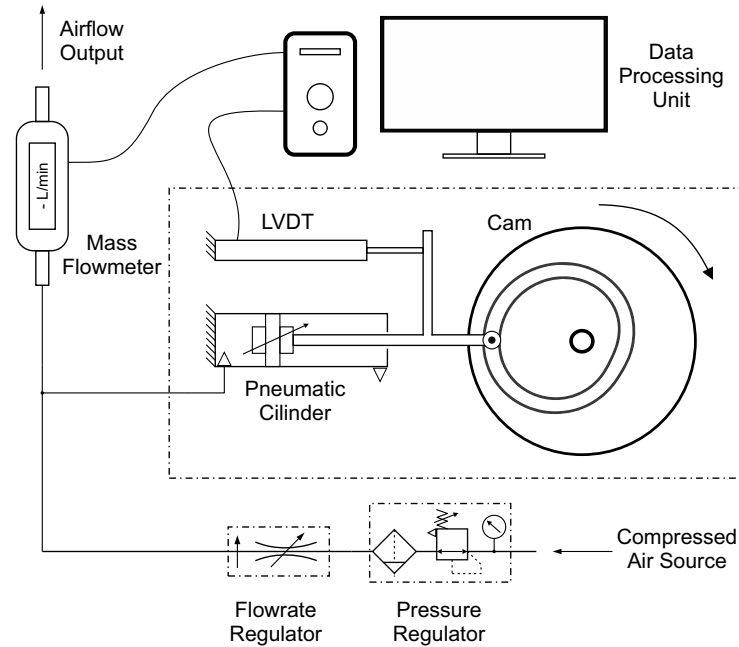
Figure 4.21: Breath machine validation setup

The data from both sensors were processed in an instrumentation software (LabVIEW 2010 from

National Instruments, USA), and then were analysed and compared to the theoretical profiles of

displacement and flow rate (which were the input of the cam profile creation).

Comparison graphs are shown in Figures 4.22 and 4.23. Minimum differences were found for

the displacement profile (see Figure 4.22). However, the flow rate results presented an irrelevant

inconsistency in the peak of the inhalation (see Figure 4.23), which might be associated to backlash

caused by high curvature of the cam profile. That could be mitigated by increasing the base

diameter of the cam profile, which would not be fit within the existing metal framework dimensional

restrictions. Another possibility, would be the use of a custom-made pneumatic cylinder with larger

piston diameter.
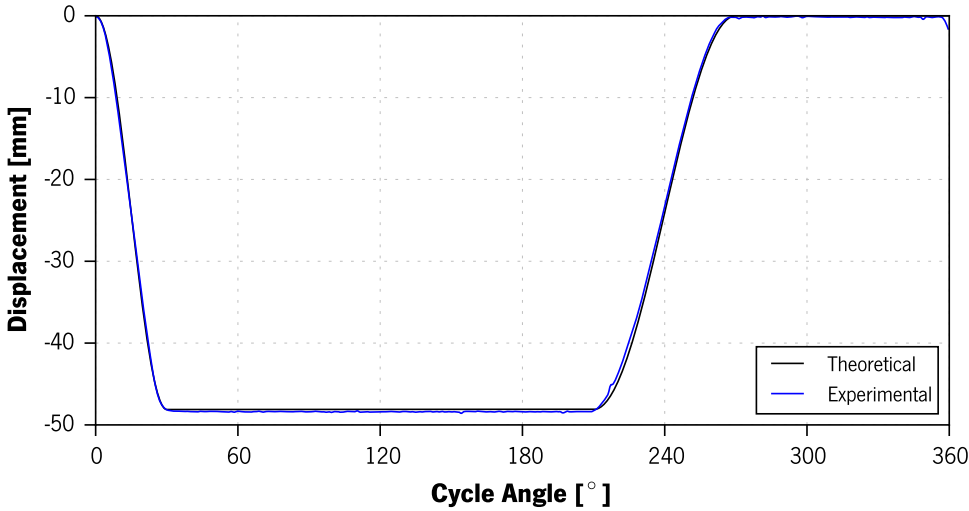
Figure 4.22: Displacement validation results from breath machine, comparing the theoretical with the experimental profiles
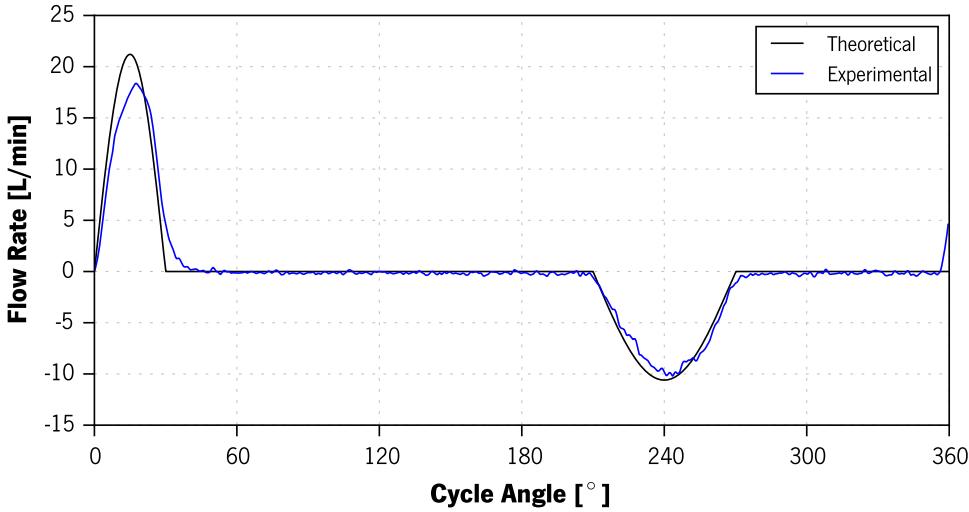
Figure 4.23: Flowrate validation results from breath machine, comparing the theoretical with the experimental profiles

5 Experimental Methodology

5.1 Experimental Test Procedure

5.1.1 Washing Procedure

Each VHC was submerged in an anionic soap aqueous solution (1:250) during one hour and left drying out for 24 hours, prior to the experimental procedure, as reported in the literature [FZ98]. This pre-treatment method was suggested by Mitchell and Nagel (2007), where the electrostatic charge in VHC devices can be mitigated (mainly in those made of non-dissipative materials) [MN07].

This procedure sets a baseline for all the different devices and reduces the inconsistency of the Total Emitted Mass (TEM), caused by accumulated electrostatic charges. A soapy bath or initial priming, are methodologies suggested by the majority of the VHC manufacturers to reduce electrostatic charges. The service actuator that was used throughout all the tests was also immersed in the soap solution, rinsed with tap water and left for drying during 24 hours, between each experimental test.

This washing procedure, executed with all the devices, was thought to mimic the regular in-house washing methodology performed by the patient. Since the main objective of the experimental study is to obtain conclusions on how device's geometric features affect the output performance, the soapy bath will nullify the influence of the material type regarding electrostatic charges.

5.1.2 Experimental Protocol

The experimental steps necessary to execute the assessment procedure at **constant flow rate** are the following:

1. Once the experimental setup parts were all connected, the vacuum system was turned on and the flow rate was set at the USP throat entrance, to the desired value. The flow rate value was marked in the rotameter (D10A11 from ABB, Switzerland) placed between the MSLI and the vacuum system.

2. The silicon universal adapter was fitted to the USP throat entrance and connected to the device (e.g. VHC + pMDI or pMDI solo).

3. The pMDI canister was shaken during 5 seconds and fired twice to waste from the pMDI original actuator.

4. Subsequently, the canister was placed in the service actuator, already attached to the VHC (or directly attached to the universal throat adapter).

5. A total of 40 puffs were made (20 puff for the case when the pMDI was tested alone), while shaking the canister for 5 seconds between each puff.

6. When the firing step was completed, the vacuum system was left running for 30 seconds period and then it was turned off. The vacuum system was disconnected from the MSLI.

7. The pMDI canister was removed from the service actuator and stored in its original package.

8. Every stage of the experimental setup was washed with 0.01M NaOH solution [Fin98] into volumetric flasks: primarily, the pMDI actuator into a 25 mL flask, then the VHC device into a 100 mL flask, the USP throat to a 50 mL flask, each MSLI stage to a 20 mL flask, and finally, the filter to a 50 mL flask. To improve the drug solubility and its release from the filter, this was placed into an ultrasonic shaker for 5 minutes.

9. Each washing solution absorbance (λ=244 nm [Fin98]) was measured three time by means of a UV-Vis spectrophotometer (UV-2401PC from Shimadzu Corporation®, Japan).

10. The concentration of each solution was estimated through the use of a calibration curve for salbutamol sulphate in 0.01M NaOH (R^2= 0.99996 from 0.01 to 2.0 abs).

11. At the end of each experiment, the MSLI was disassembled and its components were

washed with tap water, rinsed with distilled water and dried in an oven at 60 °C. The same procedure was followed for the rest of the laboratory glass material used. Silicon components were dried outside the oven.

A minimum of six repetitions of each test were performed, in order to reduce protocol errors and achieve low uncertainty.

All pMDI's were stored, horizontally, in a cool and dry closet protected from light. The sequence of steps for this procedure was implemented in Java programing language, in the form of a mobile app for Android Operating System (OS), which allowed an easy interface and helped the operator to follow the protocol closely without the possibility of any counting errors.

The determination of retained mass allowed an extensive analysis of the distribution of mass deposition for each VHC device, as well as, the drug emitted by each device and its aerodynamic characteristics. Values of the total mass collected in each test were also determined and used to evaluate the accuracy of the test. Only tests with total mass recovery (i.e. sum of mass from all zones) between 85% and 125% of the label claim were considered as valid [CZR08].

Experiments were conducted at an average temperature of 22.2 ± 0.3 °C and at an average relative humidity of 38 ± 1%, measured with a weather station (W.155 Weather station from Ventus, Denmark).

The assessment procedure at a **variable flow rate**, using a breath profile (see section 4.3.1), is described below:

1. Once the experimental setup parts were all connected, the vacuum system was turned on and the flow rate was set to 60 L/min at the USP throat entrance. The flow rate value was marked in the rotameter (D10A11 from ABB, Switzerland) placed between the MSLI and the vacuum system.

2. The compressed air source was open and, using the mass flowmeter (Model 4043 from TSI, USA), the flow rate was set to 60 L/min by adjusting the flow regulator (FCA88 from Brooks, USA).

3. The silicon universal adapter was fitted in the USP throat entrance and connected to the

assessed device (e.g. VHC + pMDI or pMDI solo).

4. By initialising the breath simulator the system was operated with the necessary waveform that was reproduced at the USP throat entrance. In some devices this could be verified by observing the valve's movement.

5. The pMDI canister was shaken during 8 seconds (i.e. duration of a full breath cycle) and fired twice to waste from the pMDI original actuator.

6. Subsequently, the canister was placed in the service actuator, previously attached to the VHC (or directly attached to the universal throat adapter).

7. A total of 40 puffs were made (20 puffs for the case where the pMDI was tested alone), by firing once per cycle at the beginning of the inhalation, while shaking the canister for 8 seconds between each puff.

8. Once the firing step was completed, the assessed device was disconnected from the universal throat adapter, the breath machine turned off, then the compressed air source shut followed by the vacuum system. The connection between the mixer and the breath machine was ceased, as well as, the vacuum system with the MSLI.

9. The pMDI canister was removed from the service actuator and stored in its original package.

10. Every stage of the experimental setup was washed with 0.01M NaOH solution [Fin98] and the liquid collected into volumetric flasks: primarily, the pMDI actuator into a 25 mL flask, then the VHC device into a 100 mL flask, the USP throat to a 50 mL flask, the Mixer to a 50 mL flask, each MSLI stages to a 20 mL flask, and finally, the filter to 50 mL flask. To improve the drug solubility and its release from the filter, this was previously placed into an ultrasonic shaker for 5 minutes.

11. Followed by steps 9 through 11 such as with constant flow rate procedure.

5.2 UV-Vis Spectrophotometry Analysis

Spectrophotometry is the interaction between light (i.e. electromagnetic radiation) and matter. A photon is composed by both an electric (E) and a magnetic fields (M), oscillating perpendicularly to each other. Wavelength (λ) is a characteristic of these fields, and it quantifies the distance between

two wave peaks (measured in an adequate unit). The electromagnetic spectrum is composed by a set of wavelengths ranging from radio (large wavelengths with low energy) to gamma ray waves (small wavelengths with high energy).

There are several types of analytical spectroscopy: absorption, fluorescence, emission and reflection. The focus is on the absorption spectroscopy that quantifies the amount of electromagnetic radiation absorbed by the matter, more specifically that within the UV wavelength range (185 - 400 nm).

At room temperature, the molecules of a certain substance are at the lowest energy levels (E_0) but when those molecules absorb UV light from electromagnetic radiation wave, the outmost pair of electrons is raised to a higher energy level state (E_n). The difference between these energy states is known as electronic transition (δE) [PLK01].

As a solution is crossed by a monochromatic radiation, the decrease in the incident radiation intensity is directly proportional to the thickness of the illuminated solution (i.e. Lambert's law). This means that each solution layer (with equal thickness) absorbs the same amount of energy. Beer's law states that the energy absorbed by a solution with fixed thickness, is proportionally related to its concentration [PLK01].

Beer-Lambert law is the main mathematical principle of absorption spectroscopy and it is described by Equation 5.1:

$$A = \varepsilon \cdot C \cdot l \qquad\qquad (5.1)$$

Considering:

A – absorbance $[-]$

ε – molar absorptivity $[dm^3 \cdot mol^{-1} \cdot cm^{-1}]$

C – concentration of substance $[mol \cdot dm^{-3}]$

l – thickness of solution $[cm]$

Each chemical structure of a substance has a specific absorbance spectrum, due to the distinct bonds present in the structure. In a solution form, the drug structure is dissolved in a solvent, which contributes to a modification of the drug structure that causes a shift in the absorbance

peak shift. There are four main types of peak shifts: bathochromic, hypsochromic, hyperchromic and hypochromic (see Figure 5.1) [PLK01].

Bathochromic shift (also known as red shift) is a movement of the absorbance spectrum from short to longer wavelength, caused by the addition of a change of the solvent with an auxochrome group (i.e. –OH, -OCH3).

Hypsochromic shift (also known as blue shift) is a movement of the absorbance spectrum from long to shorter wavelength, caused by the addition of a change of the solvent with an acidic medium.

Hyperchromic shift is characterised by an increase in the absorption intensity (ε), due to an introduction of the auxochrome compound in the drug structure.

Hypochromic shift is characterised by a reduction in the absorption intensity (ε), due to a removal of the auxochrome compound from the drug structure.
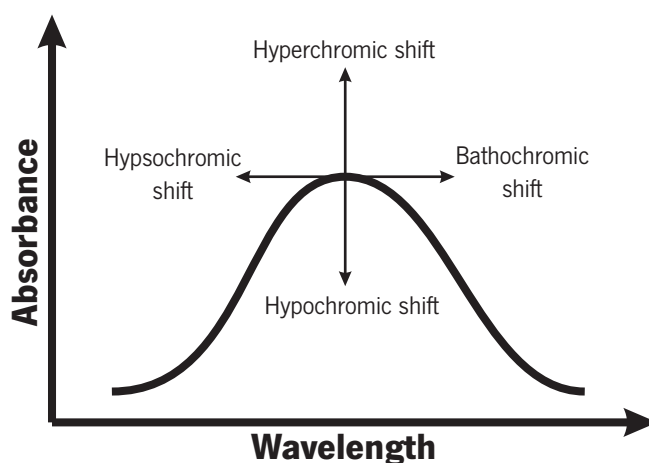
Figure 5.1: Representation of the possible absorbance peak shifts

The drug salbutamol sulphate concentration is quantified by absorption spectroscopy. The European Pharmacopeia describes a procedure to analyse this substance under absorption spectroscopy, which consists in a preparation of an acid solution (i.e. HCl) that will have an optimum peak at 276 nm.

Because such solvents are not easy to obtain and handle, an alternative procedure, given in literature, was explored. Firstly, distilled water was used as solvent which lead to fluctuations on solution pH and peak shifts. A solution of 0.01M NaOH (Eka Pellets from AkzoNobel, Sweden) was

prepared, accordingly to literature [FZ98, Fin98], and its pH value was controlled by measurements (micropH 2000 from Crison, Spain) for each 6 L batches (showing 11.29 ± 0.05). It shows a maximum absorbance peak at 244 nm, and the results (see Figure 5.2) show bathochromic and hyperchromic shifts.

Figure 5.2: Absorbance spectrum comparison of salbutamol sulphate dissolved in distilled water and in 0.01M NaOH solution
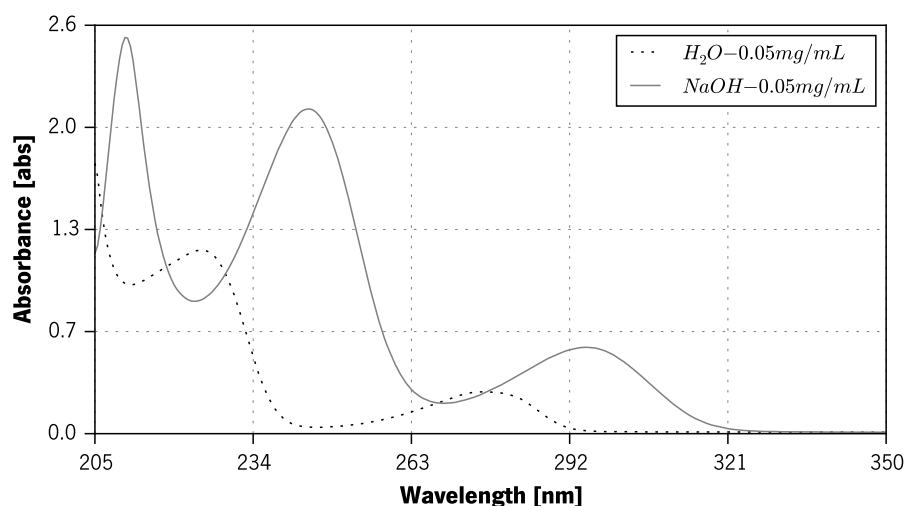
The measurements were carried out in a UV-Vis spectrophotometer (UV-2401PC from Shimadzu Corporation®, Japan) with double beam in space, which allows the direct comparison between a reference cuvette and a sample cuvette (see Figure 5.3).

The radiation is originated from two possible sources (λ = 160 – 375 nm): a halogen lamp and a deuterium lamp. The mirror rotation or lamp mount allows the selection of the lamp source that goes into the monochromator. The latter is composed by an entrance slit, a collimating lens, a diffraction grating (which causes the dispersion of the light in a discretized spectrum), a focusing lens and an exit slit. Whereas, by adjustment of the lens position, only the desired wavelength pass through the exit slit. The monochromatic beam passes through a beam splitter that divides it into two identical beams. Each one crosses a cuvette measurement slot (whereas a sample is positioned). Afterwards, both beams are steered to a photomultiplier detector, for differential comparison of light intensity between the reference and sample. The resulting data is processed
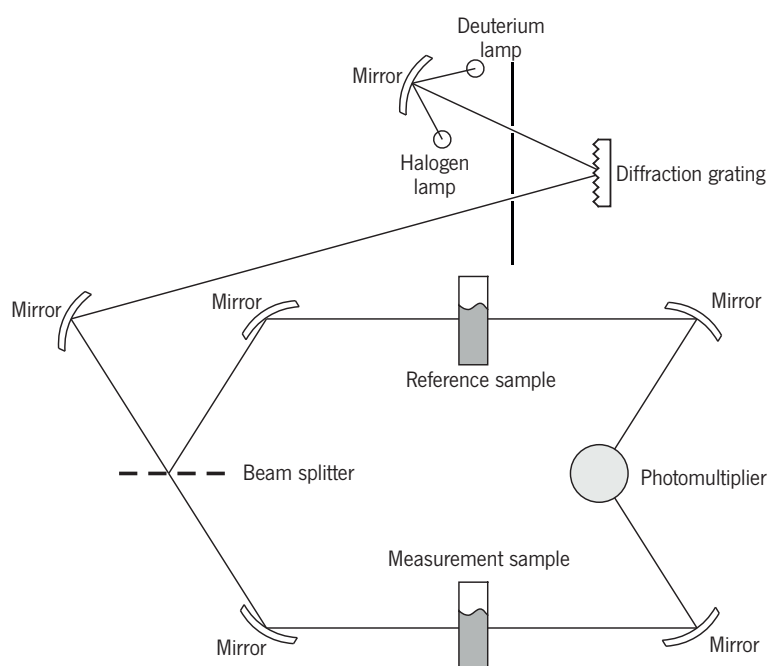
Figure 5.3: Simplified schematic of the UV-Vis spectrophotometer optical system

by computer software that provides the absorbance values, also allowing a spectrum range scan of the sample substance [Shi97].

The cuvette (or sample cell) for the UV analysis, needs to be transparent to the wavelength range of analysis, being quartz, the material of choice. A pair of cuvettes with calibrated path length is important for a precise analysis, and its selection should be made accordingly to the amount of sample available and to the equipment slot size. Cuvettes with longer path length are used for increasing the measured absorbance (accordingly to Equation 5.1).

5.2.1 Measurement Protocol

The measurement protocol is composed by various steps that were defined by combining several tests for a stable measurement methodology, and the equipment operating manual:

1. Turn on the UV-Vis equipment and the computer for data acquisition

2. Wait during 15 min for the equipment lamp to heat up and stabilizes

3. Setup the measurement software to the desired method and wavelength interval of scanning

(i.e. 220 nm to 270 nm)

4. Put on latex gloves

5. Rinse twice both cuvettes (10 mm quartz vol. = 3.5 mL from Zuzi) with 0.01M NaOH solution

6. Fill both cuvettes with 0.01M NaOH solution and place them into the sample and the reference equipment slots

7. Execute a measurement for a reference baseline

8. Remove the sample cuvette and drain it to waste

9. Shake the measurement solution flask for a 1 minute period to improve homogenisation of the solution.

10. Pour a sample into the cuvette and empty it to waste. Now pour again into the cuvette, clean any droplets in the cuvette surfaces with laboratory soft paper, and place it into the equipment measurement sample slot.

11. Take a measurement and save data through the data acquisition software

12. Repeat twice steps 8 through 11

13. Empty the cuvette

14. Rinse with 0.01M NaOH solution and empty it three times

15. Repeat the steps 8 through 14 for all unknown solutions

16. Turn off the equipment

The data were exported to .txt format files and the obtained curves were processed using a Python code script. Each measurement curve was read and the averaged (of the three measurements) absorbance value at 244 nm was calculated along with its corresponding error (halve of the amplitude). The calibration curve parameters provided the means to obtain the corresponding concentrations. Each solution concentration was then multiplied by the flask volume and the mass was calculated.

These new data were saved to a file, whereas the setup stage name was included as well as its salbutamol mass, number of puffs executed, total mass expected and total mass collected.

5.2.2   Calibration Curve

A calibration curve is necessary for the calculation of the salbutamol sulphate drug concentration in each solution was assessed UV-Vis absorption spectrophotometry. Since this assessment method provides us with an absorption value at a certain light wavelength for a given unknown concentration solution, it was necessary to get a calibration curve that relates the concentration with the absorbance. To create such calibration curve, it was firstly necessary to create a stock concentration solution that gave origin to several diluted solutions of smaller concentration. This stock concentration solution was created by dissolving 99 mg of salbutamol sulphate into 1000 mL of 0.01M NaOH, giving origin to a concentration of 0.099 mg/mL. This solution was then diluted into 13 smaller concentration solutions with concentrations that allowed the points to be equally spaced over the range of interest. The measurement of the solutions was repeated three times and the values of absorbance are shown in Figure 5.4. It shows the absorbance curve, for each solution, along a span of light wavelength. The experimental uncertainty is represented as error bars for each measurement point that compose each solution curve. It can be seen that no error is found within the measured curves, which point to a well-executed measurement technique. The wavelength value of 244 nm was selected; therefore those values will be used to create the calibration curve, shown in Figure 5.5, along with the linear fitting parameters which were calculated by least-squares method. The goodness of fit value is very high (i.e. R^2 = 0.9999), which indicates that a fair amount of linearity is found between the 0.009 and 1.844 of absorbance. Hence, it is valid to use this curve for unknown concentration solutions with absorbance values within this interval. This linear assumption allowed the calculation of the curve characteristics (i.e. A - slop and B – y-intercept), that will be used in the determination of the concentration form an absorbance measurement of unknown solutions from the setup stages.
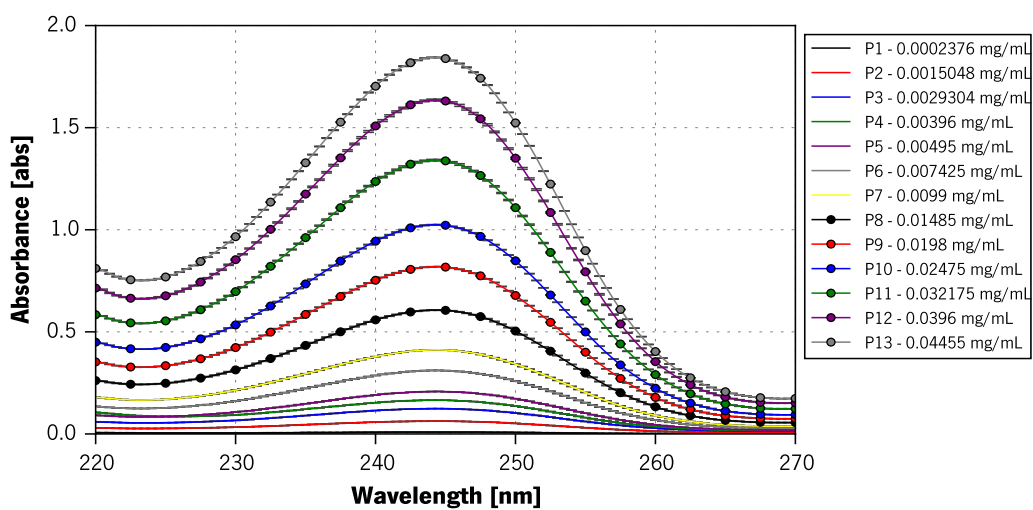
Figure 5.4: Absorbance values obtained for the calibration curve solutions, including the experimental uncertainty represented as error bars
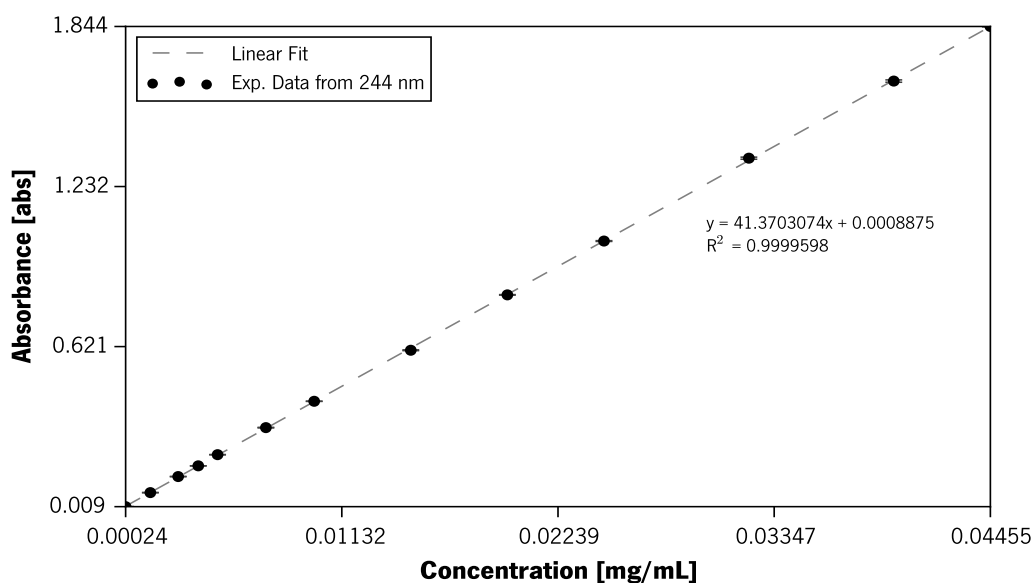

Figure 5.5: Calibration curve used for concentration determination from known absorbance values at 244 nm of light wavelength for salbutamol sulphate in 0.01M NaOH solution. Linear fit parameters are represented, along with the goodness of fit value

5.3   Data analysis

Data analyses were performed using Excel® (Office 2010 from Microsoft, USA). The mass collected in each solution was divided by the numbers of injected puffs. The following subsections explain in detail the procedures for data treatment and mathematical operations used for data treatment and presentation in the results section.

5.3.1   Uncertainty Analysis

Whenever the word "error" is employed, it actually means uncertainty. These errors are not mistakes and cannot be eliminated by being very careful during the measurement procedure. The uncertainty is inevitable in all process of data gathering and sometimes are found to be random or systematic (even both). The best that can be done is to estimate the uncertainty of our measurements to the best of our knowledge. For that, several rules can be applied, most of them are fairly well described in various literature sources. In the case of estimating the uncertainty of experimental measurements John R. Taylor [Tay97] provides very good and intuitive guidelines on how to deal with this matter.

By repeating the measurements, the uncertainty caused by random errors can be discovered; those that cannot are known as systematic errors. Systematic errors are hard to find, and sometimes expensive to eliminate. Usually they are originated in the usage of equipment with bad calibration (e.g. the case of a ruler that suffered a stretching deformation). That can only be verified by changing the equipment with a new/improved one. Also systematic operator wrong measurement procedure can be a cause of a systematic error (e.g. parallax error by always looking on the same wrong side of the equipment scale). Random errors can be caused by sudden power break that leads to a failure in data gathering, mechanical vibrations, badly positioned equipment that caused an unexpected flow leakage, parallax error that randomly overestimates and underestimated the manometer needle. These errors can easily be spotted by repeating the measurement several times, which eventually will cause them to be cancelled.

The most famous schematic example to describe the comparison between random and systematic

errors is the target practice board described in Figure 5.6. Whereas the shooting board centre stands for the true value, a shooter aim can be within four scenarios:

- (a) high precision (with small systematic error) and high accuracy (with small random error);
- (b) low precision (with large systematic error) and high accuracy (with small random error);
- (c) high precision (with small systematic error) and low accuracy (with large random error);
- (d) low precision (with large systematic error) and low accuracy (with large random error).
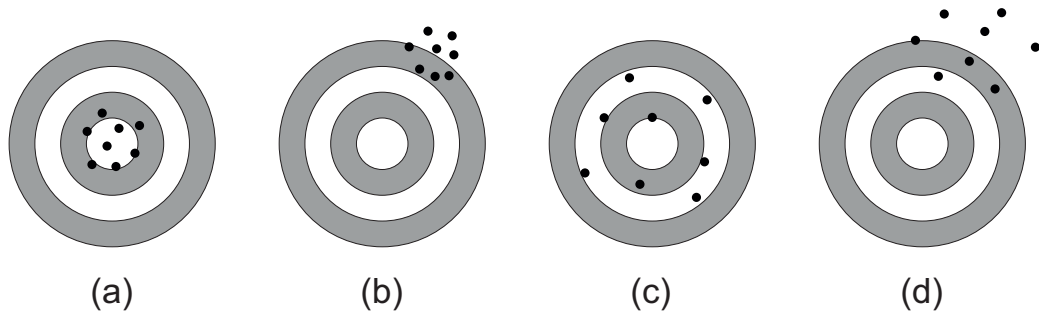

Figure 5.6: Comparison between the random and systematic errors, using the example of target practicing

In the experimental activity, measurements are only performed because the true value of a quantity is unknown. Therefore if Figure 5.6 is visualized without the board, there is no way to be aware of the existence of systematic errors neither their size.

The correct notification for presenting a measured value is given by the best estimate followed by the uncertainty (δx) (see Equation 5.2).

$$x = x_{best} \pm \delta x \tag{5.2}$$

The calculation of the uncertainty, in a single measurement, is usually defined by halving the difference between the two closest numbers (bellow and above) that can be evaluated with some degree of certainty. This means that the value is found between $x_{best} + \delta x$ and $x_{best} - \delta x$.

The calculation of the uncertainty from various measurements is calculated by the Standard Deviation Of the Mean (SDOM), described in Equation 5.3.

$$\sigma_{\bar{x}} = \frac{\sigma_x}{\sqrt{N}} \tag{5.3}$$

Whereas the N stands for size of the sample and the σ_x for the sample standard deviation (see Equation 5.4). The sample standard deviation is preferable in comparison to the population standard deviation, since it is more accurate for small values of N.

$$\sigma_x = \sqrt{\frac{1}{N-1}\sum\left(x_i - \bar{x}\right)^2} \tag{5.4}$$

considering the i as the ith measurement in the sample. The standard deviation provides us with 68% confidence that any measurement will fall within $x_{best} + \sigma_x$ and $x_{best} - \sigma_x$.

Accordingly to the American Society of Mechanical Engineers (ASME) guidelines for test uncertainty in instruments and apparatus [ASM98], it is advisable that the results are presented with a uncertainty for a 95% confidence interval. Therefore, an expanded uncertainty should be calculated through the multiplication of the SDOM by a expansion factor (B) (see Equation 5.5). This factor is obtained by means of a t-student distribution for 95% and using the Degrees Of Freedom (DOF) (i.e. $DOF = N - 1$).

$$\delta x = \sigma_{\bar{x}} \cdot B \tag{5.5}$$

B - expansion coefficient

Concluding, the presented experimental data uncertainty was calculated by following two simple rules, accordingly to the size of N:

- $2 \leqslant N < 5 : \delta x = \left(max_x - min_x\right)/2$;
- $N \geq 5 : \delta x = \sigma_{\bar{x}} \cdot B$.

Whenever it is necessary to combine two or more $(x, ..., z)$ measurable variables (each with its own uncertainty $\delta x, ..., \delta z$) in an equation (q), an general formula (see Equation 5.6) can be applied to calculate the propagation of the uncertainty (δq).

$$\delta q = \sqrt{\left(\frac{\partial q}{\partial x}\delta x\right)^2 + \cdots + \left(\frac{\partial q}{\partial z}\delta z\right)^2} \tag{5.6}$$

5.3.2 Statistical Significance Analysis

Data were composed by two types of variables: nominal and measurement. Nominal variables are such as Valve Design Type or Name of the Device. Measurement variables are all the other used, from throat deposition to the performance metrics.

Statistical analysis (SPSS v21.0 from IBM, USA) is performed upon the reported data whenever is needed for a comparison between two or more experimental data sets. The test of choice was the one-way Analysis Of Variance (ANOVA). This statistical test is adequate with one nominal variable and one measurement variable. Its null hypothesis states that the means of the measurement variable are the same for all the different data sets. As example: is the mean throat deposition the same for all VHC devices tested? One-way ANOVA will evaluate the null hypothesis and consider it false if the P value is lower than 0.05.

This test is based in some assumptions:

- Data within each group are normally distributed
  - The number of observations made is not big enough for this criterion to be met with certainty. Although it has been reported that the one-way ANOVA is not very sensible to deviations from the normality distributions [McD14].
- The data are homoscedastic (i.e. have similar standard deviation in the data sets)
  - One-way ANOVA is not very sensitive to heteroscedasticity, unless the size of the data sets is very different from each other. Given that the data sets have $N < 10$ and that some of them have large standard deviations, the Welch's ANOVA test was applied to these cases distributions [McD14].

5.3.3 Devices Performance Analysis

The analysis of the experimental data was carried out in terms of indices that compare the efficiency of the VHC in comparison to the use of pMDI solo. The procedure for the calculation of such indices is presented below. The formulae described originates in the US Pharmacopeial Forum as a stimulus for the USP revision: <1602> Spacers and valved holding chambers used with

inhalation aerosols (USP38-NF33) [US 14].

The TEM by the device, is the sum of the drug mass present in all zones of the setup downstream the device under testing. This includes the throat and all the stages of the impactor.

The FPM is the amount of mass present in the stages of the impactor with cut-off point below μm. In the case that no stage cut-off point coincides with the 5 μm value, it is necessary to proceed with the construction of the cumulative mass-weighted Aerodynamic Particle Size Distribution (APSD) and interpolate it from there. That was the case for the impactor used in this study.

The Coarse Particle Mass (CPM) is calculated as the difference between the TEM and the FPM. This assumes that the mass in the throat is all composed by coarse particles. Although it is not a fully correct assumption, it is considered as acceptable.

The Extra-Fine Particle Mass (EFPM) is calculated as the mass of particles bellow 1 μm of diameter. The procedure for the calculation was similar to the one used for the FPM calculation.

The Coarse Particle Fraction (CPF) is calculated in percentage according to Equation 5.7.

$$CPF = \left[\frac{CPM}{TEM} \right] \times 100 \tag{5.7}$$

Equation 5.8 presents the calculation of the Fine Particle Fraction (FPF) in percentage.

$$FPF = \left[\frac{FPM}{TEM} \right] \times 100 \tag{5.8}$$

The Extra-Fine Particle Fraction (EFPF) is given by Equation 5.9:

$$EFPF = \left[\frac{EFPM}{TEM} \right] \times 100 \tag{5.9}$$

The guidelines state that a properly functioning VHC shall have its FPF value above 60%, and CPF below 40%. The EFPF is strongly related to the drug formulation APSD, however its value can vary from < 20% to 50% FPF.

Three indices are used to evaluate the use of a VHC when compared to a pMDI solo. These ratios compare the coarse mass (Rc), fine mass (Rf) and extra-fine mass (Re), and they are presented

from Equation 5.10 to 5.12.

$$Rc = \frac{\text{CPM}_{VHC}}{\text{CPM}_{MDI}} \qquad (5.10)$$

$$Rf = \frac{\text{FPM}_{VHC}}{\text{FPM}_{MDI}} \qquad (5.11)$$

$$Re = \frac{\text{EPM}_{VHC}}{\text{EPM}_{MDI}} \qquad (5.12)$$

A properly functioning VHC shall operate within an Rc ≤ 0.6 and with both Rf and Re close to 1.0.

This page was intentionally left in blank

6 Experimental Results

In this chapter, the obtained experimental results from the pMDI solo or attached to a VHC device are presented and discussed. The tests were executed using a Full Dose setup and a Cascade Impactor (i.e. MSLI) setup. The influence of air flow rate in the devices performance was assessed at 30 L/min, 60 L/min and using a Breath Profile. The raw data is given by Tables B.1 to B.5. Several performance metrics were used to make different conclusions about the device's performance and their relationship with the geometric features.

6.1 Full Dose Results

6.1.1 Constant Flow Rate (30 L/min)

Full Dose mass collection results at constant flow rate of 30 L/min are depicted in Figure 6.1, along with the 95% confidence uncertainty represented in form of error bars. Mass was captured in a MN 1674 paper filter, enclosed in the house-made aluminium filter casing. Detailed information regarding the experimental setup can be found in section 4.1.1).

The mass deposition on the pMDI actuator appears to have a constant value of approximately 10 µg. Throat (i.e. filter casing) and filter deposition is greatly reduced by the usage of the pMDI combined with a VHC. Some VHC devices present greater reduction than others: Nebuchamber, Optichamber and Vortex (devices with the duck type valve) show higher throat deposition. As the

air flow downstream the VHC valve is greatly dependent on the valve design, a duck type valve might lead to higher velocities, which causes, instabilities in the flow (such as turbulence), resulting in higher wall deposition.
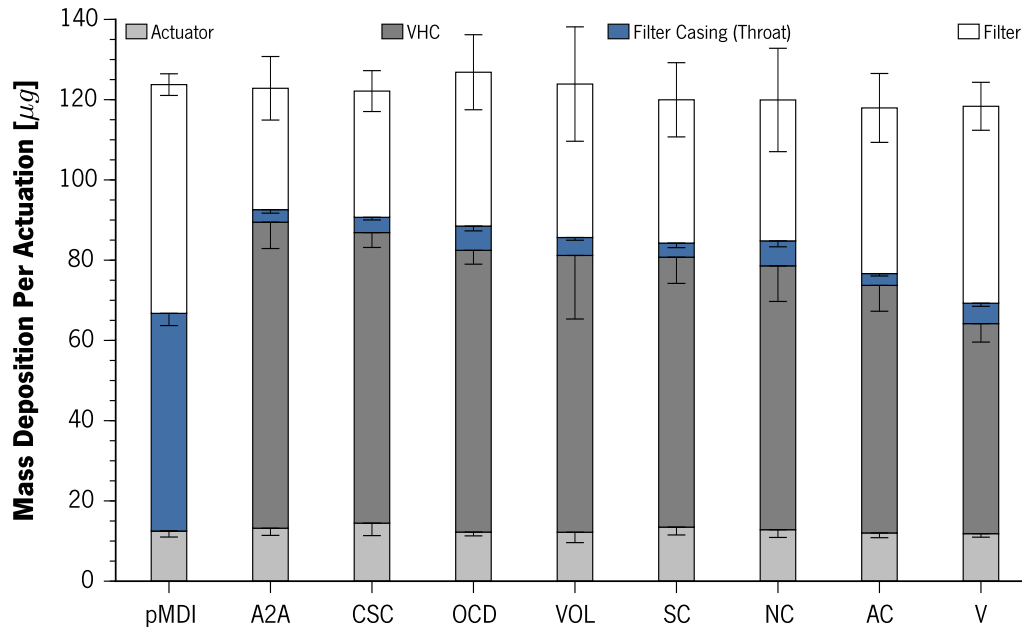

Figure 6.1: Salbutamol deposition mass (normalised for one actuation) in each setup zone for all tested devices at 30 L/min

6.1.2 Breath Pattern

The full dose emitted by the VHC devices when exposed to a breath pattern (described in section 4.3.1) is presented in Figure 6.2. The setup used in fully described in section 4.1.1.

Mass deposition in the pMDI actuator shows a value of approximately 20 µg, which is twice that observed for a constant air flow of 30 L/min. This is an expected behaviour, since the air flow is not in steady state, a higher amount of mass sediments on it. Throat (i.e. filter casing) and filter is lower under a breath pattern than at constant flow rate. However, a higher throat deposition can be found for duck type valved devices, which suggests that this effect is independent of the flow rate.
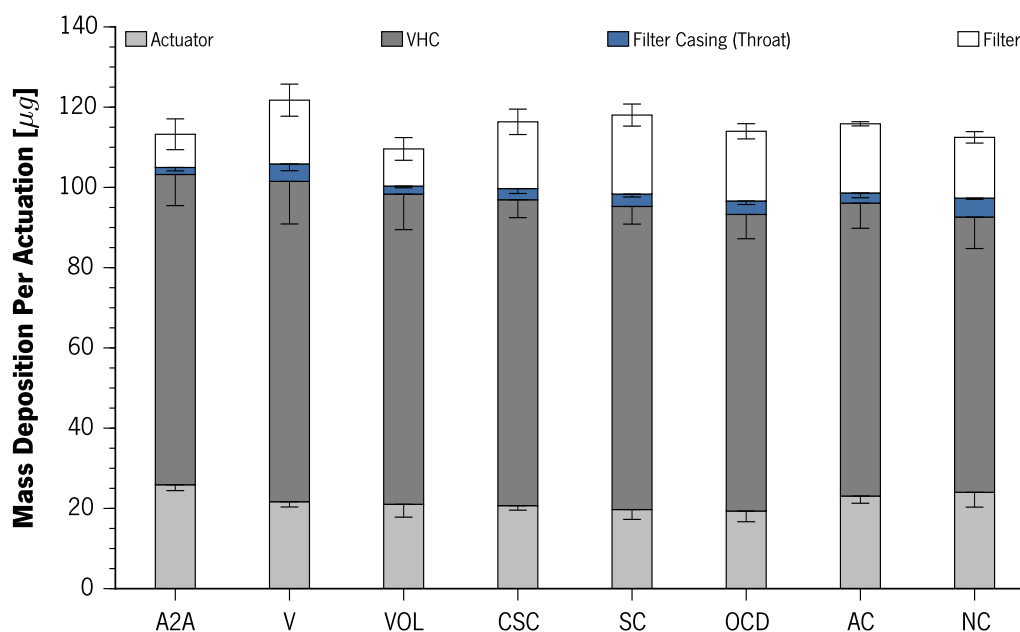
Figure 6.2: Salbutamol deposition mass (normalised for one actuation) in each setup zone for all tested devices under a breath pattern

6.2 Cascade Impactor Results

6.2.1 Constant Flow Rate (30 L/min)

Results for the mass deposition using a constant flow setup (described in section 4.1.2) at 30 L/min are shown in Figure 6.3.

Actuator deposition is approximately 10 µg for all tested devices, with no statistical differences between the devices (p>0.05). Analysing the TEM it is obvious that the pMDI solo emits a higher amount of mass than the other devices (p<0.0001). However no statistical significant differences were found between the VHC devices (p>0.05).

The usage of a VHC greatly reduces the mass deposition in the throat (i.e. induction port), which is one of the main objectives of the VHC device. Some VHC devices are better at this function than others (p<0.0001), as shown in Figure 6.4, where the percentage reduction of mass throat deposition in comparison to pMDI solo usage is presented.
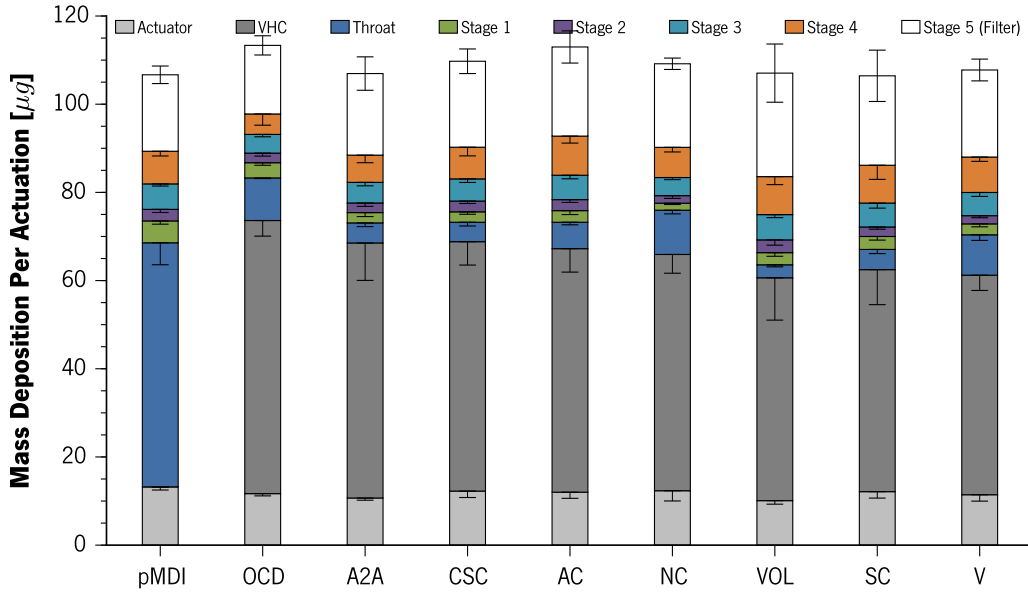
Figure 6.3: Salbutamol deposition mass (normalised for one actuation) in each setup zone for all tested devices at 30 L/min using the MSLI. Error bars indicates the limits of the uncertainty within a 95% confidence interval
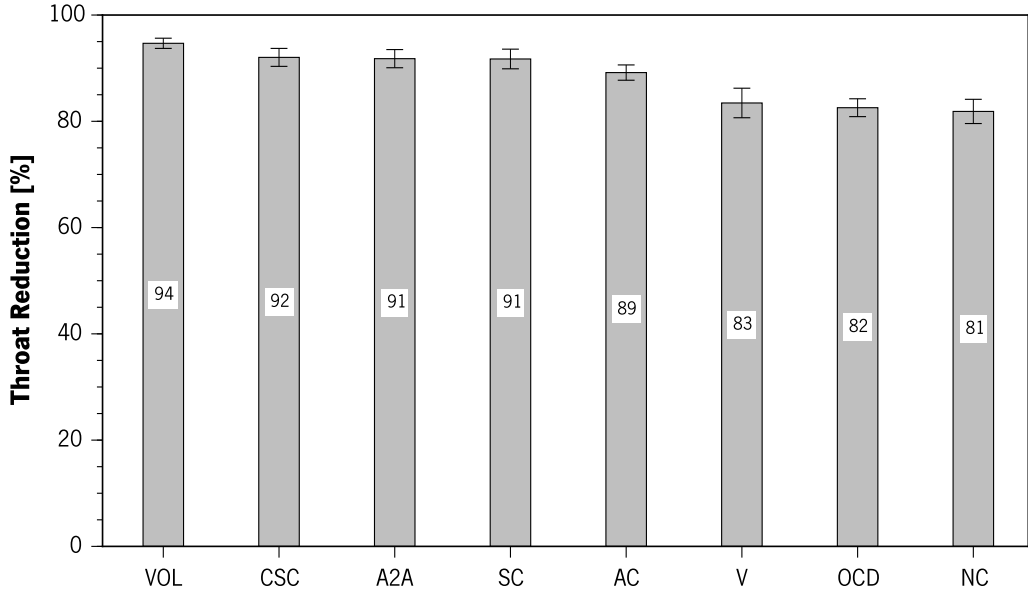

Figure 6.4: Percentage reduction in mass throat deposition in comparison with the pMDI solo at 30 L/min. Error bars indicates the limits of the uncertainty within a 95% confidence interval

Deposition of salbutamol in the throat is reduced between 95% and 82% when the pMDI is used coupled to a VHC. The Nebuchamber, Optichamber and Vortex have the lowest reduction (all devices from Duck valve type group, p>0.05), while the highest reduction is found for Volumatic (Coin type valve), followed by the Leaflets valve type devices (p>0.05) and the Aerochamber (Annulus Flap valve type). The results suggest that throat deposition is highly related to the valve type, whereas statistical significant differences were found between all valve type groups (p<0.05).

Using the MSLI 4 last stages (i.e. 2nd to 5th stage), the sum of these masses corresponds to the Sizable Mass (SM) in the impactor. Cumulative fractions were then calculated by incrementally add the mass in the stages (starting on the 5th) and dividing it by the SM. The cumulative mass fraction chart is created by plotting these fractions against the cut-off particle aerodynamic diameters of each corresponding stage (see Figure 6.5). The procedure for creating such graph is fully described in Pharmacopeia and referenced in section 5.3.3.
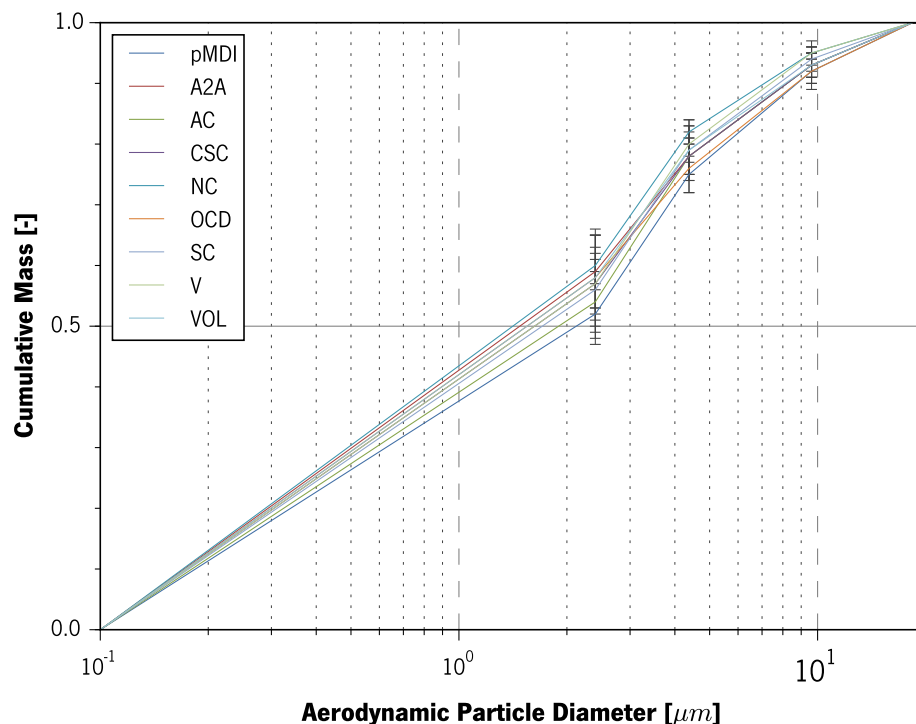

Figure 6.5: Cumulative mass fraction versus the aerodynamic particle diameter for tested devices at 30 L/min. Error bars indicates the limits of the uncertainty within a 95% confidence interval

Figure 6.5 allows to conclude that, for pMDI emitted plume, approximately 50% of the SM is composed by particles with aerodynamic diameter below 2.4 μm. As shown in Figure 6.5, the usage of any VHC coupled to the pMDI increases the fraction of particles lower than 2.4 μm available to the patient. These values were normalised for each device SM emitted.

The fine particles (i.e. 4.7 μm) mass fraction was interpolated from those curves and then multiplied by the corresponding SM value, giving the FPM emitted. The results are depicted in Figure 6.6.
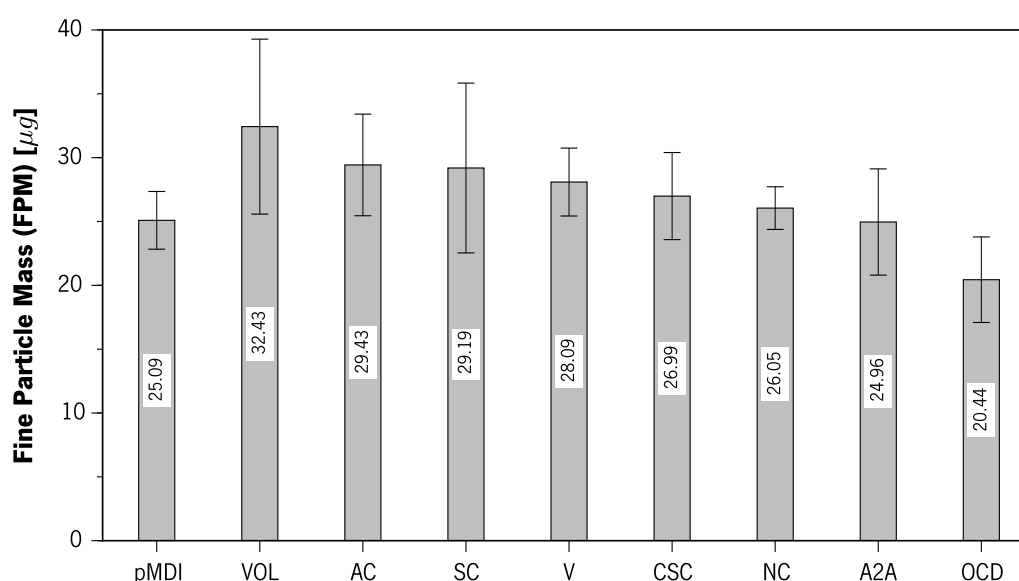

Figure 6.6: Emitted FPM at 30 L/min for the devices various. Error bars indicate the experimental uncertainty for 95% confidence intervals

It is evident that using a VHC coupled to the pMDI is an advantage to the patient inhalation treatment, because it provides an increase of the FPM in comparison to the use of pMDI solo, except for Optichamber and A2A. The FPM emitted from the VHC devices shows no statistically significant differences (p>0.05) when compared to the pMDI solo. There is not statistical evidence that valve type is related to the emitted FPM at 30 L/min (p>0.05).

The values of the MMAD can be determined by interpolation of the cumulative fraction curves. It represents the aerodynamic diameter at which 50% of the SM is found. Results for the calculated
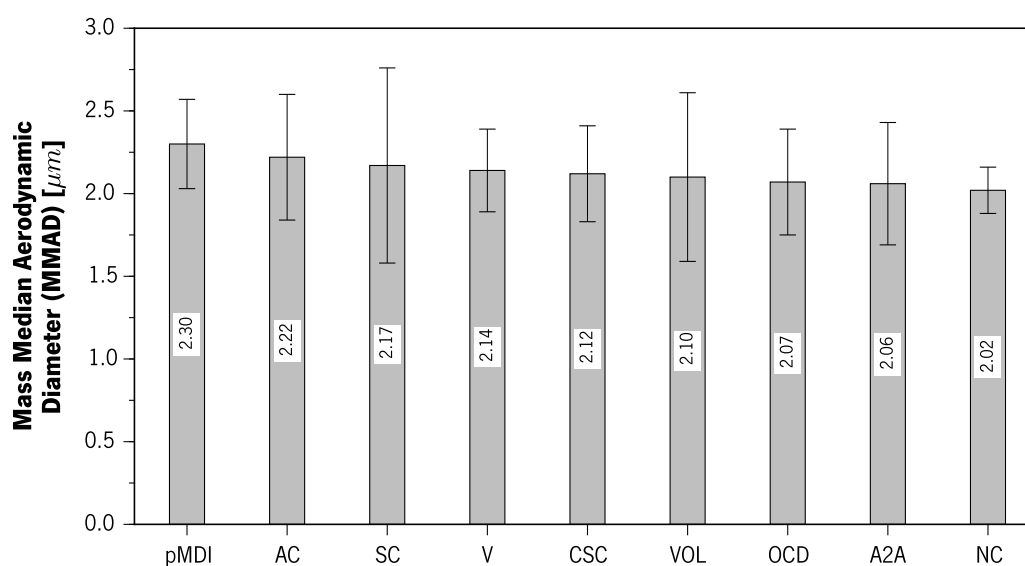
146

MMAD are given in Figure 6.7.

Figure 6.7: Emitted plume MMAD at 30 L/min for the tested devices. Error bars indicate the experimental uncertainty for 95% confidence intervals

The results show a slightly reduction of the plume aerodynamic size when using a VHC in comparison to the pMDI solo. This observation suggests that the VHC design is capable of reducing the plume coarse fraction. However this impactor apparatus (i.e. MSLI), being constituted by 5 stages, does not allow a very accurate assessment of this metric, whereas the interpolation was calculated between an experimental and an assumed value (i.e. of zero for particles lower than 0.1 μm). The MMAD emitted from the pMDI solo is statistically different from the A2A Spacer ($p<0.05$) and from the Nebuchamber ($p<0.01$), while no statistical differences were found between the other devices ($p>0.05$).

FPF is the ratio of FPM in relation to the TEM for each device and the same procedure is done for the EFPF by using the ratio of EFPM. Those metrics allow to evaluate the amount of fine particles in the emitted plume mass (the guidelines advise its value (for VHC's) to be above 60%). EFPF is related to the drug formulation itself and its value shall be between 20% FPF and 50% FPF. The results for CPF are not depicted in Figure 6.8, because this metric is complementary to the FPF. The FPF and EFPF metrics are above 60% for all VHC with the exception for the Optichamber. The

highest FPF value is found for the Volumatic (69.9%) and the lowest for the Optichamber (51.5%). EFPF metrics are between 27% and 30% of its corresponding FPF value. pMDI solo shows a FPF value of approximately 27%, hence the pMDI solo has lower fraction of fine particles in its emitted plume than pMDI coupled with VHC ($p<0.0001$). This indicates that VHC emitted plume has a lower amount of coarse particles than it has of fine particles. Therefore the VHC accomplish well its objective in reducing the coarse fraction. Devices within the Leaflets valve type group show no statistically significant differences ($p>0.05$). However, the Optichamber FPF is distinct from the other VHC devices ($p<0.05$). There is no statistical evidence suggesting that the valve type is correlated with the FPF ($p>0.05$). Figure 6.8 depicts the FPF and EFPF.
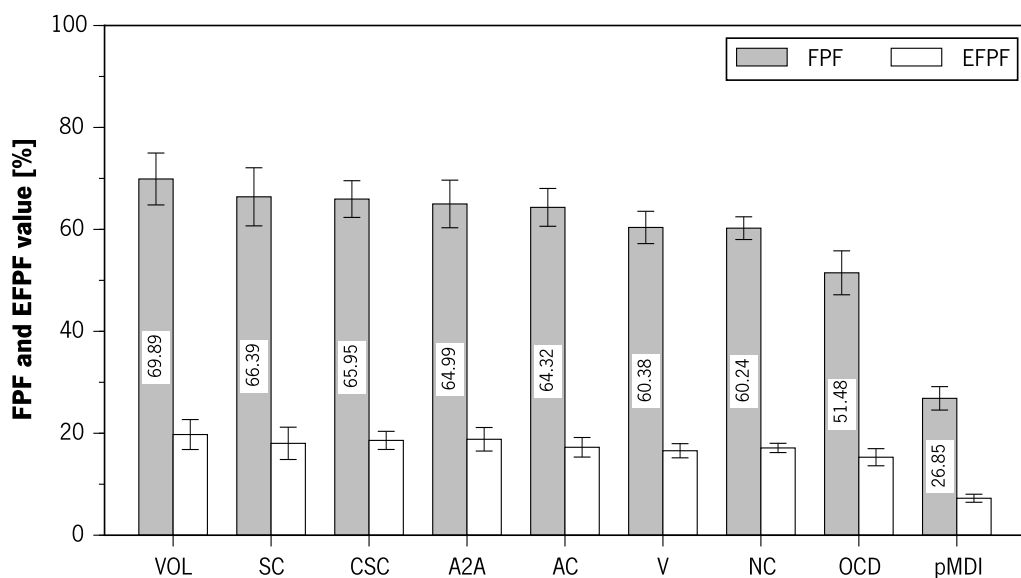

Figure 6.8: FPF and EFPF metrics of the emitted plume for each tested device at 30 L/min. Error bars indicate the experimental uncertainty for 95% confidence intervals

Given the CPM, calculated by section 5.3.3, Rc can be assessed of how much CPM reduction is due to the VHC use instead of pMDI solo. Results are depicted in Figure 6.9.

The guideline reference value for Rc should be lower than 0.3, which is observable for all tested VHC devices. These results assures that all the tested devices are in agreement with the guidelines, and they are able to reduce the coarse fraction by more than 70% in comparison with the solo pMDI usage. The Volumatic has the best capacity to reduce the CPM of the emitted plume, which

might be related to the large inner surface area when compared to the other devices. Also the Coin type valve, in Volumatic, contributes to the high reduction of coarse particles by acting as a bluff body for the air and particles stream flow. The Optichamber is the VHC with the lowest capacity to reduce the coarse fraction of the plume, along with the Vortex and Nebuchamber (all three devices have the Duck type valve, $p>0.05$). No statistically significant differences were found between the Leaflets valve type devices regarding the Rc metric ($p>0.05$). The results suggest that valve type design greatly affects the coarse particle reduction, which can be ranked as: Coin > Leaflets > Annulus Flap > Duck. The Duck type valve devices have significant differences ($p<0.0001$), in comparison to the other valve groups ($p>0.05$).
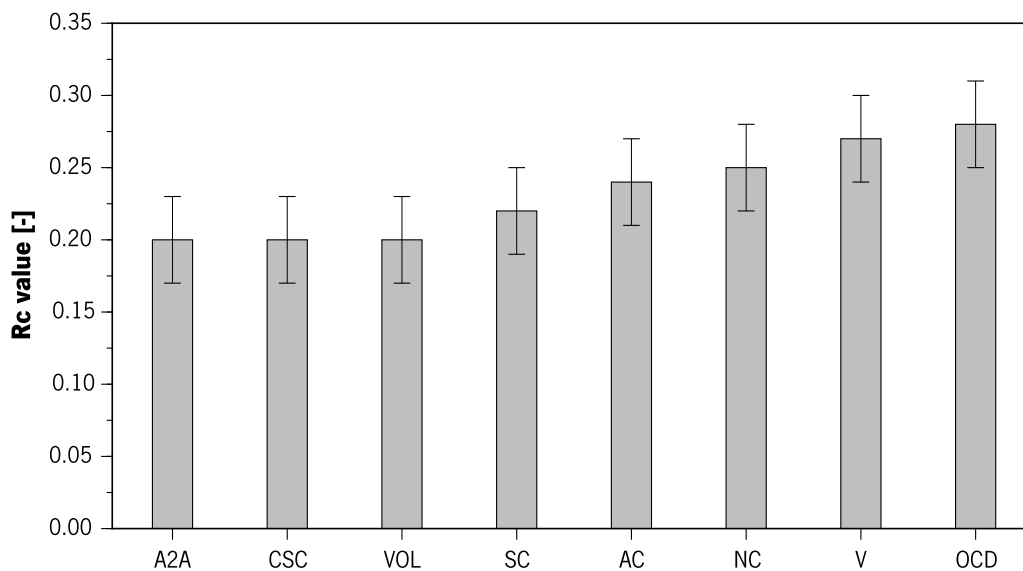

Figure 6.9: Coarse fraction reduction metric (Rc) results at 30 L/min for the tested devices. Error bars indicate the experimental uncertainty for 95% confidence intervals

The increase of FPM and EFPM in comparison to the pMDI solo is assessed through Rf and Re metrics, correspondingly. Results are shown in Figure 6.10.

The guidelines recommend that Rf and Re should be approximately 1.0, which means that using the VHC do not greatly affect the amount of FPM and EFPM available to the patient in comparison to the pMDI plume. The main reason for this guideline is that a VHC device coupled to a pMDI has to be bioequivalence to the pMDI solo. Meaning that if the VHC greatly increases the amount of

FPM to the patient, different therapeutic dosage will be delivered which can cause adverse effects [SM14]. This would require that the VHC plus pMDI and formulation to go under reassessment and recertification to be put again in the market. However, VHC act as a add-on device for the commercial pMDI's, has a simpler certification process. Results of Rf and Re are found to be between 0.8 and 1.3. All VHC devices have a similar output (p>0.05); however the Volumatic has the highest values and the Optichamber the lowest, whose comparison is statistically meaningful (p<0.05). All VHC devices increase (from 4% to 29%) the FPM in comparison to the pMDI solo, except for the Optichamber that reduces its value in 20% and the A2A Spacer that does not provide any change.
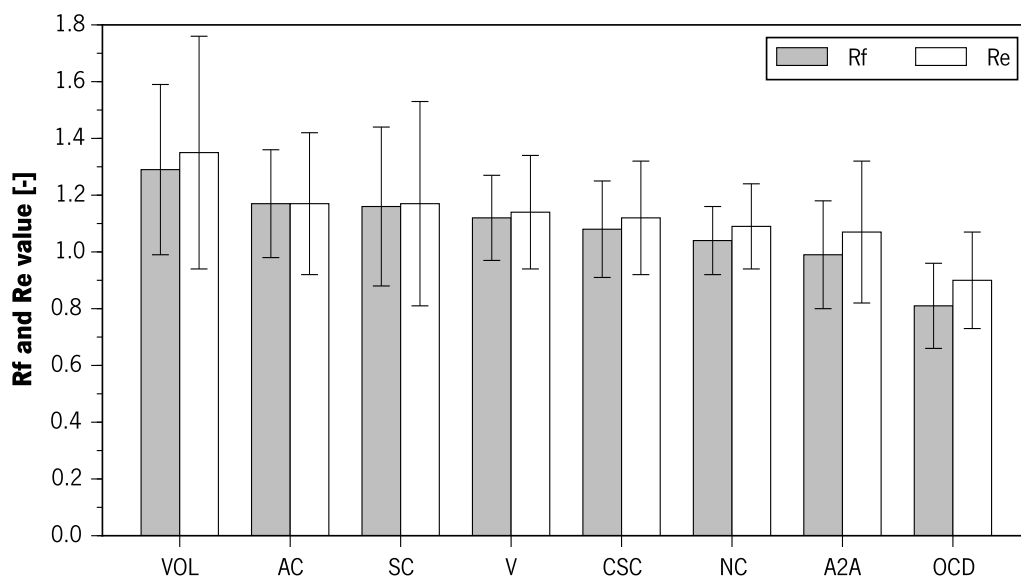

Figure 6.10: Results for the fine fraction increase metric (Rf) extra-fine fraction increase metric (Re) results at 30 L/min for the tested devices. Error bars indicate the experimental uncertainty for 95% confidence intervals

Figure 6.11 shows a comparison between the FPM emitted in each SM recovered. The dashed line represents the maximum theoretical values possible for the FPM in a certain amount of SM, logically it is impossible to the FPM be higher than the SM. All devices follow a linear trend (represented by a solid line), meaning that for a greater emitted SM, a higher amount of FPM is present. This is a logical conclusion since the FPM is obtained from the multiplication of the Fine Particle Dose (FPD) by the SM. Therefore, the trendline slope corresponds to the FPD for the

VHCs (i.e. ≈ 0.80). The pMDI solo shows similar results when compared to the VHCs. Figure 6.12 shows a comparison between the emitted FPM in each TEM recovered.
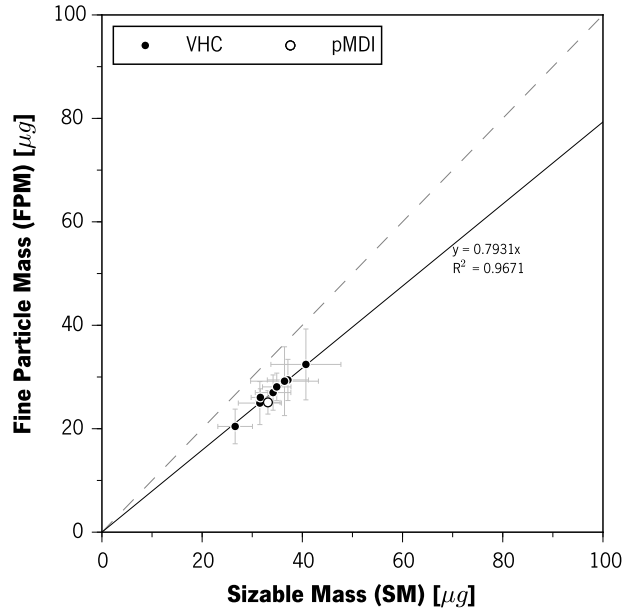

Figure 6.11: FPM versus the SM emitted by each device tested at 30 L/min. Error bars indicates the limits of the uncertainty within a 95% confidence interval
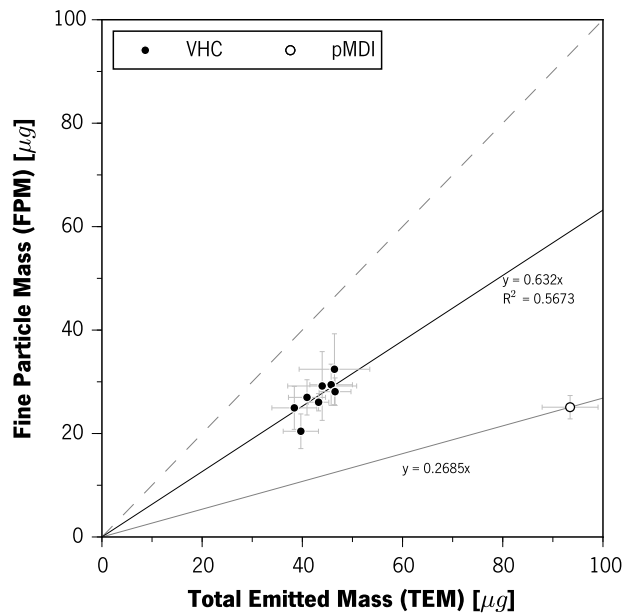

Figure 6.12: FPM versus the TEM emitted by each device tested at 30 L/min. Error bars indicates the limits of the uncertainty within a 95% confidence interval

Results show a comparison of the emitted FPM and the TEM for each device. As expected, pMDI solo has higher TEM than using a VHC. The linear trendlines for both types of devices are shown in black lines. The slope of these lines is, for all purposes, the ratio between the FPM and the TEM which is the correspondent to the FPF metric. This metric can never be higher than 1.0 (corresponding to a 45° slope), hence the dashed line. Although the VHC entrap a high amount of mass, the fraction of FPM of the emitted plume is higher than when the pMDI solo is used, proving the capacity of the VHC devices to entrap mostly the coarse particles of the pMDI plume.

6.2.2   Constant Flow Rate (60 L/min)

Results for the mass deposition using a constant flow setup (described in section 4.1.2) at 60 L/min are shown in Figure 6.13.
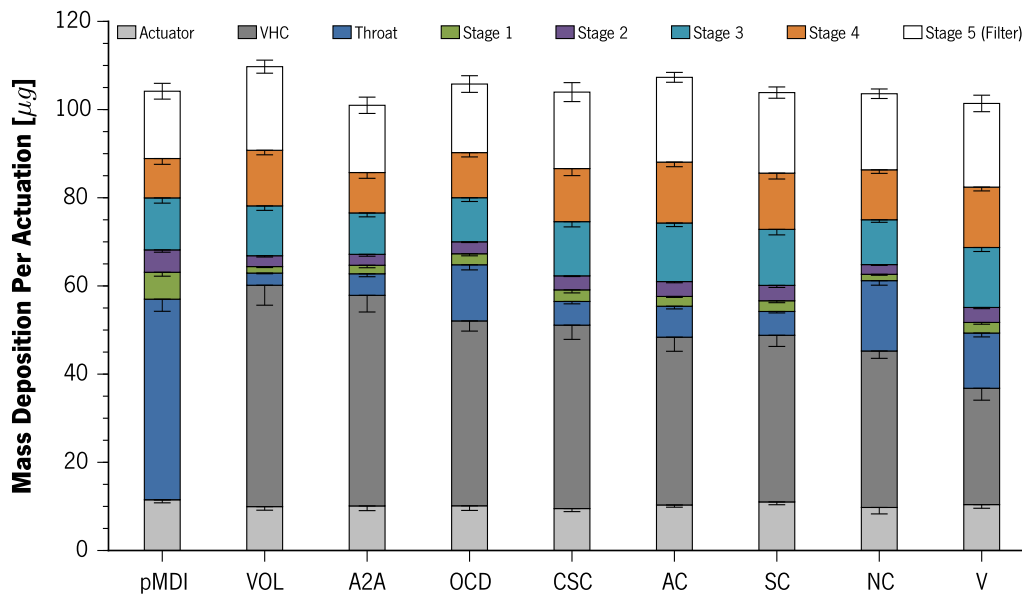

Figure 6.13: Salbutamol deposition mass (normalised for one actuation) in each setup zone for all tested devices at 60 L/min using the MSLI. Error bars indicates the limits of the uncertainty within a 95% confidence interval

It can be seen that the pMDI actuator deposition is approximately 10 μg, approximately constant for all tested devices (p>0.05), which is also observed with tests at 30 L/min. Analysing the TEM

it is obvious that the pMDI solo emits a higher amount of mass than the other devices (p<0.0001) also, there is statistically significant differences between the VHC's (p<0.0001). The throat mass deposition is greatly reduced by coupling a VHC device to the pMDI.

Figure 6.14 provides information regarding the percentage reduction of mass deposition in the throat in comparison to pMDI solo usage.
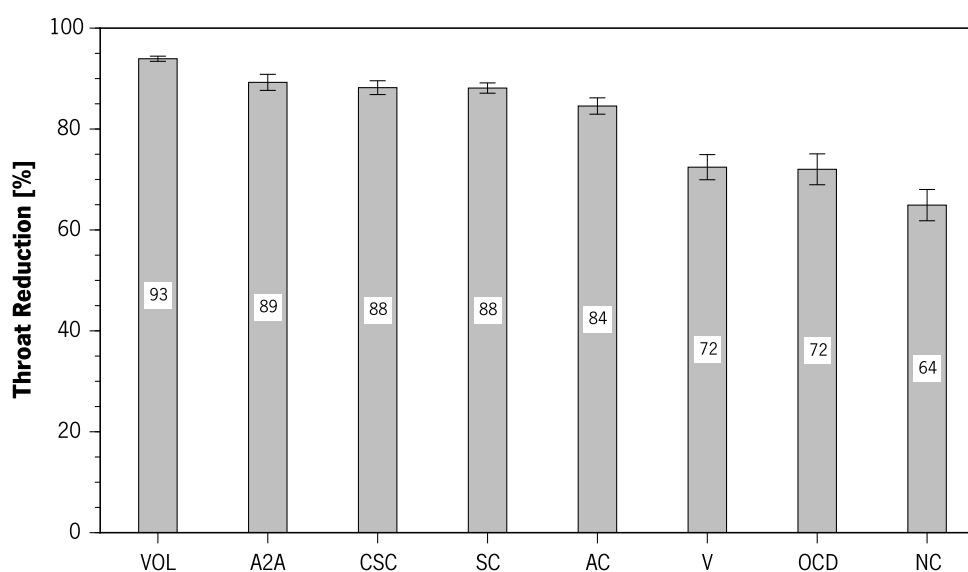

Figure 6.14: Percentage reduction in mass throat deposition in comparison with the pMDI solo at 60 L/min. Error bars indicates the limits of the uncertainty within a 95% confidence interval

Deposition of salbutamol in the throat is reduced between 94% and 65% when the pMDI is used coupled to a VHC, being distinct between them (p<0.0001). The Nebuchamber, Optichamber and Vortex have the lowest reduction (all with valve type Duck), whereas the Nebuchamber is statistically distinct from the other two (p<0.0001). While the highest reduction is found for the Volumatic (coin valve type), followed by the A2A Spacer and the Compact Space Chamber and Space Chamber (devices from the Leaflets valve type group, p>0.05). The results suggest that throat mass deposition is strongly related to the VHC valve type, ranked as: Coin < Leaflets < Annulus Flap < Duck. Statistical analysis show that the throat reduction for each valve type group is distinct from the others (p<0.0001).

Figure 6.15 depicts the cumulative mass curves for all tested devices. It shows that 50% of the SM is composed by particles with aerodynamic diameter smaller than 3.0 μm.
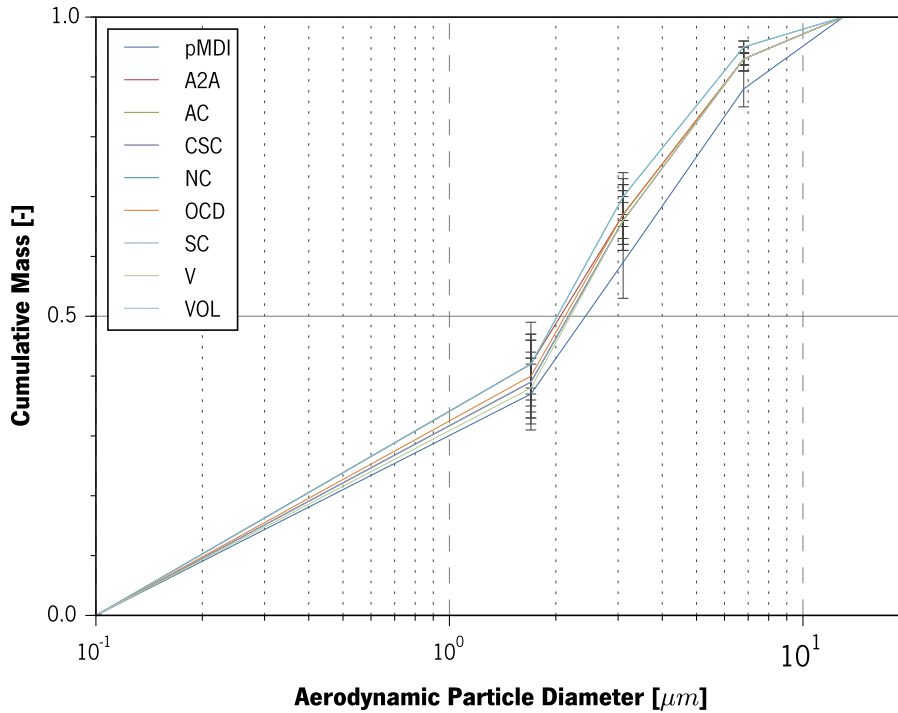

Figure 6.15: Cumulative mass fraction versus the aerodynamic particle diameter for tested devices at 60 L/min. Error bars indicates the limits of the uncertainty within a 95% confidence interval

The FPM results are depicted in Figure 6.16, and it is shown that all VHC's provide higher amount of fine particles to the patient lungs, except the A2A Spacer. The Aerochamber, Vortex and Space Chamber are the devices that emit the highest amount of FPM, while the A2A Spacer, Optichamber, and Nebuchamber emit the lowest value. The FPM emitted from all devices has statistically significant differences (p<0.0001) and the same is verified among the VHC's (p<0.0001). Similarity is found between the FPM emitted by the pMDI solo and these VHCs: A2A Spacer, Optichamber, Nebuchamber and Compact Space Chamber (p>0.05). Statistical analysis show that devices from Leaflets and Annulus Flap groups are distinct (p<0.05), however no significant differences were found (p>0.05) between the other valve type groups. Therefore, based on the observations drawn from the statistical analysis, a relationship can be found between the valve type and the FPM emitted by the VHC.
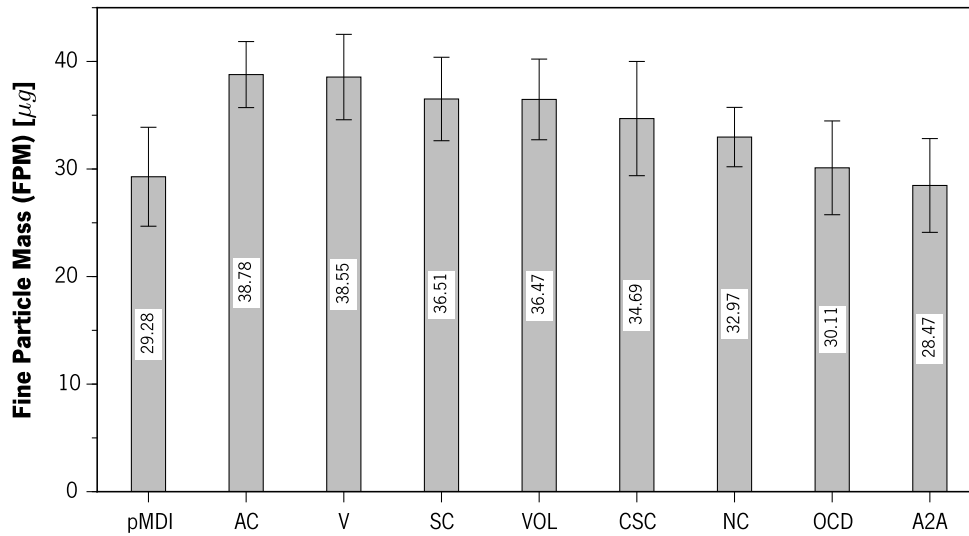
Figure 6.16: Emitted FPM at 60 L/min for the tested devices. Error bars indicate the experimental uncertainty for 95% confidence intervals

Figure 6.17 shows the calculated values for the MMAD, from the mass fraction cumulative curves depicted in Figure 6.15. As expected, the highest MMAD value can be found for the pMDI solo and the lowest one is obtained for the Nebuchamber. Nevertheless, the MMAD values for all VHC devices are very similar and lower than the pMDI solo. Therefore, it can be concluded that the commercial VHC devices ($p>0.05$) are able the actively reduce the coarse fraction in the emitted plume in comparison to the pMDI solo ($p<0.001$). The MMAD results, for the pMDI solo, has no statistically significant differences when compared with the Vortex, Space Chamber, Compact Space Chamber, Aerochamber and Optichamber ($p>0.05$).

The FPF and EFPF are depicted in the Figure 6.18. The calculated FPF values for the VHC's are above 60%, as advised in the guidelines, except for the Vortex, Nebuchamber and Optichamber devices (all with Duck type valve, $p<0.05$). The highest FPF value is found for the Volumatic and the lowest for the Optichamber ($p<0.0001$). Contrarily to the pMDI solo ($p<0.0001$), the VHC FPF indicates that the emitted plume mostly made up by fine particles. Devices with Annulus Flap valve type and Leaflets show no statistically significant differences ($p>0.05$) in terms of FPF results. The EFPF values are between 28% and 30% of the corresponding FPF value, which are within the guidelines reference values. Similarly with the results at 30 L/min, this parameter is

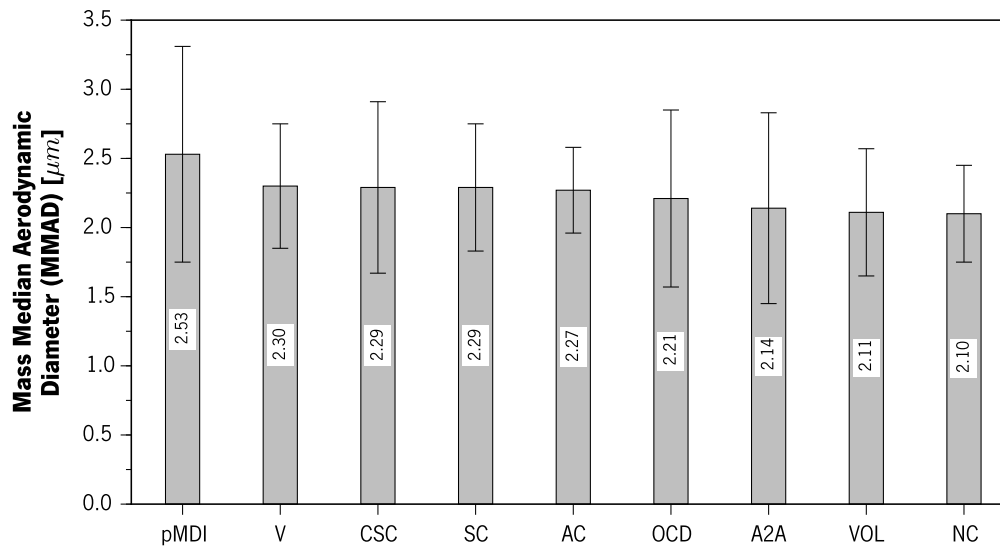highly dependent on the formulation and not in the device.

Figure 6.17: Emitted plume MMAD at 60 L/min for the tested devices. Error bars indicate the experimental uncertainty for 95% confidence intervals
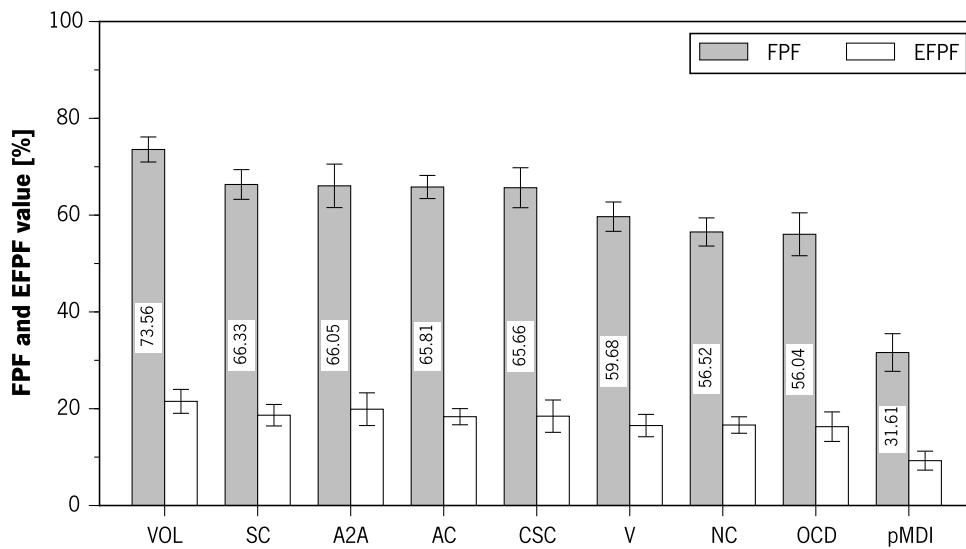

Figure 6.18: FPF and EFPF metrics of the emitted plume for each tested device at 60 L/min. Error bars indicate the experimental uncertainty for 95% confidence intervals

The Rc metric results, representing the ratio of CPM between the pMDI coupled to the VHC and the pMDI solo, are depicted in Figure 6.19. The Rc is statistically different for the tested

VHC's (p<0.0001). Results are highest for the Duck type valve devices (i.e. Optichamber, Vortex, Nebuchamber, p<0.001) and lowest for the Coin type valve (i.e. Volumatic). The results seem to be related to the valve type, ranked as: Coin < Leaflets < Annulus Flap < Duck. In fact, there is statistical significant differences between all valve groups (p<0.001), and even within the Leaflets (p<0.01) and Duck (p<0.001) groups differences were verified.

The Aerochamber, Nebuchamber, Vortex and Optichamber are slightly above the reference value of 0.3, the rest of the VHC's are within the guideline. Results point out that Volumatic has the capacity to reduce 80% of the coarse fraction emitted by the pMDI.
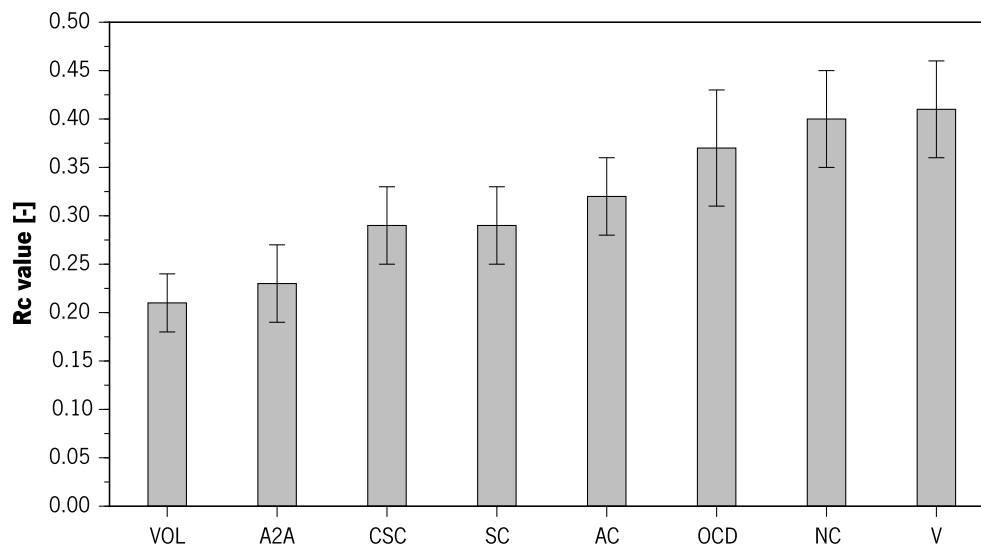

Figure 6.19: Coarse fraction reduction metric (Rc) results at 60 L/min for the tested devices. Error bars indicate the experimental uncertainty for 95% confidence intervals

The results for both the Rf and the Re metrics, are shown in Figure 6.20. It can be seen that Rf and Re are between 0.97 and 1.32, in agreement with the guideline reference. The Aerochamber has the highest Rf (increasing the delivered FPM in 32%), and the A2A Spacer has the lowest (reducing the emitted FPM in 3%). All VHC Rf values are distinct (p<0.0001), however the Aerochamber, Vortex, Volumatic, Space Chamber, Compact Space Chamber show no statistically significant differences (p>0.05). The Re values range between 1.00 and 1.26, however this metric is based in the EFPM which, due to the resolution of the impactor, is not estimated with the required accuracy.
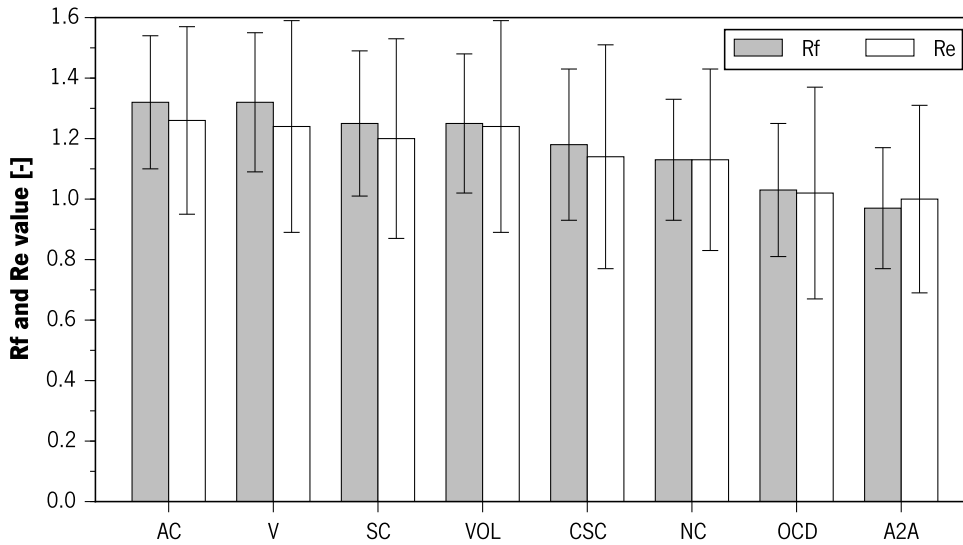
Figure 6.20: Results for the fine fraction increase metric (Rf) extra-fine fraction increase metric (Re) results at 60 L/min for the tested devices. Error bars indicate the experimental uncertainty for 95% confidence intervals

Figure 6.21 shows a comparison between the FPM emitted in each SM recovered, at 60 L/min for all the tested devices (categorised in two groups: VHC and pMDI). The dashed line delimits the upper zone, whereas no possible combinations of FPM versus SM exist (FPM cannot be higher than SM). A black line illustrates the linear trend of the VHC results, which has slope of approximately 0.8 (similar result found at 30 L/min). This value is highly related to the FPD metric previously calculated from Figure 6.15 and the results suggest that the pMDI spray technology has a typical linear trend of delivered FPM for a certain amount of SM emitted.

Figure 6.22 shows a comparison between the FPM emitted for each TEM recovered. The dashed line delimits the feasible results, and the two solid lines identify linear trends. These results show how much of the TEM is composed by FPM, which is highly related to the FPF metric. More specifically, the trend line slope is correspondent to the averaged FPF of each device type. When the FPM delivered by the use of VHC and by the pMDI solo are similar, the TEM is quite distinct (due to the removed coarse fraction performed by the VHC technology). VHC devices located above the trend line have better performance than the others bellow.

Figure 6.21: FPM versus the SM emitted by each device tested at 60 L/min. Error bars indicates the limits of the uncertainty within a 95% confidence interval

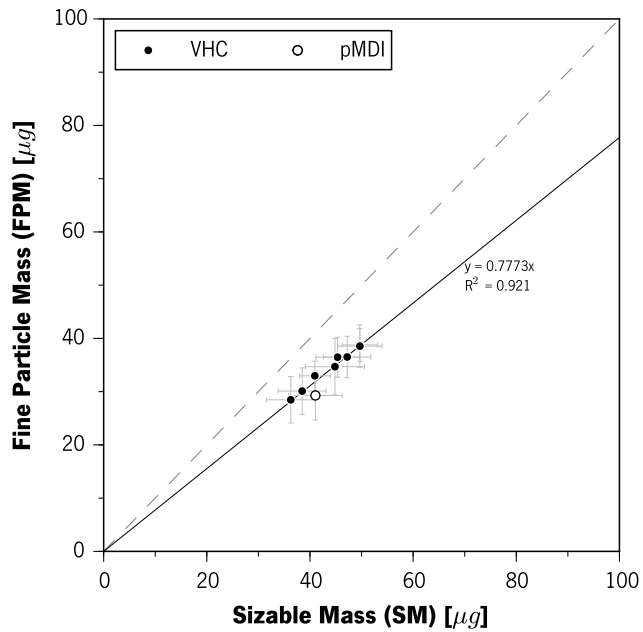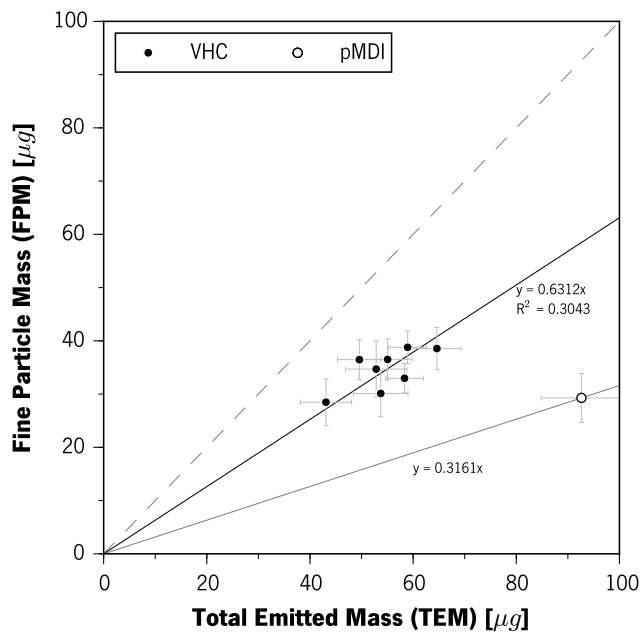Figure 6.22: FPM versus the TEM emitted by each device tested at 60 L/min. Error bars indicates the limits of the uncertainty within a 95% confidence interval

6.2.3   Breath Pattern

Results for the mass deposition using a variable flow setup (described in section 4.1.2) are shown in Figure 6.23. Herein are reported the results for the pMDI solo and combined with four VHC devices: Aerochamber, Compact Space Chamber, Vortex and Volumatic. One from each valve design type group.

Spray injection was executed in the beginning of the inhalation phase. Only four VHC devices were tested, each one with a different valve type. The actuator mass deposition is ≈ 17 µg for the tested devices (p>0.05) and, as observed for other results at constant flow, is related with the actuator geometry. The drug deposition in the VHC is higher (i.e. ≈ 72 µg) than at constant air flow (i.e. ≈ 26 µg to ≈ 50 µg, at 30 L/min), which is expected since only a small volume of air passes through the device (i.e. tidal volume of 150 mL) during the inhalation. The TEM from the pMDI is statistically different from that emitted from the VHC devices (p<0.0001), however it is similar among the VHC's (p>0.05).

The throat deposition is greatly affected by the use of a VHC device when compared with the pMDI solo; however the reduction of the mass throat deposition depends on the device, as can be seen in Figure 6.24. Deposition of salbutamol in the throat is reduced between 95% and 88% when the pMDI is used coupled to a VHC device. The Volumatic has the highest reduction, while the lowest reduction is found for Vortex. Throat reduction has significant differences between the VHC's (p<0.0001), due to the fact that the mass reduction at Volumatic is distinct from that found in other VHC devices (p>0.05). The results suggest that throat mass deposition is related to the VHC valve type, ranked as: Coin < Leaflets < Annulus Flap < Duck. Similar observations were found for the results obtained at 60 L/min flow rate.
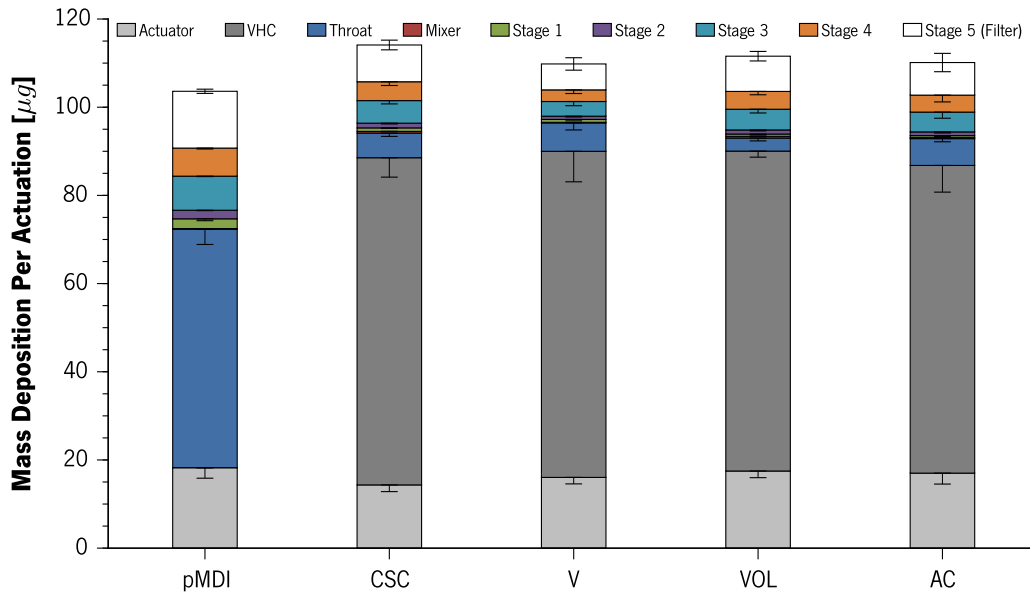
Figure 6.23: Salbutamol deposition mass (normalised for one actuation) in each setup zone for all tested devices under a breath pattern using the MSLI. Error bars indicates the limits of the uncertainty within a 95% confidence interval
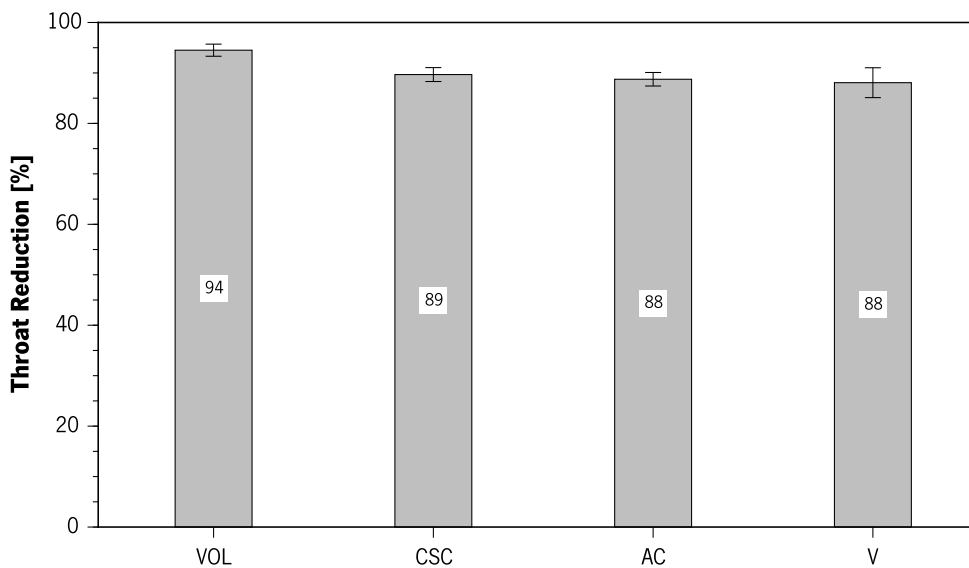

Figure 6.24: Percentage reduction in mass throat deposition in comparison with the pMDI solo under a breath pattern. Error bars indicates the limits of the uncertainty within a 95% confidence interval

Figure 6.25 depicts the cumulative mass curves for all tested devices. This graph shows that 50% of the SM is composed by particles with aerodynamic diameter smaller than 2.0 μm.
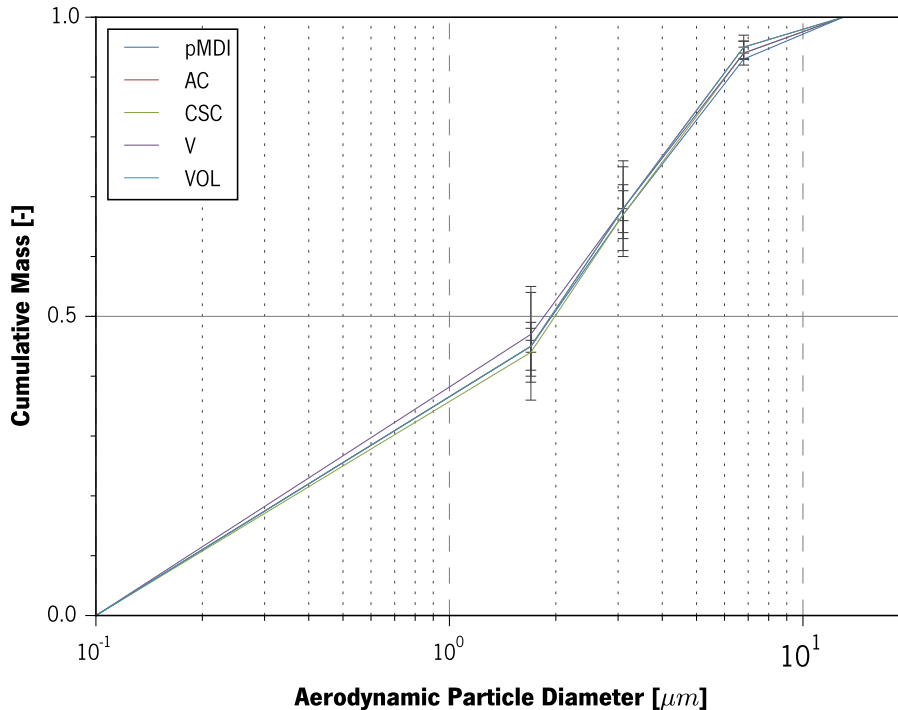

Figure 6.25: Cumulative mass fraction versus the aerodynamic particle diameter for tested devices under a breath pattern. Error bars indicates the limits of the uncertainty within a 95% confidence interval

The FPM results shown in Figure 6.26 indicate that, under a breath pattern, the FPM emitted by the VHC devices is highly reduced. This is not in according to the literature, and might be explained by the low tidal volume of the breath pattern. pMDI delivers the highest FPM (14%) and the Vortex emits the lowest (6%). FPM emitted from the pMDI solo is distinct from the VHC's ($p<0.0001$). However, the FPM emitted from the VHC devices have no statistically significant differences ($p>0.05$).

Figure 6.27 shows the calculated values for the MMAD, from the mass fraction cumulative curves depicted in Figure 6.25. The highest value for the MMAD can be found for the pMDI solo, as expected, although this parameter is very close to all the tested devices ($p>0.05$).
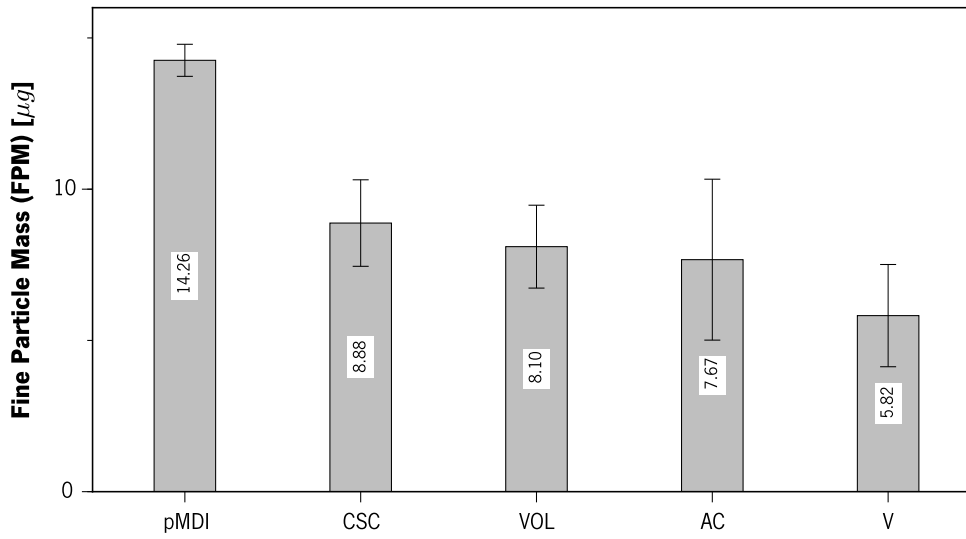
Figure 6.26: Emitted FPM under a breath pattern for the tested devices. Error bars indicate the experimental uncertainty for 95% confidence intervals
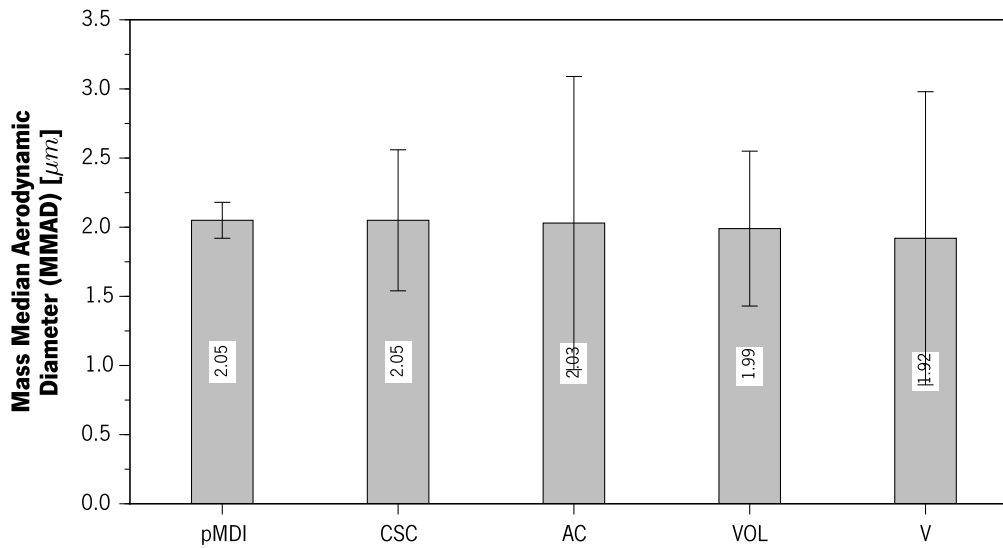

Figure 6.27: Emitted plume MMAD under a breath pattern for the tested devices. Error bars indicate the experimental uncertainty for 95% confidence intervals

Figure 6.28 depicts the FPF and EFPF emitted for each tested device under a breath pattern. The calculated FPF for the VHC's are above 40%. The Volumatic has the highest (i.e. 59%) FPF value and the pMDI the lowest (i.e. 19%). FPF from VHC is distinct from the pMDI solo ($p < 0.0001$). The Volumatic emits a FPF statistically distinct ($p < 0.0001$), to all other VHC's ($p > 0.05$). A trend is noticeable among the type of valves and the FPF, ranked as follows: Coin > Leaflets > Annulus Flap > Duck. EFPF values are between 31% and 33% of the corresponding FPF value, which is within the guidelines reference.
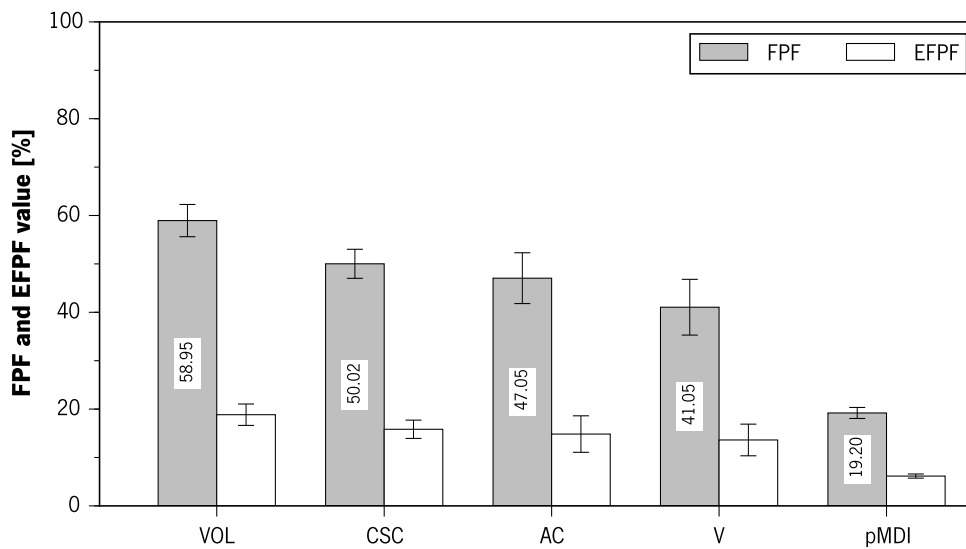
Figure 6.28: FPF and EFPF metrics of the emitted plume for each tested device under a breath pattern. Error bars indicate the experimental uncertainty for 95% confidence intervals

The Rc metric results are shown in Figure 6.29. All results are below 0.3, although the value is highest for the Compact Space Chamber (i.e. 0.15) and lowest is achieved for the Volumatic (i.e. 0.09). Results point out that the Volumatic has the ability to reduce 91% of the coarse fraction emitted by the pMDI. The Rc metric show no statistically significant differences among the VHC devices ($p > 0.05$), whereas the Aerochamber, the Vortex and the Compact Space Chamber show closer average Rc values ($p > 0.05$).

The results for both the Rf and the Re metrics, are shown in Figure 6.30. It can be seen that Rf and Re values vary between 0.41 and 0.62, which are outside the guideline reference values. The calculated Rf values show no statistically significant differences ($p > 0.05$) when comparing the VHC

devices. The Compact Space Chamber has the highest Rf value (reducing the delivered FPM in 38%), and Vortex has the lowest one (reducing the emitted FPM in 59%). Re values range between 0.42 and 0.61, however this metric is based in the EFPM which, due to the limited number of stages of the impactor, cannot be estimated with great accuracy.

Figure 6.29: Coarse fraction reduction metric (Rc) results under a breath pattern for the tested devices. Error bars indicate the experimental uncertainty for 95% confidence intervals

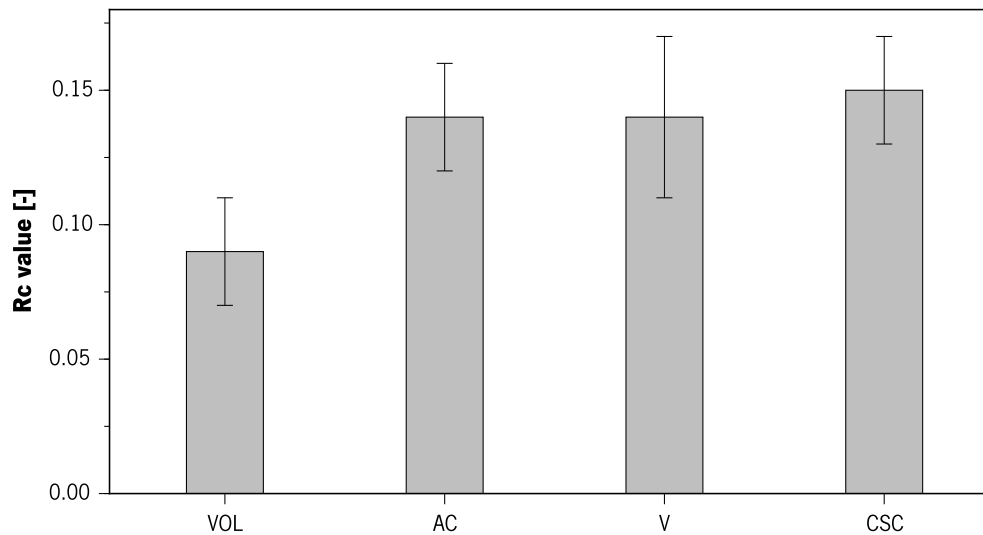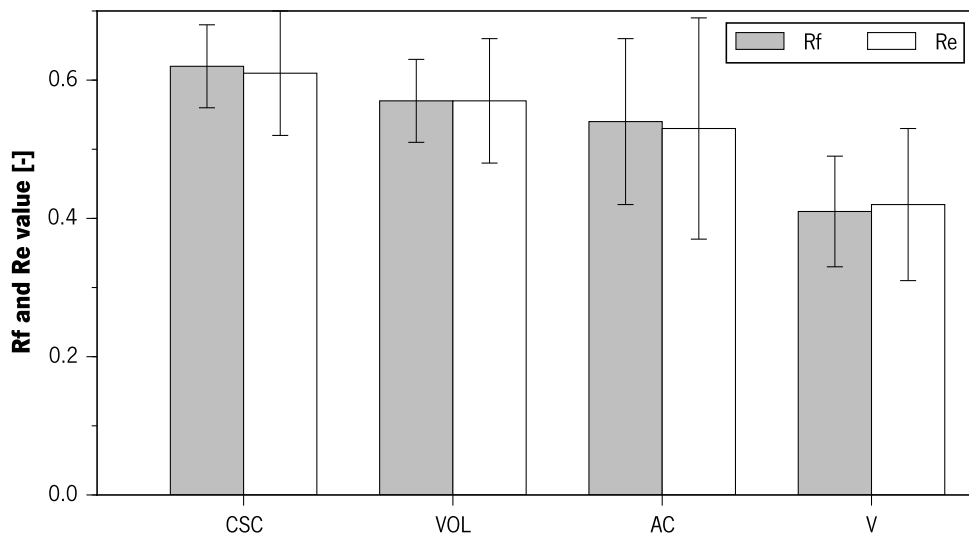Figure 6.30: Results for the fine fraction increase metric (Rf) and extra-fine fraction increase metric (Re) results under a breath pattern for the tested devices. Error bars indicate the experimental uncertainty for 95% confidence intervals

Figure 6.31 shows a comparison between the FPM emitted in each SM recovered, under a breath pattern for all the tested devices (categorised in two groups: VHC and pMDI). The dashed line delimits the upper zone, whereas no possible combinations of FPM versus SM exist. A solid line illustrates the linear trend of the VHC results, which has slope value of approximately 0.8 (similar to the results found at 30 L/min and at 60 L/min). This value is highly related to the FPD metric previously calculated from Figure 6.25 and the results suggest that the pMDI spray technology has a typical linear trend of delivered FPM for a certain amount of SM emitted.

Figure 6.32 shows a comparison between the FPM emitted in each TEM recovered. The dashed line delimits the feasible results, while the two solid lines identify linear trends. These results are highly related to the FPF metric. More specifically, the trend line slope is correspondent to the averaged FPF of each device type. Whereas the FPM delivered by the use of VHC and the pMDI solo are similar, the TEM is quite distinct. VHC data above the trend line indicate a better performance than those bellow.
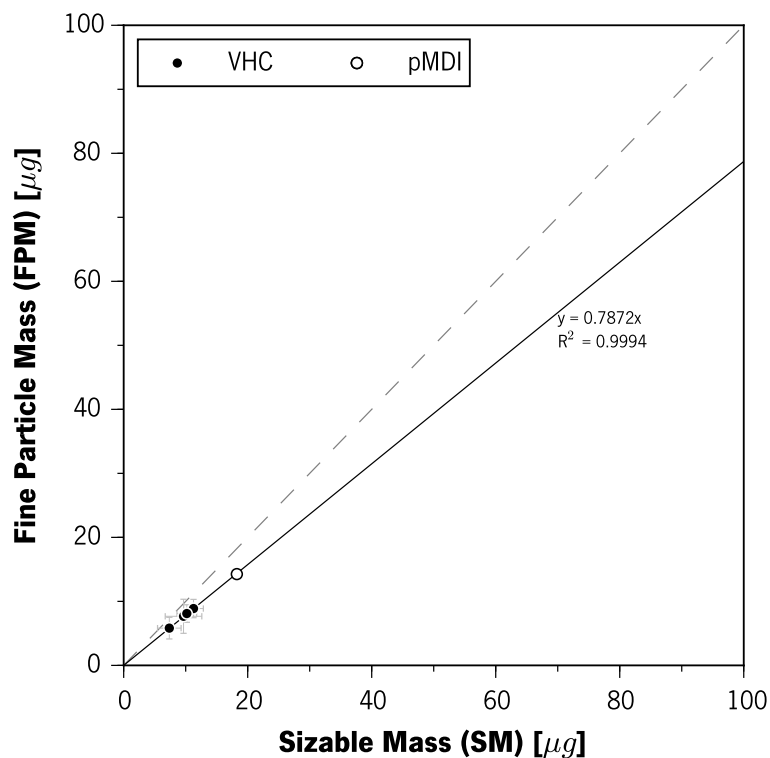
Figure 6.31: FPM versus the SM emitted by each device tested under a breath pattern. Error bars indicates the limits of the uncertainty within a 95% confidence interval
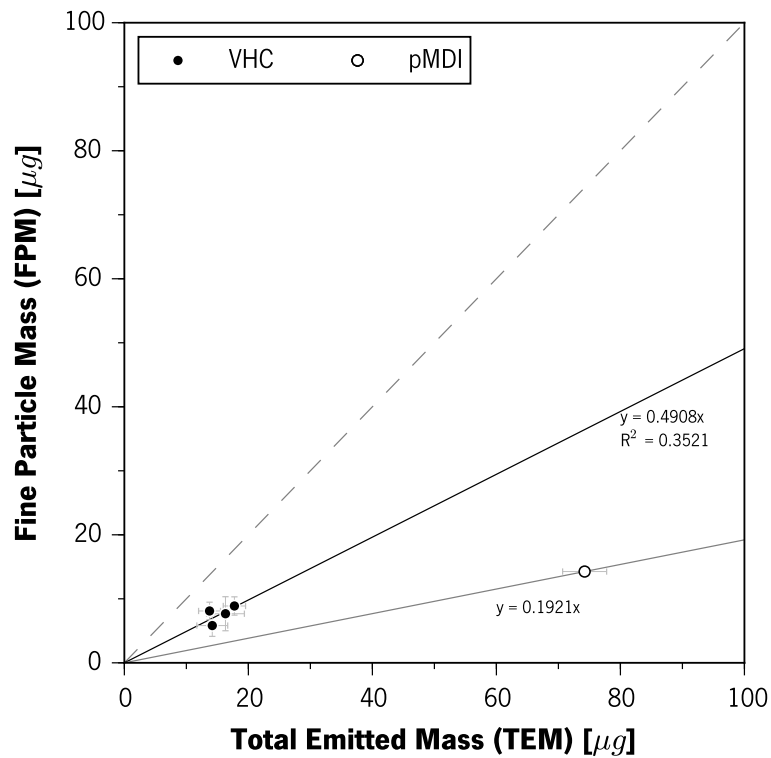
Figure 6.32: FPM versus the TEM emitted by each device tested under a breath pattern. Error bars indicates the limits of the uncertainty within a 95% confidence interval

6.3 Evaluation of the Flow Rate Effect

The following section reports the effect of flow rate in the various performance parameters, such as, the Total Emitted Mass, Fine Particle Mass, coarse and fine particles ratios.

6.3.1 Total Emitted Mass

The TEM value for the MSLI and Full Dose setups at different flow rates are presented in Figure 6.33, whereas the uncertainty within a 95% confidence interval is represented as error bars. Results show a clear reduced TEM trend with the reduction of flow rate. Higher air velocities inside the VHC reduce the deposition onto it. The results of FD setup are similar to the MSLI at the same flow rate.
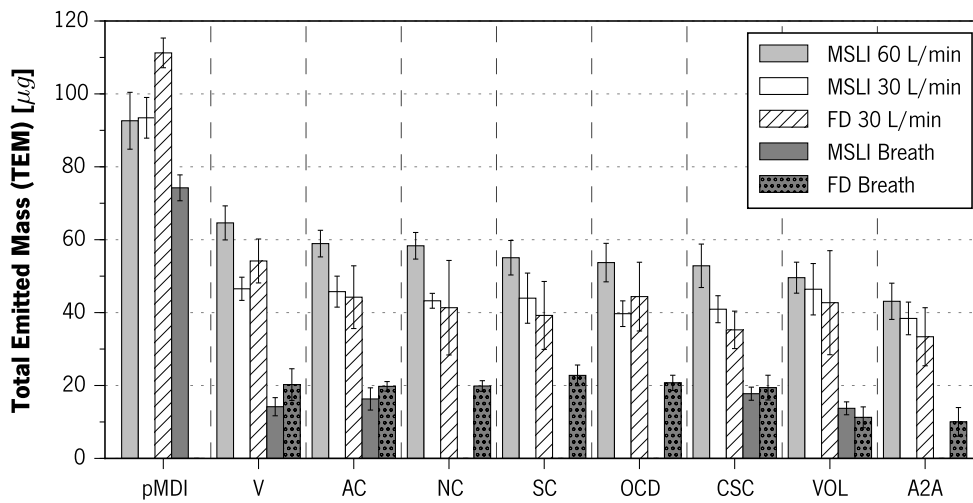
Figure 6.33: TEM values for each device tested at MSLI and FD setups under different flow rates

6.3.2 Fine Particle Mass

Figure 6.34 depicts the FPM emitted by several devices under different flow rate conditions and error bars represent the uncertainty confidence interval of 95%. Results suggest the diminishing of the FPM upon the reduction of the flow rate. Because the FPM is based in the value of SM, which is a part of the TEM, some correlation with the TEM are expected.
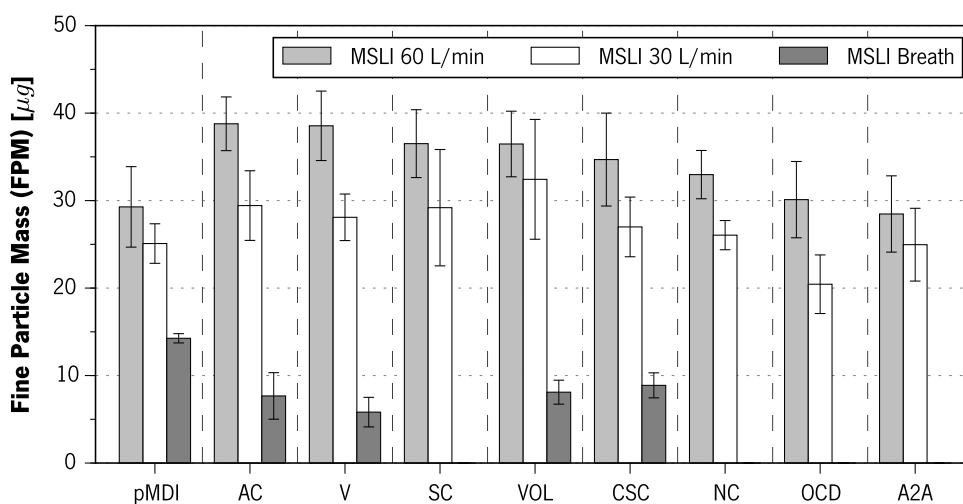
Figure 6.34: FPM values for each device tested at MSLI setup under different flow rates

Figures 6.35 and 6.36 provide further insight into the influence of the flow rate upon the FPM when compared to the SM and TEM values. A trend solid line shows that salbutamol sulphate delivered by pMDI, with or without a VHC coupled, has a linear relation between the SM and the FPM emitted which is independent of the flow rate. This indicates that the commercial VHCs are bioequivalent to the pMDI solo. The line slope represents the mass fraction of fine particles in the APSD cumulative graph, which seems to be independent from the flow rate.
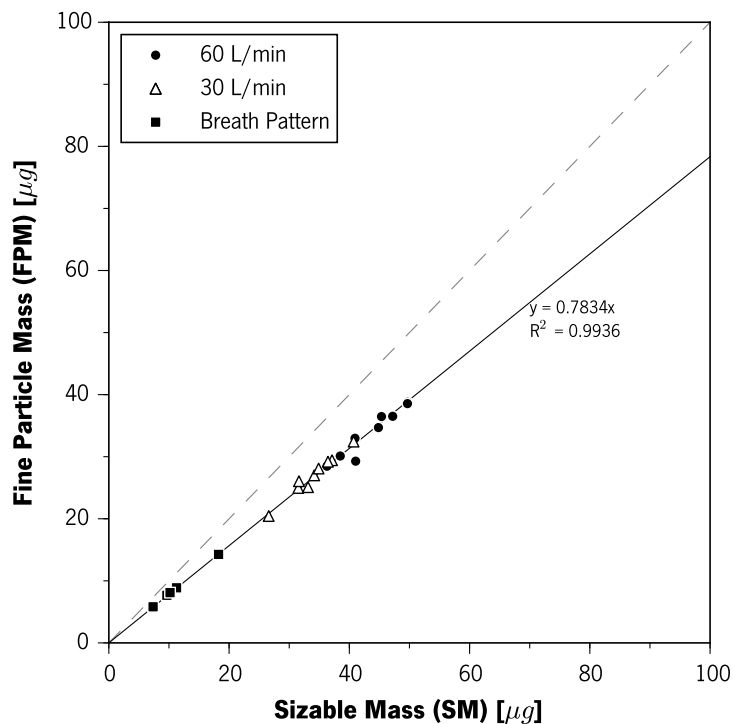
Figure 6.35: FPM versus SM for each device at different flow rates

When the FPM is plotted as a function of the TEM value two trend lines arise: a black solid one indicates the VHC results and a grey solid one for the pMDI results. Both line slopes are related to the FPF value of each corresponding device technology. Results show that FPM and TEM values increase with the flow rate, which was previously discussed.
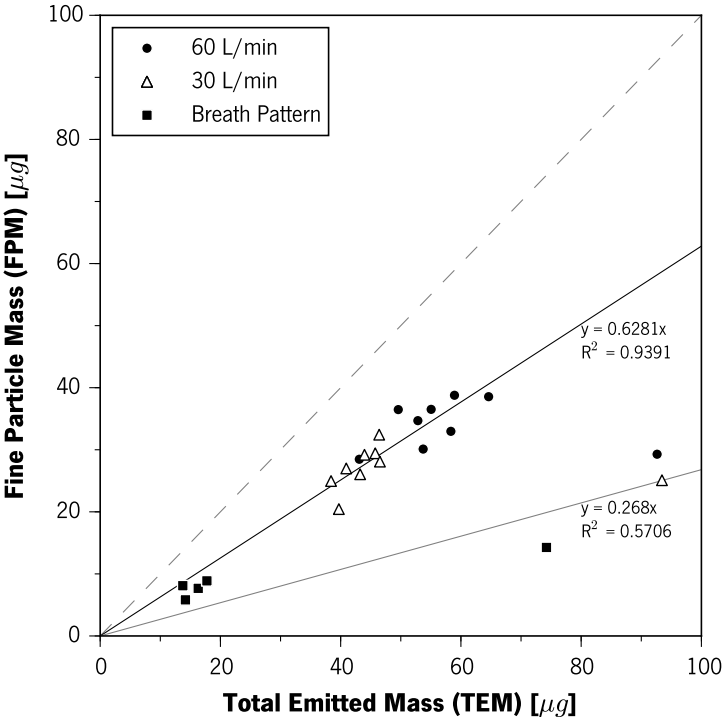
Figure 6.36: FPM versus TEM for each device at different flow rates

6.3.3   Evaluation of Rc and Rf Parameters

Figures 6.37 and 6.38 show the variation of the Rc and Rf metrics for different flow rates.
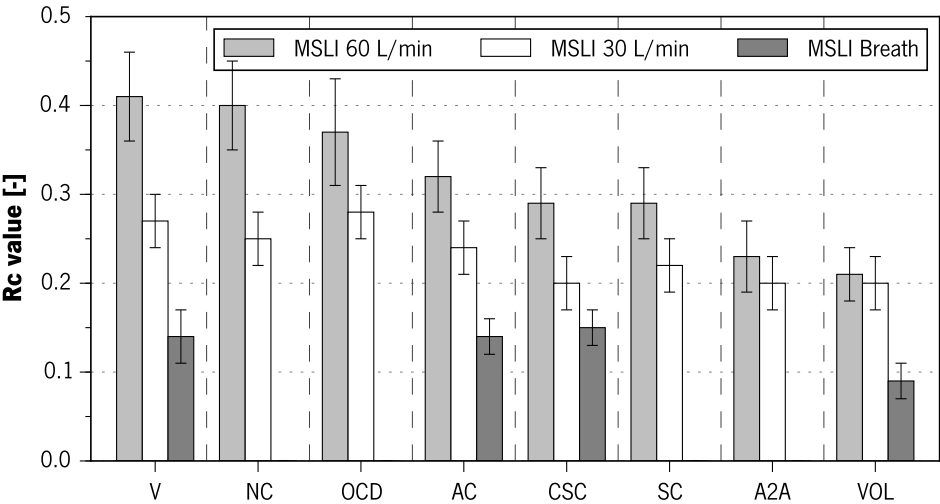
Figure 6.37: Rc metric values for several devices under different flow rates
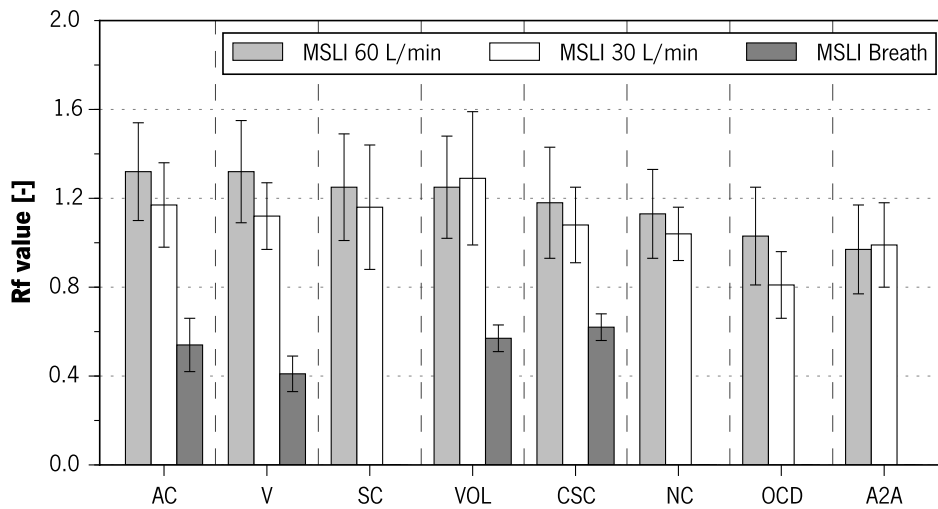
Figure 6.38: Rf metric values for several devices under different flow rates

Results suggest that Rc decreases with the reduction of the flow rate, as observable for the Rf metric results. The variation is higher in some devices than in others, although a trend is present.

6.4 Metrics Comparison

In this section, several other variables are compared, being categorised for the flow rate value and/or valve design type. Only variables that presented unequivocal of correlation were included in this section.

6.4.1 Throat Deposition versus FPM

An analysis of the Throat salbutamol deposition versus the FPM emitted by each device and categorised by valve type and flow rate, is depicted in Figure 6.39. Dashed lines indicate the linear correlation for devices with the same type of valve design. Results show distinct FPM data that increases with flow rate as previously discussed. Furthermore, the Duck type valve design seems to favour the throat deposition with increasing flow rate, though other types of valve do not present such effect. Throat deposition is higher for Duck valve devices independently of the flow rate,

171

followed by the Annulus Flap > Leaflets > Coin valve type,«. Such conclusions already have been observed previously in this chapter.
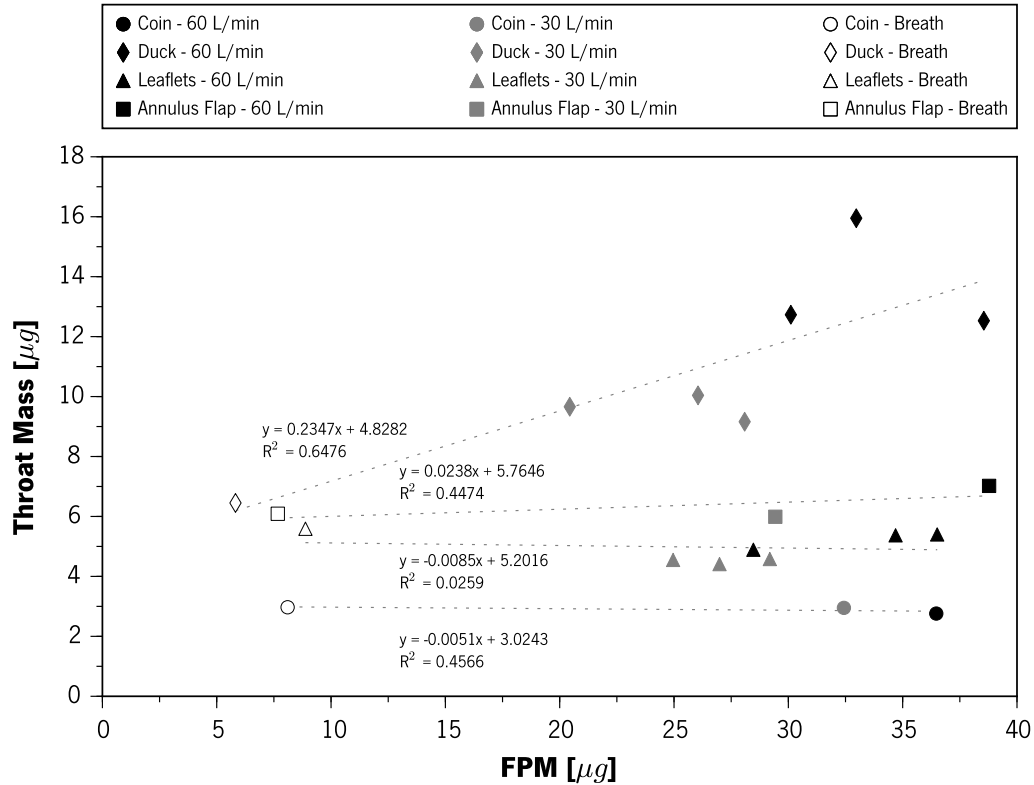
Figure 6.39: Comparison of the Throat deposition versus the FPM, categorised by valve design and flow rate value

6.4.2 MMAD versus FPM

Figure 6.40 shows the comparison of the calculated MMAD versus the FPM of the spray plume, with categorisation by the flow rate. The linear correlation of the results (dashed line) suggests that the MMAD and FPM increase with the flow rate. A higher flow rate passing through a VHC delivers more FPM to the lungs, however this plume is coarser.
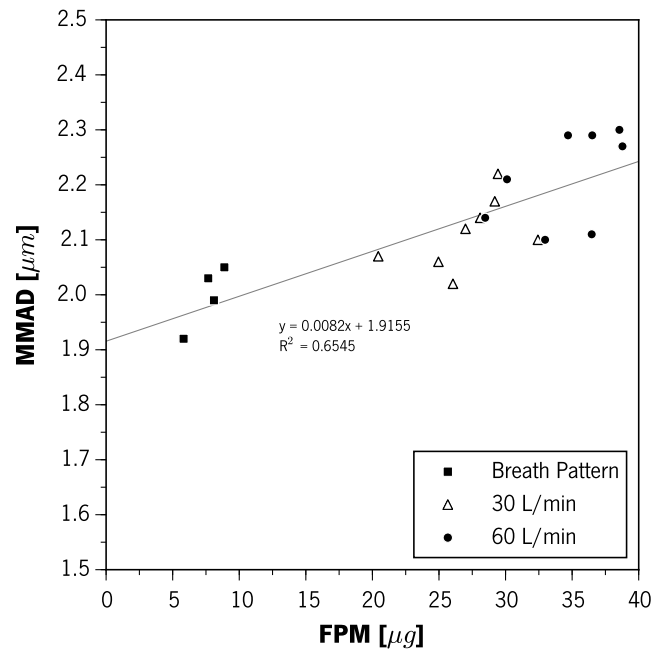
Figure 6.40: MMAD versus FPM emitted by several devices under different flow rate testing conditions

6.4.3 Device Volume versus FPM

In Figure 6.41 is depicted the salbutamol FPM against the VHC volume at 60 L/min, categorised by valve type. Additionally, the data correlation (FPM $= 0.0397492 * \ln{(Volume)} - 0.147937$, $R^2 = 0.84349$) from Barry and O'Callaghan (1995), is also shown and represented through the dashed line. This correlation was obtained from a study on sodium cromoglycate FPM emitted from tubular spacers and assessed using a glass MSLI at 60 L/min [BO95]. Results indicate that VHC devices show a distinct behaviour from an open tubular spacer, where the Volumatic (with 750 mL) should emit a higher amount of FPM. Furthermore, based in the previously discussed results, the VHC valve design seems to be more influential than the chamber body volume or the VHC shape itself. No apparent relation can be found between the valve design type and the reported results in Figure 6.41.
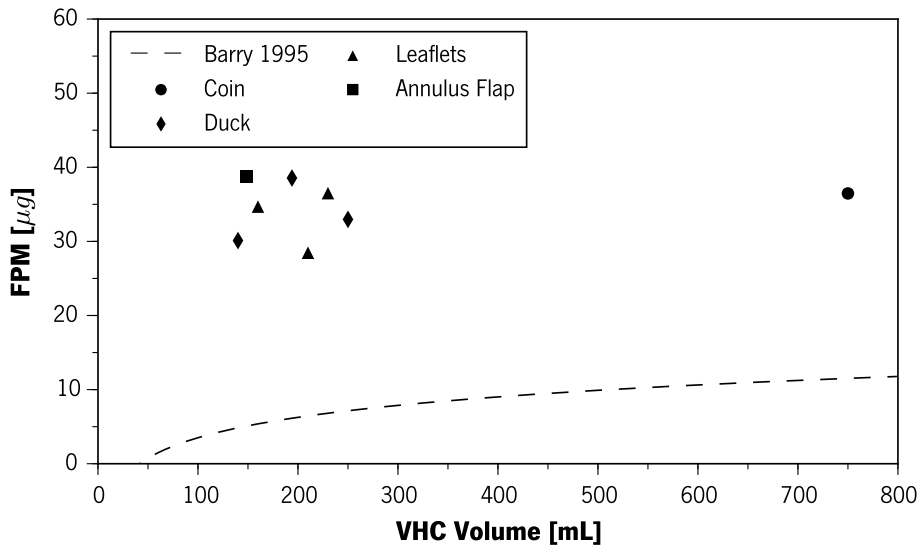
Figure 6.41: FPM versus VHC volume at 60 L/min

6.4.4   FPF and Throat Deposition versus Air Volume Drawn

Analysing the FPF (Figure 6.42) and the percentage of throat deposition regarding the TEM values (Figure 6.43), against the volume of air drawn through the device in one actuation, can provide further insight. Given the fact that some experimental data comes from unsteady flow rate setup and other part from constant flow rate, the best way to correlate them is by calculating the volume of air drawn in each actuation. The time between actuations at constant flow rate procedure was 5 s during 40 actuations plus 30 s at the end of the procedure, giving an average volume of 2875 mL for 30 L/min and 5750 mL for 60 L/min. Under the breath profile the value equals the tidal volume, i.e. 150 mL. The FPF (i.e. FPF = FPM/TEM) was plotted against the volume of air drawn during one actuation. Logarithmic correlations were be found for each valve category, represented by solid lines. There is a high degree of correlation ($R^2 > 0.78$) between the data and the logarithmic trends. Results point out that FPF increases with the amount of air drawn, whereas the valve type has clear influence in the FPF values ranked as: Coin > Leaflets > Annulus Flap > Duck. In Figure 6.43 the results reported that the mass fraction of salbutamol deposited in the throat is reduced with the volume of air passing through the VHC. Also, the valve design seems to influence this matter greatly, ranked as: Duck > Annulus Flap > Leaflets > Coin. There

174

is a high degree of correlation ($R^2 > 0.73$) between the data and the logarithmic trends.
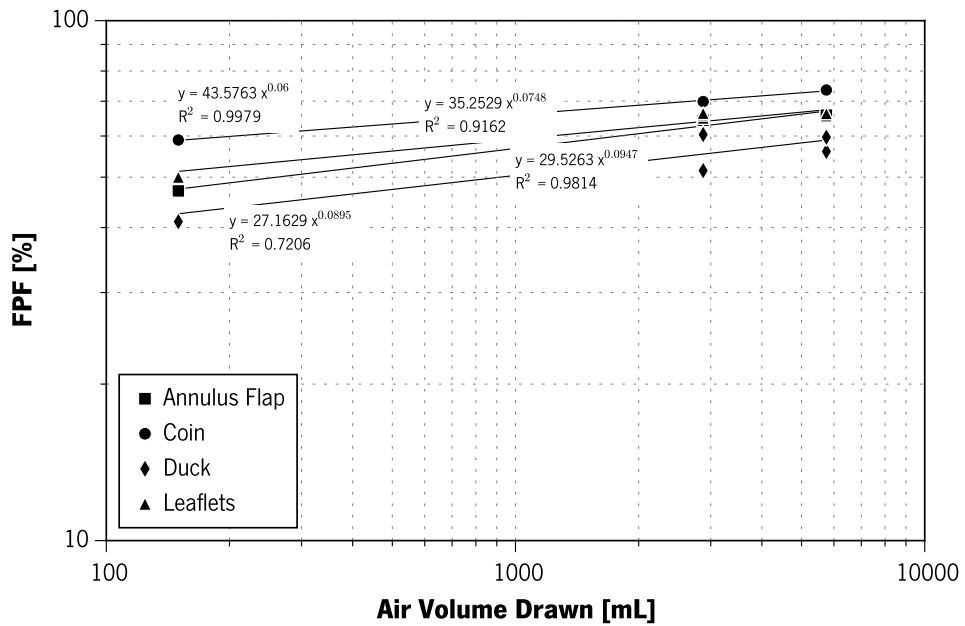
Figure 6.42: FPF versus Air Volume Drawn categorised by valve design type
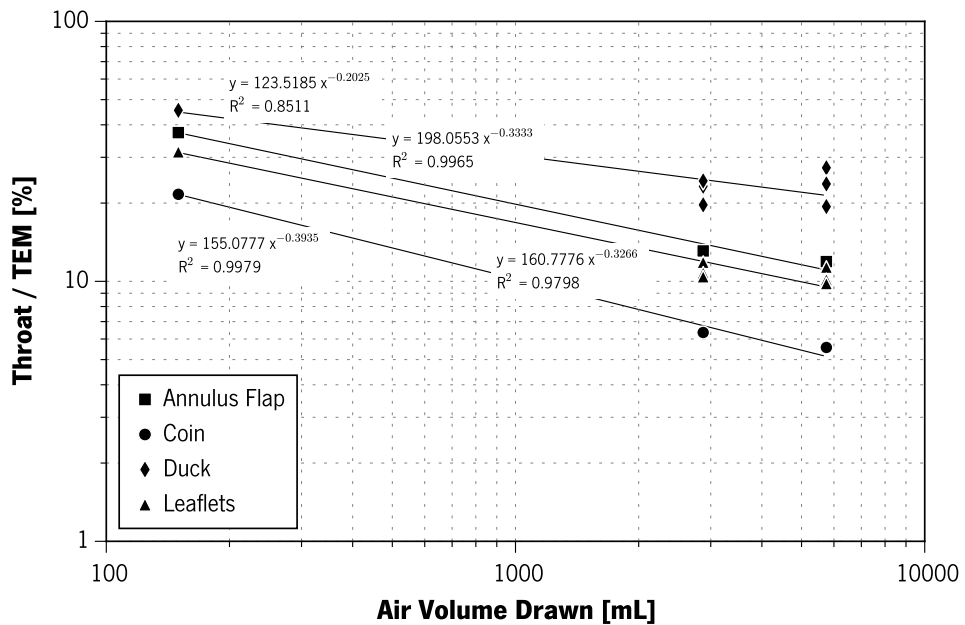
Figure 6.43: Throat mass per TEM versus Air Volume Drawn categorised by valve design type

6.5   Patient Relevant Metrics

In an effort to relate commercial devices in a friendly manner for the patient, several metrics were developed. These metrics process a certain degree of subjectivity and which are far from being universally accepted. Nevertheless they relate the device weight, volume necessary to transport it, features of interest against the price and the performance. These metrics are an attempt to facilitate the comparison between widely varying market alternatives using objective parameters. Figure 6.44 depicts the relation between the commercial VHCs weight with the transport volume (given by the volume of a cylinder that enclosures the VHC when disassembled/unmounted for transport). Devices are categorised by valve type, majority of the market devices have a transport volume between 200 and 400 mL and a weight between 40 and 80 g. However some VHC devices have high volume and high weight (i.e. Volumatic) or; in opposition to low volume and high weight (i.e. Nebuchamber – made of stainless steel).
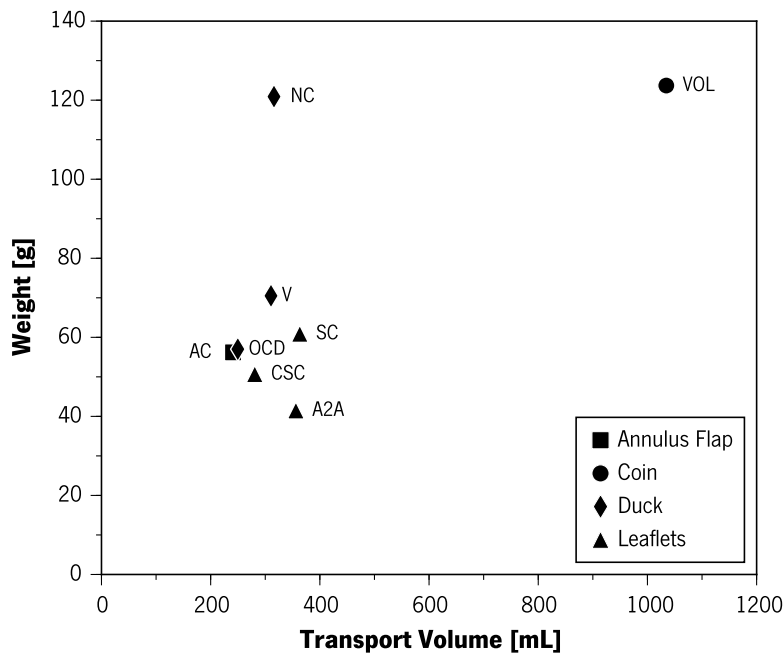
Figure 6.44: VHC weight versus transport volume, categorised by valve type

A Handling metric can be calculated by Equation 6.1, using the weight and the transport volume of the device. Higher the Handling value means that the weight and/or the transport volume are

lower.

$$\text{Handling} = \frac{1}{\text{Weight} \cdot \text{Transport Volume}} \qquad (6.1)$$

The Attractiveness of a device is averaged by the subjective evaluation given by each device characteristics, rated from 0.1 to 1.0 (bad to good), see Table 6.1. The considered features of interest were:

- existence of a universal adapter for all type of pMDI's;
- existence of an exhalation one-way valve;
- collapsibility of the device for transport;
- existence of a flow whistle for patient inspiration control;
- visibility of the valve functioning.

Table 6.1: VHC features evaluation rating

Device	Valve visibility	Flow whistle	Exhalation valve	Universal adapter	Modular transport	Attractiveness Metric
A2A	1.0	0.1	0.1	0.5	1.0	**0.54**
AC	0.5	1.0	1.0	1.0	0.1	**0.72**
CSC	1.0	0.1	1.0	1.0	0.1	**0.64**
NC	0.5	0.1	1.0	0.1	0.5	**0.44**
OCD	0.5	1.0	1.0	1.0	0.1	**0.72**
SC	1.0	0.1	1.0	1.0	0.1	**0.64**
VOL	0.5	0.1	0.1	0.1	0.5	**0.26**
V	1.0	0.1	1.0	1.0	0.1	**0.64**

Figure 6.45 depicts the comparison between the Handling and the Attractiveness metrics. Devices with low Handling are rated with poor Attractiveness. Combining these two metrics, an overall measure of patient interest in the device can be obtained. This graph indicates that devices with high volume or weight (i.e. Volumatic and Nebuchamber) also have poor features which make them unattractive.
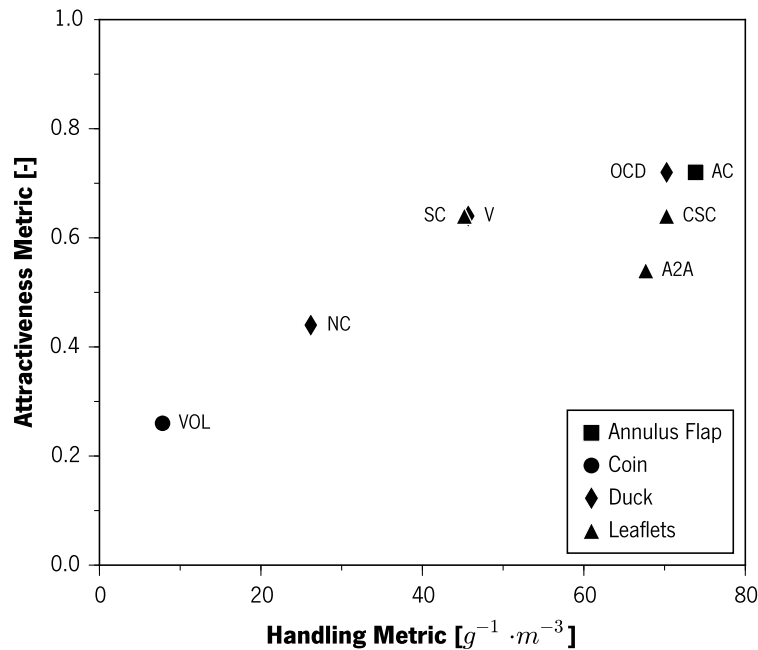
Figure 6.45: Attractiveness versus Handling metrics for VHCs

Another approach for the device evaluation is concerned to its efficiency, as one can assess the VHC by the cost of the daily therapy. The British pound (£) was the chosen monetary unit for this evaluation due to the fact that some of these devices are not available in Portugal. If a given patient uses the device twice a day, firing it twice, he uses 4 actuations per day (considering that a canister of 200 doses of salbutamol costs around 1.5 £) therefore the daily treatment cost is around 0.03 £. Adding this value to the daily cost of having a VHC (i.e. divide the device price by 12 months of advisable maximum usage), a measure of the cost of treatment is obtained. Taking the effective amount of drug inhaled daily (i.e. 4 times the FPM) and dividing it by the daily cost of treatment an interesting metric can be obtained. This gives the amount of drug per pound that a patient will obtain using that particular VHC device.

Figure 6.46 reports the comparison between these two patient relevant metrics for the four tested devices under breath simulated conditions. The most interesting devices are found in the right upper corner, while the least are found in the opposite corner. Volumatic is the device with the lowest handling and attractiveness; however it delivers a high amount of salbutamol per pound. The Vortex has a reasonable handling and attractiveness value and delivers the lesser amount of

salbutamol per pound in a daily treatment. The highest handling is found for the Aerochamber, although the cost of the device makes the daily treatment more expensive than other market alternatives.
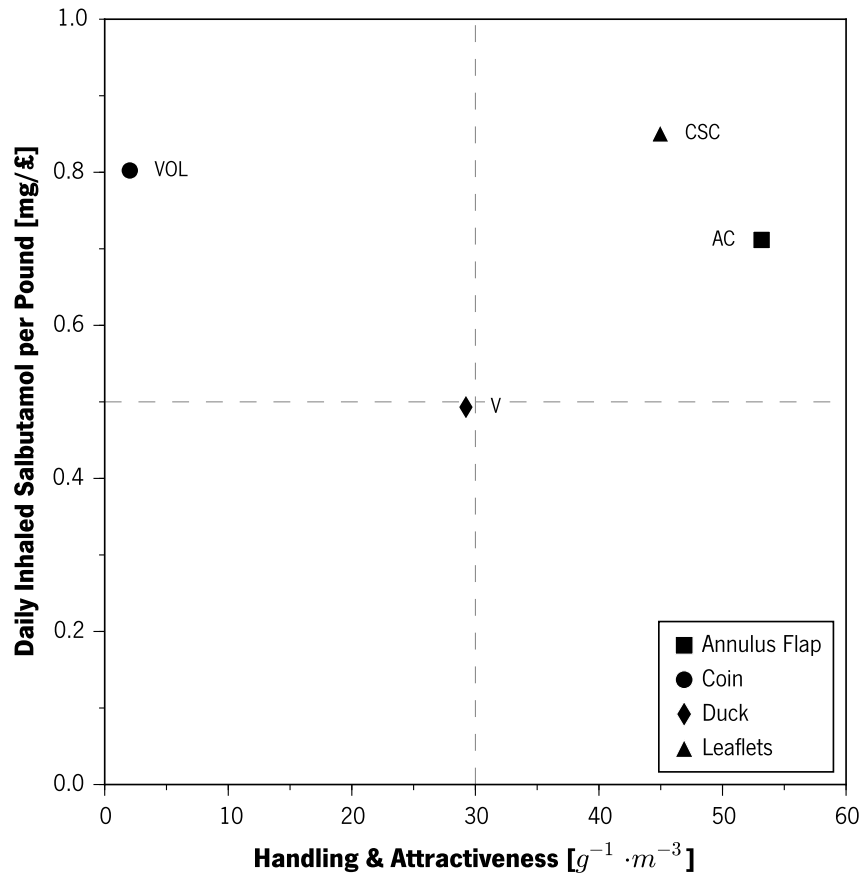
Figure 6.46: Salbutamol per pound of daily treatment versus Handling for the VHC tested under breath simulated conditions

This page was intentionally left in blank

7 Numerical Results

This chapter focus in the presentation and discussion of the numerical results obtained through the CFD simulations. These are focused on the analysis of various geometries. The results are organised into velocity, evaporation, validation and drug delivery. They can be depicted as:

- contours of a cross-section plane or surface within the geometries;
- profiles obtained from data sample along domain section lines;
- drug deposition information processed from collection files located at the boundaries of the domain;
- efficiency deposition device curve.

7.1 Velocity

The simulations were initialised with the boundary conditions defined in section 3.5, and the axial velocity profiles were assessed, over time, in different zones of the domain until a convergence of the field was reached. Convergence was obtained within 0.6 seconds and the velocity results were all took from at this moment (t = 0.6 s).

7.1.1   Contours and Streamlines

Figure 7.1 depicts the velocity magnitude contours along the symmetry plane for all the devices assessed. The contours are represented as a logarithmic greyscale for better representation of the low velocity zones (units are presented in m/s).

Figure 7.1: Compared velocity magnitude contours along the symmetry plane for all devices assessed (t = 0.6 s)

In the pMDI solo geometry, the air enters the domain at a relatively high velocity (i.e. $\approx$3.2 m/s), and upon a sudden expansion of the USP throat the velocity slightly decreases, before reaching a new maximum of 5.3 m/s at the 90 degrees bend. At this location the flow becomes very

complex due to the boundary layer detachment that leads to recirculation zones near the sharp corners of the bend. Downstream the cross-section of the USP throat increas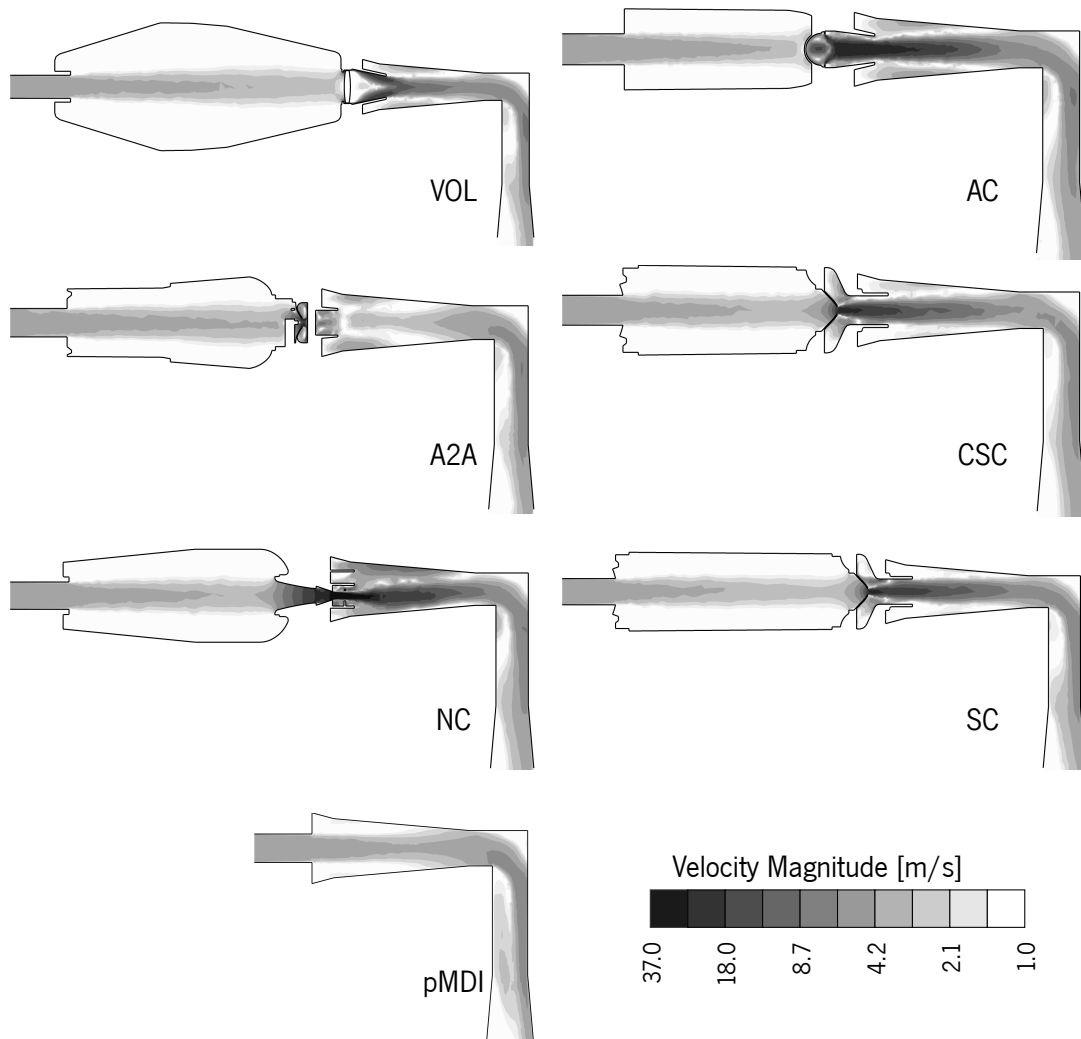es in diameter and the flow stabilizes reducing the recirculation zones, also lowering the velocity. At the bend, the air stream is directed towards the outside descending wall and this is the major reason for the particle impaction on this wall. Stagnation zones can be found at the entrance walls of the USP throat, whereas the velocity magnitude is close to zero.

Results for the VHCs are somewhat different, mostly due to the existence of a valve zone that greatly reduces the air flow cross-section, as a consequence increases the air velocity. The maximum velocity is found for the Nebuchamber (i.e. ≈37 m/s), followed by the Aerochamber (i.e. ≈30 m/s), A2A Spacer (i.e. ≈27 m/s), Volumatic (i.e. ≈24 m/s) and both Space Chambers (i.e. ≈22 m/s). As previously noted the measurement of the open valve position (for the corresponding flow rate) was not very accurate in the case of the Aerochamber and Volumatic. This influences the domain drawing and the cross-section at the valve zone, which might lead to misleading values of velocity in this zone. Therefore the validity of the results should be gauged within such limitations. The velocity contours in the VHC bodies are similar between them, whereas a high velocity air jet is found along the centreline of the body and lower air velocities near the walls (i.e. close to zero). Further analysis of the centre jet contours, shows it is possible to observe that for both the Compact Space Chamber and the Space Chamber, the air jet velocity reduces with the increase of the body length. The increase in the length might lead to improved particle evaporation and emission of finer spray plumes. The Volumatic presents similar contours due to the higher body length and volume.

As the throat deposition might depend on the air jet downstream the valve. The Aerochamber, Space Chambers and Volumatic appear to present the most symmetric and uniform pattern. Whereas, the Nebuchamber mouthpiece design yields a misalignment of the air jet with the throat centreline, which might lead to higher throat deposition.

Figure 7.2 depicts the velocity magnitude contours of half of the symmetry plane and the perpendicular plane both intersecting at the geometry centreline (i.e. x-axis). On the upper portion of the geometry (i.e. y > 0) several air flow streamlines were represented to illustrate the three

dimensional air flow patterns. The streamlines are coloured in black and the velocity contours are coloured in a logarithmic greyscale; units in m/s. The wall surfaces are represented in solid grey, and the valve surfaces are set with a transparency of 60%.
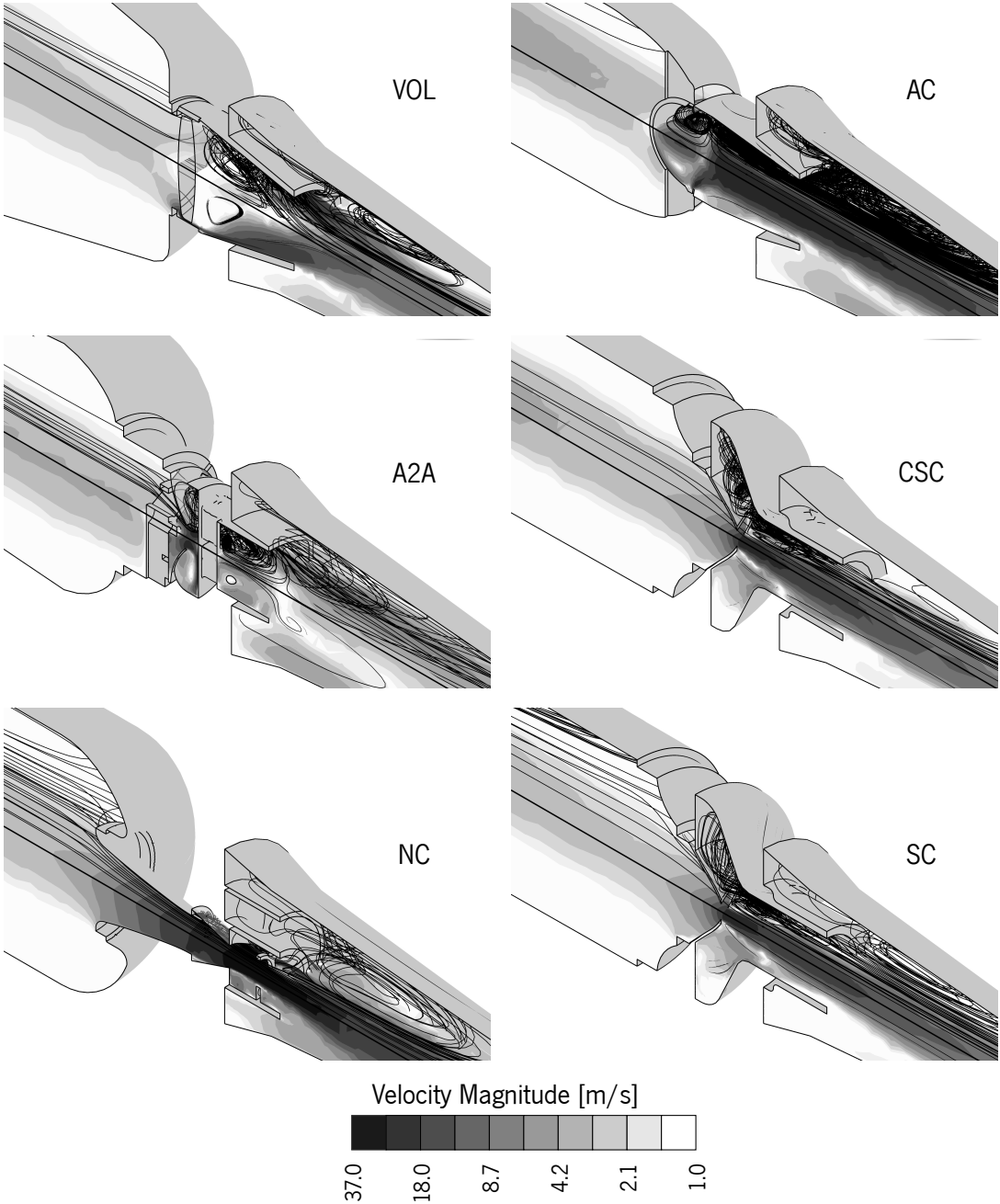

Figure 7.2: Velocity magnitude contours in two perpendicular planes (XY and XZ) intersecting in the centreline along with air flow streamlines, for all VHC devices numerically assessed (t = 0.6 s)

The results bring more three-dimensional detail into the velocity contours, specifically in cases where the geometry of the valve is not easily understood from the 2-D views (i.e. A2A Spacer, Space Chambers, Aerochamber). Valve's designs based in an obstacle (i.e. those without a open centre design) such as, Coin (i.e. Volumatic) and Annulus Flap (i.e. Aerochamber) or when an impaction zone is added downstream the valve (i.e. A2A Spacer), result in recirculation patterns downstream the cross-section contraction zone. These recirculation zones can lead to higher entrapment of drug particles and generation of turbulence, which can potentially be mitigated by removing obstacles downstream and smoothing the valve downstream design for later boundary layer reattachment, as suggested by designs from Oliveira (2012) [OTS+12].

7.1.2 Profiles

Figure 7.3 depicts the axial velocity along the centreline (i.e. x-axis) for each VHC domain. The axial distance was normalised and two grey shadowed areas identify the regions corresponding to the VHC body length and USP throat zone. The velocity units are m/s and the white region corresponds to the valve zone.

The velocity centreline profiles are relatively low in the VHC body, as previously observed in the contours, and rapidly increase to a maximum in the valve region. Negative values indicate that recirculation is present, which is noticeable for the A2A Spacer, Aerochamber and Volumatic (as previously observed in the streamlines behaviour). The Nebuchamber is the VHC with highest velocity at the valve centreline. Downstream of the valve, the axial velocity gradually reduces until it reaches a zero, which corresponds to the 90 degrees bend of the throat, where the flow changes direction. Results from A2A Spacer are the hardest to analyse. Due to the geometric configuration. In fact, the existence of several obstacles along the centreline, diverts the flow to go around them, making the centreline axial velocity extremely low.

Figure 7.4 shows the axial velocity took along three vertical lines, each one corresponding to a portion of the VHC body length (i.e. X/L = 0.3, 0.6 and 0.9). The radial coordinate was normalised by the local radius and the velocity is in m/s.
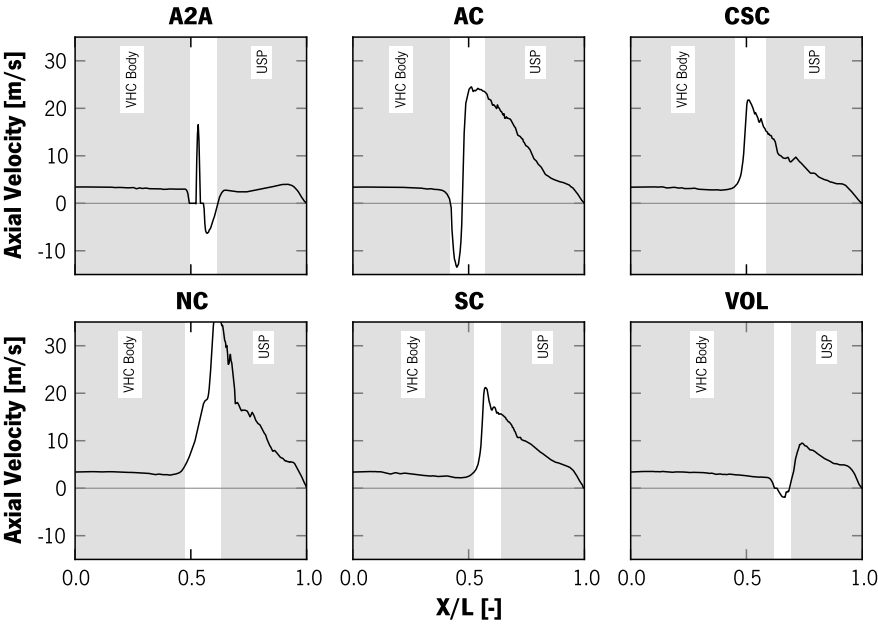
Figure 7.3: Axial velocity for six VHC, normalised along the centreline axis of each geometry. Shadowed grey areas represent the VHC body and USP throat lengths (t = 0.6 s)
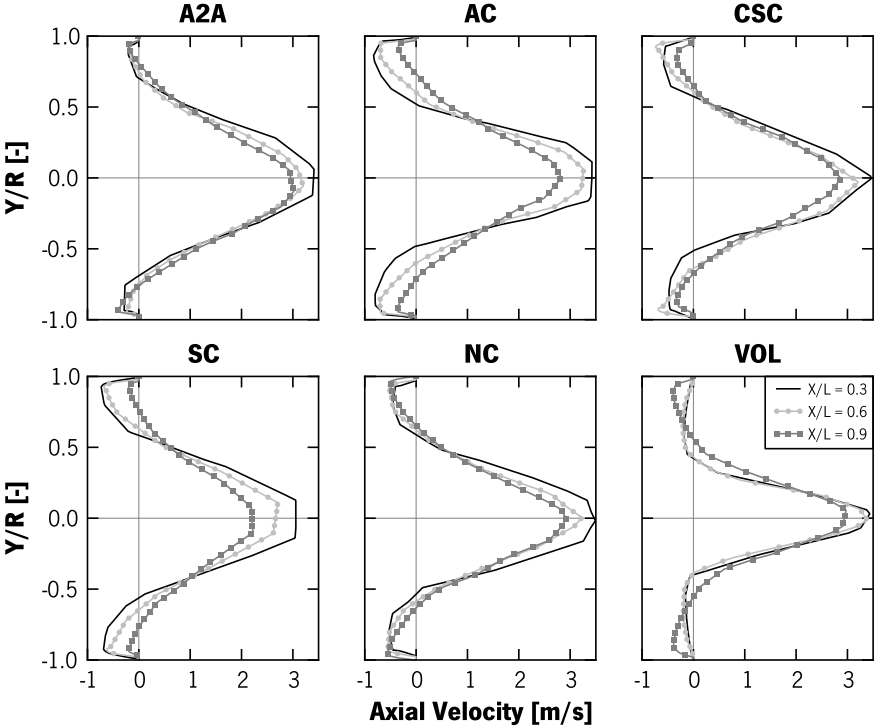
Figure 7.4: Axial velocity profiles for six VHC, normalised by the local radius axis of each geometry, at three distances (t = 0.6 s)

The velocity profiles along cross sections of the VHC body enables a rapid assessment of the proportion of the domain under recirculation, by the negative axial velocity values. It was verified that the recirculation zone tend to diminish along the body length. The Volumatic geometry has the greatest recirculation zone, followed by the Aerochamber, both Space Chambers, the Nebuchamber and the A2A Spacer. The profiles also identify that the flow inside the VHC bodies is practically symmetrical, whereas it slightly deviates for devices with non-axisymmetric geometry (i.e. A2A Spacer). Also it can also be identified a reduction of the axial velocity along the body length.

7.2 Evaporation

7.2.1 Profiles

For understanding the evaporation process during the spray release inside the VHC devices, the volume averaged HFA gas mass fraction was assessed over the time.

Results are depicted in Figure 7.5 for the Aerochamber, A2A Spacer and Volumatic devices. The shadowed area represents the duration of the pMDI spray injection. The HFA rapidly increases during the injection period where the peak is reached. Subsequently the propellant mass fraction inside the domain starts to diminish caused by the air renovation (i.e. at 60 L/min). The ratio on which the HFA leaves the domain clearly depends on the geometry shape and, mostly, of the VHC volume. The A2A Spacer and the Aerochamber have a similar rate of HFA decay, since they have similar volumes. However, the Volumatic high volume makes it harder for the HFA to rapidly leave the domain. This is identified by the instant at which the HFA reaches zero, which happens at 2.0 s for the Aerochamber, 2.8 s for the A2A Spacer and >4.0 s for the Volumatic.
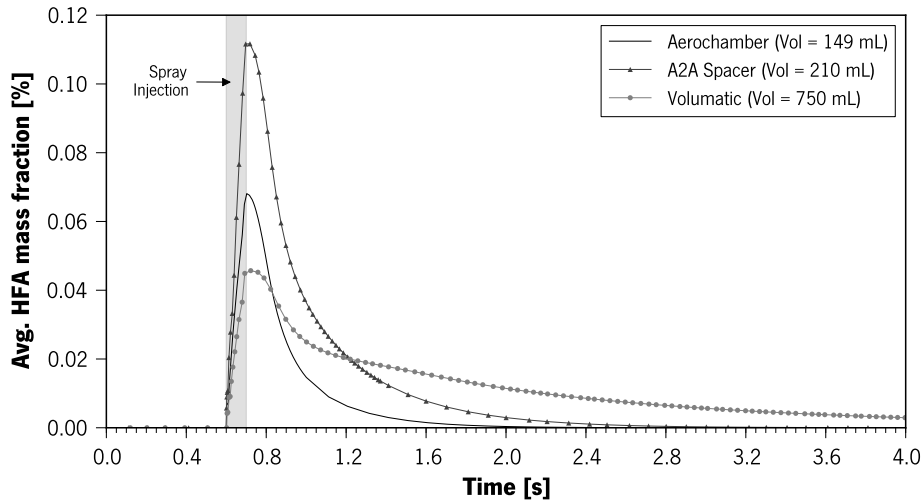
Figure 7.5: The variation of HFA mass fraction averaged over volume for the Volumatic, A2A Spacer and Aerochamber

7.2.2   Contours

Figure 7.6 depicts time evolution of the HFA mass fraction contours for the A2A Spacer, Aerochamber and Volumatic domain. The contours are displayed in a linear greyscale to a maximum of 0.15%, whereas in the initial injection moments the high values (i.e. up to 2%) saturate the contours. During the initial moments of the injection, the HFA rapidly expands throughout the domain. At the end of the injection (i.e. t = 0.69 s) all the Aerochamber volume contain HFA gas, which is due to the elevated recirculation velocities within this device and its small volume. When compared with the A2A Spacer, the region behind the spray injection cone is absent of HFA (t = 0.69 s), which only diffuses later (t = 0.8 s). For the Volumatic this is only verified much later (t = 1.5 s). The HFA reaches the lower portion of the throat firstly for the Aerochamber, followed by the A2A Spacer and finally the Volumatic. The upper portion of the throat is more densely filled with HFA in the case of the A2A Spacer, which may be related with the valve design (i.e. Leaflets - open centre design). The Aerochamber impaction cup, forces the HFA evaporation to occur mostly inside the VHC body, reducing the high concentration of the propellant in the throat zone (t = 0.69 s). At 4.0 s, the Volumatic still shows some concentration of propellant, while Aerochamber HFA concentration reaches a minimum at 1.5 s, as previously discussed (see Figure 7.5).
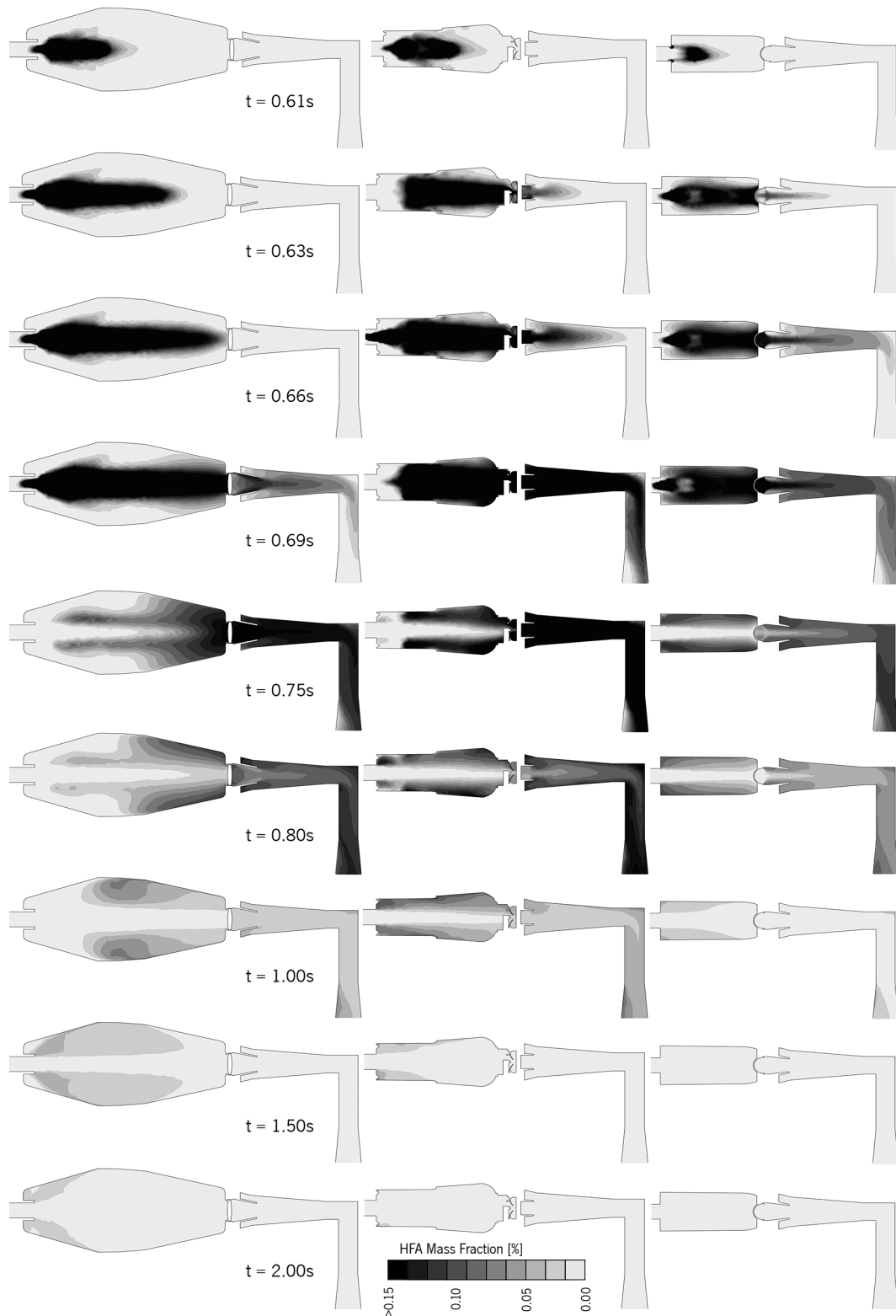
Figure 7.6: HFA gas contours over time for the Volumatic, A2A Spacer and Aerochamber from left to right, respectively

7.3   Validation

This section reports the comparison between the CFD results and the experimental data presented in chapter 6.2.2. Also, some numerical results are compared with available data (experimental and numerical) from the literature.

7.3.1   CFD versus Literature

Impaction Parameter vs Deposition Efficiency

The numerical results were compared against several literature sources in terms of Impact Parameter versus the Deposition Efficiency defined as in Equation 7.1.

$$\text{Deposition Efficiency} = \frac{\text{Entraped Mass}}{\text{Total Mass}} \tag{7.1}$$

For a particle size distribution injected into the domain, the mass of a certain particle size trapped in a surface (i.e. USP IP) is evaluated and divided by the mass injected for the same particle size. This ratio provides the efficiency of deposition for a certain particle diameter crossing that particular geometry. The Impaction Parameter is simply the air flow rate multiplied by square of the particle diameter ($d_p^2 \cdot Q$ - $\mu m^2 \cdot L \cdot min^{-1}$). This shall result in a sigmoid shaped curve, which represents free passage of particles with a small Impaction Parameter and the entrapment of particles with high Impact Parameter values. This curve is characteristic for a given geometry. Figure 7.7 reports the pMDI solo CFD data using a USP IP geometry and its corresponding data fitting curve using a Weibull function. Additionally, it can be found the results for a CFD simulation of a USP IP by Longest (2008) [LHDX08], and the experimental results from Cheng (2015) with the same geometry [CZS15]. Other numerical results for Realistic Casts of the human throat made with anatomical data [LHDX08, ZKKC04, FWZS07] and numerical prediction for an AIT geometry [MFLG04], were added.
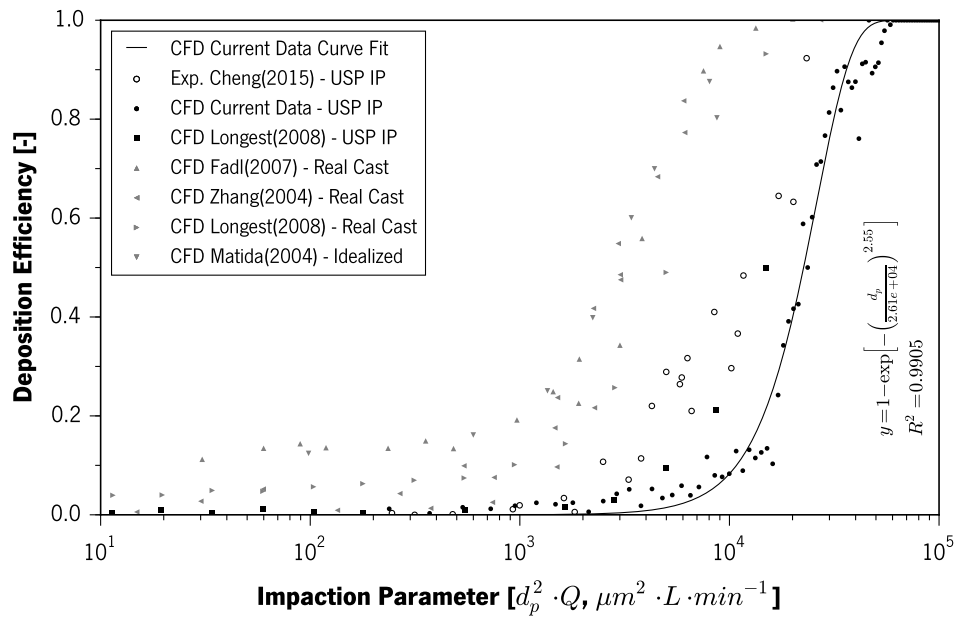
Figure 7.7: Deposition Efficiency versus Impaction Parameter for the USP IP against literature data

The CFD results from this work seems to make a fairly good prediction in comparison to the USP IP data from literature. However, the numerical predictions are globally underestimating the deposition of particles with small impaction parameter. The data fitting curve has a good coefficient of determination (i.e. $R^2 = 0.9905$).

Stokes Number versus Deposition Efficiency

The CFD data were compared against Cheng (2015) experimental assessment of the USP IP geometry in terms of deposition efficiency versus Stokes number (Stk) (see Equation 7.2).

$$\text{Stk} = \frac{\rho_p C_c d_p^2 U_{inlet}}{9\mu_f D_{min}} \tag{7.2}$$

Where the $U_{inlet} = 4Q/\pi D_{inlet}^2$ is the estimated velocity at the entrance of the geometry and C_c stands for the Cunningham slip correction factor (see Equation 3.84).

Figure 7.8 depicts the numerical results of this study versus the experimental data of Cheng (2015)

[CZS15]. The curve fit of the CFD data was made using a Weibull function and the coefficient of determination indicates a good fit (i.e. $R^2 = 0.9905$). The numerical prediction shows lower deposition efficiency for higher Stokes numbers, underestimating the deposition data from Cheng.
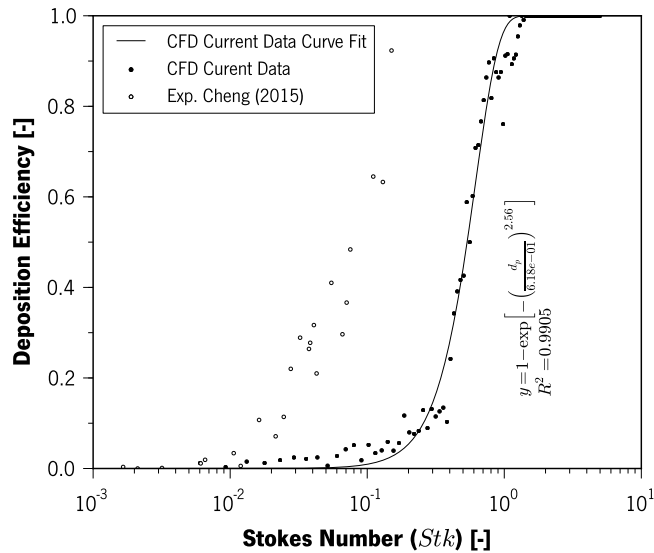
Figure 7.8: Stokes Number versus Deposition Efficiency for the USP IP against literature data

7.3.2 Experimental versus Numerical

In this section it is reported the comparison between experimental data and the numerical predictions, firstly regarding the different wall models used for handling the particle collision phenomena and lastly the drug deposition in the VHCs, throat and SM.

Comparison of Wall Models

The wall-particle interaction models tested were:

- (1) Reflect;
- (2) Trap;
- (3) Evaporation Model (any particle not fully evaporated, would behave like Trap, otherwise would be Reflect);
- (4) Evaporation Model plus Tangential Lift-off Ratio Model (any particle not fully evaporated

or with Tangential Lift-off Ratio ≥ 1.0, would be Trap otherwise Reflect);

- (5) Evaporation Model plus Critical Velocity Model (any particle not fully evaporated or with wall normal velocity component ≤ than the critical velocity, would be Trap otherwise Reflect);

Figure 7.9 shows the SM emitted by the pMDI solo and the Compact Space Chamber geometries, when five different types of wall configurations were used to handle the wall-particle interaction. Additionally, the experimental data along with its corresponding uncertainty, is given.

Using Reflect condition leads to the highest output of mass from the domain, as expected. Whereas the difference in mass (i.e. the missing injected mass to reach 100 μg) suggests that several drug particles are inside recirculation zones or hovering above lower horizontal surfaces, given the fact that no particle entrapment occurs at any surface of the domain. In the case of the pMDI solo, the rank of the closest to experimental data is: (2) – (3) – (4) – (5) – (1). Whereas in the case of the Compact Space Chamber the rank is: (3) – (5) – (2) – (4) – (1). Upon these data, the best wall model for the SM is (2 – Trap) or (3 – Evaporation Model).
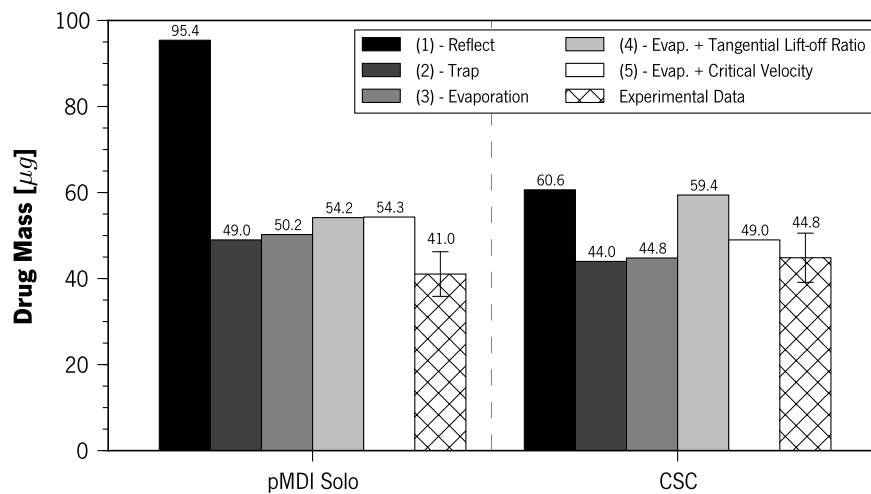
Figure 7.9: SM exited the domain using different particle-wall collision models

Figure 7.10 depicts the influence of the same wall models on the mass entrapped on the USP IP walls. The Reflect option is expected to provide zero deposition by definition. On the other side, the other wall models will vary between: the undiscriminating entrapment of any particle that collides, passing by the solely collection of liquid droplets, to the collection of liquid droplets

and solid particles of low wall normal velocity or upon the assessment of the forces equilibrium. For the pMDI solo case, the models rank as: (3) – (2) – (4) – (5) – (1). For the Compact Space Chamber case, they rank as: (3) – (2) – (5) – (4) – (1). Model (3) might be the best option for the prediction of drug entrapment in the USP throat surfaces.
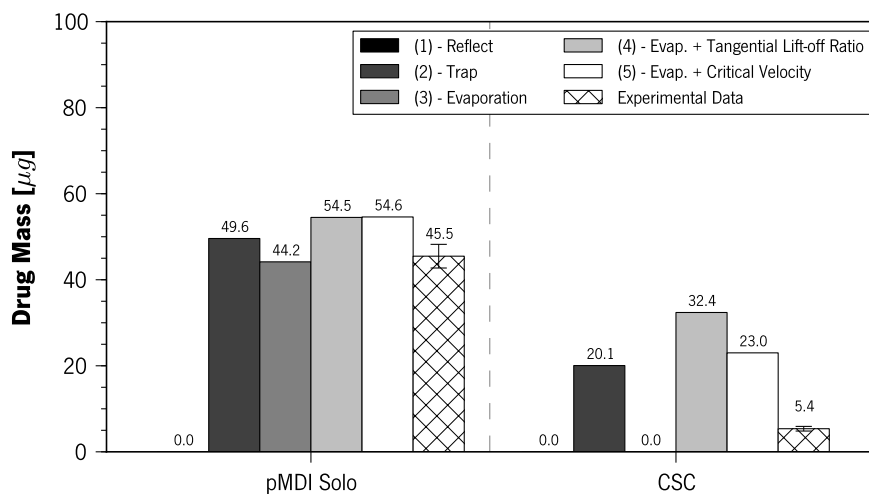
Figure 7.10: Mass entrapped in the USP throat using different particle-wall collision models

Based on the previous comparisons, the best model to be used in the simulations seems to be the Evaporation criteria, which will only entrap droplets whose evaporation process is not fully completed.

Figure 7.11 depicts the Deposition Efficiency versus the Impaction Parameter in the case of pMDI solo, for each wall-particle interaction model tested. A curve fit from Cheng (2015) experimental data was added to estimate the accuracy of each wall model [CZS15]. These results indicate that the previous conclusions, regarding the best wall model (3 - Evaporation), are not supported. This approach sets a threshold on the collection efficiency, based on the evaporation process being completed or not, resulting in a underestimation for particles with Impaction Parameter values below 1.5E4 μm$^2 \cdot$ L $\cdot$ min^{-1}. The other models seem to have a very similar performance, whereas the (2 – Trap) model predictions show highest oscillation in the values.
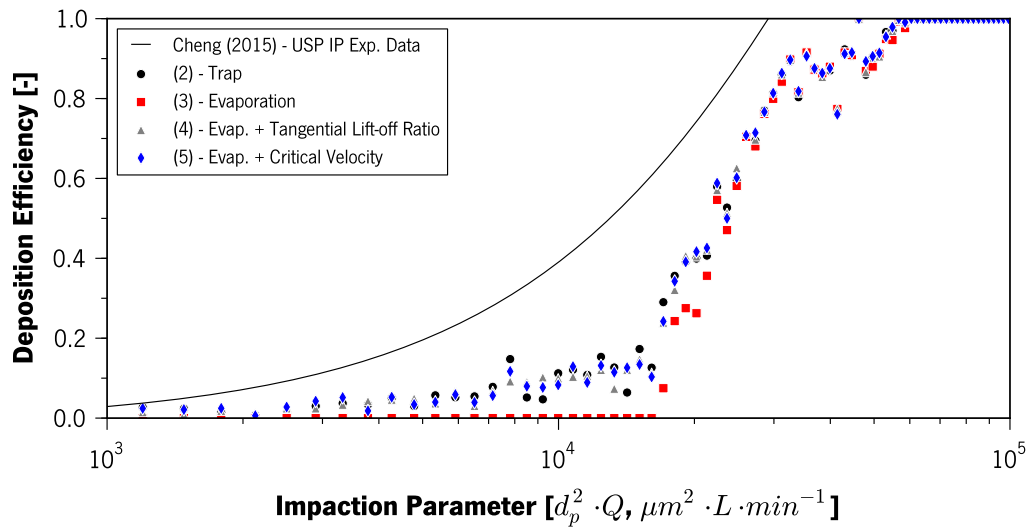
Figure 7.11: Deposition efficiency versus impaction parameter for the wall models tested in the USP throat

Figure 7.12 depicts the Deposition Efficiency versus the Impaction Parameter in the case of Compact Space Chamber, for each wall-particle interaction model tested. The results show the Deposition Efficiency on the VHC walls. It can be observed a very distinct behaviour between the wall models, which differ from the previous results. The underestimation effect of model (3) in the deposition efficiency of particles with small Impaction Parameter is more noticeable. On the hand, model (4) strongly underestimates the deposition of particles with high Impaction Parameter. This behaviour renders these two models lesser adequate for modelling the particle-wall interaction on the VHC surfaces, since it was expected that a VHC device would entrap more coarser particles than smaller ones. The other models have a similar trend.

By evaluating the effect of wall models on the Deposition Efficiency, for pMDI solo or Compact Space Chamber cases, it can be concluded that the best models are (2) and (5). Together with the previous conclusions from the drug deposition in the surfaces versus the experimental data, the model (5) was considered the best fit and used throughout the rest of the study herein reported.
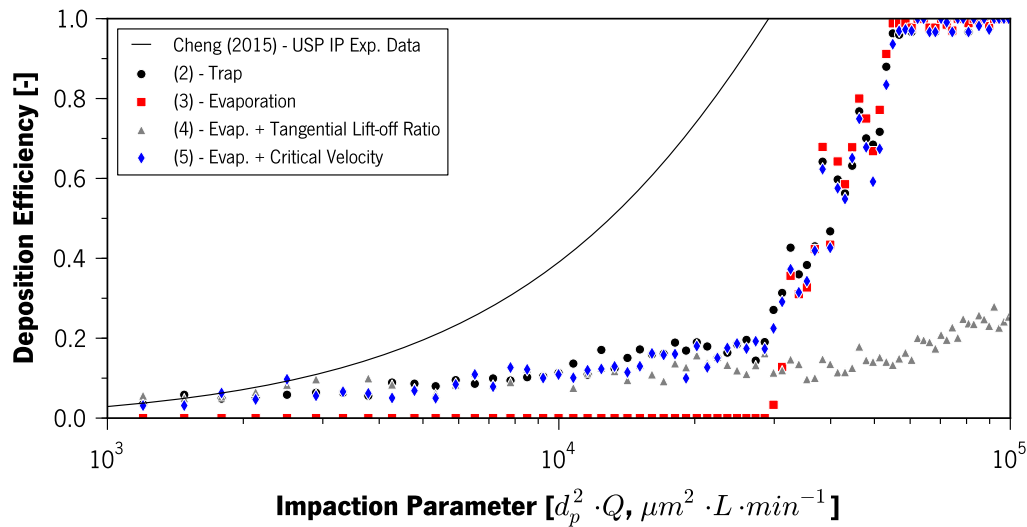
Figure 7.12: Deposition Efficiency versus Impaction Parameter for the wall models tested in the Compact Space Chamber

Drug Deposition

Taking data from the experimental assessment at 60 L/min, Figure 7.13 provides a direct comparison against the numerical predictions, for the VHC device, USP Throat and Sizable Mass (SM). The experimental data were presented together with theirs experimental uncertainty, shown as error bars.

Starting by the VHC deposition, the numerical model appears to generally underestimate the deposition inside the device. This might be linked to the wall model, which is the same applied to all surfaces and which does not consider extra forces, such as, the electrostatic attraction or adhesion forces caused by humidity. Spray parameters are other source of uncertainty like injection velocity, which was modelled as constant over time (i.e. a solver limitation) contrarily to what was experimentally observed [CJM09]. Also the spray angle and size distribution might not be accurate. Other strongly influential fact is that all droplets were modelled with the same mass fraction of API (i.e. a solver limitation), which is known not to be true [SSM12]. Analysing the results, it is observed that the calculated drug entrapment inside the device is closely related to experimental data for the Aerochamber (3.0 μg) and Space Chambers (5.1 μg and 6.9 μg), while a large deviation is observed for the Volumatic (19.6 μg) and Nebuchamber (19.3 μg).

The Volumatic is the device with highest volume, which will reduce greatly the spray impaction deposition. However, the electrostatic attraction force which is not accounted for in the wall models, may be the reason behind the great deviation of numerical prediction from the experimental results. In the Volumatic (a polycarbonate device - non-dissipative polymer) case this is more noticeable due to its high surface area. The Nebuchamber deviation from the experimental results might be explained with the lack of consideration, in the numerical model, of the surface roughness in the particle entrapment. Aluminium shaped devices have higher roughness than those produced by mould injection [BK07].
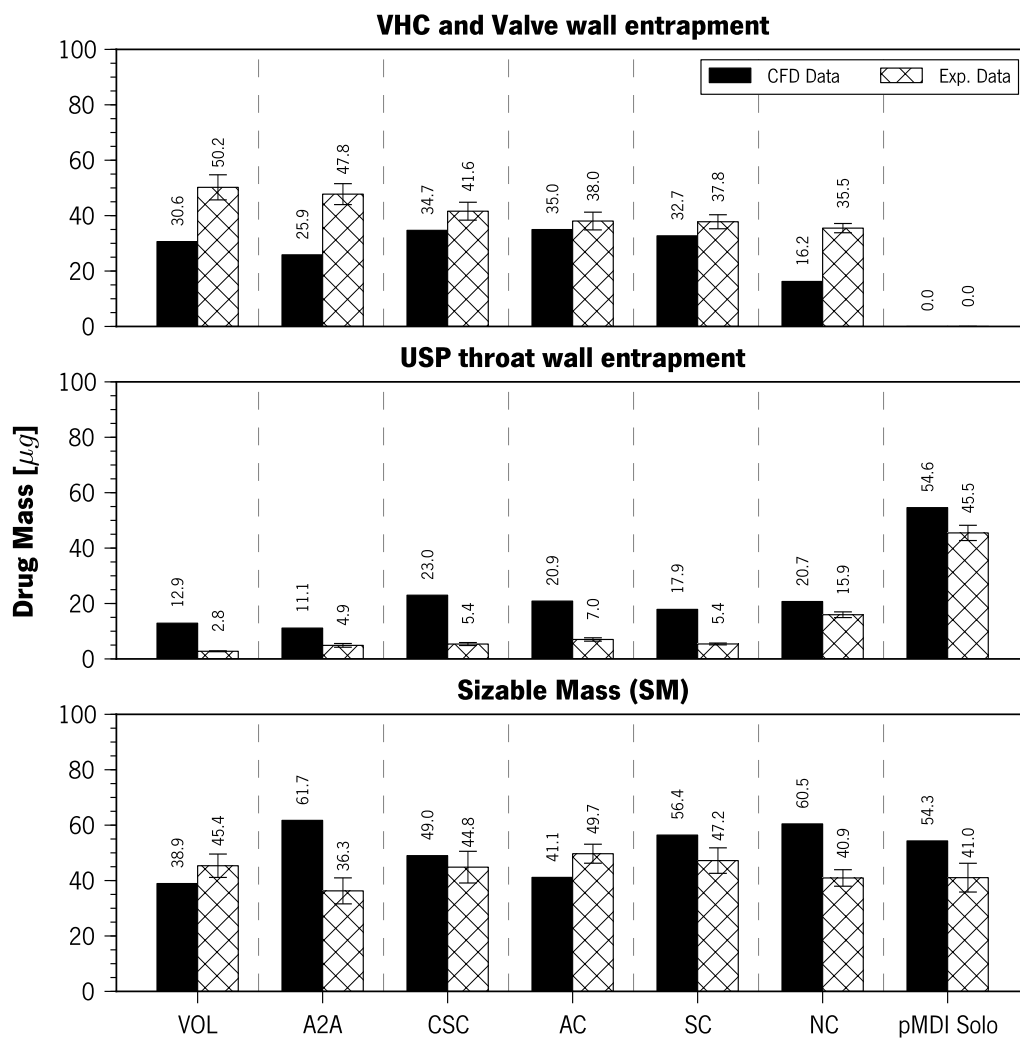

Figure 7.13: Experimental mass deposition versus CFD at three different zones, for all the assessed devices

The numerically predicted drug entrapment in USP Throat is globally overestimated when compared with the experimental results. The highest deviations are found for Compact Space Chamber (17.6 µg), Aerochamber (13.9 µg) and Space Chamber (12.5 µg); while the lowest are found for the Nebuchamber (4.8 µg) and A2A Spacer (6.2 µg). The deviations may arise from several factors:

- air flow downstream the valve is dependent on the valve opening dimensions that might be not accurate (i.e. higher jet velocities lead to higher USP deposition);
- influence of the excess of mass emitted by the VHC;
- the wall model for the USP Throat surface is not correct and should be different from that applied to the VHC surfaces.

The predicted SM mass emitted from the geometries are a balance between the overestimation of the USP Throat deposition and the underestimation of the VHC devices deposition. The results are obviously strongly influenced by the deposition on the previous stages. Nevertheless the lower deviation is found for the Compact Space Chamber (4.2 µg) and Volumatic (6.5 µg). The highest deviation is found for A2A Spacer (25.4 µg).

7.4 Drug Deposition Evaluation

The numerical results for the drug deposition were processed from collection files set at the VHC Body and Valve surfaces, USP throat surfaces and at the exit of the domain that corresponds to the drug mass passing to the MSLI, i.e. the SM. Upon the post processing of these files using sub-routines in Python language, the results were assessed in terms of total mass, emitted distribution, deposition location, and impaction parameter. All results correspond to a time of 4 seconds.

Figure 7.14 depicts the amount of mass collected in four zones of the domain, for each on of the geometries. It can be seen that using pMDI solo results in half of the drug dosage loss by throat entrapment through impaction. The majority of the particles are liquid and did not have enough volume to evaporate and decelerate before colliding against the USP throat walls. Throat deposition in the cases where the VHC device was present are completely distinct, ranging from

11.1 µg (i.e. A2A Spacer) to 23.0 µg (i.e. Compact Space Chamber). The use of the VHC reduced the throat deposition between 57.9% and 79.7%.

Valve deposition is higher for the Volumatic (8.0 µg), followed by the A2A Spacer (3.2 µg), Aerochamber (3.1 µg), Compact Space Chamber (3.0 µg), SpaceChamber (2.3 µg) and Nebuchamber (1.8 µg). This supports the previous conclusion, that valves with non-open centre design or with centralised obstacles downstream create recirculation areas that entrap more particles than other designs. Valves that create a major obstacle for the air flow are obviously zones of increased deposition by impaction, such is the case of the Volumatic Coin valve design.
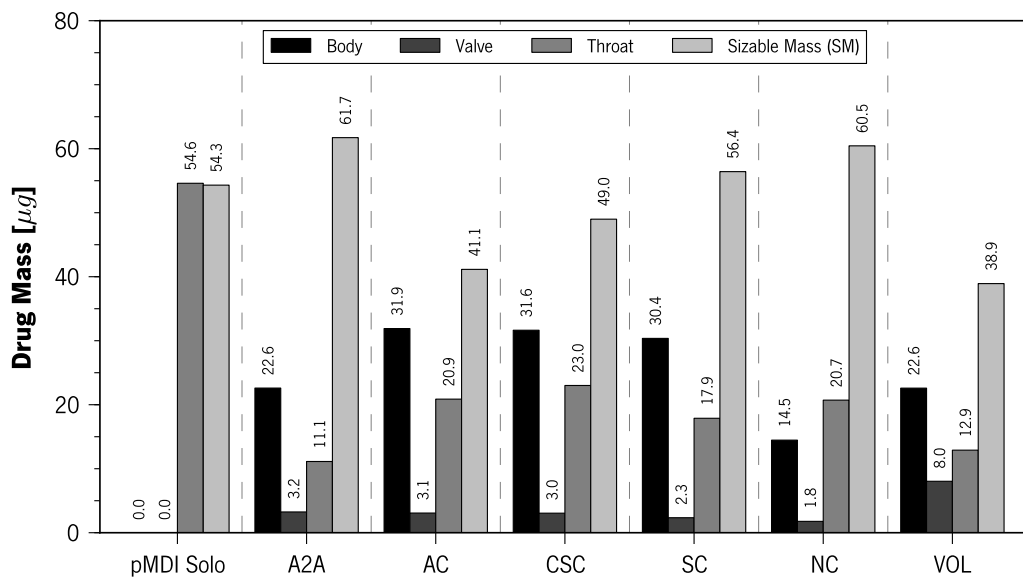
Figure 7.14: Numerical prediction of the mass collected in each zone of the domain for the different geometries (t = 4 s)

VHC Body deposition ranges as Aerochamber (31.9 µg) > Compact SpaceChamber (31.6 µg) > SpaceChamber (30.4 µg) > Volumatic (22.6 µg) > A2A Spacer (22.6 µg) > Nebuchamber (14.5 µg). The results are strongly related with the impaction distance of each device, i.e. the body length and diameter.

The SM is the amount of drug entering the MSLI (or another CI), which is the equivalent to the patient lungs. The results show the highest value for the A2A Spacer (61.7 µg), and the lowest is found for

the Volumatic (38.9 μg). Experimentally the results point to opposite conclusions, which indicates that the wall model used is missing some key parameter (such as the electrostatic attraction) and in addition some valve opening dimensions, may not be very accurate. Additionally, the wall model depends on the assumed Young Modulus and Poisson's Ratio values for the materials of each surface.

Figures 7.15 through 7.21 depict the particle drug deposition in the surfaces coloured by diameter, corresponding to pMDI solo, A2A Spacer, Aerochamber Compact Space Chamber, Nebuchamber, Space Chamber, and Volumatic respectively. Each figure is composed by an isometric view of the domain deposition and two closer views of the deposition upstream and downstream the device's valve.
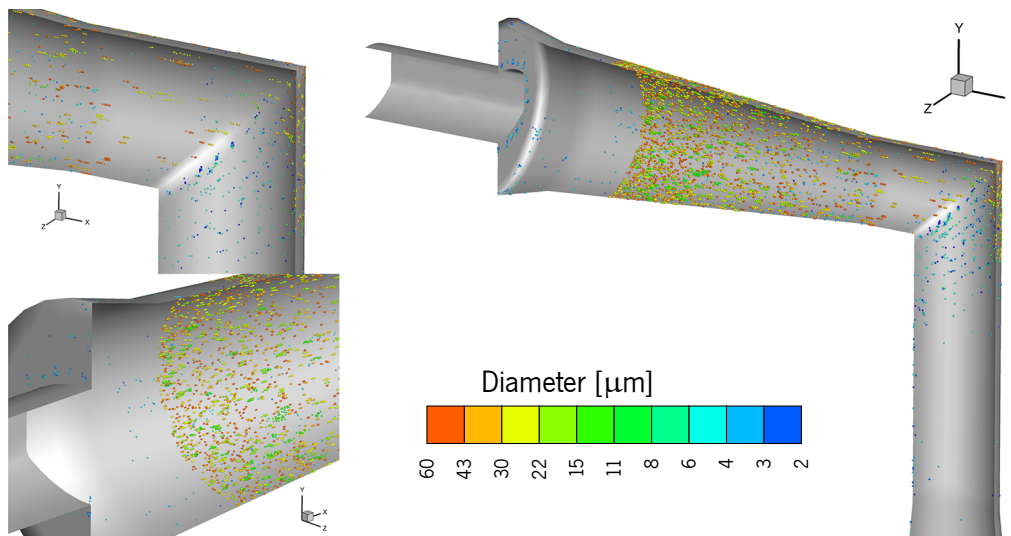
Figure 7.15: Particle deposition locations coloured by diameter for the pMDI solo geometry

From the previous results, it is known that the drug deposition in the throat is higher for the case where the pMDI is used without a VHC, this also can be observed in Figures 7.15 through 7.21. It is noticeable that the larger particles deposit mainly by impaction in the upper portion of the throat. In the case where a VHC is used, the VHC body deposition is mainly made by impaction of the bigger particles (i.e. >17 μm), and by sedimentation of those above 3 μm. The throat deposition when a VHC is used, is lower and is mainly composed by small particles (i.e. < 6 μm). Some devices, more than others, show a radially uniform deposition in the upper portion of the throat,

200

which indicates a more stable airflow downstream the of valve. A2A Spacer has the lowest throat deposition results (see Figure 7.14) as it can be observed in Figure 7.16. Throat deposition pattern is most uniform in the Aerochamber (see Figure 7.17).
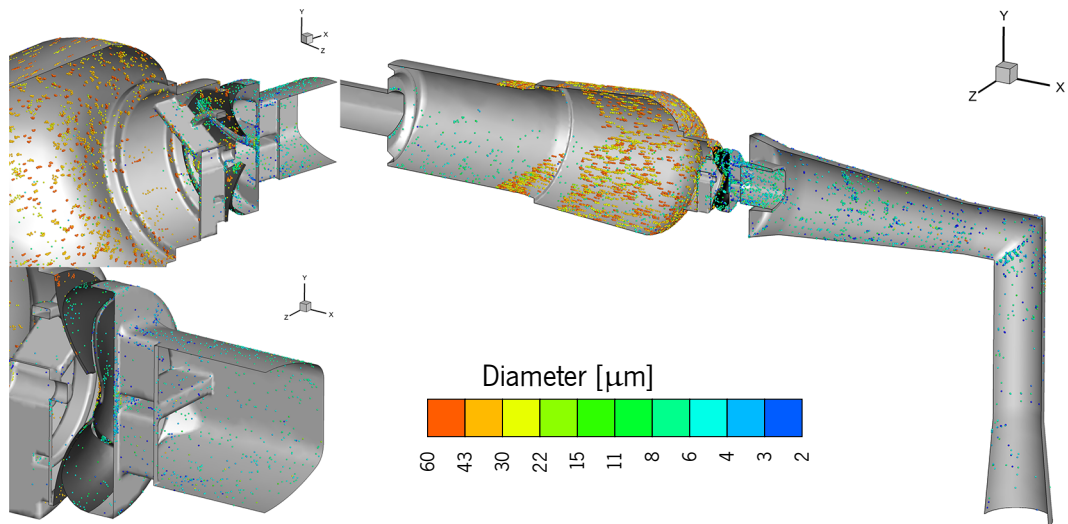
Figure 7.16: Particle deposition locations coloured by diameter for the A2A Spacer geometry
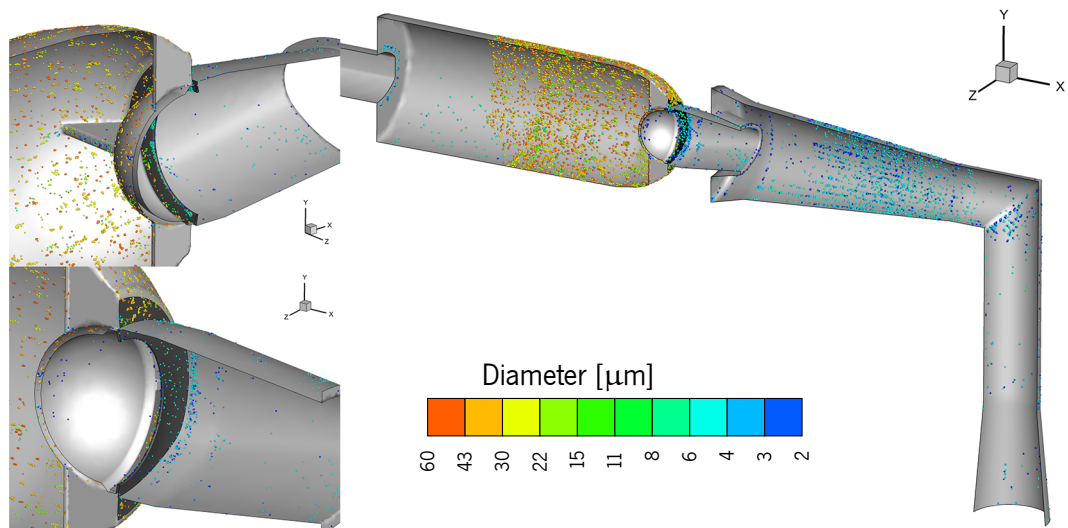
Figure 7.17: Particle deposition locations coloured by diameter for the Aerochamber geometry
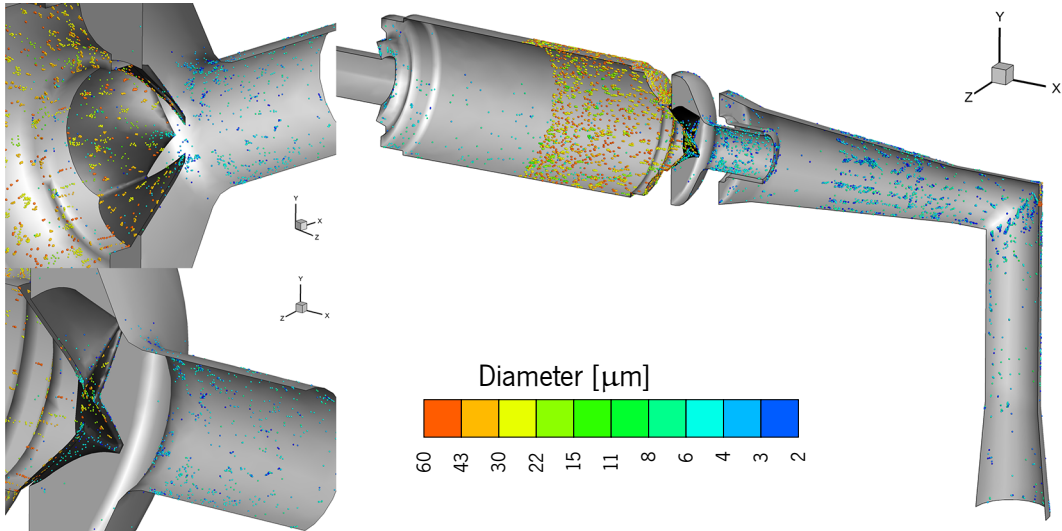
Figure 7.18: Particle deposition locations coloured by diameter for the Compact Space Chamber geometry
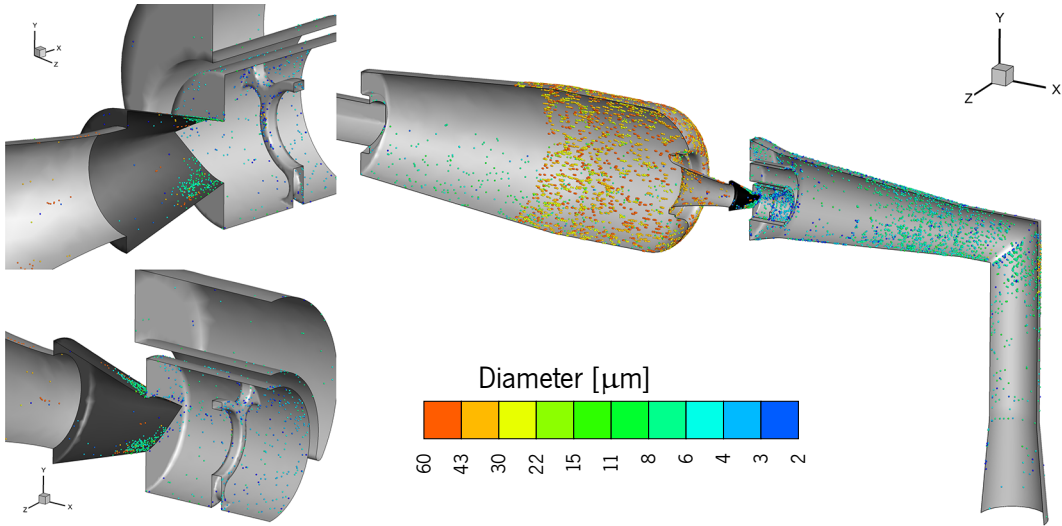
Figure 7.19: Particle deposition locations coloured by diameter for the Nebuchamber geometry
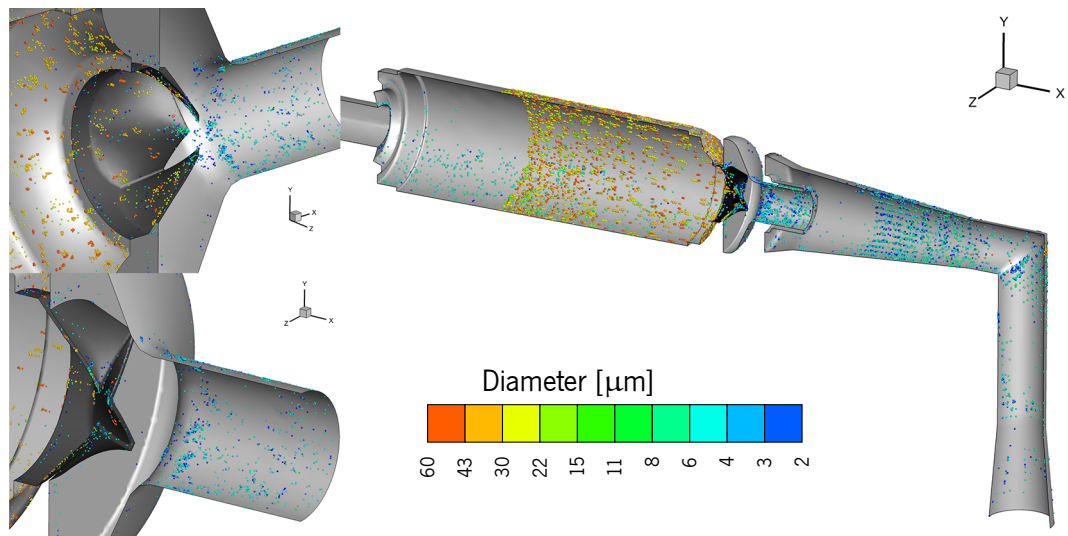
Figure 7.20: Particle deposition locations coloured by diameter for the Space Chamber geometry
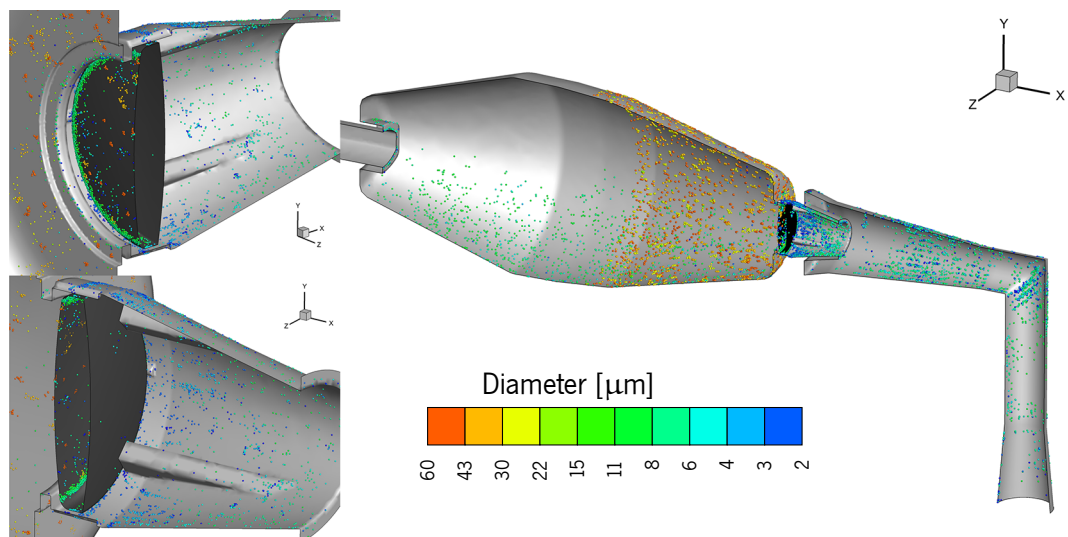
Figure 7.21: Particle deposition locations coloured by diameter for the Volumatic geometry

VHC valve deposition is more noticeable for particles with sizes around 7 μm, which may be due to the fact that those with higher diameter are entrapped inside the VHC body before they reach the valve, while the smallest can pass through the domain without colliding. In devices for which the valve geometry causes great recirculation downstream, it is noticeable that the deposition of smaller particles in the valve and mouthpiece is higher and more spatially scattered, as previously

hypothesised from the velocity streamline results. The Aerochamber impaction cup (closely located to the valve) illustrates the entrapment of high diameter particles (see Figure 7.17), reduce their oral deposition, as opposed to the open centre valve designs (see Figures 7.16, 7.18, 7.20 and 7.19).

Figure 7.22 depicts the Deposition Efficiency in the VHC surfaces (i.e. body and valve) versus the particle diameter (d_p). The Nebuchamber shows the lowest deposition efficiency for all
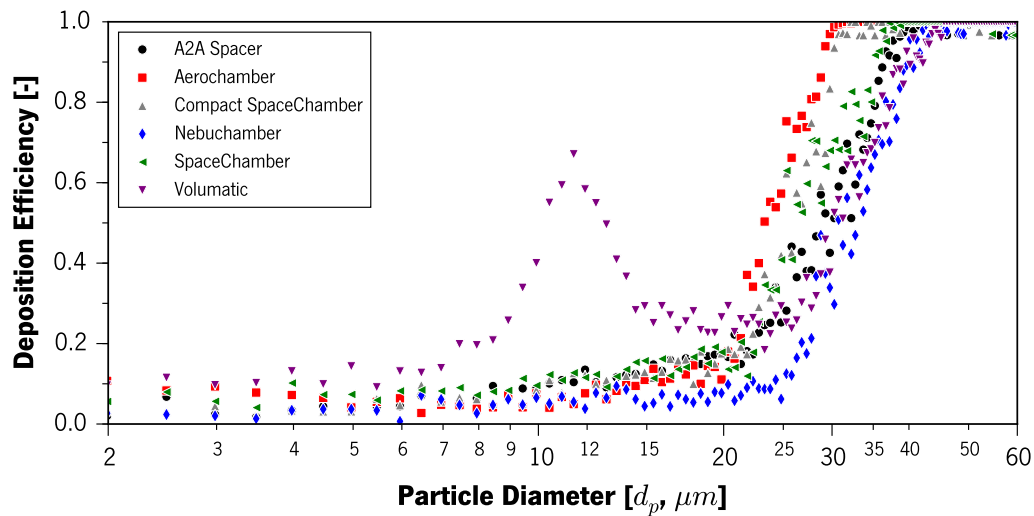
Figure 7.22: Deposition Efficiency versus the Impaction Parameter for the mass retrained by each VHC device (t = 4 s)

particle size range. The Aerochamber has the highest deposition for particles above 20 μm. Volumatic presents an unexplainable peak of deposition for particles around 11 μm. The other VHCs have similar deposition efficiency curves. Devices with open-centre valve design (i.e. Nebuchamber, A2A Spacer, Compact Space Chamber and Space Chamber) do not present 100% high diameter particle entrapment. Some of the higher size particles pass in the centre of the valve and impact in the USP IP.

8 Optimisation of the VHC Geometry Using CFD Models

8.1 DOE Study of VHC Body Shape

8.1.1 Geometry Definition

An idealised VHC geometry is given in Figure 8.1. This has smooth curves, $\overline{AB}$ for the expansion region and $\overline{BC}$ for the contraction region, connected at point B. The latter is a corner point of an expansion zone, and since one of the objectives of the VHC device is to reduce spray velocity, the greater the internal volume of the device the better it can perform this function. The further the point B is from the central axis, the greater this area shall be; however this increase comes with a weight cost (i.e. latter resulting in production, material, packing and shipping costs). Additionally, the radial distance of point B is directly connected to the increase of the recirculation area inside of the VHC body, due to the early flow detachment from wall [OTMT12]. The research hypothesis is that the increase of the recirculation area is strongly linked to the entrapment of small drug particles resulting in a reduction of the FPM emitted by the device. A previous study made with a dispersion of solid particles (without accounting for evaporation and complex wall models) did not found a correlation between both events [OTMT14b].
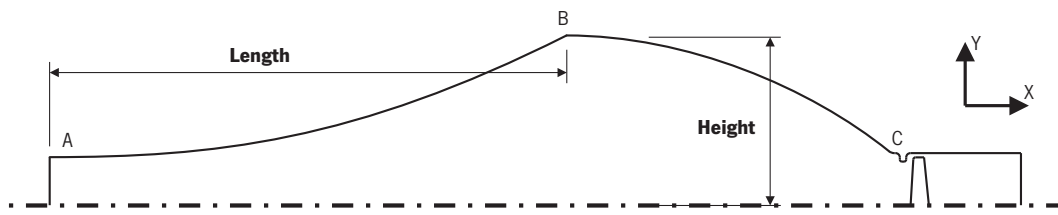
Figure 8.1: Geometry used in the design study

In the idealised geometry, several dimensions were kept constant, as well as some geometrical constraints were added. The valve was based in the Volumatic shape and size. The entrance ($\oslash$ 22.6 mm) and exit ($\oslash$ 24.5 mm) dimensions were based on those from a typical commercial VHC device. In the study herein, the position of point B is moved in length (axially) and height (radially) for different spatial geometrical combinations. Two quadratic curves were used as segments $\overline{AB}$ and $\overline{BC}$, with zero derivative in points A (for segment $\overline{AB}$) and B (for segment $\overline{BC}$). Additionally, all other dimensions were kept constant.

Geometric limits vary between a length of 30 mm to 150 mm, and a height of 30 mm to 70 mm. The spatial combinations of point B were made accordingly to a full factorial design, yielding a total of 30 combinations.

8.1.2   Mesh Generation

The mesh is created in Meshing software from ANSYS, with boundary layer refinements for the valve and body walls, whereas the first layer height was made to be y^+ close to 1 (as required by the $k - \omega$ SST model). Local mesh refinement was applied in a radius of 30 mm from the point B (size of 0.5 mm) and at 15 mm surrounding the valve walls (size of 0.1 mm). Additionally, a global automatic refinement for proximity and curvature in the geometry, was applied. A good mesh quality was assured by manually assessing the meshes created for the extreme cases within the 30 combinations created. The meshes size ranged from 56.5k to 70.4k elements.

8.1.3   Boundary Conditions

The boundary conditions are similar to those previously reported in chapter 3.5.However the velocity was provided by a turbulent flow profile defined by the 1/7 power law (Equation 8.1). The latter was used on the solver though a UDF, which calculated the average velocity based in the flow rate of 30 L/min (this air flow rate is closer to the human PIF).

$$U_x\left(y\right) = 1.2244 \cdot \overline{U} \cdot \left(\frac{R - y}{R}\right)^{1/7} \tag{8.1}$$

with R as the maximum radius of the entrance, y is the radial coordinate and U_x and $\overline{U}$ is the axial and average velocity, respectively.

8.1.4   Solver Configuration

The solver of choice was FLUENT from ANSYS, and the models employed here were the same as described in chapter 3.6. The properties of the materials and spray definition were the same as for all simulations. The major differences are that this study was carried in 2D axisymmetric manner, improving the balance between the mesh resolution and the computational time required. Additionally, the spray injection was modelled for a 2D geometry (using the same inputs as chapter 3.7). Another limitation is that, due to the 2D axisymmetric study, no gravity acceleration was accounted for. The simulations ran for 4 s, whereas the spray was only injected at 0.6 s for a total duration of 0.1 s. The particle-wall collision was treated as a combination of the evaporation entrapment for liquid particles and the solid particles entrapment/reflection was decided upon the critical velocity model (considering all walls made of polycarbonate).

8.1.5   Post-Processing

The particles were collected at the exit, at the valve and on other walls. Afterwards, these data were post-processed using custom made Python scripts. Whereas, the FPM emitted was evaluated, as well as, the size distribution, temperature, evaporated fraction and spatial distribution. CFD-Post from ANSYS was used for post-processing the HFA concentration and the value for the recirculation

area in the body of the VHC design by a methodology based in the stream function, reported elsewhere [OTMT12].

This method was previously employed in a computational simulation study for estimating the amount of recirculation area created by stent struts in the blood stream [BSM$^+$00]. It consists in creating a field contour of the stream function that ranges from a maximum (corresponding at the centre of the recirculation area) to a minimum(corresponding at the wall reattachment point). Then, it is calculated the total area of this zone, which is divided by the total area of the field. This percentage was used as an output variable for quantifying the amount of recirculation for a given geometry.

The stream function is the relation between a streamline and the mass conservation equation, through the Equation 8.2 and 8.3 [BSM$^+$00, ANS13], only applicable to 2D flow fields.

$$u = \frac{\partial \Psi}{\partial y} \tag{8.2}$$

$$v = \frac{\partial \Psi}{\partial x} \tag{8.3}$$

A streamline can be defined as a line that is tangent to the velocity vector of the moving fluid and connects points of constant stream function, $\partial \Psi = 0$. The procedure starts by identifying the location of zero wall shear stress within the spacer's body. Two points are usually found which represent the locations of flow separation and reattachment. From the reattachment point, the points with a constant stream function are located. Because of the properties of the stream function, this boundary separates the location of the flow recirculation from the main flow.

8.1.6 Results

After post-processing the numerical results for the 30 design points, the percentage recirculation area, FPM and VHC volume were used to construct correlative regression surfaces, see Figures 8.2, 8.3 and 8.4 respectively. These regression surfaces correlate the spatial position of the expansion corner (i.e. length and height) with the predicted recirculation area, emitted FPM and VHC volume. Such surfaces were produced in Surfer (from Golden software, USA) using cubic splines. From

Figure 8.2, it is possible to observe that the recirculation area decreases with the length, however it increases even more rapidly with the displacement in height. As expected, when the expansion corner point is moved further from the centre of the flow stream, the boundary layer detachment occurs over a greater extension of the geometry. On the other hand, the displacement of the corner point along the axial direction will slightly decreases the recirculation area, due to the geometrical constraints of curves $\overline{AB}$ and $\overline{BC}$. The maximum value of recirculation is set in 62% (for length = 30 mm and height = 70 mm), whereas the minimum is 22% (for length = 150 mm and height = 30 mm).
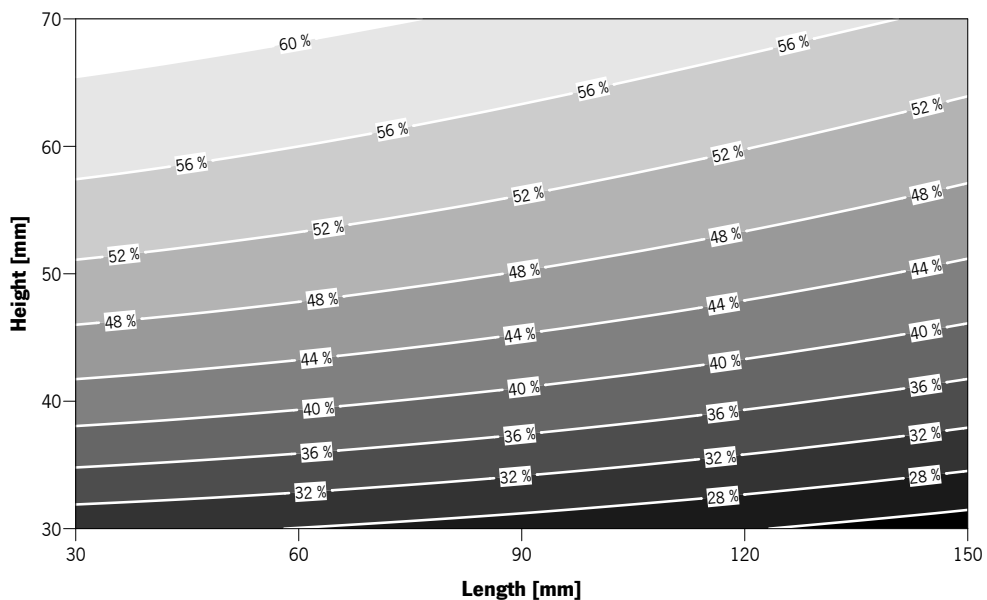
Figure 8.2: Correlative surface for the length and height with the percentage recirculation area

Results for FPM (see Figure 8.3) show a more complex pattern. Nevertheless there is an increase of the FPM with the length and reduction with the height. Values range from 34 μg (at length = 30 mm and height = 70 mm) to 57 μg (at length = 150 mm and height = 30 mm). The extreme values of FPM are opposite to those found for the recirculation area. This shows that the smaller this recirculation area, the higher emitted FPM, supporting the hypothesis of this study.

VHC Volume results (see Figure 8.4) appear to be highly related with the values of recirculation area previously reported. The increase in height leads to higher volumes than the increase of

length. The lowest volume is 270 mL (at length = 150 mm and height = 30 mm) and the highest
is 1560 mL (at length = 30 mm and height = 70 mm).
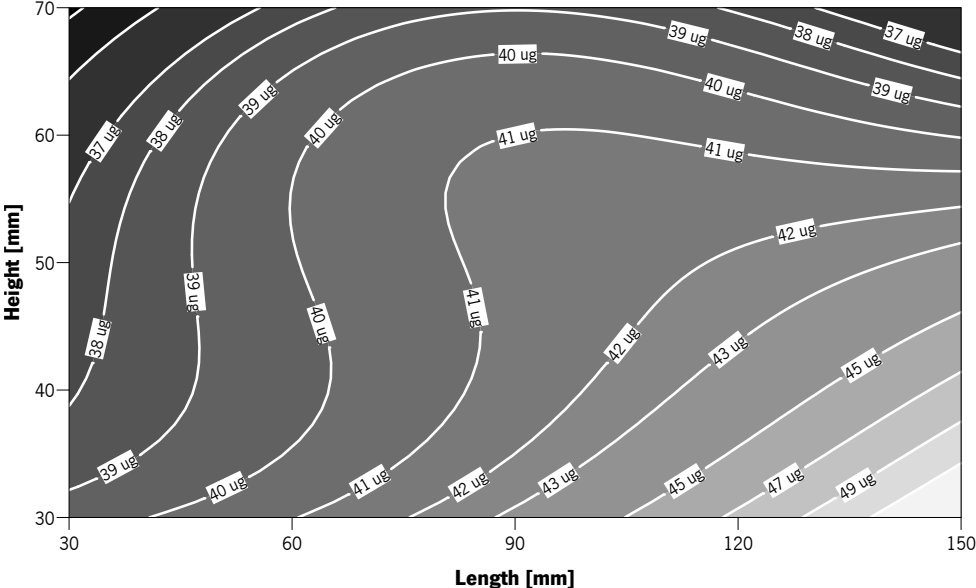

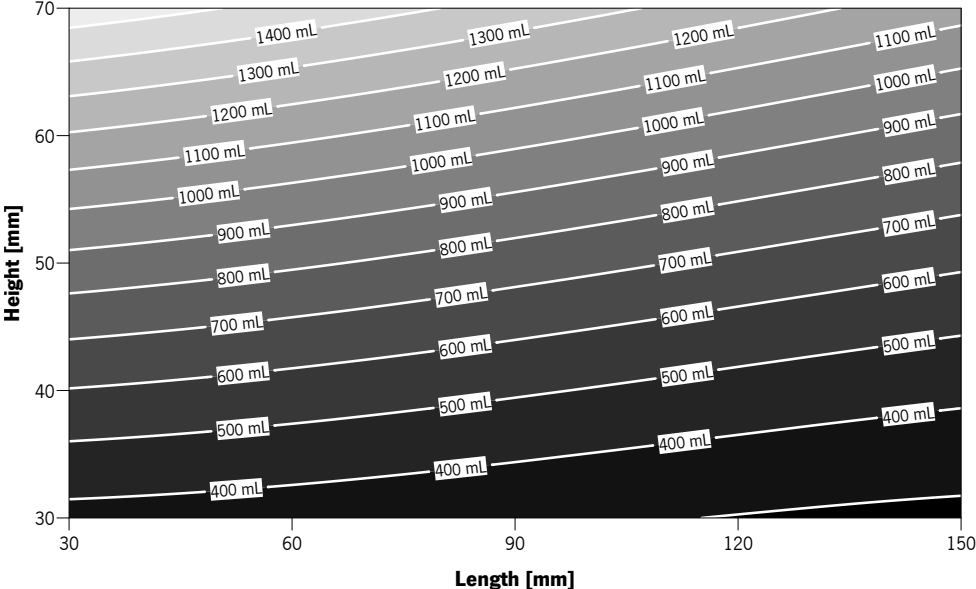Figure 8.3: Correlative surface for the length and height with the FPM

Figure 8.4: Correlative surface for the length and height with the VHC volume

The flow field for the two extreme combinations are depicted in Figures 8.5 and 8.6. Additionally, the greyscale coloured contours represent the VHC body area under recirculation, ranging from high (lighter) to the low (darker) values of the stream function.
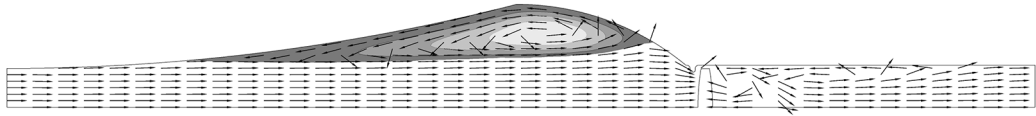
Figure 8.5: Computational results of the velocity vector field and the calculated recirculation zone (length = 150 mm and height = 30 mm)
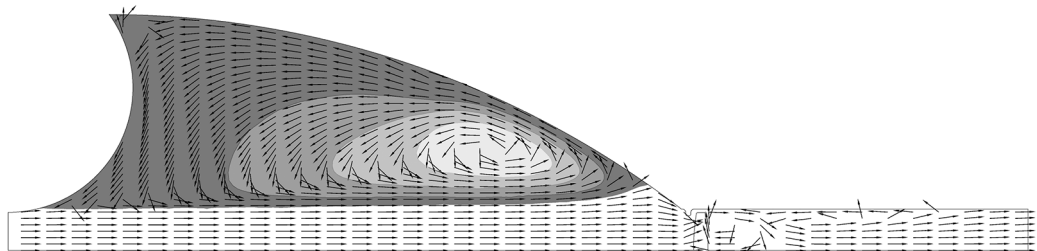
Figure 8.6: Computational results of the velocity vector field and the calculated recirculation zone (length = 30 mm and height = 70 mm)

An analysis of the domain for the presence of HFA as a vapour at 4 s, is represented in Figures 8.7 and 8.8 for the two previously discussed extreme cases. Even although 3.3 seconds after the injection of the spray is completed, some HFA can be found inside the VHC. The amount of propellant gas is very small, however, its concentration is higher for the geometry with higher recirculation area (see Figure 8.8). The recirculation zone traps the HFA in its centre, whereas the air velocity is close to zero.

By tracking the various sizes of particles released by the spray, a 3D rendering of the particles entrapped in the fluid can be represented. The particles are scaled by their diameter and the two extreme geometries are depicted (see Figures 8.9 and 8.10). Also, in the same figures, a longitudinal section of the VHC is used to show the propellant mass fraction. It can be seen that the particles suspended in the fluid are indeed entrapped mostly located in the recirculation areas. Whereas higher recirculation areas have greater amount of particles entrapped. This high

concentration of particles in the recirculation areas can explain the reason behind the higher concentration of HFA in these regions.
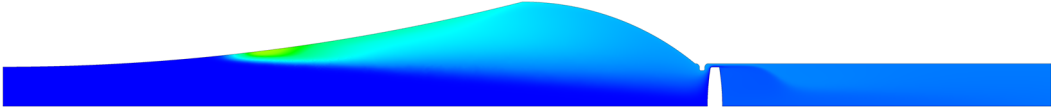
Figure 8.7: Coloured contours of the concentration of HFA propellant in the air (length = 150 mm and height = 30 mm)
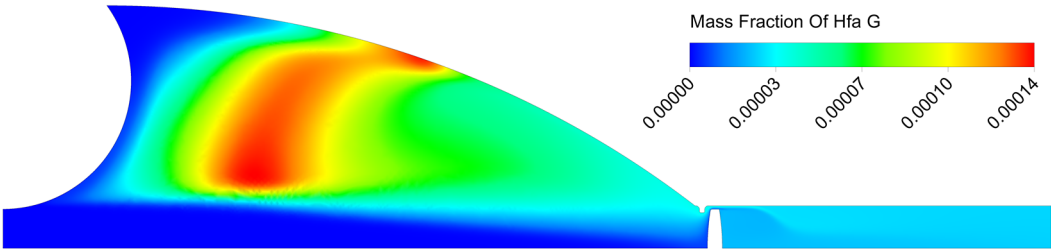
Figure 8.8: Coloured contours of the concentration of HFA propellant in the air (length = 30 mm and height = 70 mm)
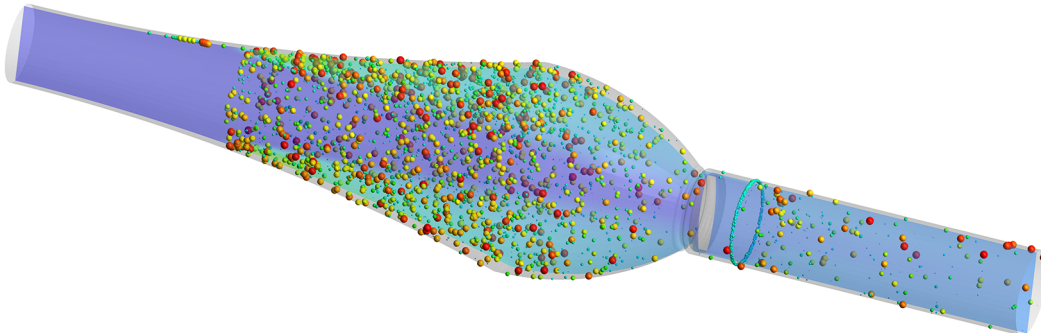
Figure 8.9: Coloured contours of the concentration of HFA propellant along with the representation of the particles entrapped in the domain at 4 seconds (length = 150 mm and height = 30 mm)
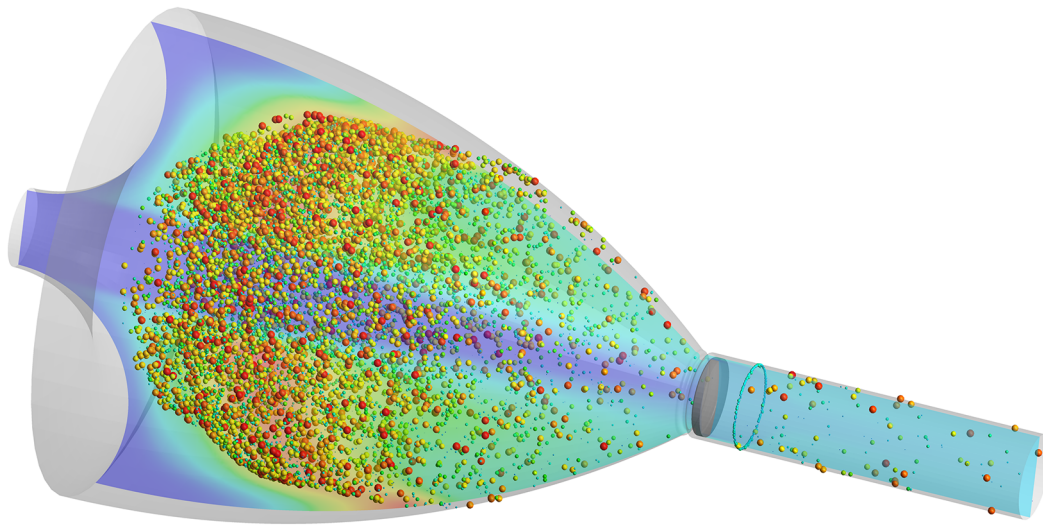
Figure 8.10: Coloured contours of the concentration of HFA propellant along with the representation of the particles entrapped in the domain at 4 seconds (length = 30 mm and height = 70 mm)

By analysing the particle size distribution at the exit for both cases (see Figure 8.11), it can be observed significant differences between both cases, and more so in comparison with the injected profile.
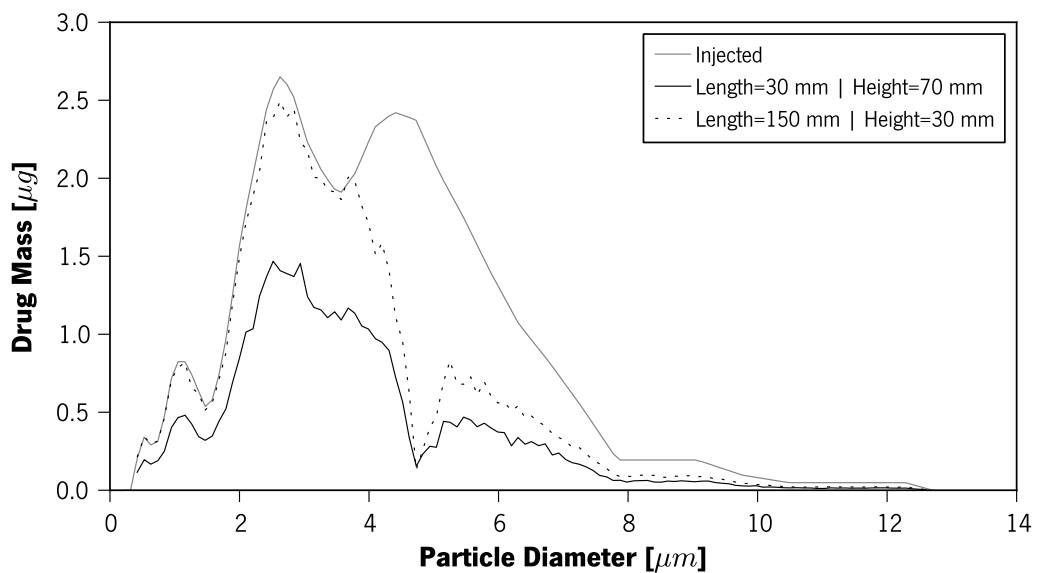
Figure 8.11: Particle size distribution of two emitted plumes in comparison with the injected salbutamol distribution

The low recirculation area configuration shows a great reduction of particles above 4 μm, leaving particles below this value practically unchanged. On the other hand, the high recirculation configuration presents a high reduction of the mass for all diameters alike.

Figure 8.12 presents the comparison between the recirculation area and the FPM for the 30 design points. Those are identified by markers for the values of height and labels identifying the values of length. From the comparison of both output variables, it is noticeable a certain degree of correlation between them. The highest recirculation areas lead to lowest emitted FPM values, and the other way around. The results for lower values of height appear to have less uncertainty and more likely to be highly correlated by the power function (FPM $= 101.805 \cdot \text{Area}^{-0.244}$; $R^2 = 0.460$). In Figure 8.12 the grey shadowed area represents the 95% confidence interval for the correlation curve.
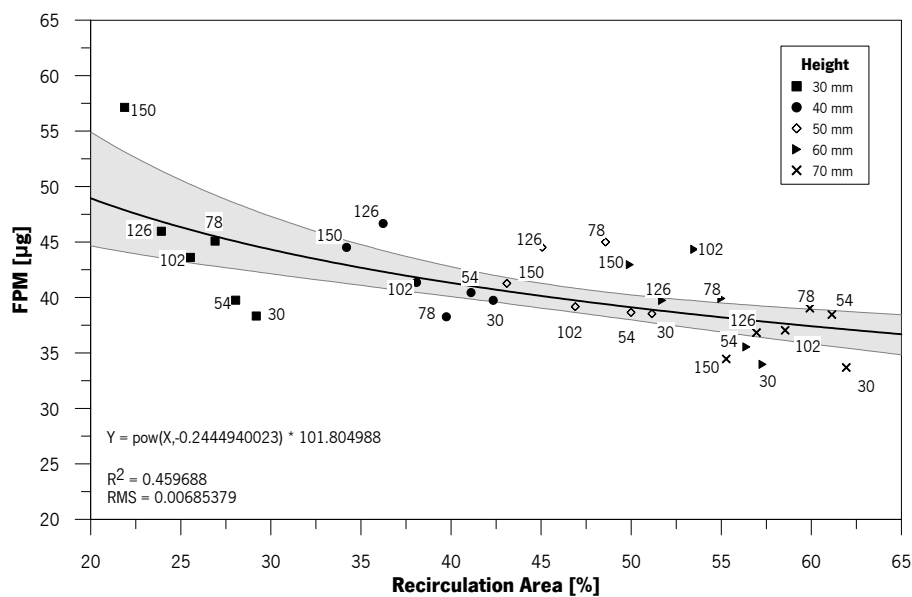
Figure 8.12: Comparison between the recirculation area and the emitted FPM (labelled with the length values)

Figure 8.13 depicts the comparison of the recirculation area versus the volume of the device, whereas is noticeable a strong correlation between both. As the volume increases by spatial

displacement of the transition point, the recirculation area increases accordingly to a logarithmic function (i.e. $\text{Area} = 23.02 \cdot \ln\left(\text{Volume}\right) - 105.78$; $R^2 = 0.992$). The grey shadowed zone indicates the 95% confidence interval. From Figures 8.2 and 8.4, is noticeable that higher values of height produce designs with higher volume and higher recirculation areas.
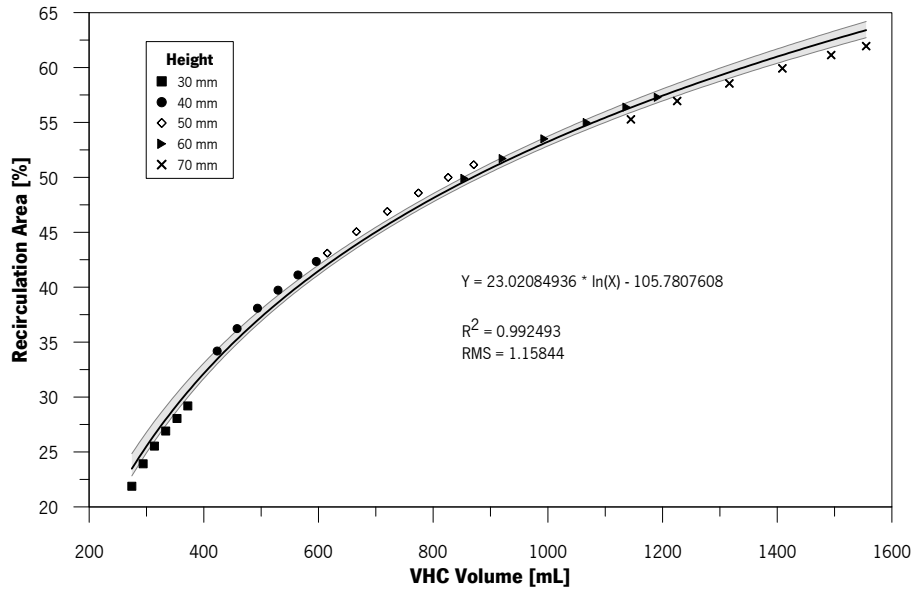
Figure 8.13: Comparison between the recirculation area and the design volume

8.2   New VHC Design

Based on the experimental and numerical conclusions obtained through this work, a new VHC design concept is proposed in this section. The body shape is built upon an axisymmetric solid, inspired in the shape of a pear. This will have smooth curvature surfaces composed by quadratic curves that meet at a transition point, whereas the influence of its position on the efficiency has been described in section 8.1. The position of the corner point is associated with a VHC volume, which is important to be adequate to lung capacity of the target patient. For a target patient, i.e., a 6 years old child, the volume should be close to the tidal volume (i.e. 150 mL); accordingly to Figure 8.4 the lowest volume corner point combination is of length equal to 150 mm and height equal to 30 mm. However, the total length of the device makes it impractical for carrying it around.

A more compact design configuration was chosen for the expansion corner: 80 mm length and 25 mm of height.

The experimental results identified the Volumatic valve as that with the lowest throat mass deposition and the highest increase in the FPM output, but this might be connected to the Volumatic high volume. However this idealised VHC design will have even a lower volume. Experimental results showed that Leaflets valve type are more effective for small volume devices, therefore the valve design should be similar to those of Compact Space Chamber or Space Chamber. This valve design has also shown virtually no air leakage (see section A.5).

This new design will be of a modular concept, made by parts easily manufactured by injection moulding. This shall keep the device production cost relatively low for a high production volume. The concept will include two additional features that can be combined with the other parts allowing the improvement of the device usability for a wide range of users characteristics and commercial formulations. One will be an expansion ring that will increase the volume of the device for patients with higher lung capacity (i.e. adults). Another improvement consists of an impaction ring that is composed by a centred half spherical cup, that will greatly increase the removal of the central spray coarse fraction. The size of the impaction rings can be tailored for different commercial spray formulations.

All parts can be combined resulting in different devices, which will produce distinct outputs for the patient:

- **A** - without extra parts
- **B** – with the impaction ring
- **C** – with expansion ring
- **D** – with the expansion and impactor rings

Figure 8.14 depicts the four possible variations of the basic design. The body of the device, as well as the extra rings can be produced in polycarbonate or ABS with anti-static properties for reducing the drug loss by electrostatic charge.
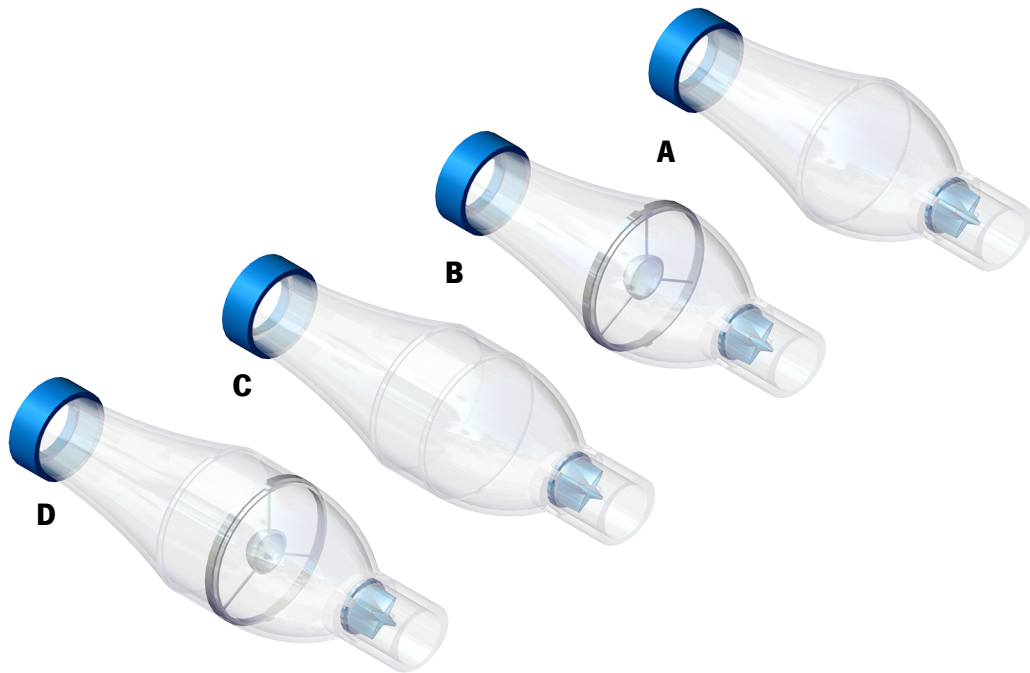
Figure 8.14: New VHC design combinations

For an easy assembly by the patient, some fool-proof features were added, such as a one-way interlock connection between the parts. That will prevent the patient to assemble the impaction ring with the concavity towards the spray. The device mouthpiece is also of oval shape on the outside so it will reduce the chances of air leakage by the patient mouth corners.

The pMDI adapter shall be universal fit design and made of silicone rubber, so it can fit all the possible commercial pMDI actuators in the market. The inhalation one-way valve shall also be produced in a silicon rubber material so it can properly function by deforming its structure by interacting with air flow solicitation.

A missing feature in this design is the exhalation valve (or vents), and the addition of a whistle for flow control during inhalation effort.

Children need to carry the VHC device around so portability is a very important feature to keep in mind when designing a new VHC device. This design has a maximum weight of 51 g (i.e. with the two extra rings) and a minimum of 42 g. The maximum dimensions for the configuration **D** are 176 mm x 54 mm of diameter. For configuration **A** is 150 mm x 54 mm of diameter.

This page was intentionally left in blank

9 Conclusions and Future Work

9.1 Main Conclusions

Herein this chapter, the most relevant conclusions regarding both experimental and numerical assessment of the VHCs performance are presented.

9.1.1 Experimental

The experimental performance assessment of eight VHC devices was done at constant and variable flow rate. For this, a Full Dose and a MSLI Cascade Impactor setups were used for collecting the salbutamol sulphate emitted by the pMDI Ventolin HFA, and evaluate its plume characteristics. Four of the VHCs were assessed at variable flow, using a breath simulator, which was developed to reproduce a typical child breath waveform. The main conclusions for the data are given bellow:

- It was noticed that the mass deposition in the pMDI actuator has a nearly constant value for all devices at constant flow rate (≈ 10 μg), and twice for variable flow rate. This indicates that the mass deposition is deeply related with the pMDI actuator design characteristic.
- The amount of drug deposited in the VHC reduces with increasing the air volume passing through the device. Results suggest that the deposition in each device is related with a considerable number of different variables.

- Throat deposition is reduced (64% - 94%) when a VHC is used, in comparison to the pMDI solo. The oropharyngeal deposition is highly related to the VHC valve type. Comparing the valve types in terms of mass deposition reduction, they can be ranked as: Duck > Annulus Flap > Leaflets > Coin. This is an effect observed through different flow rates.

- Using a VHC provides an increase of the FPM for most of the devices. The FPM emitted from the VHC devices shows no statistically significant differences (p>0.05) when compared to the pMDI solo, proving the bioequivalence of the add-on device. Also, there is not statistical evidence that valve type is related to the emitted FPM at 30 L/min (p>0.05). Similar observations were found for 60 L/min. However the FPM emited by the VHC under the breath pattern is systematically lower than the pMDI solo. These results may be indicative of a problem within the setup or that the breath pattern has a low tidal volume for these commercial devices.

- All VHC (tested at constant flow rate) are able to reduce the coarse fraction by more than 60% in comparison with the solo pMDI, as advisable by the guidelines.

- The results indicate a reduction of the FPM with the reduction of the flow rate. Thus, logarithmic correlations were found between the volume of air passing through the VHC and the emitted FPF, for each valve type group.

- Similarly, logarithmic correlations were found between the Throat mass deposited (normalised by the TEM) and the volume of air drawn, for each valve design.

- Some degree of linear correlation was found between the FPM and the oropharyngeal deposition, for each valve type.

- Limitations were found in the evaluation of the different metrics, due to the CI apparatus (i.e. MSLI) poor resolution.

9.1.2 Numerical

The numerical work consisted in the modelling of the pMDI spray using CFD tools (i.e. FLUENT). The model predicted the drug deposition in the VHC device and in the USP Induction Port surfaces. Several models for particle-wall interaction were tested and compared against literature and

experimental data. The most important conclusions can be summarised:

- The highest air flow velocities are found in the VHC regions of greater geometric constraint (i.e. valve opening). The Nebuchamber geometry induced the highest velocity ($\approx$37 m/s), while the lowest was found for the both Space Chamber devices ($\approx$22 m/s).

- The air flow pattern inside the VHC shows the formation of large recirculation regions, near the walls.

- The Nebuchamber mouthpiece design places the valve centre radially misaligned with the USP IP. This leads to a non-symmetric airflow in the upper portion of the throat.

- Air flow pattern downstream of the valve is more uniform for open-centre valve designs, rather than for the other valve types. The latter favour the appearance of recirculation regions.

- Evaporation of the propellant rapidly increases during the spray injection; afterwards it exits the VHC at a rate that is related to the device volume. Whereas, the Volumatic (with highest volume VHC) retains the HFA for a longer time period.

- The drug deposition predictions showed that the A2A Spacer geometry emitted the highest amount of drug, and that Nebuchamber had the lowest throat mass deposition. All simulated VHC geometries highly reduced the throat drug deposition.

- Validation of the numerical results with literature and experimental data have shown that the best wall-particle interaction model to be used in the USP throat surfaces is the one that considers that entrapment is only applied to liquid droplets, or to solid particles if the wall normal velocity is lower than the particle critical velocity. However, it is important to mention that this model underestimates the deposition of small particles.

- The validation of drug deposition with the experimental data, showed large differences in the drug deposition on some VHCs, namely the Volumatic, the A2A Spacer and the Nebuchamber. This may indicate that the wall-particle collision model used for the USP throat is not adequate for the VHC surfaces, as additional forces, such as the electrostatic attraction, are not taken into consideration.

- The numerical results for the drug deposited in the throat and the emitted Sizable Mass differ from the experimental data. This outcome may be the result of the inaccurate predictions

221

of deposition on the VHC walls.

- A new design with ennhanced features was proposed considering its portability and its efficiency. The feature that most contribute to the increase of efficiency is the addition of two modular parts pieces to increase the volume. This higher volume allows the device to be used by patients with higher tidal volumes, which means that it can be used by a wider age range.

9.2   Future Work

There is an ample room for improving the work developed herein this thesis, both in experimental assessment and numerical simulation.

9.2.1   Experimental

A more comprehensive set of experimental tests could be performed upon the VHCs and pMDI spray. These additional analyses should include:

- Use of a NGI apparatus to improve the accuracy of the experimental data.
- Evaluate all VHC devices under variable flow different breathing patterns (covering a range of different ages and pathologies).
- Test the effect of the delay between the actuation and the inhalation, and the actuation during exhalation phase.
- Evaluate the spray plume inside the VHCs using PIV technique and/or LDA.
- Measure the spray plume size distribution near the nozzle.

9.2.2   Numerical

The numerical model could benefit from improved input parameters and mathematical models, as well as, an extensive sensibility analysis to some parameters. Some examples of improvements to the numerical simulations include:

- The introduction of coalescence phenomena between the droplets.
- The introduction of an anisotropic correction near the wall in the turbulent dispersion for the DPM.
- Performing a sensitivity analysis to study the influence of the particle-wall model rebound coefficient in the drug deposition results.
- The addition of the effect of the electrostatic attraction to the particle body force balance.
- Modelling multi-component droplets, composed by two materials, solid API and liquid propellant.
- Study the influence of water vapour concentration (i.e. relative humidity) and temperature in the propellant evaporation and, subsequently, the plume size distribution.
- The simulation of transient air flow breathing patterns and spray injection in different moments.

This page was intentionally left in blank

A Axillary Experimental Measurements

A.1 Rotameter Validation

Two of the flowmeters used in this study are rotameters (D10A11 from ABB, Switzerland), whose reading is on a percentage scale. This is converted to the desired flow units giving a known value for the 100% mark, since flow increases linearly with the marks in the scale. This is due to the fact that the pressure drop along the rotameter tube is constant, independent of the float position. As the float rises (due to the flow rate increment), the tube cross-section area enlarges, to accommodate a constant pressure drop. The rotameter needs to be vertically positioned to properly work. In addition, the temperature, fluid viscosity, humidity and pressure, play a very important part in the real flow rate measured. Therefore it is necessary to control/quantify these variables during calibration process.

Hence it becomes necessary to know accurately the value of air flow rate that corresponds to the readings on the percentage scale. Although there are several methods to accomplish this objective, three methodologies where used:

Method 1 – Static pressure measurement at a bell mouth entrance;

Method 2 – Integration of the flow velocity profile measured by Laser Doppler Anemometry (LDA);

Method 3 – Direct comparison with a calibrated digital flowmeter.

A.1.1   Method 1

This method comprises the attachment of a bell mouth of elliptical shape, upstream of the rotameter that is going to be assessed. Between them it is advisable to include a straight section to develop the flow. The rotameter was then coupled to a vacuum system constituted by two pumps (GS-6 from General Europe Vacuum, Italy). A ball valve allowed the pressure drop regulation, controlling the flow rate through the rotameter. The static pressure was measured at the throat of the bell mouth, by means of a digital manometer (Series HM28 from Love Controls, USA). A schematic representation of the experimental setup can be found in Figure A.1.
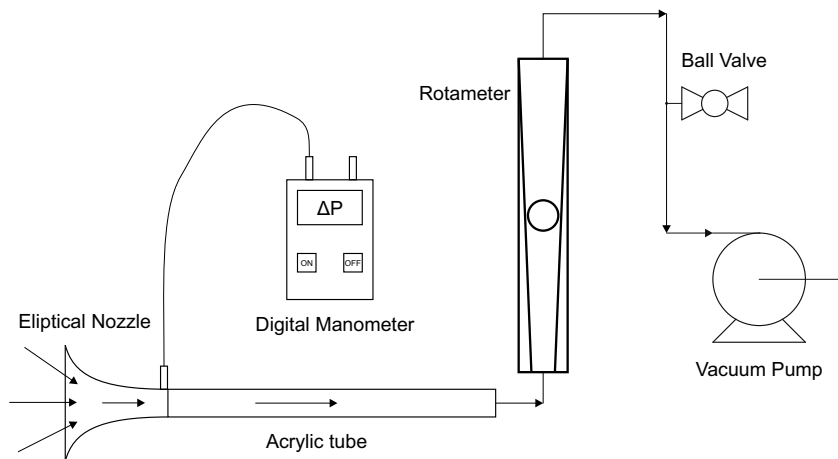
Figure A.1: Schematic representation of the setup used for calibration of the rotameter using method 1

The air entering the elliptical nozzle would smoothly accelerate from a velocity close to 0 m/s to a maximum value. At the bell mouth throat ($\oslash$ = 15 mm) a pressure taping enables the static pressure measurement that, when subtracted to the pressure at the nozzle entrance (i.e. atmospheric pressure), can be related to the fluid theoretical average velocity by Bernoulli modified Equation A.1. Finally, multiplying the velocity by the section area, the fluid flow rate is obtained.

$$U = \sqrt{\frac{2 \times \Delta P}{\rho}} \tag{A.1}$$

ρ was assumed to be 1.205 kg/m^3

The position of the float inside the rotameter, was controlled to provide readings every 10% of the scale. The results are listed in Table A.1 along with the calculated theoretical flow rates.

Table A.1: Experimental pressure drop values obtained (uncertainty within three measurements), along with the calculated flow rate values, using method 1

Rotameter Scale (%)	Rotameter 1		Rotameter 2	
	$\overline{\Delta P_3}$ - Pressure Drop (Pa)	Flowrate (L/min)	$\overline{\Delta P_3}$ - Pressure Drop (Pa)	Flowrate (L/min)
10	0.(7) ± 0.3	11.(0) ± 2.0	0.(8) ± 0.3	12.(3) ± 2.0
20	2.(2) ± 0.3	20.(1) ± 1.1	2.(0) ± 0.0	19.(3) ± 0.0
30	5.(3) ± 0.5	31.(5) ± 1.5	5.(0) ± 0.0	30.(5) ± 0.0
40	9.(2) ± 0.3	41.(4) ± 0.6	8.(8) ± 0.3	40.(6) ± 0.6
50	14.(3) ± 0.5	51.(7) ± 0.9	13.(7) ± 0.3	50.(5) ± 0.5
60	20.(2) ± 0.3	61.(3) ± 0.4	19.(7) ± 0.5	60.(6) ± 0.8
70	27.(5) ± 0.5	71.(6) ± 0.7	26.(7) ± 0.8	70.(5) ± 1.0
80	35.(5) ± 0.0	81.(4) ± 0.0	34.(5) ± 1.0	80.(2) ± 1.2
90	44.(8) ± 0.3	91.(5) ± 0.3	44.(5) ± 0.0	91.(1) ± 0.0
100	54.(5) ± 0.0	100.(8) ± 0.0	54.(8) ± 0.3	101.(2) ± 0.2

( ) - uncertain digit

$\overline{\Delta P_3}$ - averaged pressure drop of three measurements

A.1.2 Method 2

In the following methodology a LDA technique was applied to measure the velocity profile. This technique allowed the measurement of the velocity of seeding particles velocity, which followed the air flow inside of an acrylic tube ($\oslash$ = 22 mm). The probe was connected to a Burst Spectrum Analyser (BSA) unit that controlled the laser beams characteristics and processed the signal obtained through the detectors. A filter and drain were connected downstream of the acrylic tube for collection of the seeding particles. The latter connected to the entrance of the rotameter, and this one to the vacuum system along the ball valve. Figure A.2 depicts the layout of the

experimental components in the experimental setup.

A nebulizer provided the system with a seeded flow. A compressed air source from the laboratory grid atomises an aqueous solution of droplets and 2.2 μm polystyrene latex calibrated particles (Coulter Electronics, UK).
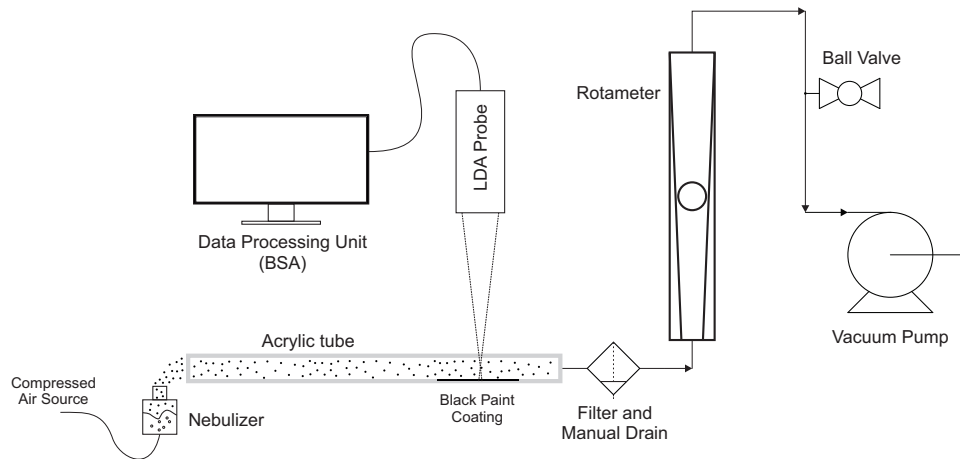

Figure A.2: Schematic representation of the setup used for calibration of the rotameter using method 2

The transparent acrylic tube had one side coated with a black extra matte paint (Cináqua from CIN, Portugal) to reduce laser reflections that would interfere in the data acquisition. The rotameter float was positioned at 100% of the scale and the several measurements were made along a diameter of the acrylic tube.

Initially the measurement volume was placed at the outer wall of the tube, and then displaced a pre-calculated distance through the wall. This value depends on the thickness of the tube, due to the fact that light scatter differently in different mediums, the passage from air to acrylic, change the laser beams angle resulting in a different point of intersection (see Figure A.3). The procedure started by placing the laser beams intersection (control volume) in the tube outer wall, at the half height of the tube diameter, and setting this position as zero axial displacement. At this position the values of h_2 and h_3 are zero, no α_2 neither α_3 are present. The value of h_0 is half of the beam spacing (S_b = 38.4 mm), and the length, on the optical axis, between the intersection and the lens is the focal length (F_L = 161.1 mm).
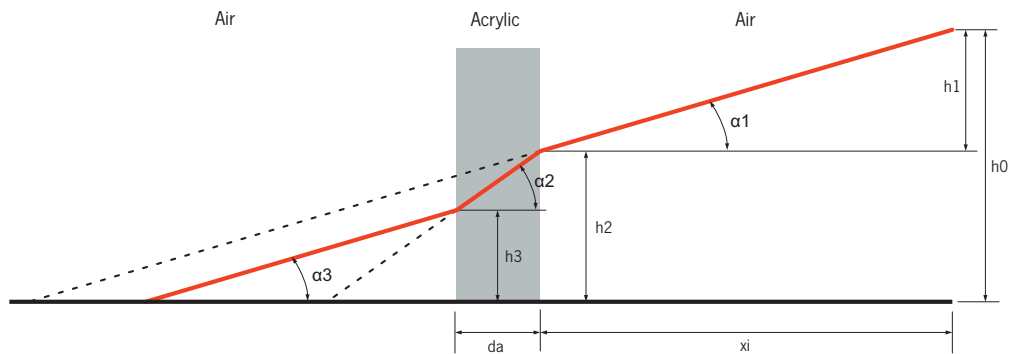
Figure A.3: Schematic representation of the laser beam crossing the different media

The angle between the beams is calculated by Equation A.2. The value of α_1 is half of the beams angle (α_0).

$$\alpha_0 = 2 \times \arctan\left(\frac{S_b}{2 \times F_L}\right) \tag{A.2}$$

The second scenario is the intersection of the laser beams in the inner wall of the acrylic tube (with thickness, d_a = 4 mm). As can be seen in Figure A.3 by the dotted lines, the beams were supposed to intersect in a certain position, however due to the acrylic medium distinct refractive index, the intersection occurs in a shorter distance. It is necessary to use Snell's law to calculate the angle of the intersecting beams inside the acrylic medium (α_{air}) Equation A.3.

$$\alpha_2 = \arcsin(\frac{n_{air} \times \sin(\alpha_1)}{n_{acrylic}}) \tag{A.3}$$

Considering:

n_{air} = 1.0 (refractive index of the air)

$n_{acrylic}$ = 1.491 (refractive index of the acrylic)

In this case the value of h_2 can be assessed through simple trigonometric calculation Equation A.4.

$$h_2 = d_a \times \tan(\alpha_2) \tag{A.4}$$

Since h_0 is the sum of h_1 and h_2, the value can be easily calculated. Hence, the distance from

the lens to the outer wall (x_i) of the tube is given by Equation A.5.

$$x_i = \frac{h_1}{\tan(\alpha_1)} = \frac{h_0 - h_2}{\tan(\alpha_1)} = \frac{(S_b/2) - (d_a \times \tan(\alpha_2))}{\tan(\alpha_1)} \tag{A.5}$$

Summarising, the distance from the lens to the probe volume when in air (F_L) is known, however given the fact that the beams crossed 4 mm of acrylic wall, x_i gives the actual distance from the tube to the lens. By subtracting one to the other (see Equation A.6), it results in the real distance (d_r = 2.672 mm) travelled for the beams to cross 4 mm of acrylic.

$$d_r = F_L - x_i \tag{A.6}$$

Once this displacement was applied to the probe, one was sure that the measurement volume ii located at the inner wall of the acrylic tube and it is ready to acquire the velocity data. By giving increments in the probe axial movement, the velocity profile along the tube section could be measured. At each location 2,000 data points were collected to retrieve the local average velocity. The results along with the error is shown in Figure A.4. By integrating the experimental data the flow rate can easily be determined. In the Figure A.4 legend the values of the flow rate at 100% rotameter scale, are shown.
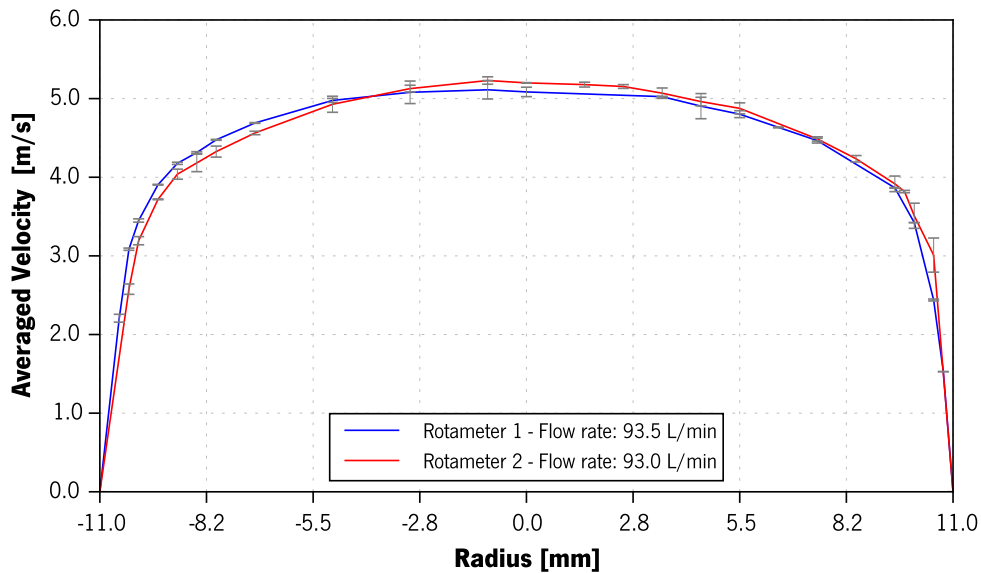

Figure A.4: Averaged velocity profiles inside of the ⌀ = 22 mm tube for both rotameters, error is represented in the form of bars. The values for the calculated flow rate are shown in the legend

A.1.3 Method 3

In this methodology the rotameters were evaluated by direct comparison with a pre-calibrated mass flowmeter (Model 4043 from TSI, USA), placed just upstream of the rotameter inlet (see Figure A.5). The float height was set, in 10% intervals, with the help of the ball valve.
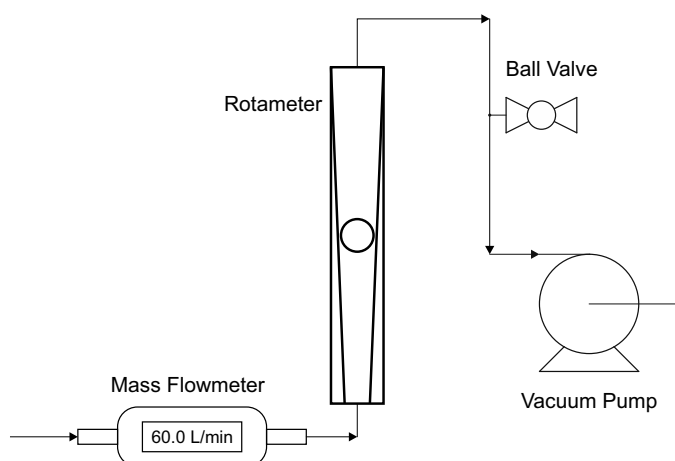

Figure A.5: Schematic representation of the setup used for calibration of the rotameter using method 3

The results are presented in the Table A.2. The values estimated for the calibration of the rotameters, obtained through the three methodologies previously presented, are not the same since each methodology rely upon some degree of experimental uncertainty added by: orthogonally misalignments, reading uncertainties, addition of dead volume to the setup, flow friction within the bell mouth. The most accurate comparison is obtained by method 3, and since the mass flowmeter was recently calibrated and it accounts for temperature and pressure corrections. Furthermore it would be used along with the rotameters in the pharmacological experimental setup.

In Figure A.6 the calibration results at 100% scale for both rotameters, is shown for the three methods. If the method 3 is considered the most accurate, the methodology 1 overestimates the flow rate while the method 2 underestimates it. The difference observed with method 2 (LDA) may be due to difficulties in guaranteeing a correct positioning of the probe volume inside the pipe section and beam reflections from the pipe walls. Method 1 might overestimate the flow rate due to the fact that friction in the bell mouth wall was not accounted for.

Table A.2: Mass flowmeter values measured according to method 3, along with the associated error

Rotameter (%)	Rotameter 1	Rotameter 2
10	7.1(7) ± 0.05	8.3(0) ± 0.15
20	18.9(0) ± 0.35	19.0(7) ± 0.35
30	28.9(3) ± 0.20	28.7(3) ± 0.20
40	38.4(8) ± 0.30	38.1(7) ± 0.05
50	48.6(0) ± 0.10	47.7(0) ± 0.10
60	58.5(7) ±0.30	57.6(0) ± 0.10
70	68.9(3) ± 0.30	67.4(3) ± 0.35
80	78.9(7) ± 0.10	77.9(0) ± 0.10
90	88.8(0) ± 0.30	88.1(7) ± 0.15
100	99.0(0) ± 0.65	98.9(0) ± 0.10

( ) - uncertain digit

averaged values from three measurements
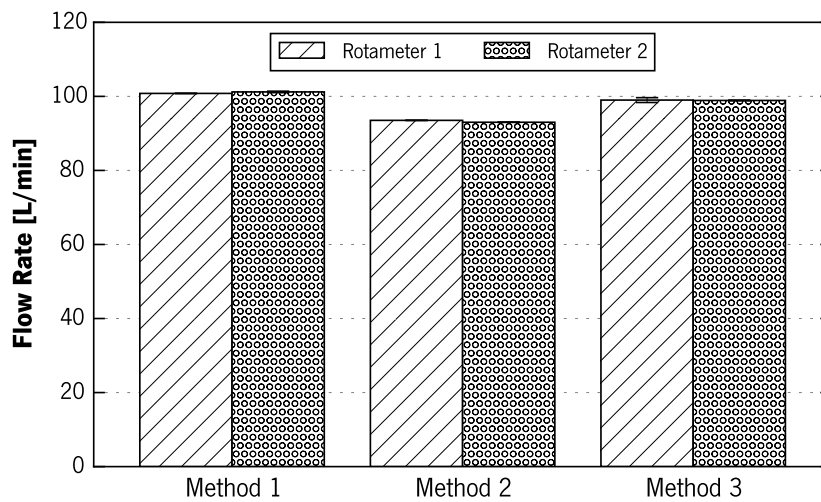
values units in L/min

Figure A.6: Comparison the results for both rotameters calibration, at 100% scale, by three methods

A.2   Paper Filter Evaluation

Upon the fact that no standard type neither specifications are given by the Pharmacopoeia for the correct paper filter to be used in the MSLI, studies were carried out to evaluate the most adequate. The three factors evaluated were:

- the amount of absorbance (considered contamination) produces;
- pressure drop versus flow rate curve (specifically at 30 and 60 L/min);
- the possible loss of drug caused by the filter porosity.

The first point was evaluated by putting a sample of each paper filter, with $\oslash$ = 38 mm, in a 20 mL solution of 0.01M NaOH and under 10 min of sonic shaking. The absorbance was then evaluated by UV-Vis spectroscopy at 244 nm of wavelength (was described in section 5.2.1), results are shown in Table A.3.

Table A.3: Evaluated characteristics of the possible paper filters for use in the MSLI

Filter Name	Particle Retention [μm]	Absorbance Peak at 244 nm[b]	Pressure drop at 60 L/min [Pa]	Total Collected Mass (mg)[e]
MN 617[c]	7.0-12.0	0.08	3.1	1.23 ± 0.03[a]
MN 619[c]	2.0-4.0	0.02	37.7	1.23 ± 0.03[a]
MN 1674[c]	2.0-4.0	0.04	58.6[f]	1.25 ± 0.02[a]
MN GF-1[c]	0.7	0.20	6.1	-
GE GF-6[d]	1.0	0.06	11.8	-
GE 934-AH[d]	1.5	0.22	5.7	-

[a] ANOVA test shows that are not statistically significant difference between the means (p > 0.05)

[b] In a solution volume of 50 mL, the same used throughout the experiments

[c] MN stands for Macherey-Nagel, Germany

[d] GE stands for GE Healthcare, UK

[e] Tests were done at 30 L/min using a full dose setup (N=7)

[f] Data obtained at 54 L/min

The pressure drop produced by each paper filter for a certain flow rate is directly related to its

porosity. This evaluation was carried out using the a setup (see Figure A.7) that was composed by a mass flowmeter (which allowed the measurement of the flow rate and pressure) placed at the inlet port of a filter casing and a negative pressure manometer (PN7009, IFM from UK) placed at the opposite side. A vacuum system extracted the air flow that passed through the filter and was regulated by a ball valve placed at a T-junction branch. This setup allowed the variation of the flow rate and reading of pressure before and after the filter. Results are presented in Figure A.8 in the form of curves relating the pressure drop with the flow rate.
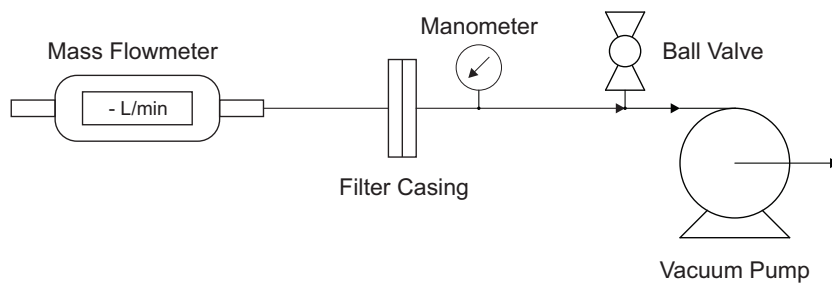

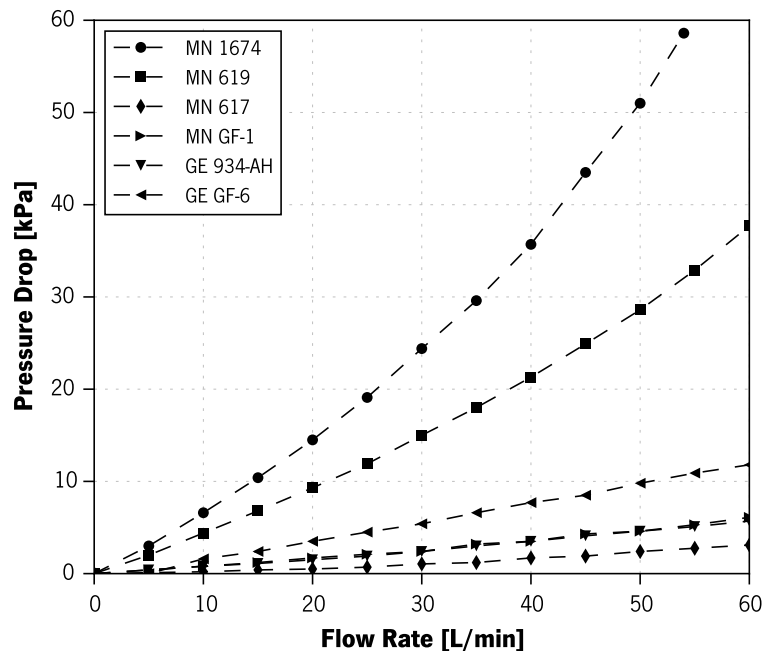Figure A.7: Schematic of the setup for measuring the pressure drop caused by different paper filters

Figure A.8: Pressure drop versus flow rate characteristic curves for several paper filter types

Upon the evaluation of the results, the MN 619 filter was selected for carrying out the experimental tests within the MSLI, as it provided a lowest contamination, low drug loss and reasonable pressure drop when compared to the other filters.

A.3   High-speed Camera Setup

The spray plume inside the VHC was analysed by means of a high-speed camera. The setup, depicted in Figure A.9, was composed by a vacuum pump (GS-6 from General Europe Vacuum, Italy) and a ball valve for flow regulation, connected to a digital mass flowmeter (Model 4043 from TSI, USA). This was connected to a filter (for drug collection), and to the VHC device tested. The high-speed camera (FASTCAM APX RS from Photron, USA) with a lens (50 mm 1:2.8 DG Macro D from Sigma, Japan), was positioned at 90 degrees to the VHC centreline and parallel to the ground plane, allowed the capture of events at a rate of 3000 frames per second. Two 1 kW lamps were added to the setup, positioned perpendicular to both the VHC and high-speed camera axis, to provide enough light for the acquisition of the photos at such high rates.

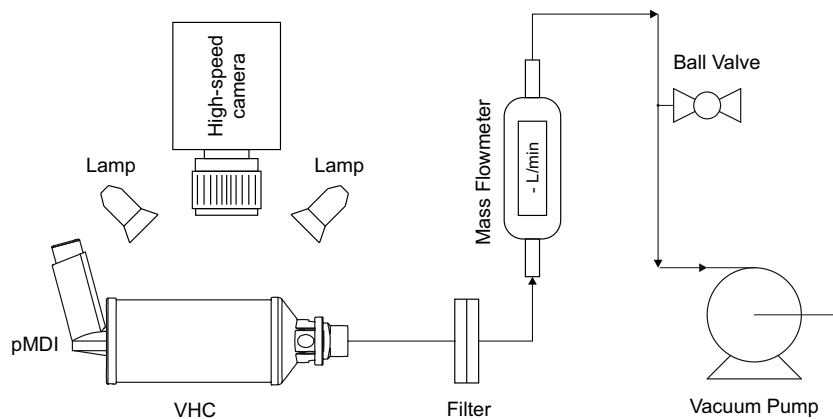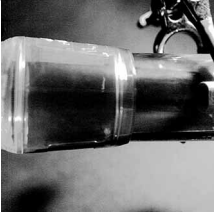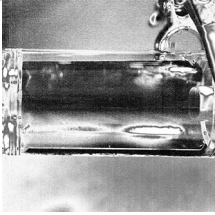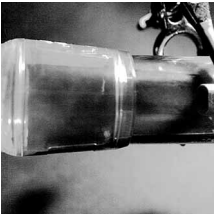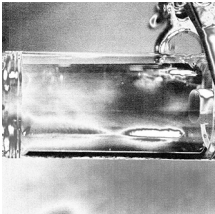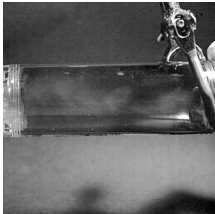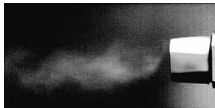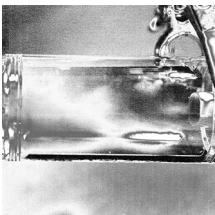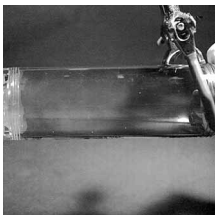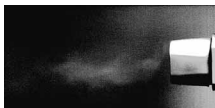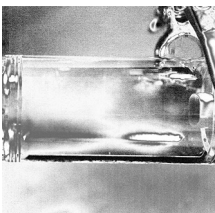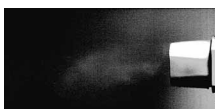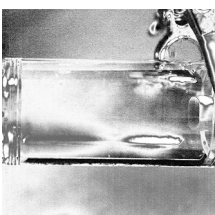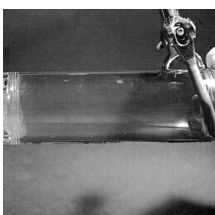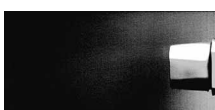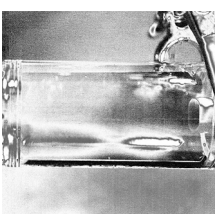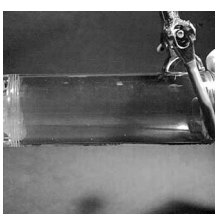Figure A.9: High-speed photographic data acquisition setup

Results are presented in Table A.4, whereas it is also included the pMDI solo into stagnant room air. In order to enhance the visualisation, the gray-scale curve was manipulated for all pictures.

Table A.4: Selected frames obtained, using high–speed camera photography, during the plume release, for the pMDI solo and coupled to the A2A Spacer, Compact Space Chamber and Space Chamber

	A2A	CSC	SC	pMDI
t=0.00s				
t=0.02s				
t=0.04s				
t=0.06s				
t=0.08s				
t=0.10s				

The assessment was made for three VHC (A2A Spacer, SpaceChamber and Compact SpaceChamber) at 30 L/min as the experiment could only be conducted in transparent devices. The necessary use of the lighting sources, lead to reflections in the devices curved surfaces, which tainted the data. After the removal of the electrostatic coating of the devices (i.e. bath in anionic soapy water followed by 24 h drying), around one third of the bottom interior surface of the VHC inner surface was covered with black tape to avoid reflections.

A.4 Valve Openning Cross-section Setup

This experimental setup consisted in placing a photographic camera with its optical axis aligned with the VHC valve centreline. This allowed the capture of photographs of the VHC valve opening cross-section, with a minimum of optical distortion, for two flow rates (i.e. 30 L/min and 60 L/min). The VHC mouthpiece was connected to a mass flowmeter (Model 4043 from TSI, USA) and subsequently to the vacuum system made up by one pump (GS-6 from General Europe Vacuum, Italy). The flow rate was regulated by a ball valve placed at a junction between the flowmeter and the vacuum system. The setup schematic can be found in Figure A.10. A total of six devices were assessed in this apparatus, each one with a distinct type of valve.
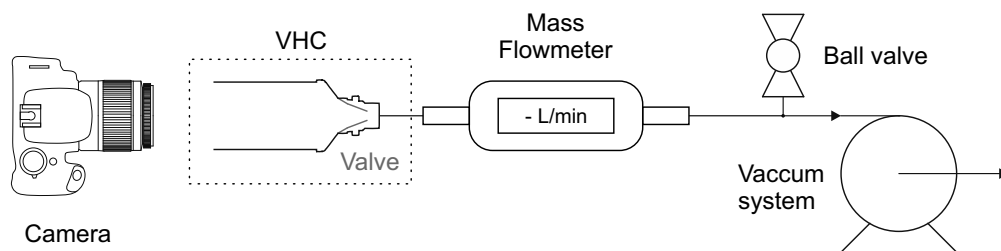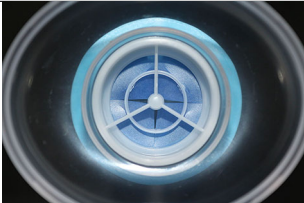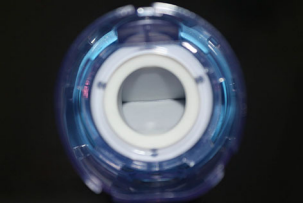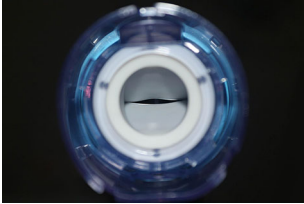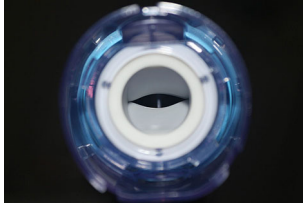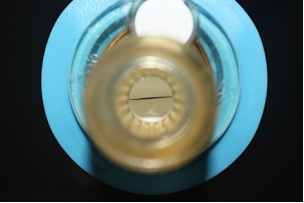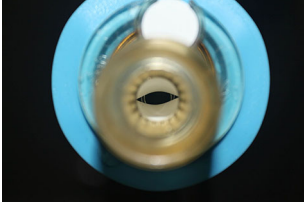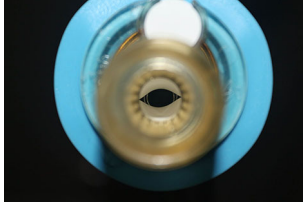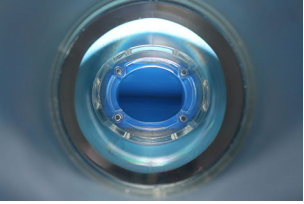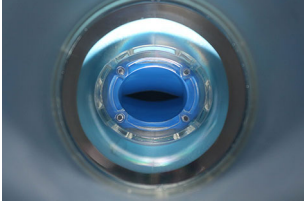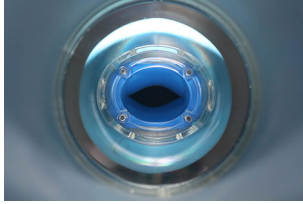
Figure A.10: Schematic representation of the experimental setup used for acquiring photographs of the valve opening shape at different flow rates

The images allowed the estimation of the shape of the cross-section shape and its area (important information for drawing the computational simulation models). Some of the VHC devices did not allowed the cross-section estimation due to the type of valve aperture being perpendicular to the optical axis, whereas the mouthpiece geometry did not allow for a clean shot (see Table A.5).

Appendix A. Axillary Experimental Measurements
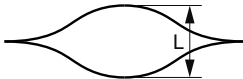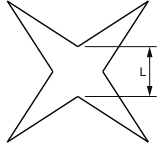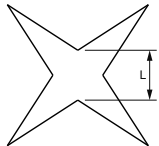
The information for those that were possible to be estimated, using an image measurement open-source software (ImageJ developed by Wayne Rasband), is given in Table A.6.

Table A.5: Photographic results of the VHC device's valves opening at different flow rates

Table A.6: Valve cross-section area and dimensions estimated from the photographs at 30 L/min and 60 L/min, for some VHC devices

VHC Device	Schematic	30 L/min	60 L/min
V		L = 3.19 mm	L = 6.12 mm
		Area = 28.48 mm^2	Area = 54.75 mm^2
NC		L = 3.44 mm	L = 4.87 mm
		Area = 24.81 mm^2	Area = 33.62 mm^2
OCD		L = 1.38 mm	L = 3.33 mm
		Area = 9.51 mm^2	Area = 27.02 mm^2
CSC		L = 2.73 mm	L = 3.33 mm
		Area = 42.44 mm^2	Area = 53.92 mm^2
A2A		L = 3.66 mm	L = 4.91 mm
		Area = 22.17 mm^2	Area = 41.90 mm^2

A.5 Leakage test Setup

The valve leakage in each VHC was evaluated through three different tests, as represented schematically in Figure A.11. Setup (a) consisted in the insufflation of compressed air at a constant flow rate directly onto the VHC valves. Whereas the inhalation valve should fully close not allowing air to escape into the VHC body, devices with an exhalation valve provide a more efficient exhaustion route for the air. The mass flowmeter (Model 4043 from TSI, USA), placed at the device's pMDI adapter, registered the amount of air passing through the inhalation valve due to leakage. Configuration (b) enables the evaluation of the flow rate passing through the VHC adapter, for a constant flow rate calibrated at the device's mouthpiece. The difference results from leakages between the device's modules; the exhalation valve; or other secondary flow passing through devices adapter / whistle. Finally, setup (c) provides a more realistic evaluation of the valves operation when presented with a patient breath waveform. Differences between the original

waveform and those registered at the device's adapter are related with the leakages evaluated at the previous setups (a) and (b).
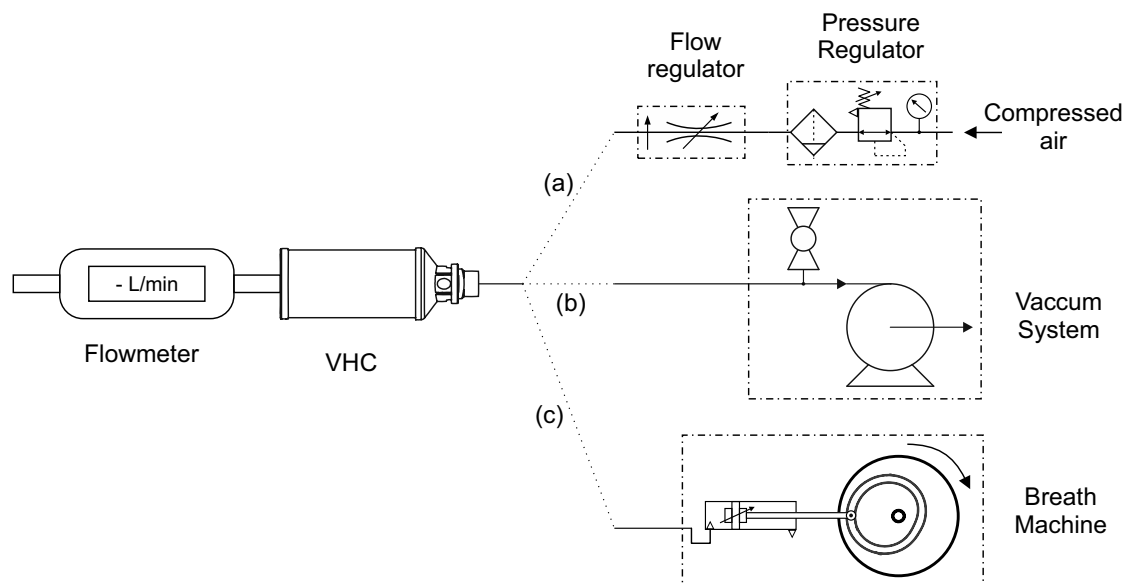
Figure A.11: VHC leakage evaluation setup: (a) with positive pressure; (b) with negative pressure and (c) with a breath profile

The results obtained from the three different tests are detailed in Table A.7 and Figures A.12 and A.13. The test using setup (a) was carried out at 30 L/min and 60 L/min and identifies the occurrence of leakage during the closure of the inhalation valve. The results point out that upon air insufflation, against the VHC valve, some have more leakage than others, with the Coin type (Volumatic) showing the worst performance (with a leakage of $\approx36\%$ of the insufflated flow). As expected, leakage increases with flow rate. Leaflets valves such as those present in the Space Chamber series (i.e. CSC and SC), show the best performance with virtually no leakages. However, the Leaflets valve type show good results, the same is not verified with the model present in A2A Spacer, which has a considerable leakage at 30 L/min (worse results could be expected for 60 L/min). The Annulus Flap type valves show a very good performance with minimal leakage, followed by the Duck valves.

Table A.7: Experimental results for the leakage tests: (a) and (b), for all the VHC devices

Valve type	Device	(a) - insufflation		(b) - suction	
		30 L/min	60 L/min	30 L/min	60 L/min
Annulus Flap	AC	0.0(4)	0.0(8)	23.6(0)	55.8(0)
Coin	VOL	10.9(0)	22.9(0)	13.9(0)	28.8(0)
Duck	NC	1.2(0)	1.8(0)	18.9(0)	45.6(0)
Duck	OCD	0.5(8)	0.7(1)	20.7(5)	48.1(0)
Duck	V	0.0(1)	0.0(2)	26.0(0)	49.0(0)
Leaflets	A2A	3.2(0)	n.p.	12.6(0)	31.2(0)
Leaflets	CSC	0.0(0)	0.0(1)	27.0(0)	56.7(0)
Leaflets	SC	0.0(0)	0.0(0)	27.5(0)	57.2(0)

( ) - uncertain digit

n.p. - not possible to execute, the valve anchor was not strong enough to handle the flow pressure and detached from the device's body

Unit in L/min

The setup (b) tests were performed by extracting a constant 30 L/min and 60 L/min flow rate. The results point out that some leakage can be found in all devices. As some of them do not possess an exhalation valve, opening vents provide the exhaust during the exhalation phase. This leads to a secondary flow of air entering the mouthpiece that reduces the flow rate passing through the device's body. The existence of such valveless vents can be found in A2A Spacer and Volumatic. Hence, the worst leakage results are found for A2A Spacer ($\approx$45% of the suction flow) and Volumatic ($\approx$47% of the suction flow). The best results are found for the SpaceChamber ($\approx$91% of the suction flow) series and Aerochamber ($\approx$80%of the suction flow). The Vortex shows a good performance, with low leakage, as approximately 90% of the flow passing through the device's body. However, the Nebuchamber and Optichamber (both with the same valve type as Vortex) present a performance of $\approx$70% of the suction flow. Results of the setup (c), depicted in Figures A.12 and A.13, point out a more realistic influence of the flow in the valves and potential leakages in the devices.
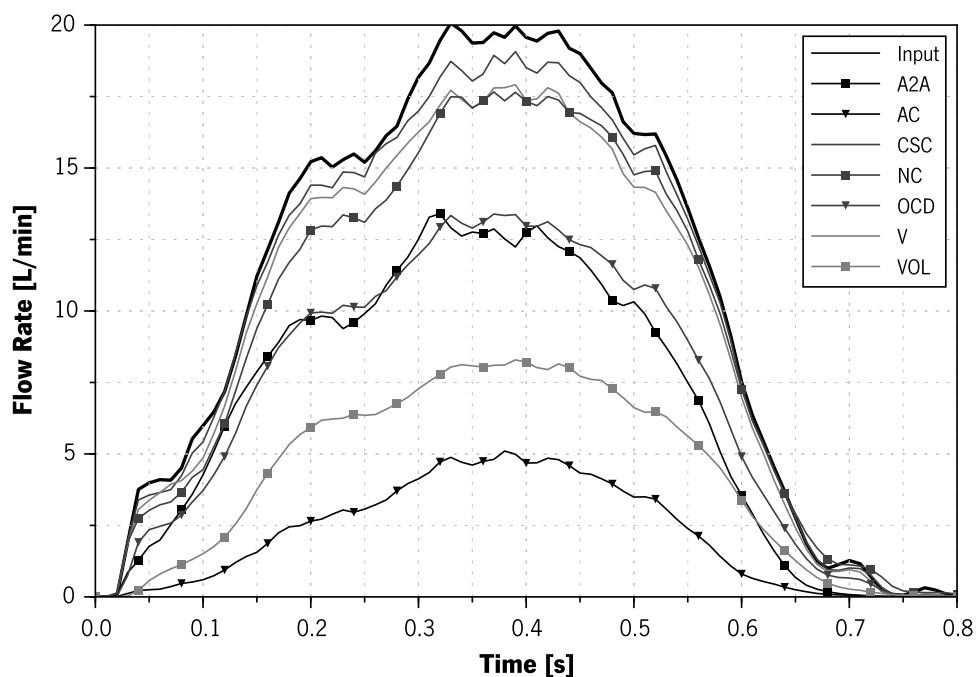
Figure A.12: Leakage results from the inhalation phase, using the setup (c), performed on the VHC devices in comparison with the input breath waveform
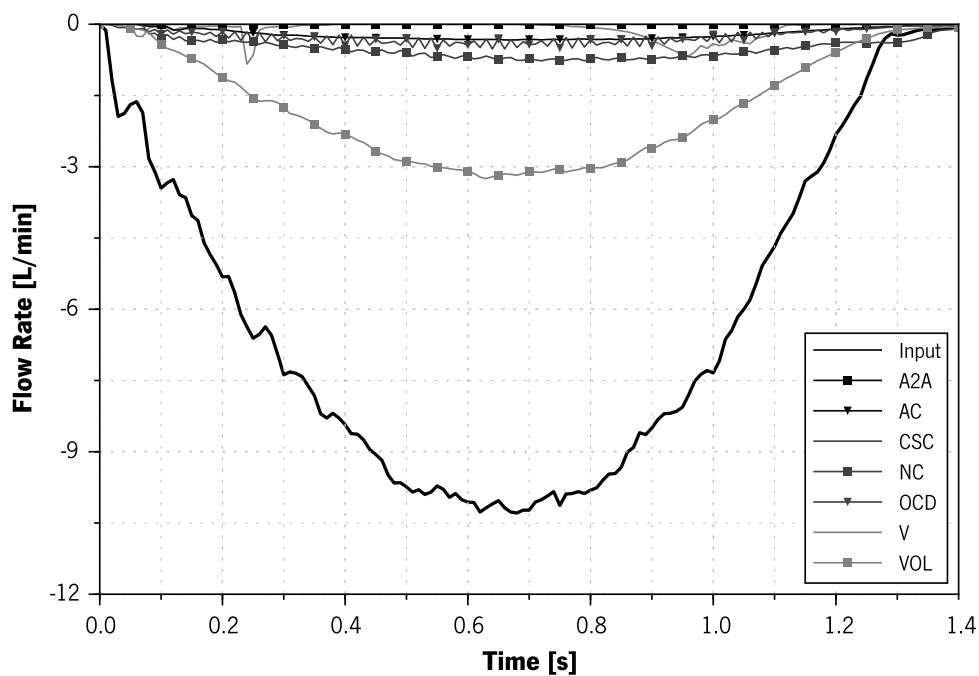
Figure A.13: Leakage results from the exhalation phase, using the setup (c), performed on the VHC devices in comparison with the input breath waveform

The tests were carried out with the mass flowmeter connected to the pMDI adapter of each VHC device, and keeping the secondary vents open (i.e. whistle, vortex channels and exhalation vents). The results show that the inhalation leakage ranked as: Aerochamber (has a whistle) > Volumatic (has exhalation vents) > A2A Spacer (has exhalation vents) > Optichamber (has a whistle) > Nebuchamber > Vortex (has helicoidal vents at the adapter)> Compact Space Chamber. The exhalation results show that only Volumatic has a considerable high leakage. Nebuchamber, Optichamber, Aerochamber and Vortex present a minor leakage during exhalation phase.

This page was intentionally left in blank

B Drug Assessment Raw Data

Table B.1: Experimental salbutamol sulphate mass collected in Full Dose setup at a constant flow rate of 30 L/min

Devices	Actuator	VHC	Filter Casing	Filter
MDI solo (*N*=2)	12.50±1.50	-	54.25±3.05	57.00±2.70
A2A Spacer (*N*=8)	13.20±1.79	76.26±6.56	3.12±0.87	30.25±7.92
AeroChamber (*N*=5)	12.02±1.19	61.69±6.44	2.95±0.60	41.28±8.59
Compact SpaceChamber (*N*=8)	14.47±3.12	72.41±3.71	3.81±0.66	31.45±5.10
Nebuchamber (*N*=6)	12.82±1.93	65.76±8.87	6.22±1.48	35.12±12.88
Optichamber (*N*=4)	12.24±0.95	70.21±3.45	6.05±1.20	38.34±9.35
SpaceChamber (*N*=6)	13.48±1.96	67.27±6.53	3.52±1.14	35.71±9.25
Vortex (*N*=4)	11.84±0.88	52.35±4.60	5.09±0.78	49.08±5.98
Volumatic (*N*=6)	12.20±2.60	68.98±15.84	4.47±0.68	38.24±14.25

Table B.2: Experimental salbutamol sulphate mass collected in Full Dose setup at a variable flow rate

Devices	Actuator	VHC	Filter Casing	Filter
MDI solo	-	-	-	-
A2A Spacer (*N*=5)	25.89±1.46	77.33±7.76	1.75±0.85	8.27±3.84
AeroChamber (*N*=3)	23.08±1.80	73.00±6.27	2.53±1.20	17.23±0.52
Compact SpaceChamber (*N*=5)	20.68±1.12	76.24±4.46	2.79±1.23	16.63±3.17
Nebuchamber (*N*=4)	24.01±3.70	68.60±7.85	4.72±0.30	15.14±1.42
Optichamber (*N*=6)	19.34±2.66	73.92±6.05	3.36±0.88	17.37±1.89
SpaceChamber (*N*=4)	19.71±2.45	75.54±4.40	3.09±0.72	19.69±2.75
Vortex (*N*=5)	21.66±1.31	79.83±10.60	4.36±1.70	15.89±4.00
Volumatic (*N*=5)	21.03±3.21	77.29±8.85	2.01±0.43	9.26±2.83

Table B.3: Experimental salbutamol sulphate mass collected in MSLI setup at a constant flow rate of 30 L/min

Devices	Actuator	VHC	Throat	Mixer	Stage 1	Stage 2	Stage 3	Stage 4	Stage 5 (Filter)
MDI solo (N=6)	13.22±0.72	-	55.35±4.98	-	4.96±0.74	2.62±0.71	5.78±0.49	7.40±1.07	17.34±1.99
A2A Spacer (N=5)	10.69±0.50	57.84±8.49	4.55±0.84	-	2.34±0.90	2.18±0.77	4.67±0.78	6.18±1.72	18.50±3.79
AeroChamber (N=6)	12.01±1.39	55.23±5.32	5.99±0.58	-	2.63±0.89	2.50±0.64	5.53±0.81	8.88±1.59	20.21±3.65
Compact SpaceChamber (N=7)	12.26±1.46	56.56±5.30	4.41±0.85	-	2.36±0.55	2.45±0.56	5.02±0.81	7.19±1.97	19.49±2.79
Nebuchamber (N=5)	12.34±2.32	53.58±4.25	10.04±0.83	-	1.59±0.30	1.71±0.63	4.11±0.48	6.85±1.05	18.95±1.29
Optichamber (N=5)	11.68±0.51	61.94±3.54	9.66±0.15	-	3.45±0.58	2.18±0.68	4.24±0.54	4.64±2.55	15.55±2.18
SpaceChamber (N=6)	12.13±1.46	50.35±7.94	4.58±0.94	-	2.94±0.82	2.16±0.51	5.42±1.15	8.58±3.21	20.28±5.82
Vortex (N=5)	11.43±1.45	49.79±3.46	9.16±1.27	-	2.48±0.67	1.86±0.47	5.26±0.89	8.04±0.98	19.74±2.47
Volumatic (N=6)	10.09±0.80	50.54±9.60	2.95±0.46	-	2.75±0.82	2.90±1.20	5.73±0.69	8.62±1.82	23.47±6.60

Table B.4: Experimental salbutamol sulphate mass collected in MSLI setup at a constant flow rate of 60 L/min

Devices	Actuator	VHC	Throat	Mixer	Stage 1	Stage 2	Stage 3	Stage 4	Stage 5 (Filter)
MDI solo (N=6)	11.52±0.71	-	45.48±2.75	-	6.10±0.89	5.08±0.53	11.79±1.19	8.93±1.32	15.26±1.79
A2A Spacer (N=8)	10.11±1.07	47.76±3.78	4.89±0.67	-	1.93±0.56	2.48±0.43	9.39±0.89	9.16±1.31	15.25±1.85
AeroChamber (N=7)	10.33±0.51	38.05±3.20	7.02±0.61	-	2.22±0.22	3.37±0.27	13.29±0.82	13.81±1.05	19.22±1.12
Compact SpaceChamber (N=8)	9.51±0.69	41.60±3.23	5.37±0.54	-	2.63±0.69	3.18±0.16	12.29±1.19	12.04±1.60	17.34±2.15
Nebuchamber (N=6)	9.76±1.46	35.49±1.67	15.95±1.03	-	1.44±0.22	2.20±0.18	10.17±0.58	11.33±0.81	17.25±1.08
Optichamber (N=6)	10.14±1.05	41.93±2.31	12.73±1.16	-	2.50±0.47	2.71±0.17	10.00±0.86	10.23±0.98	15.55±1.89
SpaceChamber (N=6)	11.02±0.64	37.79±2.53	5.40±0.33	-	2.43±0.44	3.49±0.47	12.70±1.25	12.76±1.34	18.26±1.28
Vortex (N=8)	10.41±0.83	26.38±2.70	12.53±0.88	-	2.40±0.40	3.40±0.27	13.60±0.91	13.70±0.87	18.97±1.87
Volumatic (N=6)	9.95±0.81	50.21±4.53	2.76±0.16	-	1.47±0.22	2.46±0.29	11.31±1.02	12.61±1.03	18.96±1.48

Table B.5: Experimental salbutamol sulphate mass collected in MSLI setup at a variable flow rate

Devices	Actuator	VHC	Throat	Mixer	Stage 1	Stage 2	Stage 3	Stage 4	Stage 5 (Filter)
MDI solo (N=6)	18.25±2.39	-	54.10±3.48	0.13±0.00	2.21±0.43	1.94±0.09	7.73±0.10	6.37±0.21	12.88±0.48
A2A Spacer	-	-	-	-	-	-	-	-	-
AeroChamber (N=7)	17.01±2.48	69.78±6.05	6.09±0.72	0.21±0.00	0.46±0.16	0.85±0.25	4.49±1.39	3.85±1.54	7.39±2.08
Compact SpaceChamber (N=7)	14.34±1.52	74.20±4.40	5.59±0.75	0.38±0.00	0.80±0.10	1.07±0.18	5.12±0.75	4.27±0.85	8.34±1.10
Nebuchamber	-	-	-	-	-	-	-	-	-
Optichamber	-	-	-	-	-	-	-	-	-
SpaceChamber	-	-	-	-	-	-	-	-	-
Vortex (N=7)	16.04±1.47	73.95±6.91	6.45±1.60	0.13±0.00	0.65±0.15	0.74±0.17	3.33±0.95	2.64±0.83	5.88±1.41
Volumatic (N=7)	17.49±1.51	72.55±1.37	2.97±0.65	0.39±0.00	0.51±0.17	0.93±0.22	4.70±0.85	4.04±0.76	7.99±1.08

Bibliography

[Abr07]   Sofia Abreu. Study of different spacers for pressurized inhalers. Master thesis, University of Minho, Braga, 2007.

[ALCH04]   Michael J Asmus, Judy Liang, Intira Coowanitwong, and Günther Hochhaus. In Vitro Performance Characteristics of Valved Holding Chamber and Spacer Devices with a Fluticasone Metered-Dose Inhaler. Pharmacotherapy, 24(2):159–166, feb 2004.

[ANS13]   ANSYS. ANSYS FLUENT Theory Guide. ANSYS Inc, Canonsburg, PA, USA, release 15 edition, 2013.

[AR85]   Michael D. Allen and Otto G. Raabe. Slip Correction Measurements of Spherical Solid Aerosol Particles in an Improved Millikan Apparatus. Aerosol Science and Technology, 4(3):269–286, jan 1985.

[ASAT08]   Sofia Abreu, Luís F Silva, Henedina Antunes, and Senhorinha F. C. F. Teixeira. Multiphase flow inside the Volumatic spacer: a CFD approach. In E C Ferreira and M Mota, editors, Proceedings of the 10th International Chemical and Biological Engineering Conference - CHEMPOR 2008, page 6, Braga, 2008.

[ASM98]   ASME. PTC 19.1 - 1998 - Test Uncertainty, 1998.

[BCLM11]   G. Brambilla, T. Church, D. Lewis, and B. Meakin. Plume temperature emitted from metered dose inhalers. International Journal of Pharmaceutics, 405(1-2):9–15, 2011.

Bibliography

[BD92]   Raymond M. Brach and Patrick F. Dunn. A Mathematical Model of the Impact and Adhesion of Microsphers. Aerosol Science and Technology, 16(1):51–64, jan 1992.

[BD95]   Raymond M. Brach and Patrick F. Dunn. Macrodynamics of Microparticles. Aerosol Science and Technology, 23(1):51–71, jan 1995.

[Bis95]   Hans Bisgaard. A metal aerosol holding chamber devised for young children with asthma. European Respiratory Journal, 8(5):856–860, 1995.

[BK07]   J T Black and Ron Kohser. DeGarmo's Materials & Processes in Manufacturing. John Wiley & Sons, USA, 10th edition, 2007.

[BO95]   P.W. Barry and Chris O'Callaghan. The Optimum Size and Shape of Spacer Devices for Inhalational Therapy. Journal of Aerosol Medicine, 8(3):303–305, jan 1995.

[BO99a]   Peter W Barry and Chris O'Callaghan. A comparative analysis of the particle size output of beclomethasone diproprionate, salmeterol xinafoate and fluticasone propionate metered dose inhalers used with the Babyhaler, Volumatic and Aerochamber spacer devices. British Journal of Clinical Pharmacology, 47(4):357–360, dec 1999.

[BO99b]   Peter W Barry and Chris O'Callaghan. The output of budesonide from spacer devices assessed under simulated breathing conditions. Journal of Allergy and Clinical Immunology, 104(6):1205–1210, dec 1999.

[BOS01]   Hans Bisgaard, Chris O'Callaghan, and Gerald C. Smaldone. Drug Delivery to the Lung, 2001.

[BP09]   Elna B Berg and Robert J Picard. In vitro delivery of budesonide from 30 jet nebulizer/compressor combinations using infant and child breathing patterns. Respiratory care, 54(12):1671–8, dec 2009.

[BRW$^+$01] D Brocklebank, F Ram, J Wright, Peter W Barry, C Cates, L Davies, G Douglas, M Muers, D Smith, and J White. Comparison of the effectiveness of inhaler devices

in asthma and chronic obstructive airways disease: a systematic review of the literature. Health technology assessment, 5(26):1–149, jan 2001.

[BSM$^+$00] Joel L Berry, Aland Santamarina, James E. Moore, Jr., Suranjan Roychowdhury, and William D Routh. Experimental and Computational Flow Evaluation of Coronary Stents. Annals of Biomedical Engineering, 28(4):386–398, apr 2000.

[CAM$^+$01] A L Coates, P D Allen, C F MacNeish, S L Ho, and L C Lands. Effect of size and disease on estimated deposition of drugs administered using jet nebulization in children with cystic fibrosis. Chest, 119(4):1123–30, apr 2001.

[Can08] Arnaldo Cantani. Asthma. In Ute Heilmann, editor, Pediatric Allergy, Asthma and Immunology, chapter Chapter 11, pages 725–873. Springer Berlin Heidelberg, Berlin, Heidelberg, 2008.

[CAS99] R.P. Chhabra, L Agarwal, and N.K. Sinha. Drag on non-spherical particles: an evaluation of available methods. Powder Technology, 101(3):288–295, mar 1999.

[CC00] N Y Chew and H K Chan. The effect of spacers on the delivery of metered dose aerosols of nedocromil sodium and disodium cromoglycate. International journal of pharmaceutics, 200(1):87–92, apr 2000.

[CFYZ01] Y.S. S Cheng, C.S. S Fu, D. Yazzie, and Y. Zhou. Respiratory Deposition Patterns of Salbutamol pMDI with CFC and HFA-134a Formulations in a Human Airway Replica. Journal of Aerosol Medicine, 14(2):255–266, jun 2001.

[CGR$^+$08] Ismail B. Celik, Urmila Ghia, Patrick J. Roache, Christopher J. Freitas, Hugh Coleman, and Peter E. Raad. Procedure for Estimation and Reporting of Uncertainty Due to Discretization in CFD Applications. Journal of Fluids Engineering, 130(7):078001, 2008.

[CGW05] Roland Clift, John R. Grace, and Martin E. Weber. Bubbles, drops, and particles. Dover Publications, 2005.

Bibliography

[Che14]   Yung Sung Cheng. Mechanisms of Pharmaceutical Aerosol Deposition in the Respiratory Tract. AAPS PharmSciTech, 15(3):630–640, 2014.

[CJM09]   Brian Michael Crosland, Matthew Ronald Johnson, and Edgar Akio Matida. Characterization of the spray velocities from a pressurized metered-dose inhaler. Journal of aerosol medicine and pulmonary drug delivery, 22(2):85–97, jun 2009.

[Cla91]   Andrew Reginald Clark. Metered Atomisation for Respiratory Drug Delivery. Phd thesis, Loughborough University of Technology, 1991.

[Cla96]   Andrew R Clark. MDIs: physics of aerosol formation. Journal of aerosol medicine, 9 Suppl 1(s1):S19–26, mar 1996.

[Cro06]   Graham Crompton. A brief history of inhaled asthma therapy over the last fifty years. Primary Care Respiratory Journal, 15(6):326–31, dec 2006.

[CRR04]   José a Castro-Rodriguez and Gustavo J Rodrigo. Beta-Agonists through Metered-Dose Inhaler with Valved Holding Chamber versus Nebulizer for Acute Exacerbation of Wheezing or Asthma in Children under 5 Years of Age: A Systematic Review with Meta-Analysis. The Journal of pediatrics, 145(2):172–7, 2004.

[Cun10]   E. Cunningham. On the Velocity of Steady Fall of Spherical Particles through Fluid Medium. Proceedings of the Royal Society A: Mathematical, Physical and Engineering Sciences, 83(563):357–365, mar 1910.

[CYF+14a]   Yang Chen, Paul M. Young, David F. Fletcher, Hak Kim Chan, Edward Long, David Lewis, Tanya Church, and Daniela Traini. The Effect of Actuator Nozzle Designs on the Electrostatic Charge Generated in Pressurised Metered Dose Inhaler Aerosols. Pharmaceutical Research, 32(4):1237–1248, 2014.

[CYF+14b]   Yang Chen, Paul M. Young, David F. Fletcher, Hak Kim Chan, Edward Long, David Lewis, Tanya Church, and Daniela Traini. The Influence of Actuator Materials and Nozzle Designs on Electrostatic Charge of Pressurised Metered Dose Inhaler (pMDI) Formulations. Pharmaceutical Research, 31(5):1325–1337, may 2014.

[CZR08]   CAN/CSA-Z264.1-02(R2008). Spacers and Holding Chambers for Use with Metered-Dose Inhalers. Canadian Standards Association, Toronto, Canada, 2008.

[CZS15]   Yung Sung Cheng, Yue Zhou, and Wei-Chung Su. Deposition of Particles in Human Mouth–Throat Replicas and a USP Induction Port. Journal of Aerosol Medicine and Pulmonary Drug Delivery, 28(3):147–155, jun 2015.

[DD11]   Myrna B. Dolovich and Rajiv Dhand. Aerosol drug delivery: developments in device design and clinical use. Lancet, 377(9770):1032–1045, mar 2011.

[Deh08]   A. Dehbi. Turbulent particle dispersion in arbitrary wall-bounded geometries: A coupled CFD-Langevin-equation based approach. International Journal of Multiphase Flow, 34(9):819–828, sep 2008.

[Deh11]   A Dehbi. Prediction of Extrathoracic Aerosol Deposition using RANS-Random Walk and LES Approaches. Aerosol Science and Technology, 45(5):555–569, 2011.

[DF01]   Myrna B. Dolovich and James B. Fink. Aerosols and devices. Respiratory care clinics of North America, 7(2):131–173, jun 2001.

[DGB03]   J.C. Dubus, C Guillot, and M Badier. Electrostatic charge on spacer devices and salbutamol response in young children. International Journal of Pharmaceutics, 261(1-2):159–164, aug 2003.

[DH00]   Craig A. Dunbar and Anthony J. Hickey. Evaluation of probability density functions to aporoximate particle size distributions of representative pharmaceutical aerosols. Journal of Aerosol Science, 31(7):813–831, jul 2000.

[DM04]   Myrna B. Dolovich and Jolyon P Mitchell. Canadian Standards Association standard CAN/CSA/Z264.1-02:2002: a new voluntary standard for spacers and holding chambers used with pressurized metered-dose inhalers. Canadian respiratory journal, 11(7):489–95, oct 2004.

Bibliography

[DMZ$^+$14] William Ditcham, Jasminka Murdzoska, Guicheng Zhang, Christina Roller, Dirk von Hollen, Kurt Nikander, and Sunalene G Devadason. Lung Deposition of 99m Tc-Radiolabeled Albuterol Delivered through a Pressurized Metered Dose Inhaler and Spacer with Facemask or Mouthpiece in Children with Asthma. Journal of Aerosol Medicine and Pulmonary Drug Delivery, 27(S1):S–63–S–75, 2014.

[Dol04] Myrna B. Dolovich. In my opinion - Interview with the Expert. Pediatric Asthma Allergy & Immunology, 17(4):292–300, 2004.

[DS03] Richard Dalby and Julie Suman. Inhalation therapy: technological milestones in asthma treatment. Advanced drug delivery reviews, 55(7):779–91, jul 2003.

[Dun96] Craig A. Dunbar. An experimental and theoretical investigation of the spray issued from a pressurised metered-dose inhaler. Phd thesis, University of Manchester, 1996.

[Dun97] Craig A. Dunbar. Atomization mechanisms of the pressurized metered dose inhaler. Particulate Science and Technology, 15(3-4):253–271, jul 1997.

[DWM97] Craig A. Dunbar, A P Watkins, and J F Miller. An experimental investigation of the spray issued from a pMDI using laser diagnostic techniques. Journal of Aerosol Medicine, 10(4):351–68, jan 1997.

[EABB11] Najla El Gharbi, Rafik Absi, Ahmed Benzaoui, and Rachid Bennacer. An improved near-wall treatment for turbulent channel flows. International Journal of Computational Fluid Dynamics, 25(1):41–46, jan 2011.

[EFAvV$^+$04] J E Esposito-Festen, B Ates, F J M van Vliet, A F M Verbraak, J C de Jongste, and H A W M Tiddens. Effect of a facemask leak on aerosol delivery from a pMDI-spacer system. Journal of aerosol medicine : the official journal of the International Society for Aerosols in Medicine, 17(1):1–6, jan 2004.

[FBGD00] M R Feddah, K F Brown, E M Gipps, and N M Davies. In-vitro characterisation of metered dose inhaler versus dry powder inhaler glucocorticoid products: influence of

inspiratory flow rates. Journal of pharmacy & pharmaceutical sciences : a publication of the Canadian Society for Pharmaceutical Sciences, Societe canadienne des sciences pharmaceutiques, 3(3):318–24, 2000.

[Fin98]   Warren H. Finlay. Inertial sizing of aerosol inhaled during pediatric tidal breathing from an MDI with attached holding chamber. International Journal of Pharmaceutics, 168(2):147–152, jun 1998.

[Fin01]   Warren H. Finlay. The mechanics of inhaled pharmaceutical aerosols: an introduction. Academic Press, 2001.

[FK99]   Scott A Foss and Jean W Keppel. In Vitro Testing of MDI Spacers: A Technique for Measuring Respirable Dose Output with Actuation In-Phase or Out-of-Phase with Inhalation. Respiratory Care, 44(12):1474–1485, 1999.

[FK13]   Y. Feng and C. Kleinstreuer. Analysis of non-spherical particle transport in complex internal shear flows. Physics of Fluids, 25(9):091904, 2013.

[Flo09]   Paulo Flores. Projecto de mecanismos Came-Seguidor. Publindústria, Porto, Portugal, 2009.

[Fol02]   A Foland. Improvement of metered-dose inhaler administration technique: the effect of training sessions at a specialized pediatric asthma compliance and technique clinic. Current Therapeutic Research, 63(2):142–147, feb 2002.

[FP03]   Joel H Ferziger and Milovan Peric. Computational methods for fluid dynamics. Springer, 3 edition, jul 2003.

[FWZS07]   Ahmed Fadl, Jinbo Wang, Zongqin Zhang, and Yung Sung Cheng. Effects of MDI spray angle on aerosol penetration efficiency through an oral airway cast. Journal of Aerosol Science, 38(8):853–864, aug 2007.

[FZ98]   Warren H. Finlay and P. Zuberbuhler. In Vitro Comparison of Beclomethasone and Salbutamol Metered-Dose Inhaler Aerosols Inhaled During Pediatric Tidal Breathing From Four Valved Holding Chambers. Chest, 114(6):1676–1680, dec 1998.

Bibliography

[FZM97]   Warren H. Finlay, P. Zuberbuhler, and M. Mandl. Particle Size Measurements for the Space-Chamber Metered Dose Inhaler Holding Chamber Compared with Aerochamber and Metered Dose Inhaler Alone. Journal of Aerosol Medicine, 10(3):213–219, jan 1997.

[GA04]   Athanasia M. Goula and Konstantinos G. Adamopoulos. Influence of Spray Drying Conditions on Residue Accumulation—Simulation Using CFD. Drying Technology, 22(5):1107–1128, 2004.

[GAN$^+$13]   Talita Mota Goncalves, Kamel Alhanout, Alain Nicolay, Jean-Christophe Dubus, Davi Pereira de Santana, and Veronique Andrieu. Comparative In Vitro Performance of Three Small-Volume Valved Holding Chambers with Beclomethasone/Formoterol Pressurized Metered Dose Inhaler. Journal of Aerosol Medicine and Pulmonary Drug Delivery, 26(4):223–227, aug 2013.

[GL83]   A. D. Gosman and E. Loannides. Aspects of Computer Simulation of Liquid-Fueled Combustors. Journal of Energy, 7(6):482–490, nov 1983.

[Glo14]   Global Initiative for Asthma. Global strategy for asthma management and prevention. Technical report, GINA, 2014.

[GSV99]   B J Gabrio, S W Stein, and D J Velasquez. A new method to evaluate plume characteristics of hydrofluoroalkane and chlorofluorocarbon metered dose inhalers. International journal of pharmaceutics, 186(1):3–12, sep 1999.

[Hic03]   Anthony J. Hickey. Pharmaceutical inhalation aerosol technology. Marcel Dekker, Inc., New York, USA, 2nd editio edition, 2003.

[Hin99]   William C. Hinds. Aerosol Technology: Properties, Behavior, and Measurement of Airborne Particles. John Wiley & Sons, New York, USA, 2nd edition, 1999.

[HvHSS14]   Ross H M Hatley, Dirk von Hollen, Dennis Sandell, and Lois Slator. In vitro characterization of the OptiChamber Diamond valved holding chamber. Journal of aerosol medicine and pulmonary drug delivery, 27 Suppl 1:S24–36, aug 2014.

[IDQ08]   A.H. Ibrahim, P.F. Dunn, and M.F. Qazi. Experiments and validation of a model for microparticle detachment from a surface by turbulent air flow. Journal of Aerosol Science, 39(8):645–656, aug 2008.

[JAC⁺05]   L. L. Janssen, N. J. Anderson, P. E. Cassidy, R. A. Weber, and T. J. Nelson. Interpretation of Inhalation Airflow Measurements for Respirator Design and Testing. Journal of the International Society for Respiratory Protection, 22(3):122–141, 2005.

[JBGJ00]   G Jepson, T Butler, D Gregory, and K Jones. Prescribing patterns for asthma by general practitioners in six European countries. Respiratory medicine, 94(6):578–583, jun 2000.

[JKR71]   K. L. Johnson, K. Kendall, and A. D. Roberts. Surface Energy and the Contact of Elastic Solids. In Proceedings of the Royal Society of London. Series A, Mathematical and Physical Sciences, volume 324, pages 301–313. The Royal Society, 1971.

[JWE⁺02]   R Janssen, M Weda, M B Ekkelenkamp, J-W J Lammers, and P Zanen. Metal versus plastic spacers: an in vitro and in vivo comparison. International journal of pharmaceutics, 245(1-2):93–8, oct 2002.

[KCC06]   Philip Chi Lip Kwok, Richard Collins, and Hak-Kim Chan. Effect of spacers on the electrostatic charge properties of metered dose inhaler aerosols. Journal of Aerosol Science, 37(12):1671–1682, dec 2006.

[KCD⁺05]   D Keochkerian, M Chlif, S Delanaud, R Gauthier, Y Maingourd, and S Ahmaidi. Timing and driving components of the breathing strategy in children with cystic fibrosis during exercise. Pediatric pulmonology, 40(5):449–56, nov 2005.

[KHDL15]   Navvab Khajeh-Hosseini-Dalasm and P. Worth Longest. Deposition of particles in the alveolar airways: Inhalation and breath-hold with pharmaceutical aerosols. Journal of Aerosol Science, 79:15–30, jan 2015.

Bibliography

[Kir72]   W.F. Kirk. In Vitro Method of Comparing Clouds Produced from Inhalation Aerosols for Efficiency in Penetration of Airways. Journal of Pharmaceutical Sciences, 61(2):262–265, feb 1972.

[KSZ07]   Clement Kleinstreuer, Huawei Shi, and Zhe Zhang. Computational analyses of a pressurized metered dose inhaler and a new drug-aerosol targeting methodology. Journal of aerosol medicine, 20(3):294–309, jan 2007.

[KTH+06]   Yasmeen Khan, Yufei Tang, Guenther Hochhaus, Jonathan J. Shuster, Terry Spencer, Sarah Chesrown, and Leslie Hendeles. Lung bioavailability of hydrofluoroalkane fluticasone in young children when delivered by an antistatic chamber/mask. Journal of Pediatrics, 149(6):793–797, 2006.

[LA85]   David Leighton and Andreas Acrivos. The lift on a small sphere touching a plane in the presence of a simple shear flow. ZAMP Zeitschrift fur angewandte Mathematik und Physik, 36(1):174–178, jan 1985.

[LDG12]   Xiaofei Liu, William H Doub, and Changning Guo. Evaluation of metered dose inhaler spray velocities using Phase Doppler Anemometry (PDA). International journal of pharmaceutics, 423(2):235–239, feb 2012.

[LHCB07]   P. Worth Longest, Michael Hindle, Suparna Das Choudhuri, and Peter R. Byron. Numerical Simulations of Capillary Aerosol Generation: CFD Model Development and Comparisons with Experimental Data. Aerosol Science and Technology, 41(10):952–973, aug 2007.

[LHDX08]   P. Worth Longest, Michael Hindle, Suparna Das Choudhuri, and Jinxiang Xi. Comparison of ambient and spray aerosol deposition in a standard induction port and more realistic mouth–throat geometry. Journal of Aerosol Science, 39(7):572–591, jul 2008.

[LMF16]   E.W. Lemmon, M.O. McLinden, and D.G. Friend. Thermophysical Properties of Fluid Systems. In P.J. Linstrom and W.G. Mallard, editors, NIST Chemistry WebBook,

NIST Standard Reference Database Number 69. National Institute of Standards and Technology, Gaithersburg MD, 2016.

[LV07]   P. Worth Longest and Samir Vinchurkar. Effects of mesh style and grid convergence on particle deposition in bifurcating airway models with comparisons to experimental data. Medical Engineering and Physics, 29:350–366, 2007.

[LX07]   P. Worth Longest and Jinxiang Xi. Effectiveness of Direct Lagrangian Tracking Models for Simulating Nanoparticle Deposition in the Upper Airways. Aerosol Science and Technology, 41(4):380–397, mar 2007.

[MA72]   S. A. Morsi and A. J. Alexander. An investigation of particle trajectories in two-phase flow systems. Journal of Fluid Mechanics, 55(02):193, sep 1972.

[MAK13]   J. Milenkovic, A.H. Alexopoulos, and C. Kiparissides. Flow and particle deposition in the Turbuhaler: A CFD simulation. International Journal of Pharmaceutics, 448(1):205–213, may 2013.

[Mar04]   Virgil a. Marple. History of Impactors—The First 110 Years. Aerosol Science and Technology, 38(3):247–292, mar 2004.

[Mar07]   J A Marques. Asma. In M A Ferreira and E Loureiro, editors, O Essencial da Saúde, volume 15. QuidNovi, Lisboa, 2007.

[McD14]   John H. McDonald. Handbook of Biological Statistics. Sparky House Publishing, Baltimore, Maryland, USA, 3rd edition, 2014.

[MD12]   Jolyon P Mitchell and Myrna B Dolovich. Clinically relevant test methods to establish in vitro equivalence for spacers and valved holding chambers used with pressurized metered dose inhalers (pMDIs). Journal of aerosol medicine and pulmonary drug delivery, 25(4):217–42, aug 2012.

[Men93]   Florian R. Menter. Zonal Two Equation k-omega Turbulence Models for Aerodynamic Flows. In 24th AIAA Fluid Dynamics Conference, page 21, Orlando, FL; United States, 1993.

[MFHB04]   Matthew Masoli, Denise Fabian, Shaun Holt, and Richard Beasley. The global burden of asthma: executive summary of the GINA Dissemination Committee report. Allergy, 59(5):469–78, may 2004.

[MFLG04]   E. A. Matida, Warren H. Finlay, C. F. Lange, and B. Grgic. Improved numerical simulation of aerosol deposition in an idealized mouth–throat. Journal of Aerosol Science, 35(1):1–19, jan 2004.

[MGH$^+$99]   T Manczur, A Greenough, R Hooper, K Allen, S Latham, J F Price, and G F Rafferty. Tidal breathing parameters in young children: comparison of measurement by respiratory inductance plethysmography to a facemask pneumotachograph system. Pediatric pulmonology, 28(6):436–41, dec 1999.

[Mil02]   Nicholas C. Miller. US 6435004 - Apparatus and process for aerosol size measurement at varying gas flow rates, 2002.

[Mil05]   M. R. Miller. Standardisation of spirometry. European Respiratory Journal, 26(2):319–338, aug 2005.

[MKBZ12]   Jacquelyn Cruz McCabe, Franciscus Koppenhagen, Julian Blair, and Xian-Ming Zeng. ProAir HFA Delivers Warmer, Lower-Impact, Longer-Duration Plumes Containing Higher Fine Particle Dose Than Ventolin HFA. Journal of Aerosol Medicine and Pulmonary Drug Delivery, 25(2):104–109, 2012.

[MN97]   Jolyon P Mitchell and Mark W Nagel. In vitro performance testing of three small volume-holding chambers under conditions that correspond with use by infants and small children. Journal of Aerosol Medicine, 10(4):341–349, 1997.

[MN03]   Jolyon P Mitchell and Mark W Nagel. Cascade impactors for the size characterization of aerosols from medical inhalers: their uses and limitations. Journal of Aerosol Medicine, 16(4):341–77, jan 2003.

[MN07]   Jolyon P. Mitchell and Mark W. Nagel. Valved holding chambers (VHCs) for use with pressurised metered-dose inhalers (pMDIs): A review of causes of inconsistent medication delivery. Primary Care Respiratory Journal, 16(4):207–214, 2007.

[MNT00]   Edgar Akio Matida, Koichi Nishino, and Kahoru Torii. Statistical simulation of particle deposition on the wall from turbulent dispersed pipe flow. International Journal of Heat and Fluid Flow, 21(4):389–402, aug 2000.

[Mon11]   Matteo Monticelli. Generalized Wall Functions for RANS Computation of Turbulent Flows. Master thesis, Politecnic of Milan, 2011.

[Mor78]   Folke Morén. Drug deposition of pressurized inhalation aerosols I. Influence of actuator tube design. International Journal of Pharmaceutics, 1(4):205–212, jul 1978.

[MSDK^{+}16] Nicholas Mason-Smith, Daniel J. Duke, Alan L. Kastengren, Peter J. Stewart, Daniela Traini, Paul M. Young, Yang Chen, David A. Lewis, Julio Soria, Daniel Edgington-Mitchell, and Damon Honnery. Insights into Spray Development from Metered-Dose Inhalers Through Quantitative X-ray Radiography. Pharmaceutical Research, feb 2016.

[MvHvK^{+}14] Kirby Tong Minh, Dirk von Hollen, Annemieke J. von Königslöw, Kurt Nikander, and Hettie M. Janssens. An Instrumented Valved Holding Chamber with Facemask to Measure Application Forces and Flow in Young Asthmatic Children. Journal of Aerosol Medicine and Pulmonary Drug Delivery, 27(S1):S–55–S–62, aug 2014.

[MW79]   Nils F E Moren and Kjell I L Wetterlin. Device for use with medicinal inhalation devices, 1979.

[Nat07]   National Heart Lung and Blood Institute. Expert Panel Report 3: Guidelines for the Diagnosis and Management of Asthma. Technical report, National Heart Lung and Blood Institute (NHLBI), Bethesda, 2007.

Bibliography

[NDSW01]   Kurt Nikander, John Denyer, Nick Smith, and Per Wollmer. Breathing Patterns and Aerosol Delivery: Impact of Regular Human Patterns, and Sine and Square Waveforms on Rate of Delivery. Journal of Aerosol Medicine, 14(3):327–333, sep 2001.

[New04]   Stephen P Newman. Spacer devices for metered dose inhalers. Clinical pharmacokinetics, 43(6):349–360, jan 2004.

[New05]   Stephen P Newman. Principles of metered-dose inhaler design. Respiratory care, 50(9):1177–1190, sep 2005.

[New06]   Stephen P Newman. Aerosols. In Geoffrey J. Laurent and Steven D. Shapiro, editors, Encyclopedia of Respiratory Medicine, pages 58–64. Elsevier, 2006.

[NMLJ$^+$84] S P Newman, A B Millar, T R Lennard-Jones, F Morén, and S W Clarke. Improvement of pressurised aerosol deposition with Nebuhaler spacer device. Thorax, 39(12):935–941, 1984.

[NNDP14]   Kurt Nikander, Clare Nicholls, John Denyer, and John Pritchard. The Evolution of Spacers and Valved Holding Chambers. Journal of aerosol medicine and pulmonary drug delivery, 27(S1):S4–S24, 2014.

[Nor02]   Robert L. Norton. Cam design and manufacturing handbook. Industrial Press, New York, USA, 2002.

[NWBM02]   Mark W Nagel, Kimberly J Wiersema, Sara-Lou Bates, and Jolyon P Mitchell. Performance of large- and small-volume valved holding chambers with a new combination long-term bronchodilator/anti-inflammatory formulation delivered by pressurized metered dose inhaler. Journal of aerosol medicine : the official journal of the International Society for Aerosols in Medicine, 15(4):427–433, 2002.

[OFT$^+$14]   Ricardo F Oliveira, Ana C M Ferreira, Senhorinha F. C. F. Teixeira, José Carlos Teixeira, and Helena Maria Cabral Marques. A CFD Study of a pMDI Plume Spray.

In Gi-Chul Yang, Sio-Iong Ao, and Len Gelman, editors, Transactions on Engineering Technologies, pages 163–176. Springer Netherlands, 2014.

[O'N68]   M.E. O'Neill. A sphere in contact with a plane wall in a slow linear shear flow. Chemical Engineering Science, 23(11):1293–1298, nov 1968.

[OTMT12]   Ricardo F Oliveira, José Carlos Teixeira, Helena Maria Cabral Marques, and Senhorinha Teixeira. Modeling Flow Recirculation Inside a Holding Chamber. In Volume 2: Biomedical and Biotechnology, page 325, Houston, Texas, USA, nov 2012. ASME.

[OTMT14a]   Ricardo F Oliveira, Senhorinha F C F Teixeira, Helena Maria Cabral Marques, and José Carlos Teixeira. Efficiency evaluation of VHC: a CFD comparison study at constant flow. In Proceedings of the 2014 International Conference on Mechanics, Fluid Mechanics, Heat and Mass Transfer, Interlaken, Swiss, 2014. EUROPMENT.

[OTMT14b]   Ricardo F Oliveira, Senhorinha F C F Teixeira, Helena Maria Cabral Marques, and José Carlos Teixeira. Flow Recirculation in VHC Designs. In Eugenio Oñate, Xavier Oliver, and Antonio Huerta, editors, 6th European Conference on Computational Fluid Dynamics (ECFD VI), volume VI, pages 7342–7350, Barcelona, Spain, 2014. International Center for Numerical Methods in Engineering (CIMNE).

[OTS+12]   Ricardo F Oliveira, Senhorinha F C F Teixeira, Luís F Silva, José C F Teixeira, and Henedina Antunes. Development of new spacer device geometry: a CFD study (part I). Computer methods in biomechanics and biomedical engineering, 15(8):825–833, jan 2012.

[OTT+12]   Ricardo F Oliveira, Senhorinha F. C. F. Teixeira, José Carlos Teixeira, Luís F Silva, and Henedina Antunes. pMDI Sprays: Theory , Experiment and Numerical Simulation. In Chaoqun Liu, editor, Advances in Modeling of Fluid Dynamics, chapter 11, page 300. Intech, Rijeka, Croatia, 2012.

Bibliography

[PCS01]   Lexley Pinto Pereira, Yuri Clement, and Donald Simeon. Educational intervention for correct pressurised metered dose inhaler technique in Trinidadian patients with asthma. Patient Education and Counseling, 42(1):91–97, jan 2001.

[PLK01]   Donald L Pavia, Gary M Lampman, and George S Kriz. Introduction to Spectroscopy: A guide for students of organic chemistry. Thomson Learning Inc., USA, 3rd edition, 2001.

[PM61]   Irving Porush and George Louis Maison. Aerosol dispensing apparatus, 1961.

[RCN$^+$06] Joseph L Rau, Dominic P Coppolo, Mark W Nagel, Valentina I Avvakoumova, Cathy C Doyle, Kimberly J Wiersema, and Jolyon P Mitchell. The importance of nonelectrostatic materials in holding chambers for delivery of hydrofluoroalkane albuterol. Respiratory care, 51(5):503–510, 2006.

[RG99]   D L Ross and B J Gabrio. Advances in metered dose inhaler technology with the development of a chlorofluorocarbon-free drug delivery system. Journal of aerosol medicine : the official journal of the International Society for Aerosols in Medicine, 12(3):151–60, jan 1999.

[RJF13]   Conor A Ruzycki, Emadeddin Javaheri, and Warren H. Finlay. The use of computational fluid dynamics in inhaler design. Expert opinion on drug delivery, 10(3):307–23, mar 2013.

[RMSBCR12]   Carlos E. Rodriguez-Martinez, Mónica P. Sossa-Briceño, and Jose A. Castro-Rodriguez. Comparison of the bronchodilating effects of albuterol delivered by valved vs. non-valved spacers in pediatric asthma. Pediatric Allergy and Immunology, 23(7):629–635, 2012.

[RR13]   Bart L. Rottier and Bruce K. Rubin. Asthma medication delivery: Mists and myths. Paediatric Respiratory Reviews, 14(2):112–118, jun 2013.

[RZLF02]   Muhib F Rahmatalla, Peter C Zuberbuhler, Carlos F Lange, and Warren H. Finlay. In vitro effect of a holding chamber on the mouth-throat deposition of QVAR

(hydrofluoroalkane-beclomethasone dipropionate). Journal of aerosol medicine, 15(4):379–385, jan 2002.

[San07]   Mark Sanders. Inhalation therapy: an historical review. Primary care respiratory journal, 16(2):71–81, apr 2007.

[SB07]   Liming Shi and David J. Bayless. Comparison of boundary conditions for predicting the collection efficiency of cyclones. Powder Technology, 173(1):29–37, apr 2007.

[SB11]   Scottish Intercollegiate Guidelines Network and British Thoracic Society. British guideline on the management of asthma: A national clinical guideline. Technical report, BTS and SIGN, UK, 2011.

[SB13]   Mark J Sanders and Ronald Bruin. Are we misleading users of respiratory spacer devices? Primary Care Respiratory Journal, 22(4):466–467, nov 2013.

[SBB+06]   Hugh Smyth, Geoff Brace, Tony Barbour, Jim Gallion, Joe Grove, and Anthony J. Hickey. Spray pattern analysis for metered dose inhalers: effect of actuator design. Pharmaceutical research, 23(7):1591–6, jul 2006.

[SBKM14]   Poonam Sheth, Matthew D. Bertsch, Carrie L. Knapp, and Paul B. Myrdal. In vitro evaluation of nonconventional accessory devices for pressurized metered-dose inhalers. Annals of Allergy, Asthma & Immunology, 113(1):55–62, jul 2014.

[SH91]   Olof Selroos and Maija Halme. Effect of a volumatic spacer and mouth rinsing on systemic absorption of inhaled corticosteroids from a metered dose inhaler and dry powder inhaler. Thorax, 46(12):891–894, dec 1991.

[SHB+06]   H Smyth, Anthony J. Hickey, G Brace, Tony Barbour, Jim Gallion, and J Grove. Spray pattern analysis for metered dose inhalers I: Orifice size, particle size, and droplet motion correlations. Drug development and industrial pharmacy, 32(9):1033–1041, oct 2006.

[Shi97]   Shimadzu Corporation. Intruction Manual User's System Guide Spectrophotometer UV-2401PC. Technical report, Shimadzu Corporation, Kyoto, Japan, 1997.

Bibliography

[SLT09]   Mark Saunders, Philip Lewis, and Adrian Thornhill. Research Methods for Business Students. FinancialTimesPrentice-Hall, Harlow, England, 5th. editi edition, 2009.

[SM09]   Pavel E. Smirnov and Florian R. Menter. Sensitization of the SST Turbulence Model to Rotation and Curvature by Applying the Spalart–Shur Correction Term. Journal of Turbomachinery, 131(4):041010, 2009.

[SM14]   Dennis Sandell and Jolyon P Mitchell. Considerations for Designing In Vitro Bioequivalence (IVBE) Studies for Pressurized Metered Dose Inhalers (pMDIs) with Spacer or Valved Holding Chamber (S/VHC) Add-on Devices. Journal of aerosol medicine and pulmonary drug delivery, 27(0):1–26, aug 2014.

[SMB00]   Thomas Stifter, Othmar Marti, and Bharat Bhushan. Theoretical investigation of the distance dependence of capillary and van der Waals forces in scanning force microscopy. Physical Review B, 62(20):13667–13673, nov 2000.

[Smy03]   H Smyth. The influence of formulation variables and the performance of alternative propellant-driven metered dose inhalers. Advanced Drug Delivery Reviews, 55:807–828, 2003.

[Spr14]   Elizabeth Sprigge. Non uniform deposition of pMDI aerosol in a large volume spacer. Master thesis, Carleton University, 2014.

[SSHM13]   Stephen W. Stein, Poonam Sheth, P. David Hodson, and Paul B. Myrdal. Advances in Metered Dose Inhaler Technology: Hardware Development. AAPS PharmSciTech, 15(2):326–338, 2013.

[SSM12]   Stephen W Stein, Poonam Sheth, and Paul B Myrdal. A model for predicting size distributions delivered from pMDIs with suspended drug. International journal of pharmaceutics, 422(1-2):101–15, jan 2012.

[Sul00]   Sulzer Innotec. Best Practices Guidelines: ERCOFTAC Special Interest Group on "Quality and Trust in Industrial CFD". ERCOFTAC, 2000.

[Tan15]   Akihiko Tanaka. Past, Present and Future Therapeutics of Asthma: A Review. Journal of General and Family Medicine, 16(3):158–169, 2015.

[Tas98]   Donald P. Tashkin. New devices for asthma. Journal of Allergy and Clinical Immunology, 101(2):S409–S416, feb 1998.

[Tay97]   John Robert Taylor. An introduction to error analysis: the study of uncertainties in physical measurements. University Science Books, Sausalito, California, 2nd edition, 1997.

[TIA13]   Jiyuan Tu, Kiao Inthavong, and Goodarz Ahmadi. The Human Respiratory System. In Elias Greenbaum, editor, Computational Fluid and Particle Dynamics in the Human Respiratory System, Biological and Medical Physics, Biomedical Engineering, chapter 2, pages 19–44. Springer Netherlands, Dordrecht, 2013.

[Tom06]   J. Tomas. Mechanics of Particle Adhesion. Technical report, Otto-von-Guericke-University, Magdeburg, Germany, 2006.

[US 14]   US Pharmacopeial Convention. <1602> Spacers and valved holding chambers used with inhalation aerosols (USP38-NF33): In-Process Revision, 2014.

[VCD$^+$08]   J C Virchow, G K Crompton, R Dal Negro, S Pedersen, A Magnan, J Seidenberg, and Peter J. Barnes. Importance of inhaler devices in the management of airway disease. Respiratory medicine, 102(1):10–19, jan 2008.

[VLP09]   Samir Vinchurkar, P. Worth Longest, and Joanne Peart. CFD simulations of the Andersen cascade impactor: Model development and effects of aerosol charge. Journal of Aerosol Science, 40(9):807–822, sep 2009.

[VM95]   Henk K. Versteeg and W. Malalasekera. An introduction to computational fluid dynamics: the finite volume method. Longman, Harlow, England, 1995.

[vS59]   Wilton E van Sickle. Enclosed medicament container and atomizer, 1959.

Bibliography

[VVSV04]   Sylvia Verbanck, Chris Vervaet, Daniel Schuermans, and Walter Vincken. Aerosol Profile Extracted from Spacers as a Determinant of Actual Dose. Pharmaceutical Research, 21(12):2213–2218, dec 2004.

[WDH$^+$96]   J H Wildhaber, S G Devadason, M J Hayden, R. James, A P Dufty, R A Fox, Q A Summers, and P N LeSouëf. Electrostatic charge on a plastic spacer device influences the delivery of salbutamol. The European respiratory journal, 9(9):1943–1946, sep 1996.

[WFT$^+$12]   William Wong, David F. Fletcher, Daniela Traini, Hak Kim Chan, and Paul M. Young. The use of computational approaches in inhaler development. Advanced Drug Delivery Reviews, 64(4):312–322, 2012.

[Whi98]   Frank M White. Fluid Mechanics. McGraw-Hill, New York, 4th edition, 1998.

[WJ99]   Yi Wang and P. W. James. On the effect of anisotropy on the turbulent dispersion and deposition of small particles. International Journal of Multiphase Flow, 25(3):551–558, 1999.

[WVH02]   G. Wigley, H. K. Versteeg, and D. Hodson. Near-orifice PDA measurements and atomisation mechanism of a pharmaceutical pressurised metered dose inhaler. In ILASS-Europe, Zaragoza, 2002.

[XHvH$^+$14]   Zhen Xu, Wenchi Hsu, Dirk von Hollen, Ashwin Viswanath, Kurt Nikander, and Richard Dalby. Methodology for the In Vitro Evaluation of the Delivery Efficiency from Valved Holding Chambers with Facemasks. Journal of Aerosol Medicine and Pulmonary Drug Delivery, 27(S1):S–44–S–54, aug 2014.

[YIT15]   Morteza Yousefi, Kiao Inthavong, and Jiyuan Tu. Microparticle Transport and Deposition in the Human Oral Airway: Toward the Smart Spacer. Aerosol Science and Technology, 49(11):1109–1120, nov 2015.

[YNY⁺14]   A. Yazdani, M. Normandie, M. Yousefi, M.S. Saidi, and G. Ahmadi. Transport and deposition of pharmaceutical particles in three commercial spacer–MDI combinations. Computers in Biology and Medicine, 54:145–155, nov 2014.

[ZFM04]   Y. Zhang, Warren H. Finlay, and E. A. Matida. Particle deposition measurements and numerical simulation in a highly idealized mouth–throat. Journal of Aerosol Science, 35(7):789–803, jul 2004.

[ZKKC04]   Zhe Zhang, Clement Kleinstreuer, Chong S. Kim, and Yung S. Cheng. Vaporizing Microdroplet Inhalation, Transport, and Deposition in a Human Upper Airway Model. Aerosol Science and Technology, 38(1):36–49, jan 2004.

[ZSB⁺08]   Mira G Zuidgeest, Henriëtte A Smit, Madelon Bracke, Alet H Wijga, Bert Brunekreef, Maarten O Hoekstra, Jorrit Gerritsen, Marjan Kerkhof, Johan C. de Jongste, and Hubert G Leufkens. Persistence of asthma medication use in preschool children. Respiratory Medicine, 102(10):1446–1451, oct 2008.